MICROCOPY RESOLUTION TEST CHART
NATIONAL BUREAU OF STANDARDS 1963-A

AD-A168 115

DNA-TR-85-85

THE SRI IONOSPHERIC STRUCTURE AND DYNAMICS PROGRAM—1985 RESULTS

James F. Vickrey   Nancy B. Walker
Robert C. Livingston   Teri M. Dabbs
Roland T. Tsunoda   Robert M. Robinson
Charles L. Rino   Roderick A. Heelis
SRI International
333 Ravenswood Avenue
Menlo Park, CA 94025-3434

30 June 1985

Technical Report

CONTRACT No. DNA 001-83-C-0034

Approved for public release;
distribution is unlimited.

Prepared for
   Director
   DEFENSE NUCLEAR AGENCY
   Washington, DC 20305-1000

86   5   22   009

Destroy this report when it is no longer needed. Do not return to sender.

AD.A168115

REPORT DOCUMENTATION PAGE

1a. REPORT SECURITY CLASSIFICATION	1b. RESTRICTIVE MARKINGS
UNCLASSIFIED	

2a. SECURITY CLASSIFICATION AUTHORITY	3. DISTRIBUTION / AVAILABILITY OF REPORT
N/A since Unclassified	Approved for public release; distribution is unlimited.
2b. DECLASSIFICATION / DOWNGRADING SCHEDULE	
N/A since Unclassified	

4. PERFORMING ORGANIZATION REPORT NUMBER(S)	5. MONITORING ORGANIZATION REPORT NUMBER(S)
SRI Project 5416	DNA-TR-85-85

6a. NAME OF PERFORMING ORGANIZATION	6b. OFFICE SYMBOL (If applicable)	7a. NAME OF MONITORING ORGANIZATION
SRI International		Director Defense Nuclear Agency

6c. ADDRESS (City, State, and ZIP Code)	7b. ADDRESS (City, State, and ZIP Code)
333 Ravenswood Avenue Menlo Park, CA 94025-3434	Washington, DC 20305-1000

8a. NAME OF FUNDING / SPONSORING ORGANIZATION	8b. OFFICE SYMBOL (If applicable)	9. PROCUREMENT INSTRUMENT IDENTIFICATION NUMBER
		DNA 001-83-C-0034

8c. ADDRESS (City, State, and ZIP Code)	10. SOURCE OF FUNDING NUMBERS			
	PROGRAM ELEMENT NO	PROJECT NO	TASK NO	WORK UNIT ACCESSION NO.
	62715H	I25AMXI	0	DH006533

11. TITLE (Include Security Classification)

THE SRI IONOSPHERIC STRUCTURE AND DYNAMICS PROGRAM—1985 RESULTS

12. PERSONAL AUTHOR(S)

Vickrey, James F.; Livingston, Robert C.; Tsunoda, Roland T; Rino, Charles L.;

13a. TYPE OF REPORT	13b. TIME COVERED	14. DATE OF REPORT (Year, Month, Day)	15. PAGE COUNT
Technical	FROM 830103 TO 850629	850630	222

17	COSATI CODES		18. SUBJECT TERMS (Continue on reverse if necessary and identify by block number)
FIELD	GROUP	SUB-GROUP	Radio-Wave Scintillation; Total Electron Content
17	02	.1	Plasma Turbulence; Convective Plasma Instabilities.
20	09		Ionospheric Irregularities;

19. ABSTRACT (Continue on reverse if necessary and identify by block number)

This report describes recent observations of high-latitude ionospheric structure and dynamics from the HILAT satellite and the Sondrestrom and EISCAT incoherent-scatter radars. Plasma turbulence theory and ionospheric plasma diffusion processes are also described. Measured variations in latitude and local time of total electron content, levels of radio-wave scintillation, and magnetospheric electrodynamics are presented for the northern polar regions. Seasonal and solar cycle variations of these phenomena are examined. Magnetic-flux-tube interchange produced by magnetospheric electrostatic turbulence (rather than local instability polarization fields) is suggested as an important source of high-latitude ionospheric structure. The large-scale magnetospheric-potential field is also shown to be capable of steepening and structuring plasma gradients. These processes would certainly structure late-time nuclear-produced plasma.

20. DISTRIBUTION / AVAILABILITY OF ABSTRACT	21. ABSTRACT SECURITY CLASSIFICATION
☐ UNCLASSIFIED/UNLIMITED ☒ SAME AS RPT ☐ DTIC USERS	UNCLASSIFIED

22a. NAME OF RESPONSIBLE INDIVIDUAL	22b. TELEPHONE (Include Area Code)	22c. OFFICE SYMBOL
Betty L. Fox	(202) 325-7042	DNA/STTI

DD FORM 1473, 84 MAR

83 APR edition may be used until exhausted
All other editions are obsolete

12. PERSONAL AUTHOR(S) (Continued)

Walker, Nancy B.; Dabbs, Teri M.; Robinson, Robert M.; and Heelis, Roderick A.

18. SUBJECT TERMS (Continued)

High-Latitude Ionospheric Dynamics

Accession For	
NTIS GRA&I	☒
DTIC TAB	☐
Unannounced	☐
Justification	
By	
Distribution/	
Availability Codes	
Dist	Avail and/or Special
A-1	

QUALITY INSPECTED 3

TABLE OF CONTENTS

TABLE OF CONTENTS (Continued)

2

TABLE OF CONTENTS (Continued)

TABLE OF CONTENTS (Concluded)

LIST OF ILLUSTRATIONS

5

LIST OF ILLUSTRATIONS (Continued)

LIST OF ILLUSTRATIONS (Continued)

8

LIST OF ILLUSTRATIONS (Continued)

LIST OF ILLUSTRATIONS (Concluded)

12

SECTION I
INTRODUCTION AND EXECUTIVE SUMMARY

To predict the propagation disturbance on Department of Defense (DoD) satellite communication and surveillance channels, the spectrum of plasma density fluctuations along the ray path must be known. At any given time, this spectrum constitutes a balance between the strengths and scale-size dependencies of the structure's driving and dissipative mechanisms. The physical processes that produce or erode plasma structure in both naturally occurring and nuclear-produced plasma at late times are the same. Of course, the magnitude of the driving forces and the plasma densities themselves are much larger in the nuclear case. Nevertheless, a thorough understanding of the balance between sources and sinks of naturally occurring plasma structure can lead to extrapolations appropriate for nuclear conditions.

In addition to being a natural analog of the nuclear environment, high-latitude ionospheric structure degrades DoD satellite systems in strategically important geographic regions. For this reason, a long-term DoD goal is to develop a predictive capability for high-latitude ionospheric structure and its effects on rf propagation. Improved theoretical modelling focussed on the data being collected by the DNA HILAT satellite and ground-based observatories is making substantial progress toward this goal.

The study of ionospheric plasma structure and high-latitude dynamics is a rapidly evolving field. The progress being made is in large part a result of the conscious interaction between theory, experiment, and innovative data analysis techniques. Blending of the diverse, but complementary, expertise that is required for progress in this area is illustrated in this report.

13

Despite the variety of physical processes that contribute to the irregularity spectrum that we ultimately observe, we have found that the framework that we proposed earlier for structure morphology is still applicable. That framework consists of accurately specifying (1) the source of plasma structure, (2) the lifetime of structure once produced, and (3) where structure convects to during its lifetime. This report is organized along these same lines. In Section II, we show that important sources of high-latitude F-layer plasma are directly tied to the convection pattern. For example, enhanced electron densities and soft auroral arcs are consistently seen at the afternoon-sector convection-reversal boundary where the magnetospheric electric field converges. We also point out that solar-produced plasma convected from lower latitudes is an important source of polar-cap ionization. This fact suggests seasonal variations in polar-cap morphology, which have been borne out in the HILAT observations.

In Section II, we also examine the precipitation-source function in the nighttime auroral oval. We show that a precipitation-source function coincident with the upward field-aligned current pattern at the Harang discontinuity is required to reproduce Chatanika radar observations. This modelling effort also shows that plasma structuring and steepening is a natural consequence of incompressible convection—even in a well-behaved potential pattern.

The HILAT program is especially well suited for hypothesis testing because, in addition to measuring the forces that produce plasma structure, the structure itself is diagnosed. The growing data base of scintillation statistics provided by HILAT is the "answer" against which predictive models will eventually be tested. A summary of some spectral characteristics that survive averaging over diverse magnetic conditions is presented in Section II. More restrictive sorting techniques that are tied to magnetospheric boundaries are currently being developed and will be reported elsewhere.

The possibility of producing structure in plasma density by a structured convection-velocity field has been recognized for some time. It has

14

only been through innovative analysis of HILAT observations, however, that velocity structure has been quantitatively assessed and appreciated as an important source of high-latitude irregularities. Some preliminary quantitative observations are presented in Section III.

Any credible, predictive physical model of solar-wind magnetosphere-ionosphere interaction must accurately represent the interchange of energy at various scale-size regimes. This implies that the current-voltage relationships of the magnetosphere-ionosphere circuit are properly accounted for. In Section III, we present observations showing that these electrodynamic relationships are a function of scale size. Statistical radar observations imply that at global scale sizes the cross-polar cap potential and total dissipative ionospheric current are linearly related. At smaller scales (tens of km), however, HILAT observations indicate that the magnetosphere behaves more like a constant current source; magneto-meter fluctuation levels are nearly independent of season and hence, of ionospheric conductivity. This fundamental property of the magnetosphere discovered by HILAT, has dramatic implications for the production of velocity and, ultimately, density structure. For example, to preserve divergence-free current flow everywhere, we might expect the velocity field structure to be enhanced in the lower conducting winter hemisphere. This tendency is very striking in the observations presented in Section III.A. In Section III.B, we review the results of some recent experiments that address the effectiveness of polarization fields in structuring plasma at very large-scale sizes, say greater than 50 km.

Turning to scale sizes smaller than the neutral scale height at which we expect the irregularity structure to be amenable to statistical modelling, we present in Section III.C some preliminary results that suggest that a turbulence-like cascade of structure may be responsible for the shallowly sloped intermediate-scale spectral regime that dominates the average spectral characteristics. Structure in this regime is larger than the freezing scale where diffusive processes are important, yet smaller than the medium scale where aeronomic processes impart structure directly to the plasma.

15

As mentioned above, we view the observed spectrum of structure as reflecting a balance between source and dissipative mechanisms. In Section IV, we describe our experimental and theoretical attempts to examine the diffusion processes that ultimately remove F-region plasma structure. The experimental evidence indicates that the effective rate of diffusion of plasma across magnetic field lines in the F layer depends on the scale size of the structure being removed. Although this result sounds surprising at first, we show theoretically that diffusion that depends on scale size is a natural consequence of the electrical coupling along magnetic field lines between the E- and F-layers. We have developed a model that predicts the temporal evolution of an arbitrary initial spectrum of F-region structure. Although each scale size is assumed to evolve independently (i.e., nonlinear mode coupling is not included), all important E-region coupling effects (including image irregularity formation) are retained. This model has shown that E-region processes can dominate the evolution of the F-layer spectrum. The model is currently being refined and expanded to allow examination of the altitude dependence of current closure, image formation, and related effects on diffusion.

This brief summary has only highlighted a few of the significant new results coming from the DNA HILAT program. The intent, nonetheless, is to properly reflect the rapid pace at which progress in understanding plasma structuring processes is being made. A predictive physical model for high-latitude irregularities is an ambitious goal, and the continued progress, such as that reported here, makes pursuing it reasonable.

SECTION II
EARLY MORPHOLOGICAL RESULTS FROM THE
HILAT SATELLITE AND THE SONDRESTROM INCOHERENT-SCATTER RADAR

A. **Plasma Density Features Associated with Magnetospheric Convection**

A principal concern for predicting the behavior of late-time nuclear-produced plasma at high latitudes is to better define the high-latitude convection pattern and its variations. Also, as we will show in this section, there are at least two important sources of natural high-latitude ionization that are directly related to the magnetospheric convection pattern. The first is soft electron precipitation at the afternoon convection reversal boundary. The second is convection of solar-produced plasma through the dayside "throat" and into the polar cap.

Before relocating the radar to Sondre Stromfjord, the nature of the convection pattern above about 70° invariant latitude was revealed only through the combination of many "snapshots" of data taken from satellites, barium releases, balloons, and rockets. The radar provides long-term continuous coverage of the ionospheric flow above a fixed region on the globe.

The convection pattern that is observed by the radar can be described generally by two-cells whose flow direction is parallel to the auroral oval. Because the size of the cells depend on magnetic activity, the sense of the interplanetary magnetic field, and the like, there are occasions when only one side of a cell lies within the field of view of the radar. However, frequently the convection reversal boundary is near Sondrestrom for both the morning and evening cells and a clear pattern of sunward flow at lower latitudes and antisunward flow at high latitudes is revealed.

17

An example is shown in Figure II.A.1(a), which displays data from 18 May 1983. A two-celled convection pattern is evident with the convection reversal boundary nearly overhead at Sondrestrom. These reversals are shearlike, and there is no obvious evidence of a "throat" near local noon. Associated with the shear reversal in the afternoon sector are enhanced F-region densities shown in Figure II.A.1(b).

The enhanced F-region plasma is accompanied by elevated electron temperatures suggesting that soft particle precipitation is the source of the density enhancement. Indeed, models of magnetospheric electrodynamics imply that precipitation should occur in regions where the magnetospheric electric field converge, as is the case in the afternoon sector. Subsequent coordinated observations between the radar and HILAT have verified the existence of a soft electron flux carrying an upward field-aligned current along this afternoon shear reversal boundary. In the morning sector on this particular day, $\nabla \cdot E > 0$ and, correspondingly, F-region densities are not enhanced even though the flow is sheared in that region also.

A second feature of ionospheric F-region structure that has been directly linked to magnetospheric convection is an ionization enhancement that occurs at the rotational convection reversal near magnetic noon. This plasma density enhancement appears when there is a significant or dominant antisunward component of flow.

The radar data in Figure II.A.2(b) from September 1983 have a significant antisunward flow. The period of interest is the period from 1200 to 1400 local time (LT). An enhancement of approximately a factor of 3 in the electron density can be seen during this period. The local time extent of the enhancement decreases with increasing latitude and is about one hour above Sondrestrom. Unlike the ionization feature associated with the afternoon convection reversal, the electron and ion temperatures, T_e and T_i, are approximately equal within the enhancement, but T_e is somewhat elevated over T_i outside of the enhancement. This anticorrelation between T_e and N_e is expected in the absence of a heat source because the electron energy loss rate increases with N_e.

18
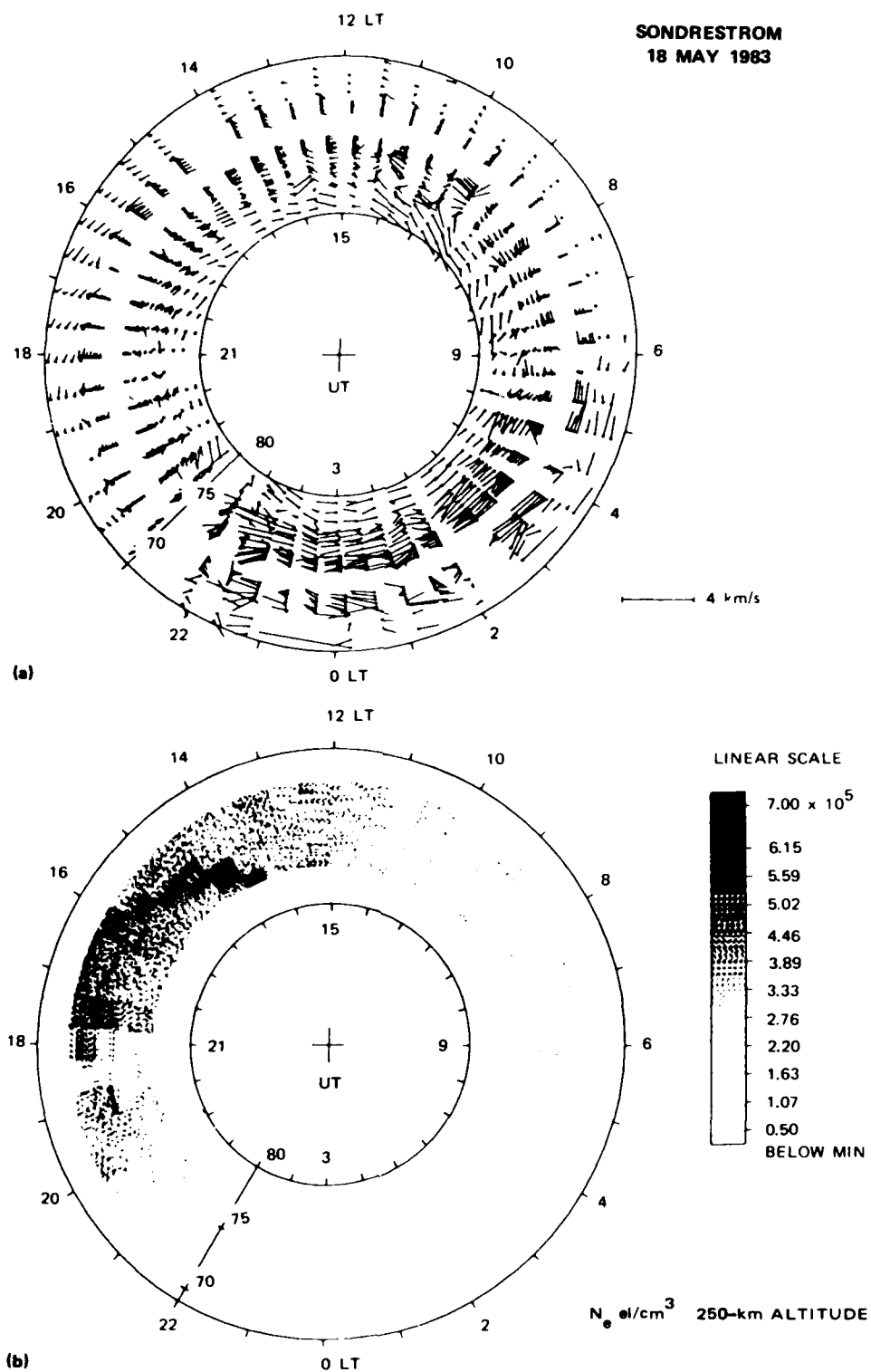
Figure II.A.1.   Diurnal patters of (a) plasma convection and
(b) F-region number density.

19

LOG SCALE

3.00×10^5
2.25
2.52
2.01
1.79
1.59
1.42
1.27
1.13
1.01
0.90
0.80
BELOW MIN

2000 m/s

(a) N_e AT 350-km ALTITUDE

(b) ION DRIFT VECTORS
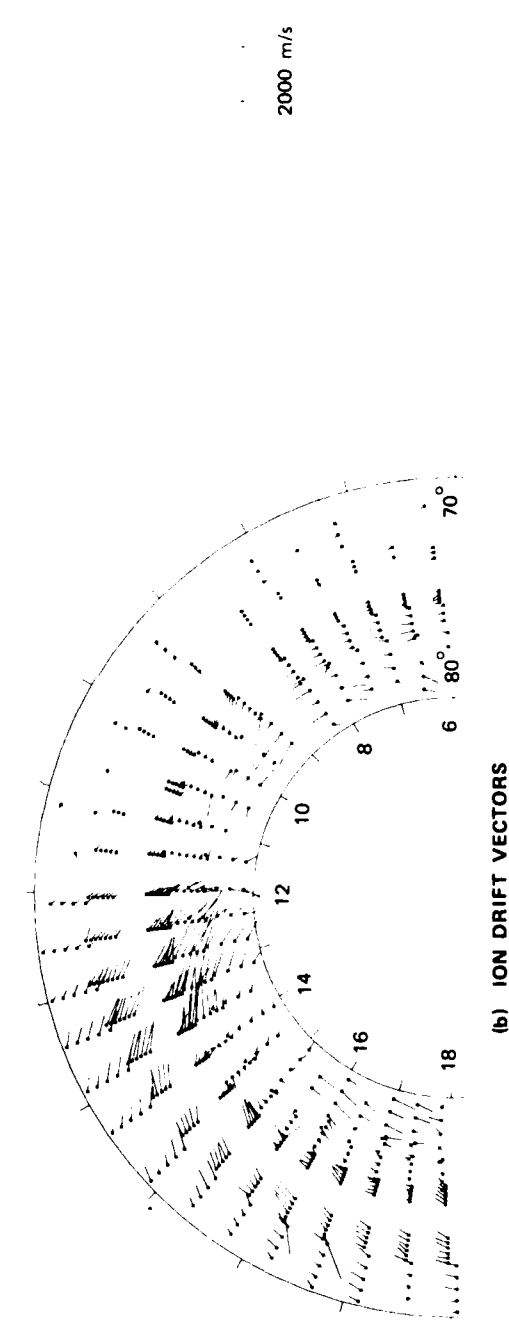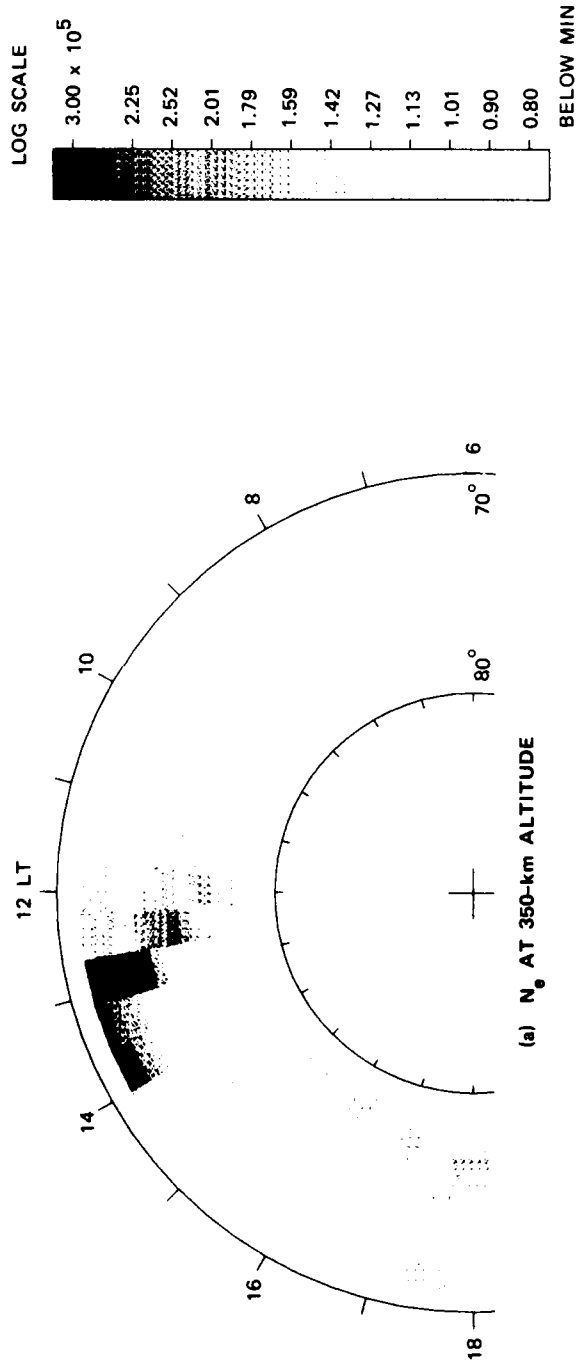
Figure II.A.2.   Clock-dial view of 14 September 1983 data from 70° to 80° Λ invariant latitude for 12 hours around noon. The feature of interest is the enhancement in N_e and the large northwest convection that occurred shortly after noon.

20

The density gradient on the northeastern edge of the enhancement is quite steep. It is along this boundary that the largest drift velocities were observed. Schunk et al. [1976][*] and Kelly and Wickwar [1981] have shown that in regions of large electric fields (i.e., large drift velocities) the F-region densities are depleted due to an enhanced loss rate of O^+ ions. Apparently, this process caused the density at the F-region peak in this region just outside of the enhancement to be even less than in other regions outside the enhancement.

High-spatial-resolution cross-sections of the ionization ridge were obtained during an orthogonal scan experiment. The experiment mode consists of consecutive scans of the antenna beam in orthogonal planes; the first along the magnetic meridian from north to south and the second orthogonal to it (i.e., magnetically west to east). Both planes contain the local zenith; hence, the east-west scan is not in the plane of the L shell, but because of the high dip angle (80.3°), there is little difference between the plane scanned and the L shell. Two pulses were transmitted alternately providing 9- and 48-km range resolution. The antenna scan limits allowed coverage in the F region of about 700-km distance from Sondrestrom at 350-km altitude. Thus, the east-west scans provide coverage of approximately one hour of local time. With the 20-min antenna-cycle time, a given local time is sampled by the radar three different times: first to the east of the radar, then overhead, and finally to the west. This overlapping coverage allows some separation of spatial and temporal variations that is not possible using only meridian scans.

Figure II.A.3 shows consecutive contour maps of electron density as a function of altitude and magnetic east-west distance from Sondrestrom. The period covered is from 1056 LT [1156 magnetic local time (MLT)] to 1224 LT on 27 February 1983. The feature of interest is the ionization enhancement (N_e $7.5 \times 10^5 cm^{-3}$) at 300 km-altitude. The enhancement was first detected to the east of the radar at about 1030 LT. As the radar rotated with the earth, the ionization enhancement eventually was overhead

---

[*] References are listed at the end of this report.

21
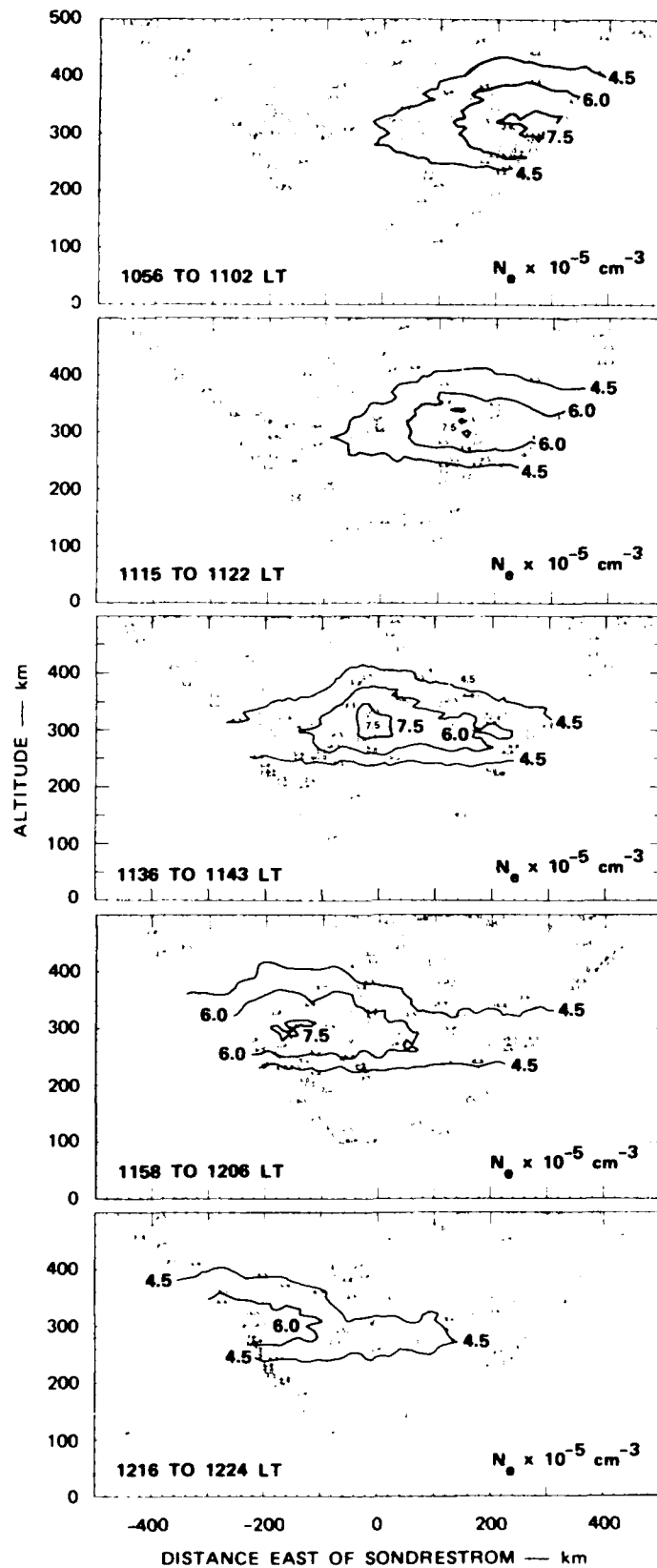
Figure II.A.3. Consecutive contour maps of electron density as a function of altitude and distance east of the radar. The contour interval is 5×10^4 cm^{-3}.

22

at ~1140 LT and later disappeared from the radar's field of view to the west. The level of the enhancement was a factor of two or more over the background and was confined to altitudes above ~ 250 km.

By comparing consecutive east-west and north-south scans, we can gain some insight into the three-dimensional character of the enhancement. Figure II.A.4 shows such a comparison. The top panel shows the east-west scan when the ionization enhancement was overhead. The bottom panel shows the next consecutive scan from north to south. In both planes the enhancement only appears at the F-layer peak and above. Interestingly, the width of the enhancement is less in the east-west plane than in the north-south plane. This is particularly apparent at the higher altitudes (i.e., 350 to 400 km). Thus, the geometry of the enhancement is anisotropic and "ridgelike" extending further in the north-south than in the east-west direction.

Figure II.A.5 shows a plan view of the ionization ridge in geographic coordinates. Indications are made along each scan plane of regions where the electron number density exceeded $6 \times 10^5 \, cm^{-3}$ and $7 \times 10^5 \, cm^{-3}$, corresponding to approximately 50 percent and 90 percent enhancement over the background. The scale of the time axis is such that the east-west distance is the same as the north-south distance at the latitude of Sondrestrom. This shows that the ridge of ionization was indeed more or less fixed in space as the radar rotated beneath it. The ridge was oriented north-northwest magnetically, in the direction of the drift velocity.

We have presented observations of the three-dimensional ionization distribution in the vicinity of the dayside cusp. The ionization signature takes the form of an anisotropic, north-south extended, ridge of ionization that is less than one hour wide in local time at the latitude of Sondrestrom. It is slanted in local time to the west of north corresponding to the direction of the drift velocity.

Observations of the electron and ion temperatures inside and outside of the 27 February enhancement have been presented by Kelly [1983]. His observations show that the ion temperature is unchanged by the presence of of enhanced density. The electron temperature, on the other hand, is
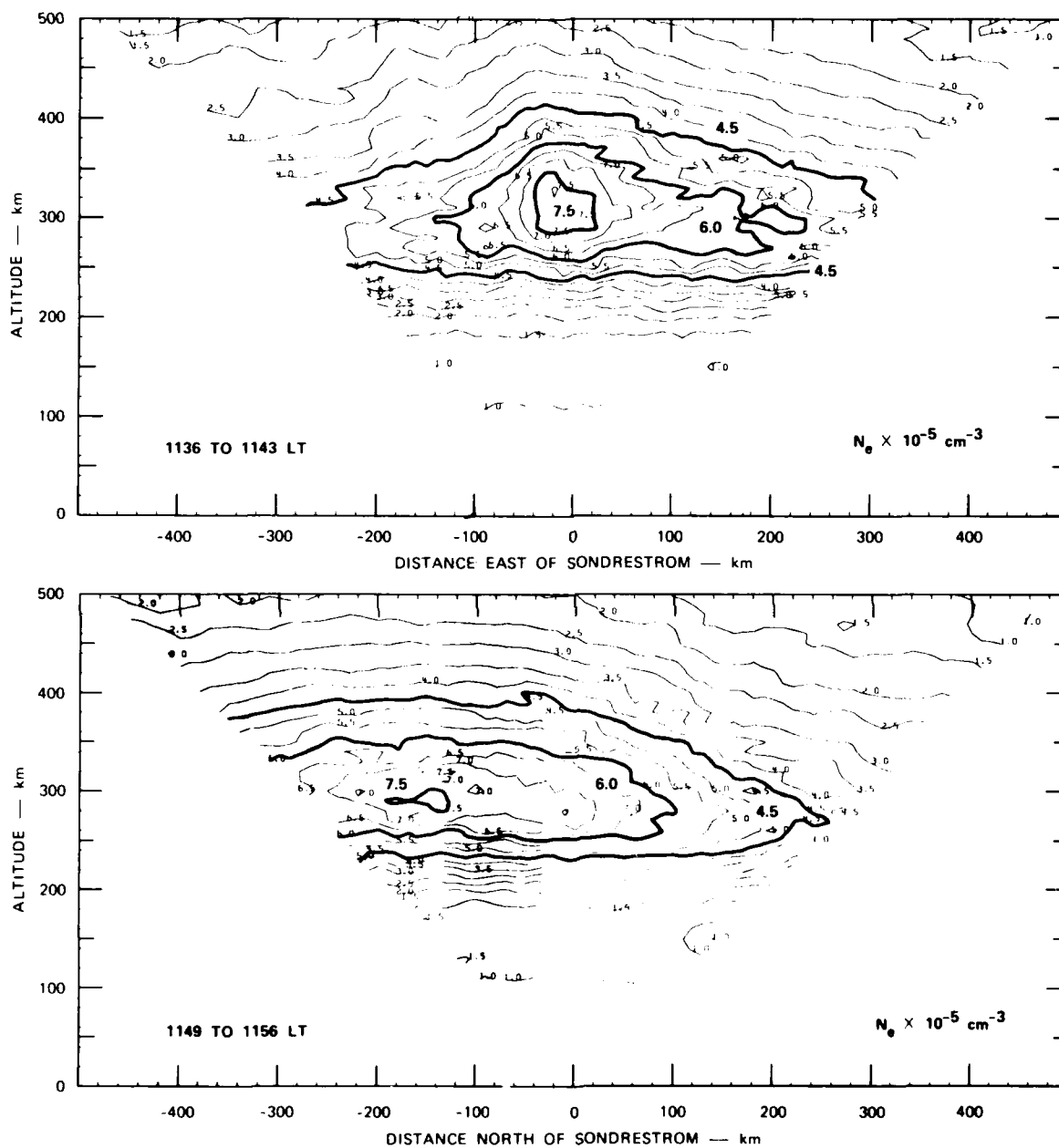
Figure II.A.4.   Cross-sectional view of the ionization enhancement in the east-west and north-south planes.

24

27 FEBRUARY 1983
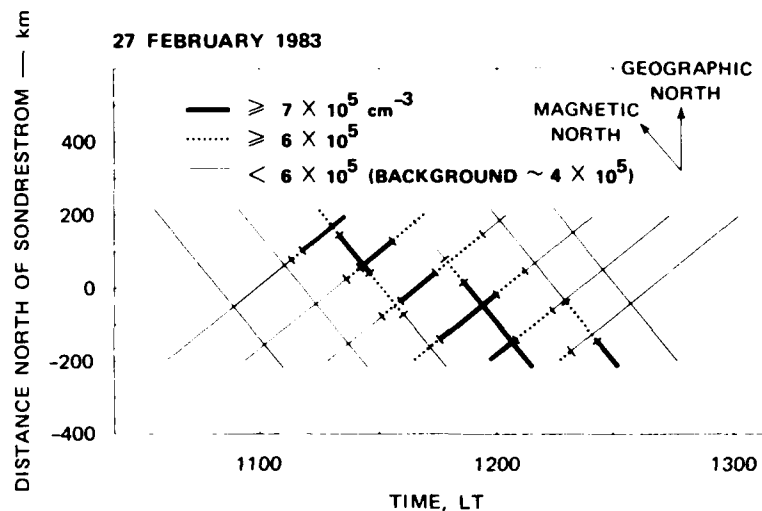
Figure II.A.5.   Plan view of the F-region ionization ridge. The dotted and bold lines indicate ionization enhancements of 50 and 90 percent, respectively, over the background.

reduced inside the enhancement. This suppression of electron temperature is consistent (provided there is no local heat source) with the expected increase in electron cooling rate where the electron number density is large [Banks and Kockarts, 1973].

Knudsen [1974] estimated that the soft-particle flux associated with the polar cusp would add approximately $2 \times 10^5 \, cm^{-3}$ to the electron number density at the F-region peak. This estimate is based on a flux of 0.2 ergs $cm^{-2} \, s^{-1} \, sr^{-1}$ and a convection velocity of 1 km/s across the cusp region assumed to be $3°$ in width. The enhancement observed in the February data is $\sim 4 \times 10^5 \, cm^{-3}$ and the convection velocity is about 600 m/s. These values are in reasonable accord with Knudsen's calculations, i.e., the convecting F region spends twice the time in the ionizing region, and the enhancement in electron number density is twice as large. However, we also note that the electron-density profiles [Kelly, 1983] indicate that diffusive equilibrium exists even at the equatorward extremes. Knudsen estimates that 75 min are required to reach diffusive equilibrium given a

25

particle energy spectrum peaked at 100 eV and to be absorbed over a 150-km altitude range. This suggests that if a soft-particle flux were the source of enhanced ionization, it must be located some 2500 km away, assuming our measured convection speed is representative for the entire path. This distance seems unreasonable. Of course, we could always postulate a spectrum of precipitating particles that would produce an altitude profile of ionization that resembled that of diffusive equilibrium. However, the spectrum assumed by Knudsen [1974] seems more reasonable because it was based on a large body of satellite measurements. Also, as discussed earlier, the electron temperature within the density enhancement is reduced as compared to regions outside the enhancement. We expect that if soft-particle precipitation were occurring, the electron temperature would be elevated.

In the September case, the convection velocity is about 1 km/s (as Knudsen assumed) in the enhanced regions, yet the density enhancement is only about 0.8 to $1 \times 10^5 cm^{-3}$. It, therefore, also appears inconsistent that the ionization enhancement is due to a local cusp-related soft-particle flux. This of course assumes that the spatial extent of the cusp does not change. Again, in this case the electron temperature was not elevated.

In an effort to provide an alternative explanation for the ionization enhancements, we have examined the electron density that would be expected if ionization were simply convected to Sondrestrom from lower latitudes where the solar zenith angle was relatively low. Using the empirical relation from Baron et al. [1983] corresponding to the February conditions, we find that at 65° geographic, for an SA equal to 138 (10.7 cm flux), the expected maximum density is $8.8 \times 10^5 cm^{-3}$. The maximum density noted in the February data overhead at Sondrestrom (67° geographic) was 7.5×10^5. In the September experiment, the expected electron density based on the empirical relation of Baron et al. [1983] for summer is $2.6 \times 10^5 cm^{-3}$ and the measured value was $3.0 \times 10^5 cm^{-3}$. The variation in the peak densities on the two days is also consistent with the known seasonal variations of the Oxygen-to-Nitrogen ratio (i.e., the winter anomaly) as discussed by Roble [1977].

26

As seen in Figure II.A.6, the lowest solar zenith angles are eastward and equatorward when Sondrestrom is at noon. Thus, the magnitude of the observed enhancements could be simply explained by transport without invoking a precipitation source. This explanation is further supported by the fact that at noon, the lowest solar zenith angles are southeast of Sondrestrom; the observed drifts were northwest.
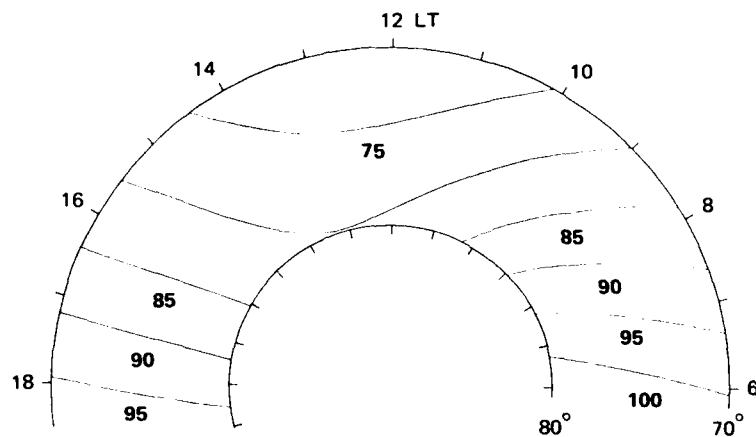
(a) FEBRUARY 1983
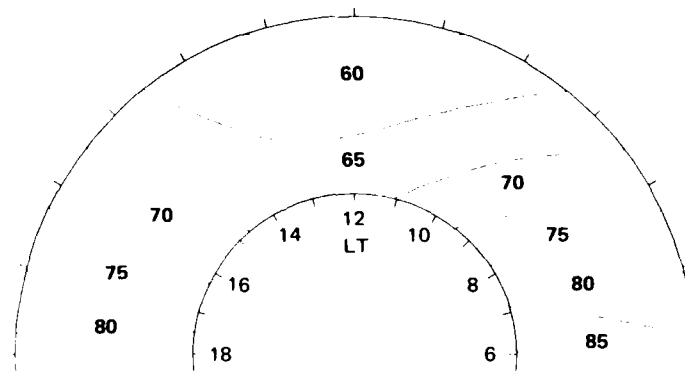
(b) SEPTEMBER 1983

Figure II.A.6. Solar zenith angles from $70°$ to $80°$ Λ invariant latitude around noon.

In summary, we have identified an important source of polar cap ionization that does not appear to be associated with soft-particle flux. Weber et al. [1984] has also reported ionization patches in the polar cap that were not coincident with a soft-particle flux. The observations

27

reported here are consistent with the idea that solar EUV produced ioniza-
tion is convected poleward from regions equatorward of the field of view
of the radar. Within the observing field of view, the enhancement is
relatively broad in local time at the lowest latitudes and becomes nar-
rower with increasing latitude. This qualitative behavior is shared by
the contours of constant solar zenith angle in Figure II.A.6. Based on
one year's observations, this ionization feature is observed whenever the
convection velocities are large and have a significant poleward component.
The fact that a large portion of polar-cap ionization may be produced by
this mechanism leads us to expect polar-cap phenomena depend strongly on
the season. This is indeed the case as will be shown in the next section.

B.   Seasonal Variations in Polar-Cap Structure

As was pointed out in the previous section, even before HILAT was
launched, we had strong evidence from Sondrestrom radar data that solar
production at low latitudes, combined with antisunward convection, con-
tribute significantly to polar-cap ionization. This led us to believe
that there are marked seasonal variations in polar-cap phenomena that
should be characterized using HILAT measurements. These seasonal effects
are very pronounced in the electrodynamic parameters as well as in the
distribution of plasma density. The electrodynamic processes will be dis-
cussed in more detail in Section III.A, which deals with the voltage-
current relationship of the magnetospheric generator. Here, we concen-
trate on in situ plasma density and variations in total electron content
(TEC).

HILAT's orbit precesses to earlier local times each day. Therefore,
we must be careful in selecting satellite passes for seasonal studies be-
cause season and local time are, to some extent, mixed. Moreover,
detailed studies of the local-time variations of specific quantities
should take into account the differences in satellite trajectory for as-
cending and descending node passes. Descending node passes are nearly
aligned with the magnetic meridian at Sondrestrom; ascending node passes
sweep through a large sector of magnetic local time. For examining the

gross seasonal changes in plasma density and TEC, however, it is suffi-
cient to sort data on the basis of date.

The data presented in Figures II.B.1(a) through (c) come from Sondre-
strom science summary files for Winter 1983, Summer 1984, and Winter 1984,
respectively. The data are plotted in invariant latitude-corrected magnetic
local-time coordinates. The rings represent 10° intervals of invariant
latitude from 50° to the pole. The data are binned and averaged in 15-min
corrected magnetic local time (CMLT) and 1° invariant latitude sectors.
Only those passes whose maximum elevation angle exceeds 45° are included in
these figures to ensure valid comparison with the TEC data presented below.

Comparison of Figures II.B.1(a) and (c) with (b) show that the in
situ plasma density at 800-km altitude is about an order of magnitude
higher in the summer than in the winter. This is true at essentially all
latitudes and local times sampled. Additionally, the somewhat lower
plasma densities in Figure II.B.1(c) compared to II.B.1(a) suggests a
general decrease in density associated with the declining solar cycle.

One should not assume that the plasma density variations at 800-km
altitude necessarily reflect those at the height of the F-layer peak.
This can be demonstrated by examining the TEC variations shown in Figures
II.B.2(a) through (c). The data are plotted in invariant latitude-cor-
rected magnetic local-time coordinates. The rings represent 10° intervals
of invariant latitude from 50° to the pole. These passes correspond to
those shown in Figure II.B.1.

Although the plasma density at 800 km was much higher in the summer
than in the winter, the TEC of the ionosphere in Figures II.B.2(a) and (b)
is comparable at these latitudes in the summer and winter. This indicates
that the density at 800 km is strongly affected by the electron tempera-
tures and, hence, the plasma scale height. In other words, the density in
the summertime is much higher at 800 km because the ionosphere is effec-
tively thicker (in altitude) than in the wintertime although the total
amount of plasma along any ray path is comparable in summer and winter.
Comparison of Figures II.B.2(a) and (c) further indicates that the solar
cycle strongly modulates the TEC at high latitudes at all local times.

SCALE   LOG N_e cm^{-3}

�> 4.40
▨ 4.10 TO 4.40
░ 3.80 TO 4.10
⠂ 3.50 TO 3.80
□ 3.20 TO 3.50
□ < 3.2
□ NO DATA

(a) WINTER 1983 (7 NOVEMBER 1983 TO 10 FEBRUARY 1984)

(b) SUMMER 1984 (5 MAY TO 8 AUGUST 1984)
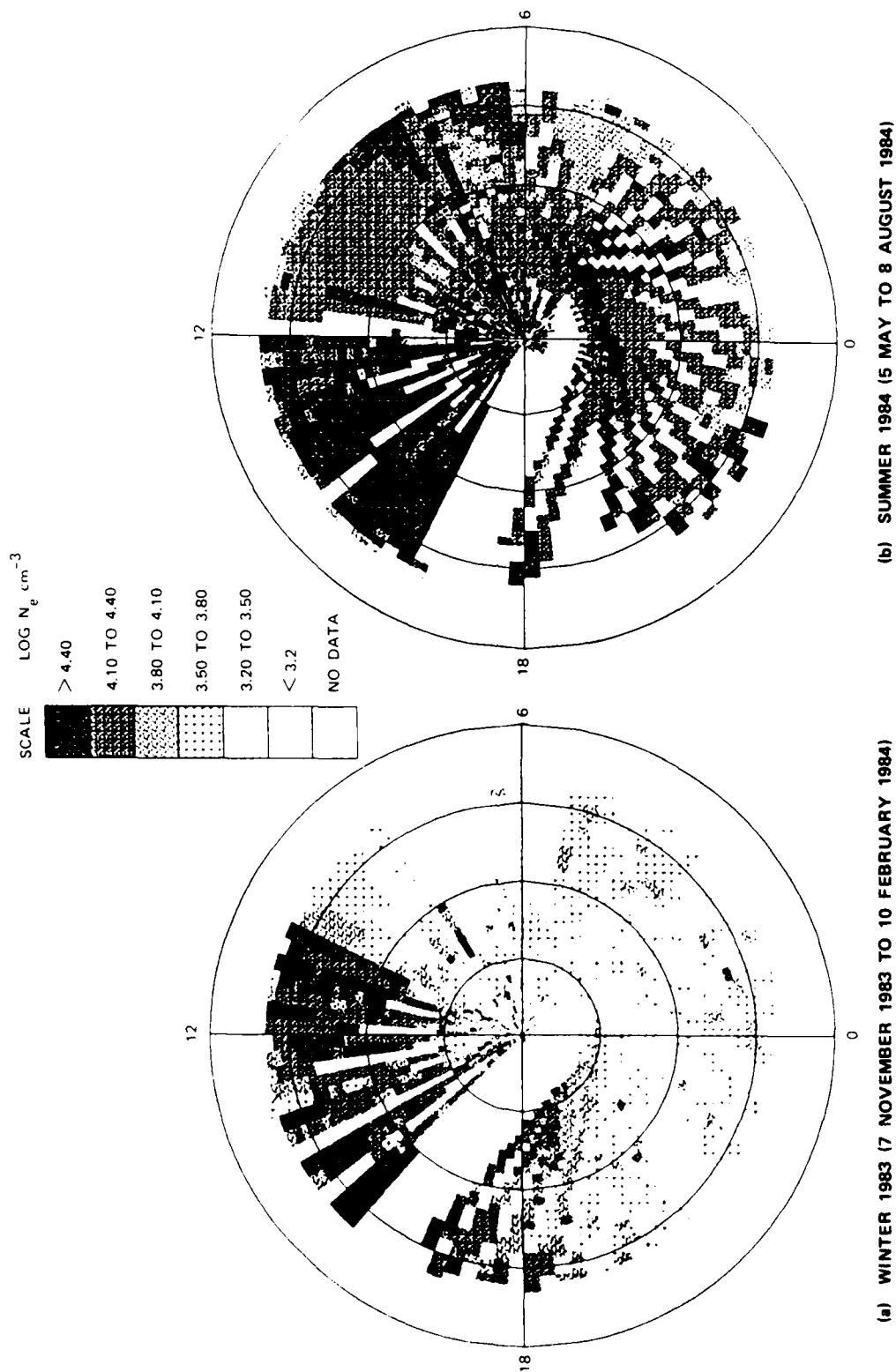
Figure II.B.1.   In SITU log plasma density measured by HILAT for high-elevation passes over Sondrestrom.

SCALE   LOG N_e cm^{-3}

■	> 4.40
▓	4.10 TO 4.40
▒	3.80 TO 4.10
⋯	3.50 TO 3.80
	3.20 TO 3.50
	< 3.2
	NO DATA
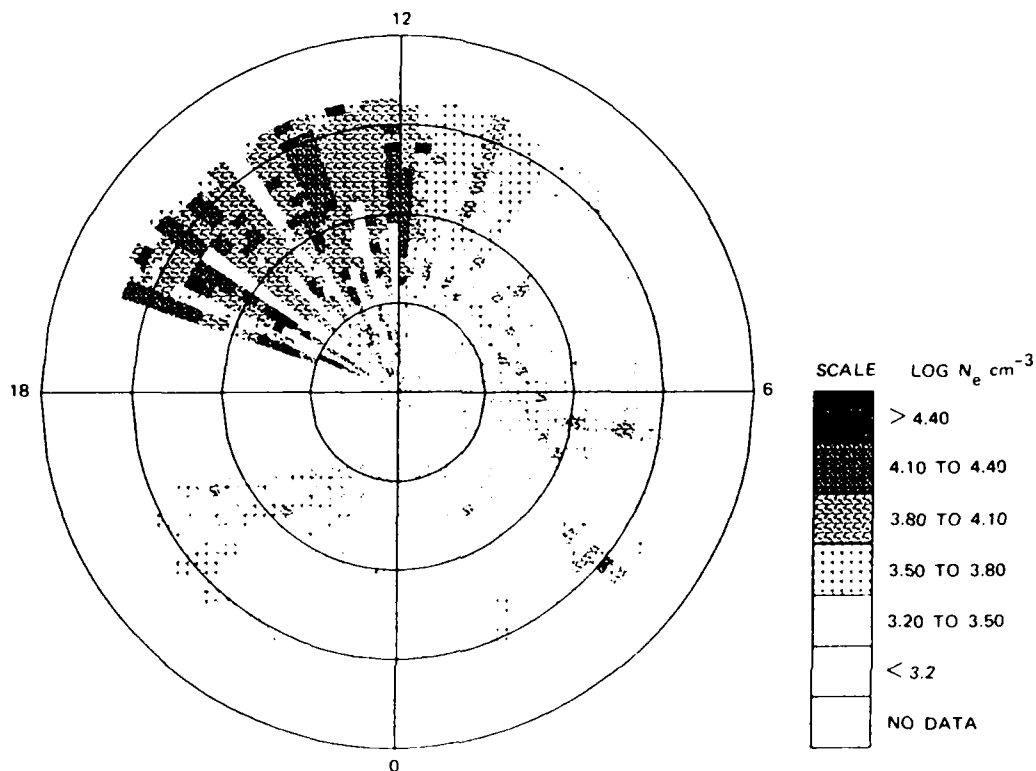
(c) **WINTER 1984 (10 NOVEMBER 1984 TO 6 FEBRUARY 1985)**

Figure II.B.1. (Concluded).

These facts have implications for scintillation morphology. For ex-
ample, in the winter, the thinner F layer must have a higher peak electron
density than in the summer for the TEC to be comparable. Therefore, if
$<|\Delta N/N|^2>$ is the same in summer and winter, the scintillation level will
be higher in winter. This general trend is in agreement with observation.
It should be kept in mind, however, that other seasonal effects are in the
same sense and may dominate this one. For example, in the summertime the
conducting E layer will short out the polarization electric fields that
drive flux tube interchange instabilities [Vickrey and Kelley, 1982].
Moreover, as is shown in Section III.A, magnetospheric electrostatic
structure is much more pronounced in the winter than in the summer. Thus,

31

SCALE   LOG TEC m^{-2}

> 17.30

17.10 TO 17.30

16.90 TO 17.10

16.70 TO 16.90

16.50 TO 16.70

< 16.50

NO DATA

(a) WINTER 1983 (7 NOVEMBER 1983 TO 10 FEBRUARY 1984)

(b) SUMMER 1984 (5 MAY TO 8 AUGUST 1984)
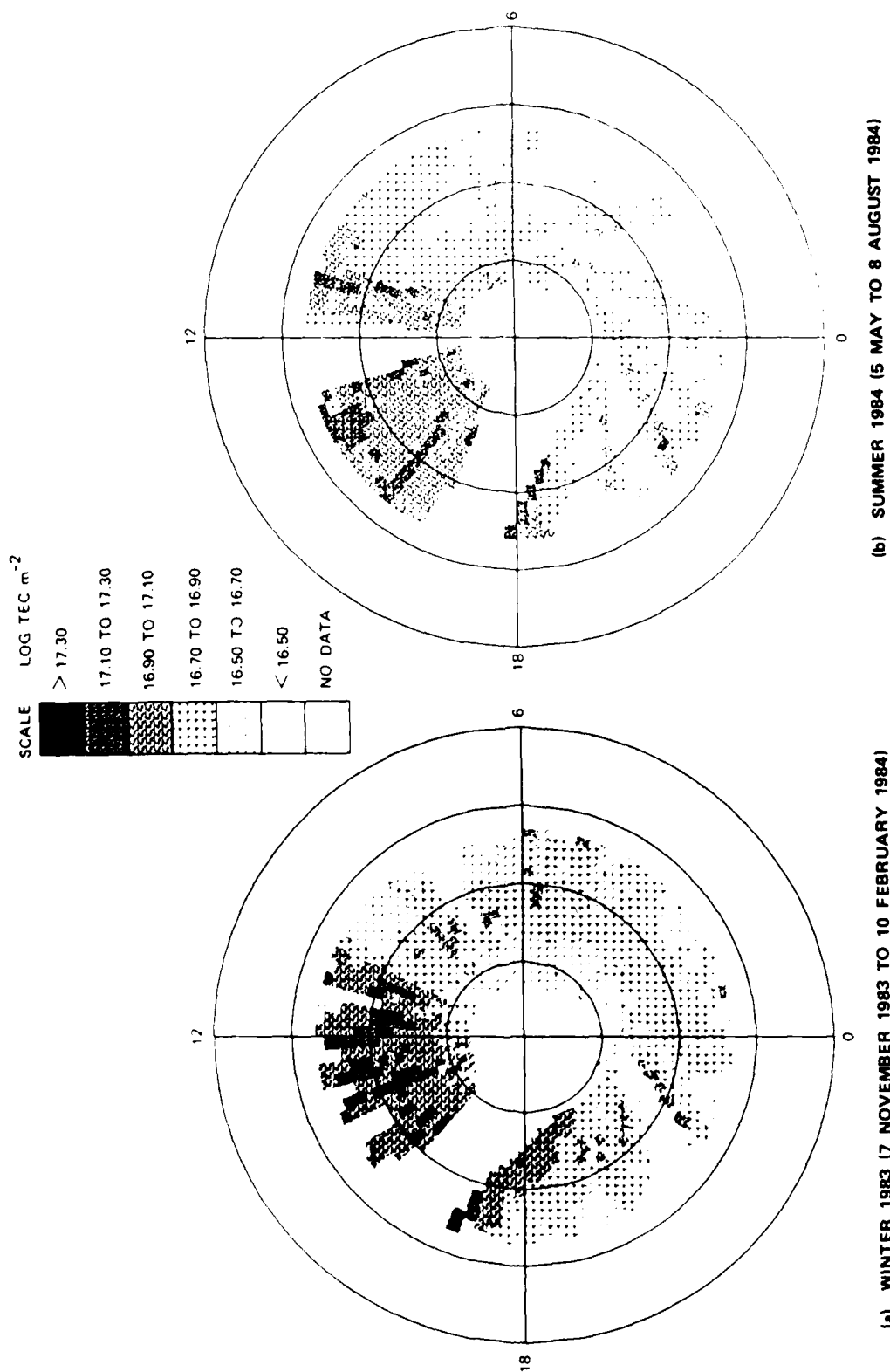
Figure II.B.2.   Log of total electron content measured at Sondrestrom for high-elevation passes at HILAT.
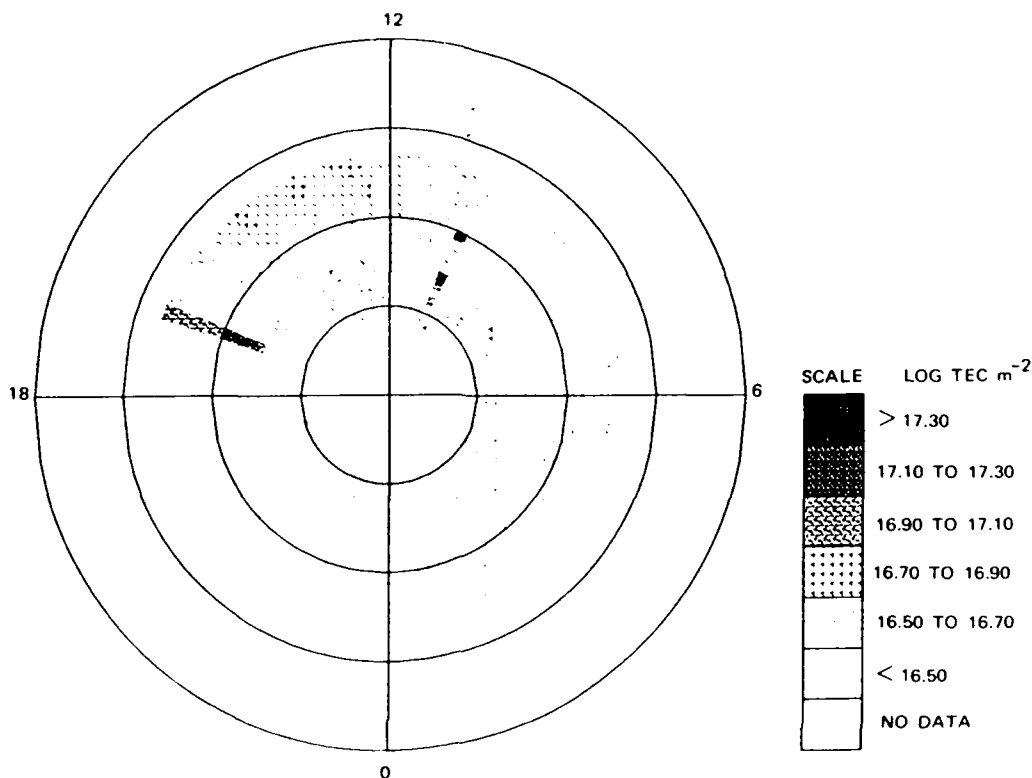
(c) WINTER 1984 (10 NOVEMBER 1984 TO 6 FEBRUARY 1985)

Figure II.B.2 (Concluded).

the seasonal trend is to (1) increase the strength of structure driving processes, (2) decrease instability damping, and (3) increase the peak plasma density being structured in the winter as compared to summer. All three of these effects should make scintillation higher in the winter than in the summer for equivalent magnetic conditions. For any given season, evidence to date suggests variations in scintillation with solar cycle are caused by the modulation in TEC.

C. Irregularity Characteristics from Phase-Scintillation Data

As mentioned in Section I, the HILAT satellite mission was specifically designed to test hypotheses. In addition to measuring the forces

that produce plasma structure, the plasma structure itself is diagnosed. The ultimate output of a predictive code will be the spectrum of plasma irregularities for a known ray path and a given set of magnetic conditions. The testing of such codes will be done by comparing them with HILAT observations. In this section, we present our preliminary summary analysis of the spectral characteristics from more than one year's data from the Sondre Stromfjord station and the first winter season's data from the Tromso station. Our first objective is to establish the average spectral characteristics as a function of invariant latitude, magnetic local time, and season. We recognize that many important dynamic features of the high-latitude ionosphere are lost in such extensive averaging. On the other hand, the robust spectral characteristics that survive the averaging can be used confidently in predictive models.

The average characteristics also provide a baseline against which variations that are induced by the more dynamic phenomena can be measured.

1.   Data Selection and Method of Analysis

For scintillation, the most important irregularities are larger than several hundred meters and have comparatively long lifetimes in the F region where they are most intense. Thus, for these structures it is valid to assume that the irregularities are "frozen" during the measurement and that time increments can be converted to space increments by using an effective scan velocity. Also, because of the noiselike character of the irregularity measurements, individual spectra exhibit a high degree of fluctuation and some means must be used to extract a measure of the average spectral density. It is generally accepted that the average spectral density function, however it is deduced, can be represented adequately by a series of power-law segments.

We have developed a procedure that allows us to fit an arbitrary number of power-law segments to measured spectral density functions (SDF)s. The number of segments and their break points are determined automatically and optimally. By applying this method to the extensive data base of HILAT phase scintillation data, we have been able to measure

34

consistent spectral characteristics without subjectively preselecting the temporal frequency intervals over which the curve fitting is performed. This is important in analyzing scintillation data because the effective scan velocity changes continuously with the propagation geometry. A fixed temporal frequency interval corresponds to a continually changing spatial interval, whereas single features in the spatial wave-number spectrum can appear at different temporal frequencies.

In the absence of diffraction and under the assumption that many irregularities intersect the propagation path, the phase SDF is directly proportional to the three-dimensional in situ SDF. Diffraction effects become increasingly important as the propagation disturbance increases, but they are most prominent at the higher temporal frequencies. The signal components that are affected by diffraction are readily detected in multifrequency data by observing departures from the nominal linear wavelength dependence. Thus, in selecting our data for summary analysis, we reject segments if the scintillation levels are very low or if there is evidence of contamination.

For the actual curve fitting, we have combined the measured VHF and UHF phase spectra to obtain a single SDF, which we normalize to the VHF phase scintillation level for an infinitely high reference frequency. Combining the measured spectra in this manner reduces the statistical fluctuations and provides a common reference level for comparisons and further analysis. In our application of the curve fitting procedure, we allow as many as six power-law segments of the form

$$\Phi(f) = T_k f^{-P_k} \qquad f_{k-1} < f < f_k \quad . \qquad (II.C.1)$$

To convert the measured temporal frequencies to a spatial wave number, we use the effective scan velocity, v_{eff}, as defined in Rino [1982]. We have used a fixed 10:1 axial ratio for rodlike irregularities. The deviations caused by varying anisotropy and sheetlike irregularities [Livingston et al., 1982] will manifest themselves principally on propagation paths that are nearly coincident with the principal irregularity

35

axes. Because the HILAT orbit drifts in local time, the number of passes that are strongly affected by deviations from the assumed anisotropy is not too large, and this procedure is adequate for determining the gross morphological features in the data.

To provide a means of normalizing our results to absolute structure levels, we assume a three-dimensional in situ irregularity spectrum of the form

$$\Phi(K, k_z) = \frac{abC_s}{[q_o^2 + q^2]^{\nu+1/2}} \quad . \quad (II.C.2)$$

It can be shown [Rino, 1982] that the corresponding one-dimensional phase SDF for $f \gg q_o v_{eff}/2\pi$ has the form

$$\Phi(f) = Tf^{-P} \qquad f \gg v_{eff} q_o/2\pi \qquad (II.C.3)$$

where

$$p = 2\nu \qquad (II.C.4)$$

$$T = C_p G \frac{\pi^{1/2} \Gamma(\nu)}{\Gamma(\nu + 1/2)} (2\pi v_{eff})^{2\nu-1} \qquad (II.C.5)$$

$$C_p = r_e \lambda \ell C_s \quad . \quad (II.C.6)$$

Definitions of the geometry-dependent factors G and v_{eff} can be found in Rino [1982].

By using Eqs. (II.C.5) and (II.C.6) with assumed anisotropy ratios and a layer thickness to estimate C_s, we can make a first-order correction for the dominant geometrical effects. If our anisotropy estimates are in error, localized enhancements or reductions will appear in the summary data. Thus, we have a means of checking sensitivity of our model to the assumed anisotropy.

36

In the summary analysis presented here, we have concentrated on the scale-size regime that encompasses structures from several tens of kilometers to less than one kilometer. These are the largest scale sizes that can be readily accommodated in a statistical model, and they are the dominant structures that cause scintillation at VHF through L band. Once the breakpoints are converted to spatial wave numbers using v_{eff}, we identify the intermediate scale as the first power-law segment with an upper break frequency that corresponds to a wavelength less than one kilometer. All the power-law segments that include structures larger than the intermediate scale are averaged together and referred to as medium-scale irregularities. We have not yet analyzed structures smaller than the intermediate scale because of possible contamination by diffraction effects and additive noise.

2. Morphology of Spectral Charcteristics

a. Spectral Index

The parameter least affected by the propagation geometry is the spectral index. In Figures II.C.1 through II.C.5, we show seasonal day-night probability distributions for intermediate-scale p index derived from the Sondre Stromfjord data. Figure II.C.6 shows the average day-night probability distributions for the entire Sondre Stromfjord data set. All the distributions are well behaved with a peak value near 2.5 for the daytime data and 2.6 for the nighttime data. For the daytime data the nonwinter seasons show slightly more spread in their range of values about the mean, but this pattern is reversed in the nighttime data. All these variations are small, however, and the overall behavior, as summarized in Figure II.C.6 is very similar to what was observed in the Wideband satellite data obtained from both equatorial and auroral-zone stations [Rino et al., 1982].

Figure II.C.7 shows the corresponding p index distribution for the first winter season from the Tromso station. The daytime distribution has many fewer points than the corresponding distribution

37
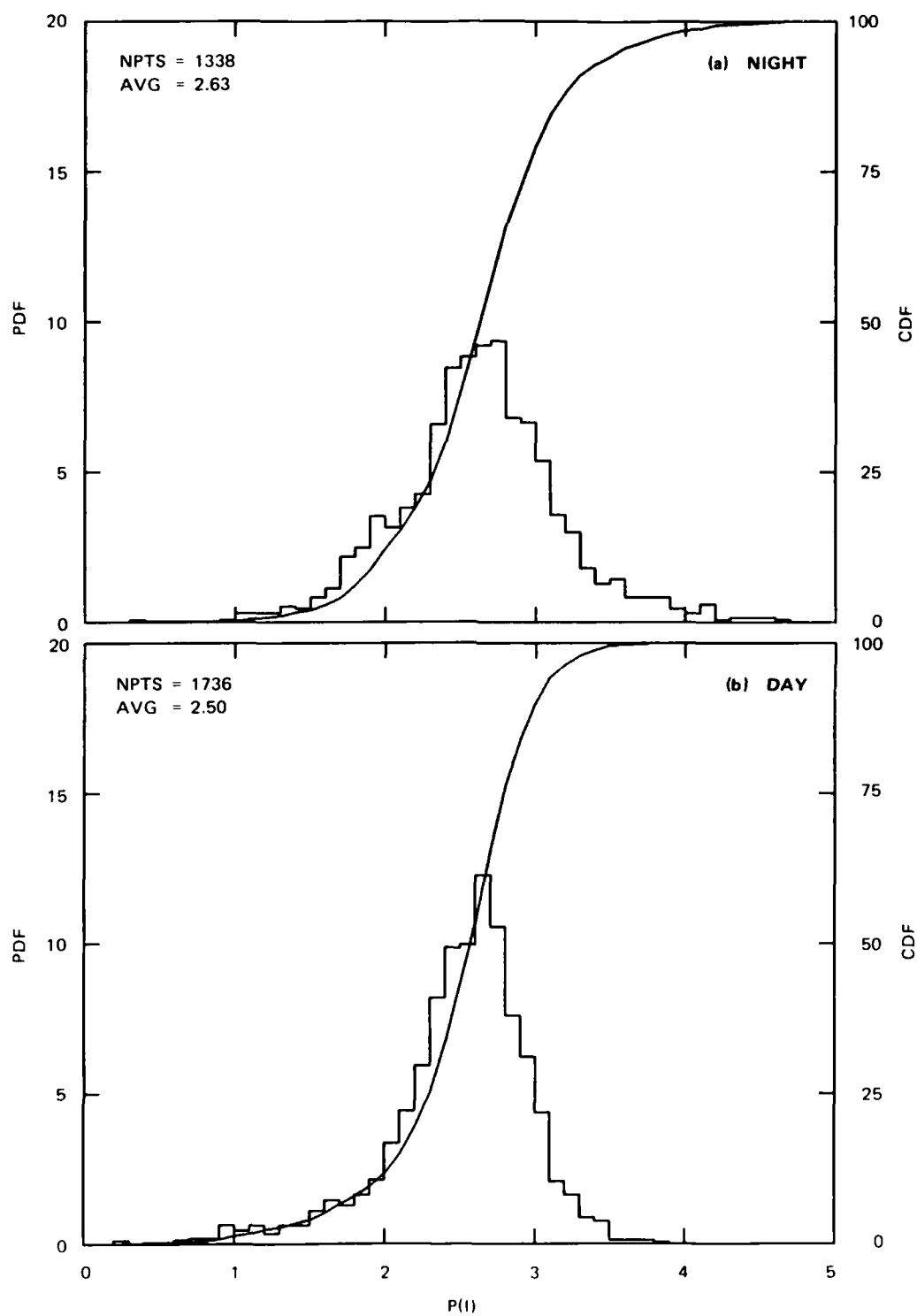
Figure II.C.1.   Sondrestrom intermediate-scale spectral-index distribution
for November 1983 to January 1984.
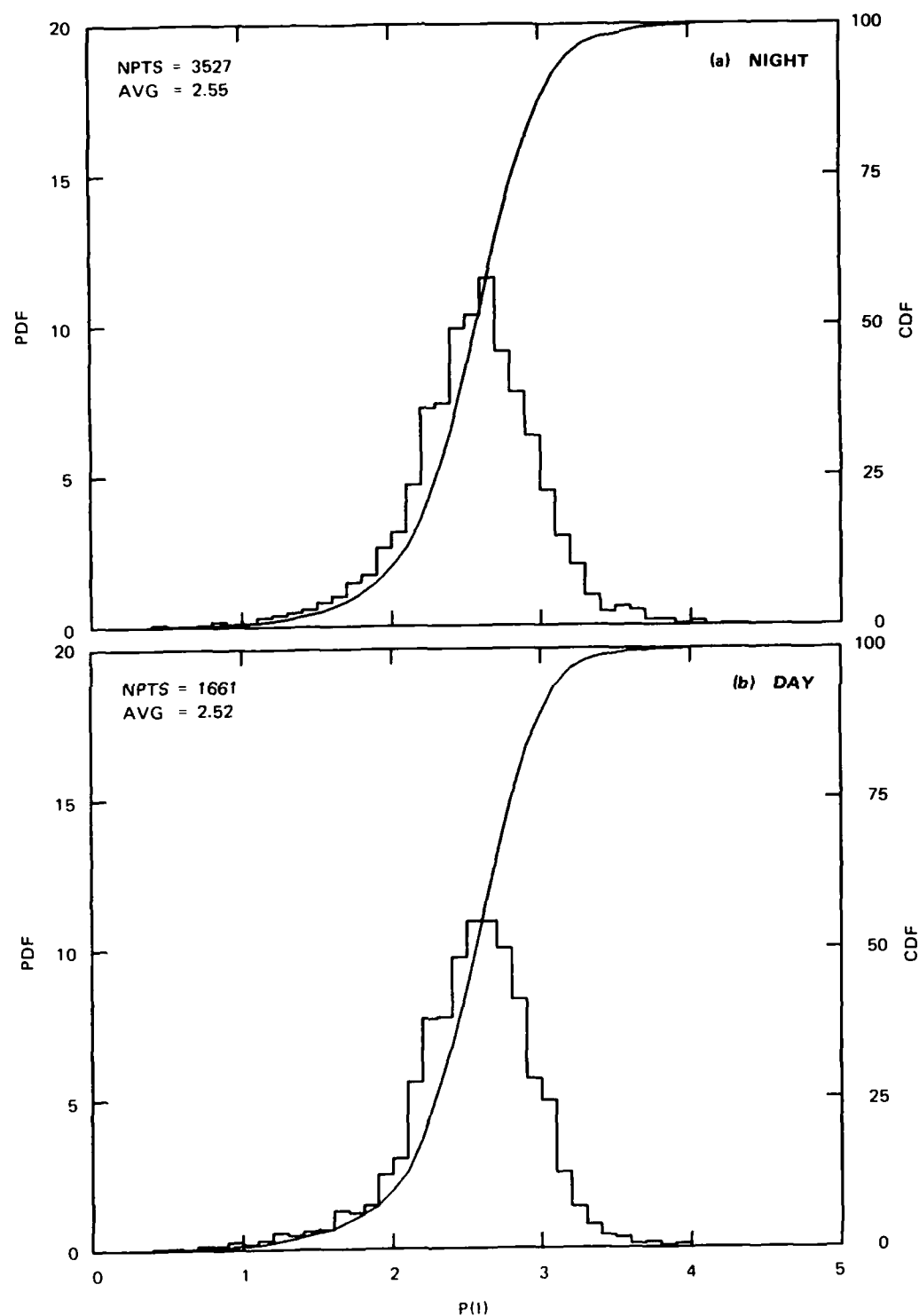
Figure II.C.2.   Sondrestrom intermediate-scale spectral-index distribution for February 1984 to April 1984.

39
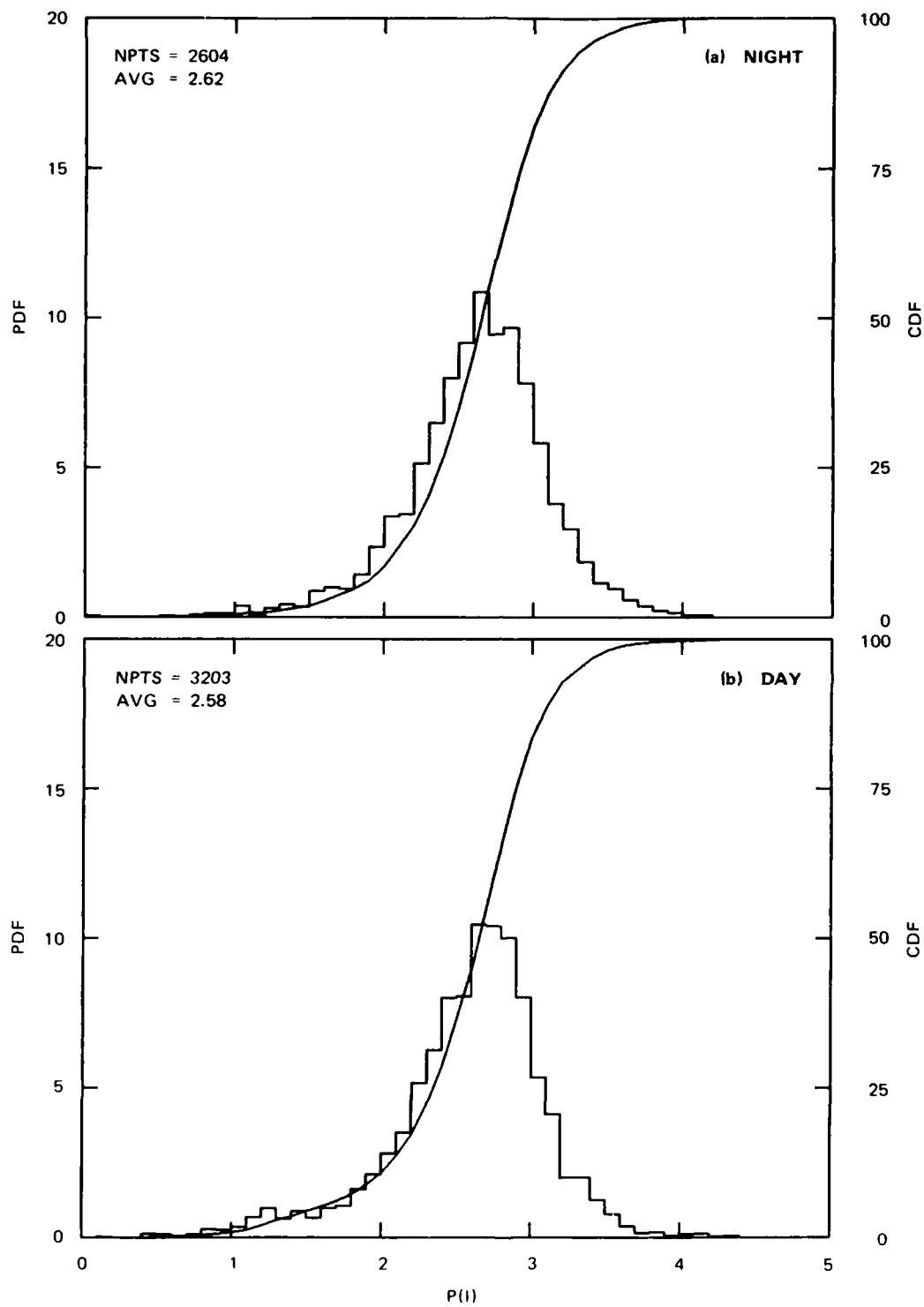
Figure II.C.3.   Sondrestrom intermediate-scale spectral-index distribution for May 1984 to July 1984.

40
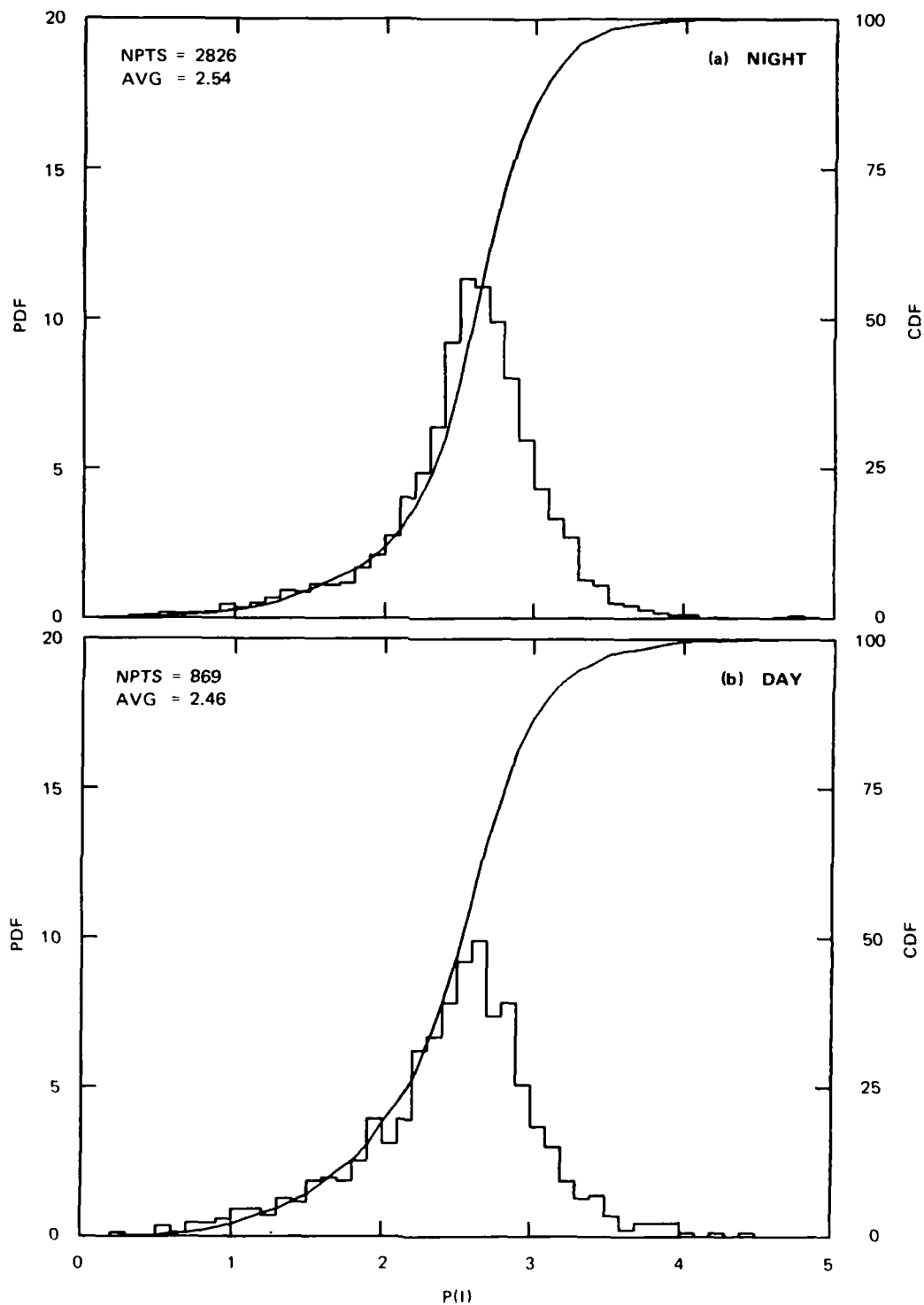
Figure II.C.4.   Sondrestrom intermediate-scale spectral-index distribution
for August 1984 to October 1984.

41
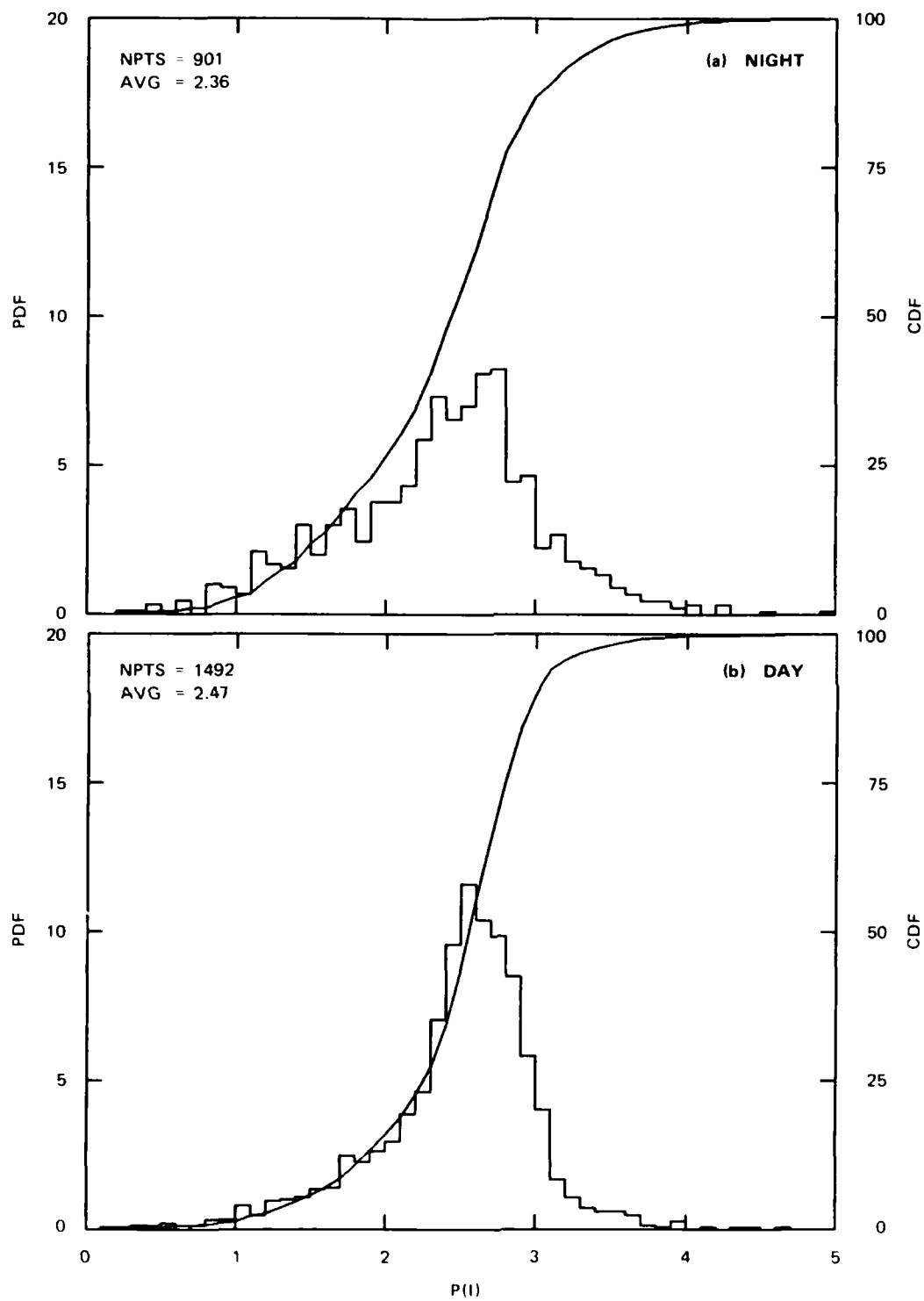
Figure II.C.5.   Sondrestrom intermediate-scale spectral-index distribution
for November 1984 to January 1985.
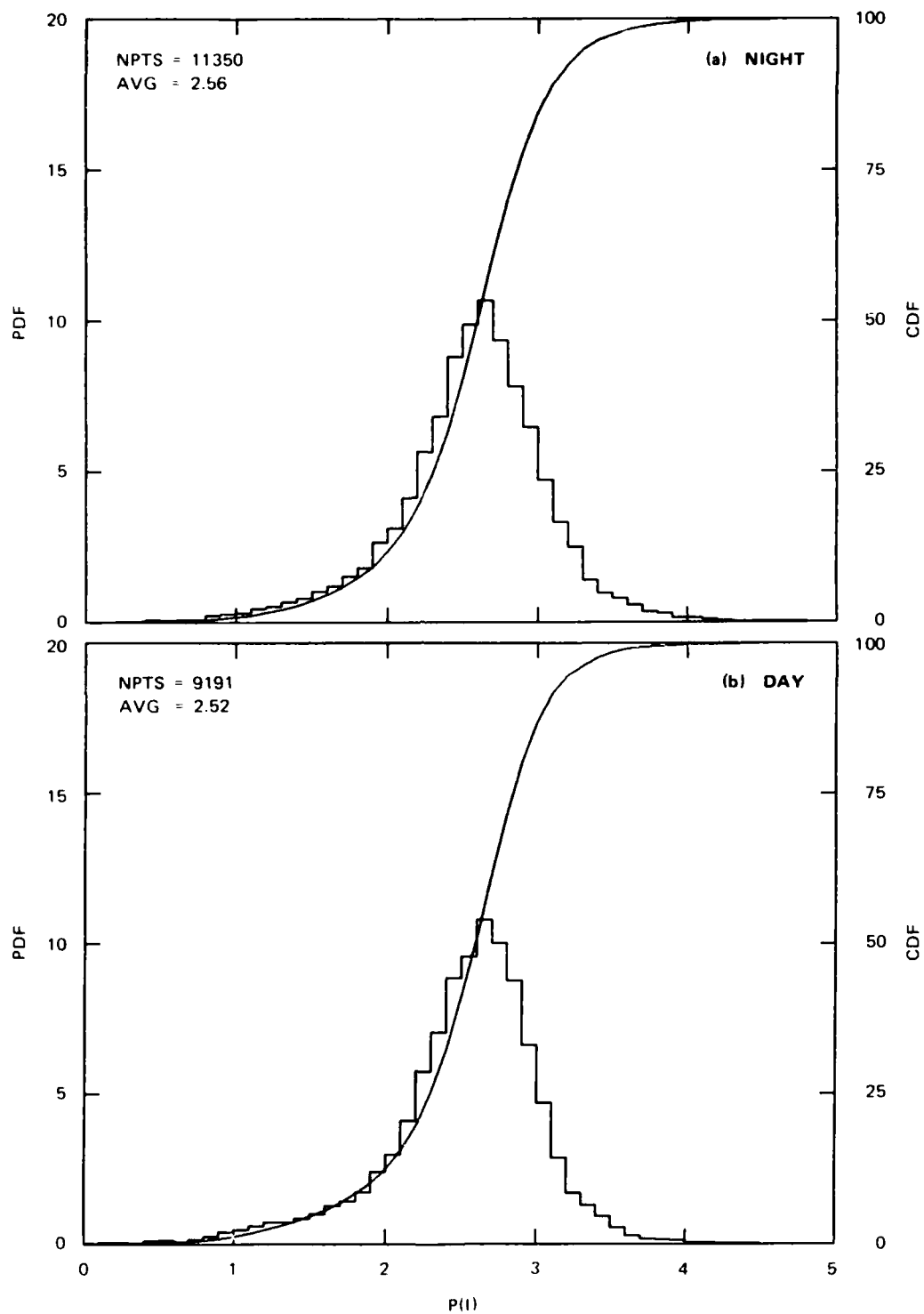
Figure II.C.6.   Sondrestrom intermediate-scale spectral-index distribution for all seasons.

43
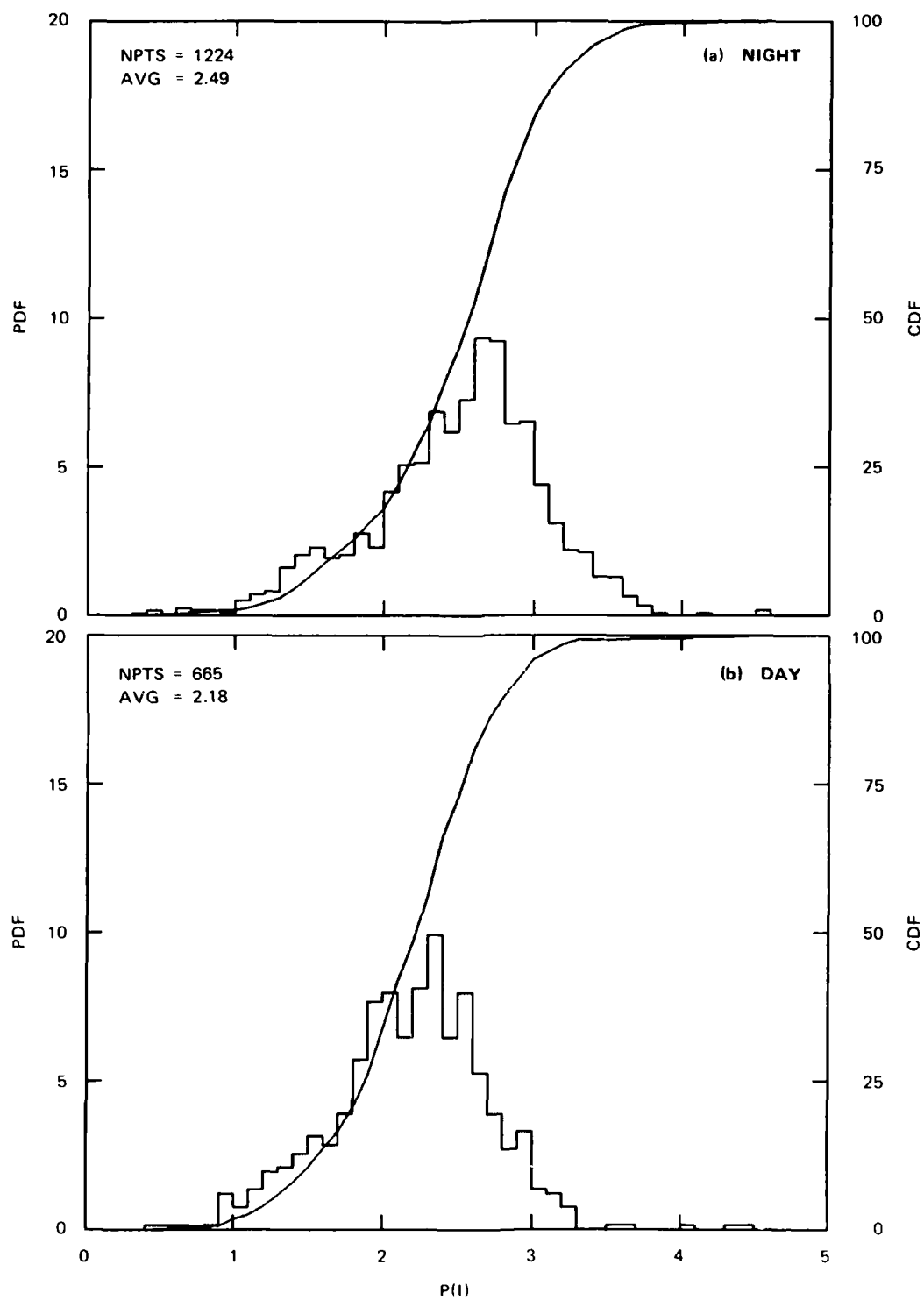
Figure II.C.7.   Tromso intermediate-scale spectral-index distribution
                   for November 1983 to January 1984.

44

from the Sondre Stromfjord data shown in Figure II.C.1. This is princi-
pally due to our selection criterion in which we reject any data segment
for which S_4 at UHF is less than 0.2 to avoid noise contamination in the
UHF phase spectra. Because of its lower magnetic latitude, the Tromso
station sees many fewer disturbed passes than the Sondrestrom station,
particularly during the daytime. It should be kept in mind, however, that
our selection procedure biases the summary statistics toward the more dis-
turbed passes. Figure II.C.8 shows the all-season distribution for the
Sondrestrom data when no S_4 selection criteria is used which can be com-
pared to Figure II.C.9. The only noticeable effect is a slight shift
toward larger p values. Because noise contamination tends to reduce the p
values, we believe the intermediate scale p indices are correct with or
without the S_4 selection criteria, but we have retained it.

Because the intermediate-scale spectral-p index does not
show any significant seasonal variations, it is appropriate to average the
data from the individual seasons together. To preserve the day-night
variation, however, we have sorted the data base by invariant latitude and
corrected geomagnetic local time. The results for the Sondrestrom data
are shown in Figure II.C.9. The largest p index values occur in the mid-
night sector below $\Lambda = 70^\circ$. The shallowest slopes are observed in an
annular ring between $\Lambda = 70^\circ$ and $\Lambda = 75^\circ$ where the slopes steepen again.

We note that the nightside enhancement is identical to
the enhancement reported in Secan and Fremouw [1982], which was found in
Wideband satellite data from an auroral-zone station. Thus, the nightside
enhancement occurs over a fixed range of invariant latitudes, which sug-
gests that a local geophysical feature is affecting the spectral shape.
Because 65° is the average location of the auroral zone, the associated
highly conducting E layer is an attractive candidate that could cause such
an effect. The more shallowly sloped intermediate-scale spectra observed
above 70° invariant latitude is more puzzling. Secan and Fremouw [1982]
also reported that the shallower spectra tended to occur when the propaga-
tion path is near the magnetic meridian. We do not observe this pattern
in the Sondre Stromfjord data shown in Figure II.C.9. Thus, a purely
geometrical explanation does not seem likely.

45
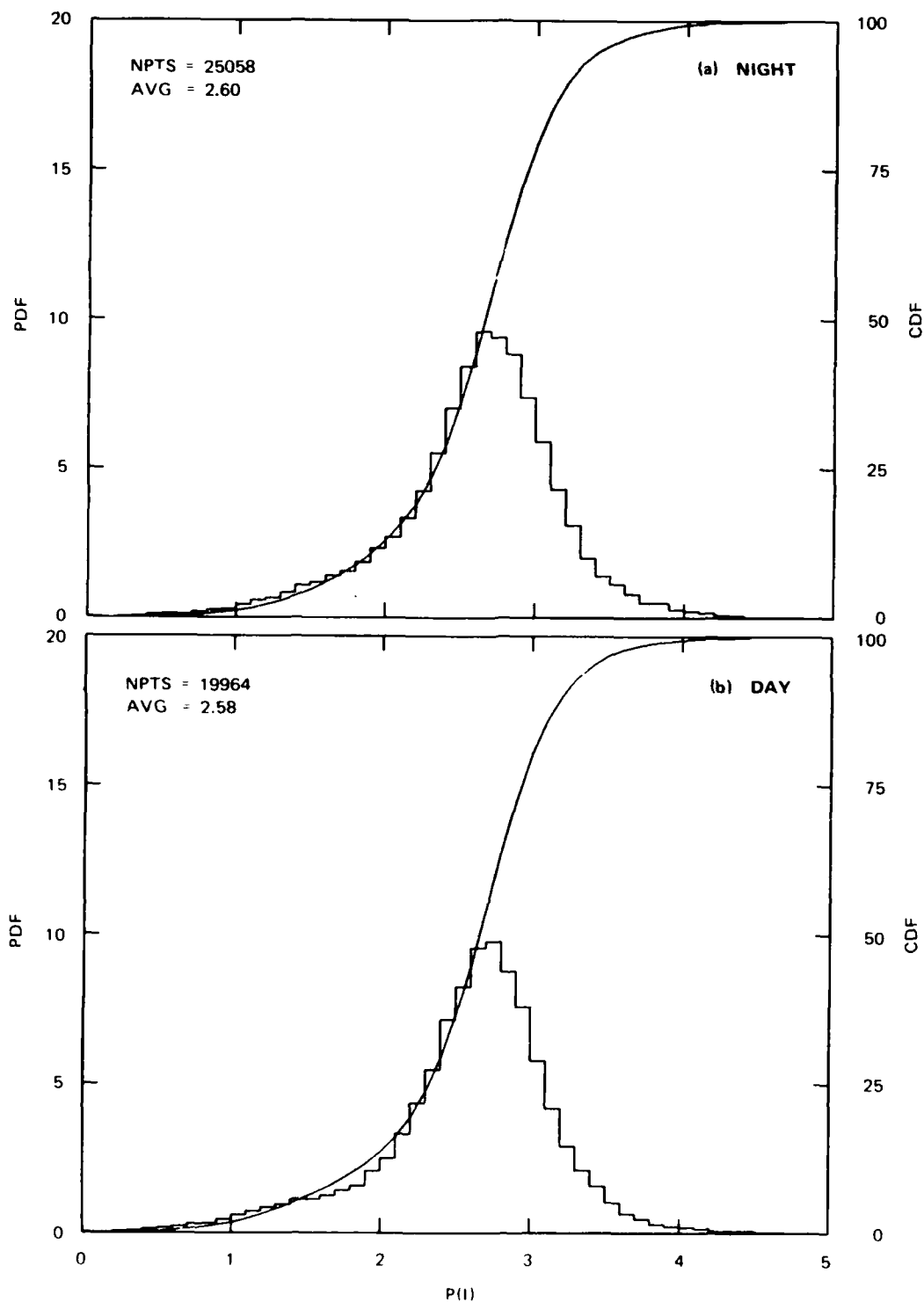
Figure II.C.8.   Sondrestrom intermediate-scale spectral-index distribution
for all seasons (all S_4 values are included).

46
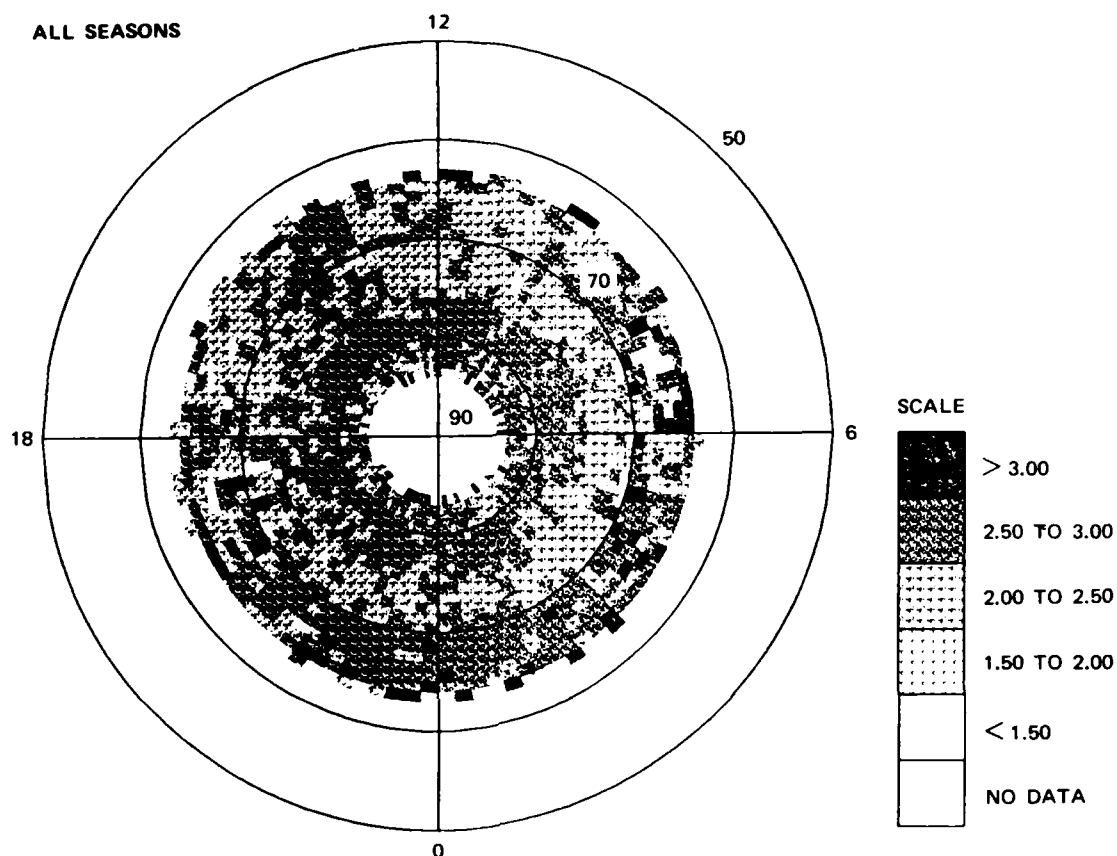
Figure II.C.9. 350-km invariant-latitude corrected-magnetic-local-time clock-dial plot of Sondrestrom intermediate-scale ν index.

Turning now to the medium-scale structure in Figure II.C.10, we show the invariant-latitude-corrected-magnetic-time display of the average medium-scale p index derived from the Sondre Stromfjord data. We present only the summary display because no prominent seasonal variation was found; however, there is pronounced steepening of p below 70° invariant latitude. Above 70°, the behavior is generally similar to that of the intermediate scale, p. This suggests that below 70° the average SDF has a distinct two-component structure with the medium scale more steeply sloped than the intermediate scale. Above 70°, the medium scale is essentially an extension of the intermediate scale.

47
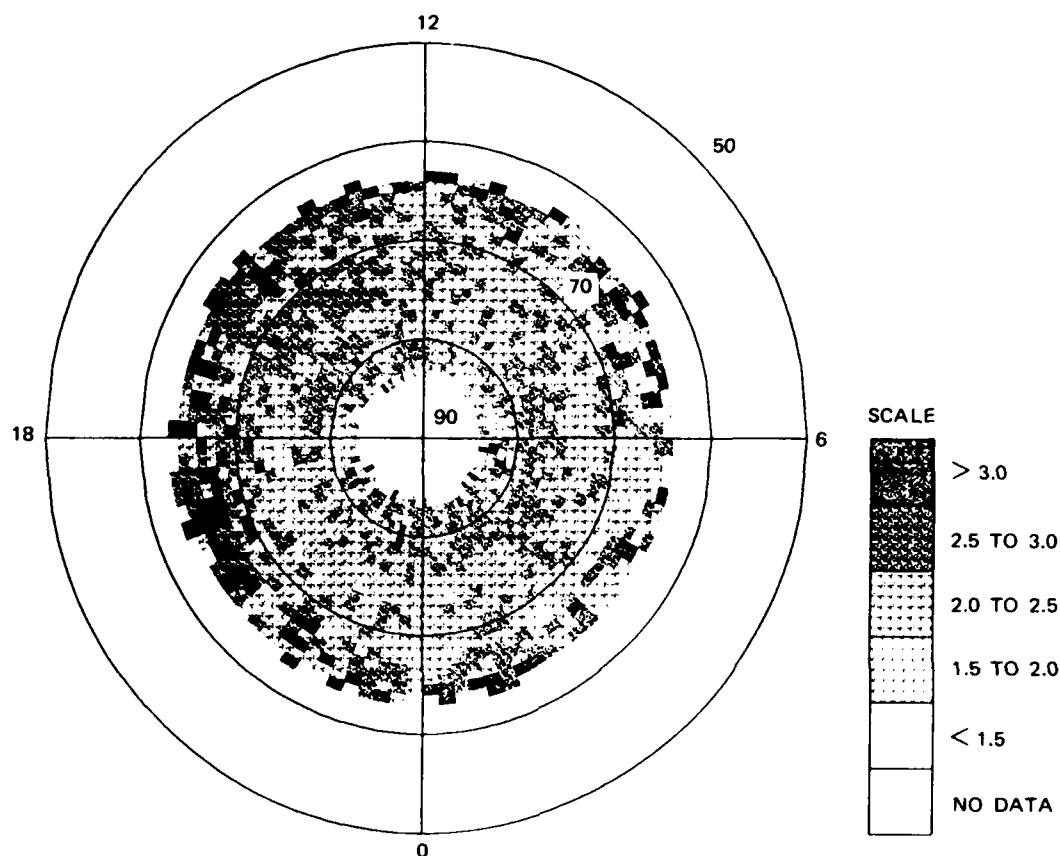
Figure   II.C.10.   350-km invariant-latitude corrected-magnetic-local-time
clock-dial plot of Sondrestrom medium-scale ν index.

The behavior of the low-frequency breakpoint of the
intermediate-scale power-law segment is shown in Figure II.C.11. There is
a considerable amount of scatter in the data, but the smallest values oc-
cur below 70° with peak values in excess of 20 km occurring in the region
where the more shallowly sloped SDFs are observed.

b.   Spectral Strength

Figure II.C.12 is a clock-dial plot of the intermediate-
scale spectral strength parameter averaged over the entire Sondre Strom-
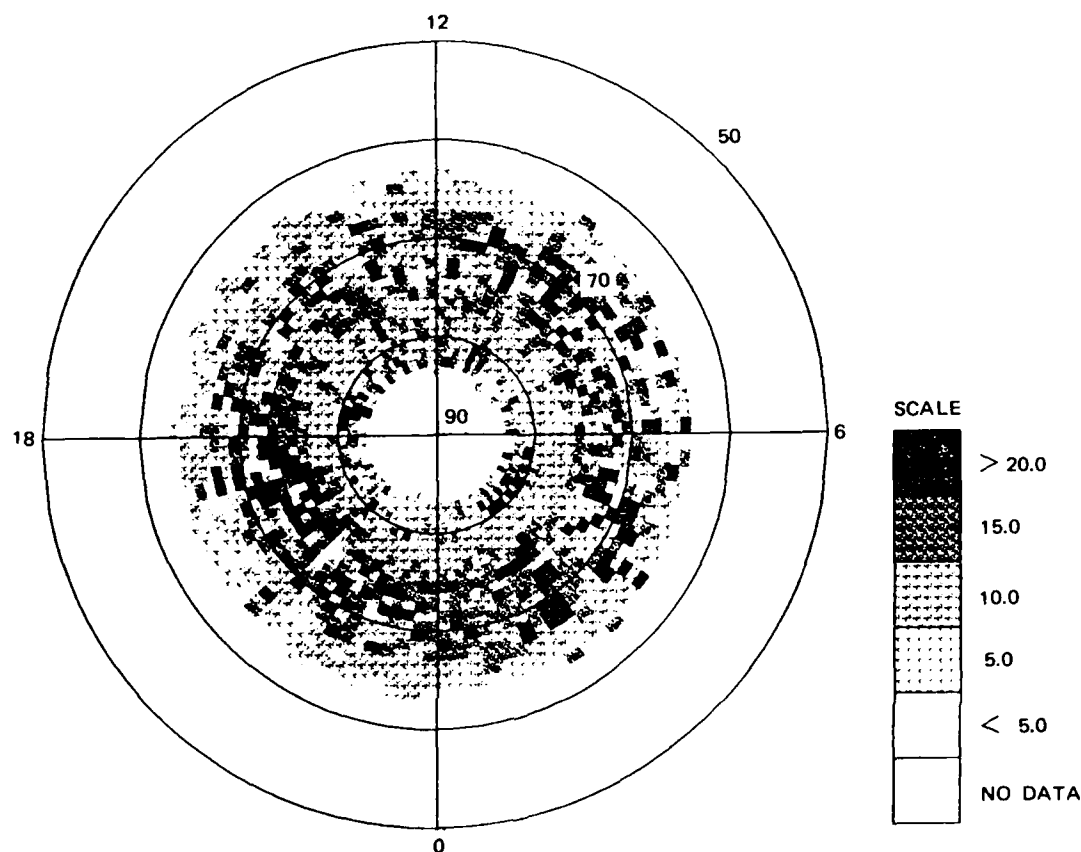
Figure   II.C.11.   350-km invariant-latitude corrected-magnetic-local-time
clock-dial plot of Sondrestrom upper break point for
intermediate scale.

fjord data base. We present the average data first to illustrate the
effects of the propagation path and the effective velocity. The phase
structure shows a pronounced increase near 70° invariant latitude. The
boundary is circular rather than oval. The most intense enhancements are
observed between 70° and 75°, primarily on the dusk side. Indeed, between
midnight and 0600 CMLT almost no localized enhancements survive the
averaging.

As discussed in Section II.C.2, we can use Eq. (II.C.5)
to make a first-order correction for the geometrical dependence of the

49
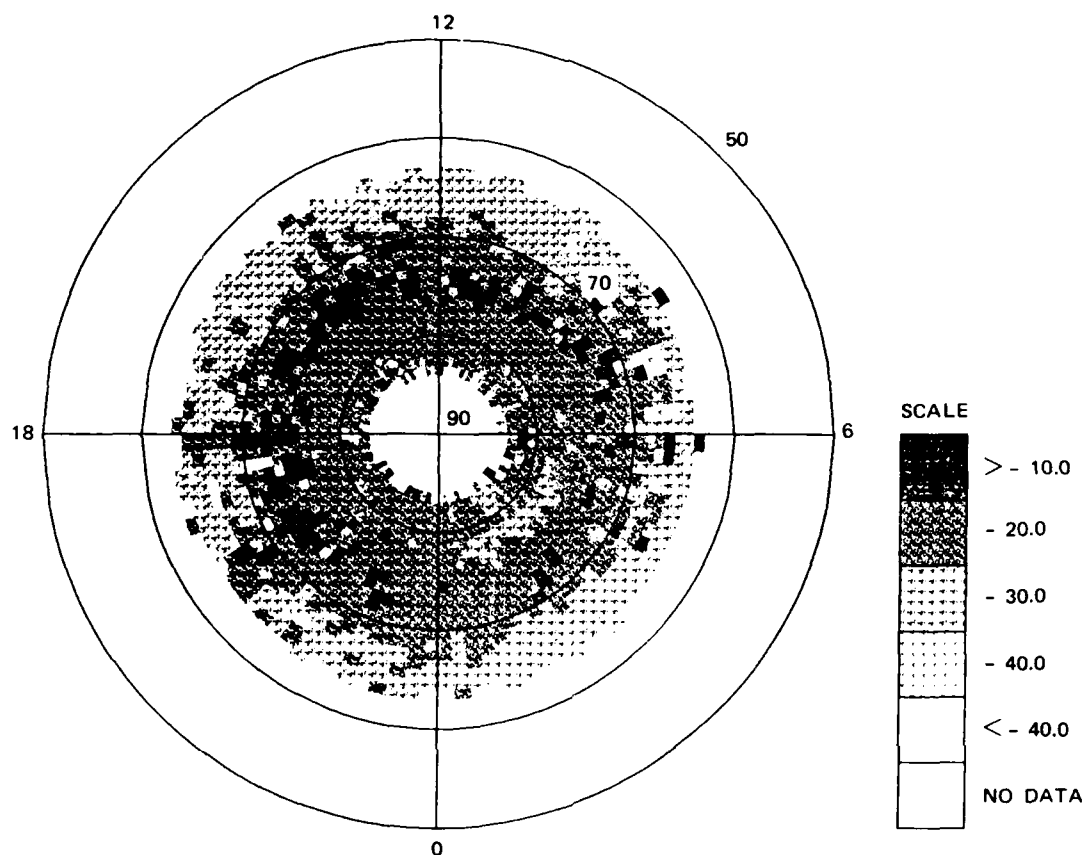
Figure II.C.12. 350-km invariant-latitude corrected-magnetic-local-time clock-dial plot of intermediate-scale spectral strength in dB (10 LOG_{10} T) for Sondrestrom data.

phase scintillation. Figure II.C.13 shows the C_s values assuming a 10:1 anisotropy and a 100-km layer thickness. The same general features are present in the C_s distribution, but the pattern is not nearly so uniform. This is principally caused by the large variations in V_{eff}, that occur for the different pass geometries. The fact that random localized enhancements survive the geometry correction indicates that they are principally source variations, although sheetlike structures could account for some of the enhancements at the extremes of the data set. In any case, the 10:1 anisotropy assumption appears to be useful for evaluating the gross morphological features that we are interested in here.
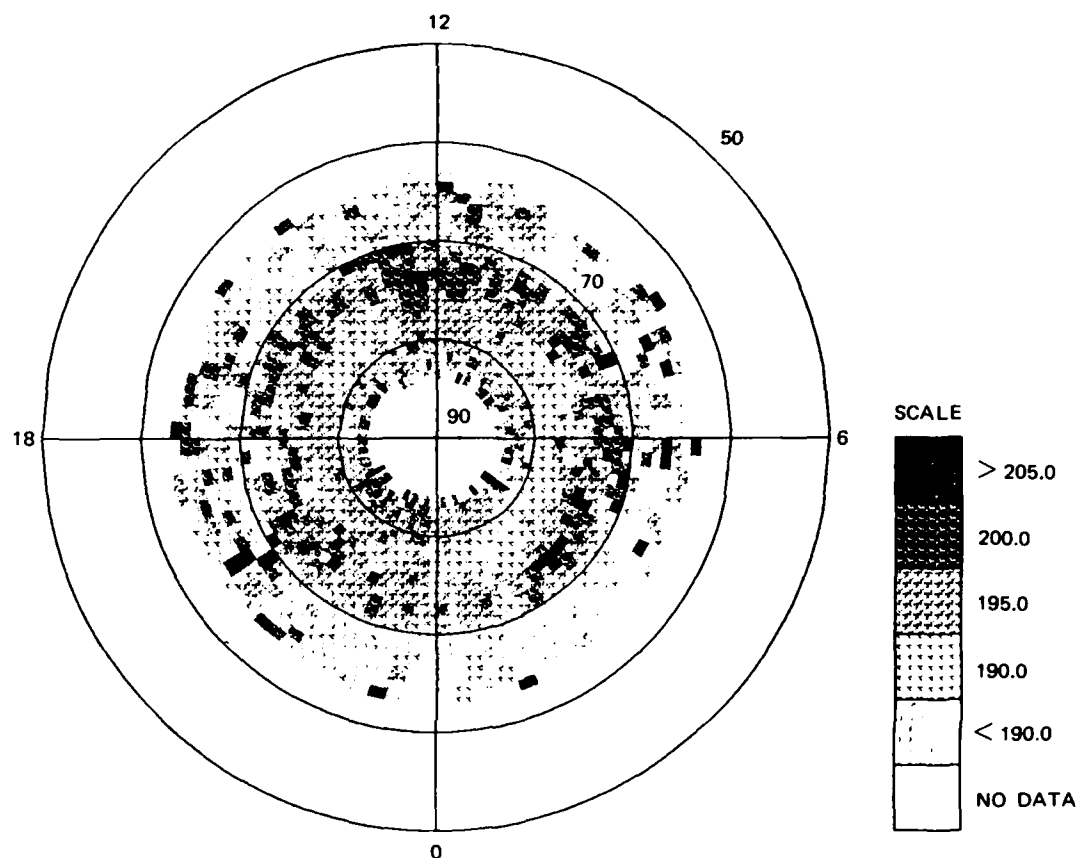
Figure II.C.13. Equivalent three-dimensional turbulent strength computed from Eqs. (II.C.5) and (II.C.6) for 10:1 rodlike irregularities.

Figures II.C.14 through II.C.18 show the seasonal day-night distributions of C_s for the Sondre Stromfjord data. Figure II.C.19 shows the corresponding distributions for the first season's data from the Tromso station. The Sondre Stromfjord overall average is shown in Figure II.C.20. The first point to note is that none of the distributions differ significantly from the Sondre Stromfjord average distributions shown in Figure II.C.20, with the single exception of the Sondre Stromfjord night-time data from the first winter season (Figure II.C.14), which showed a shift toward smaller disturbances. In particular, there is no prominent seasonal or solar cycle variation. We note, however, that the Tromso data

51
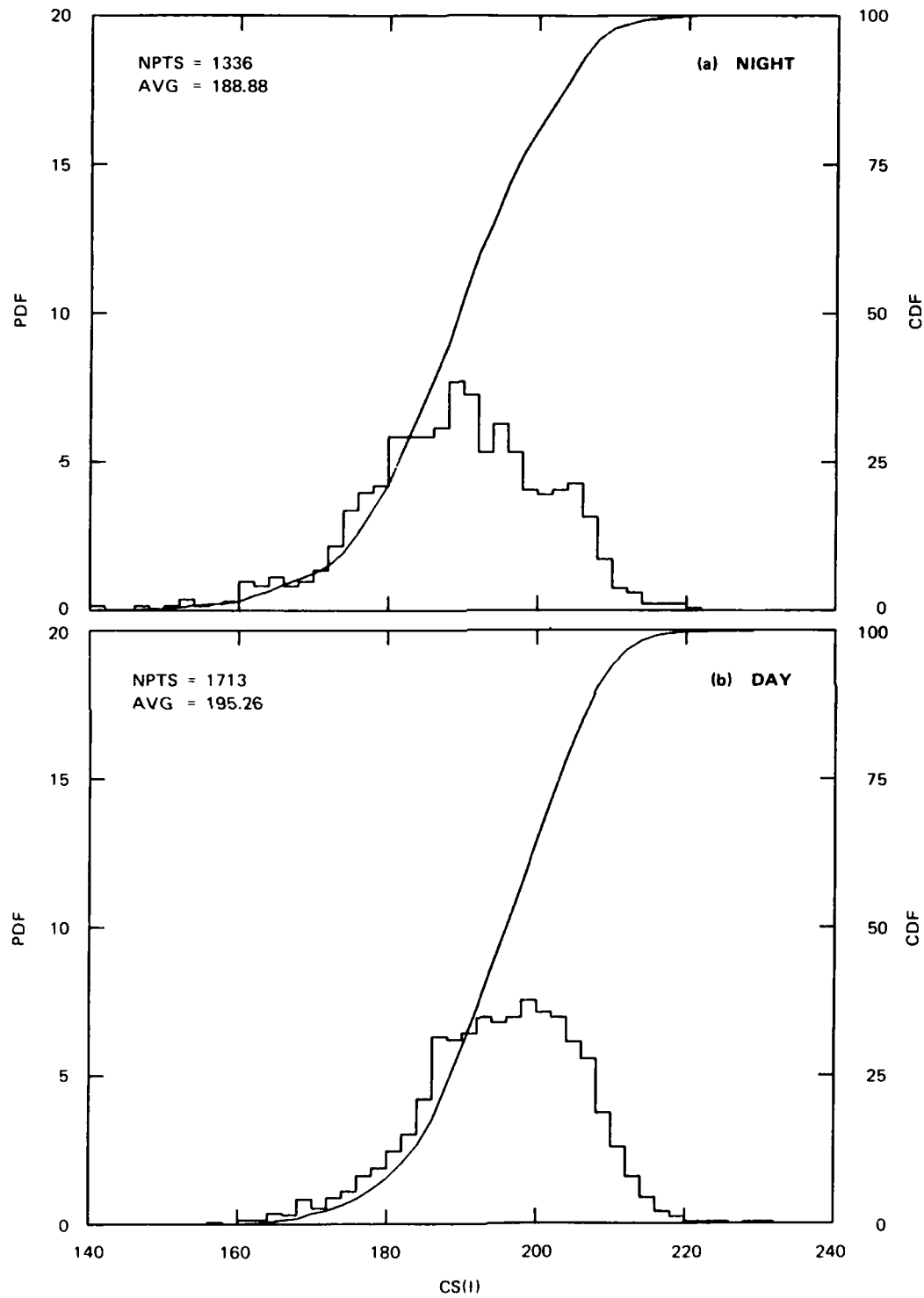
Figure II.C.14.　Distribution of Sondrestrom equivalent three-dimensional turbulent strength for November 1983 to January 1984.

52
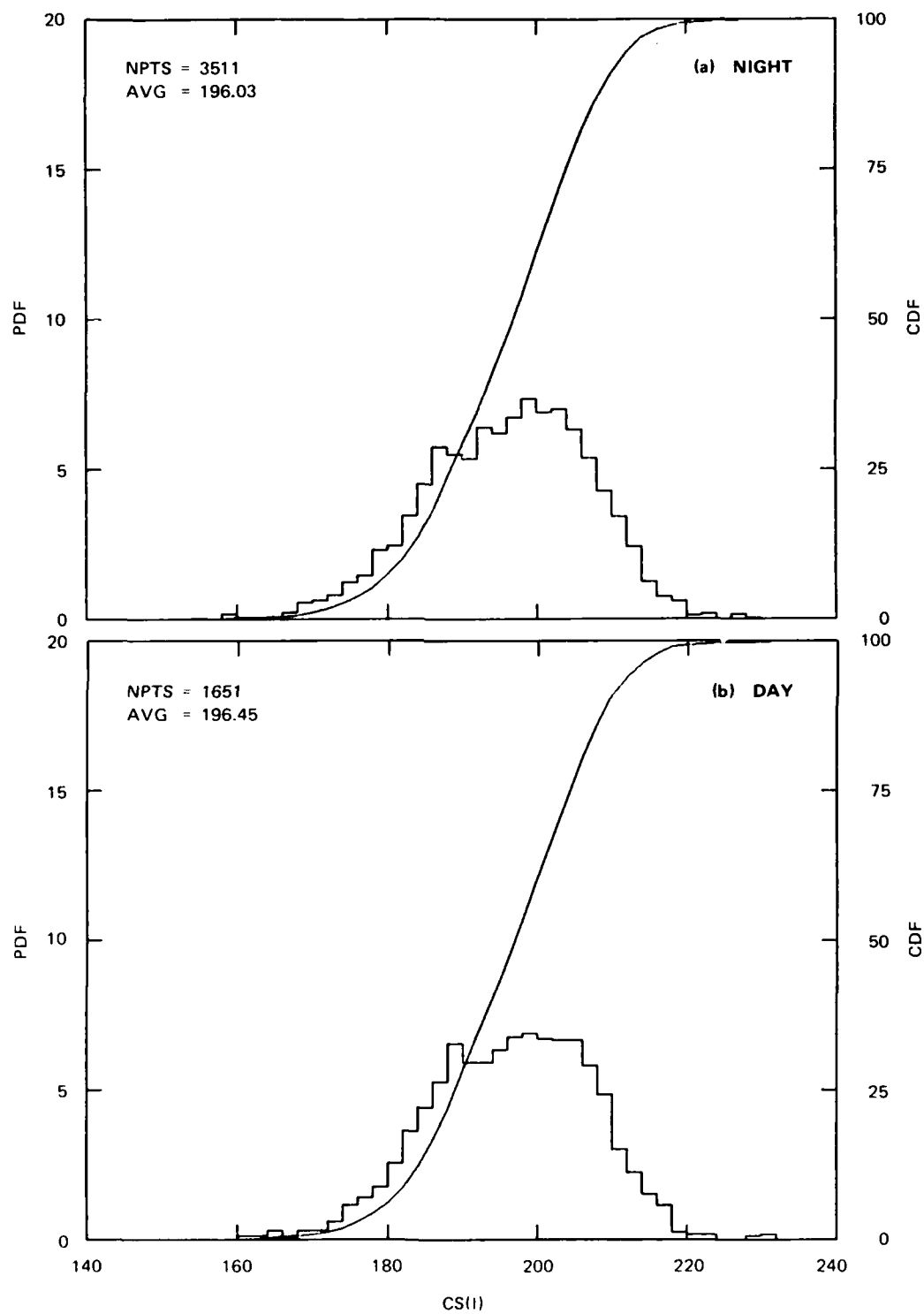
Figure II.C.15.   Distribution of Sondrestrom equivalent three-dimensional turbulent strength for February 1984 to April 1984.

53
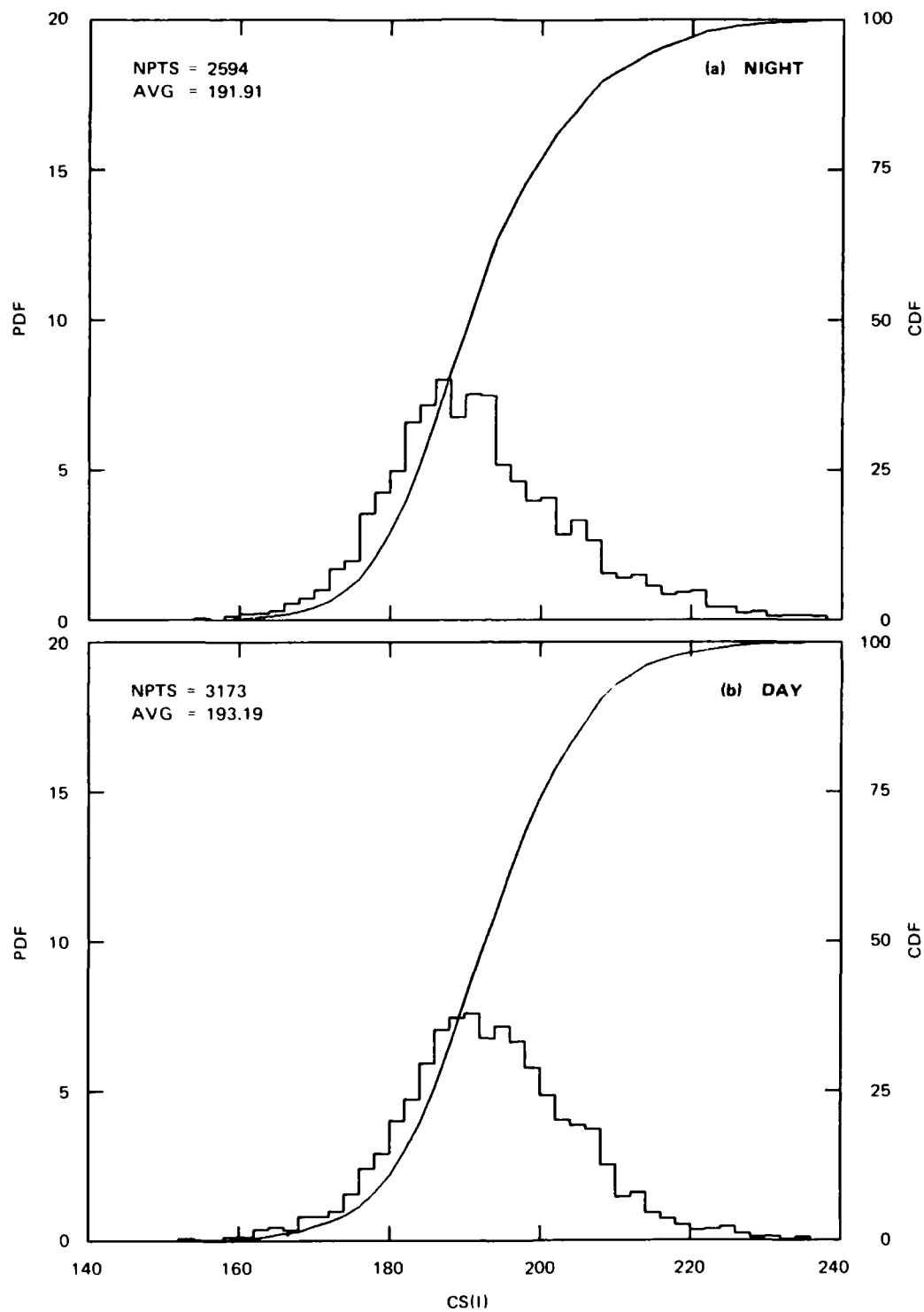
Figure II.C.16.   Distribution of Sondrestrom equivalent three-dimensional turbulent strength for May 1984 to July 1984.

54
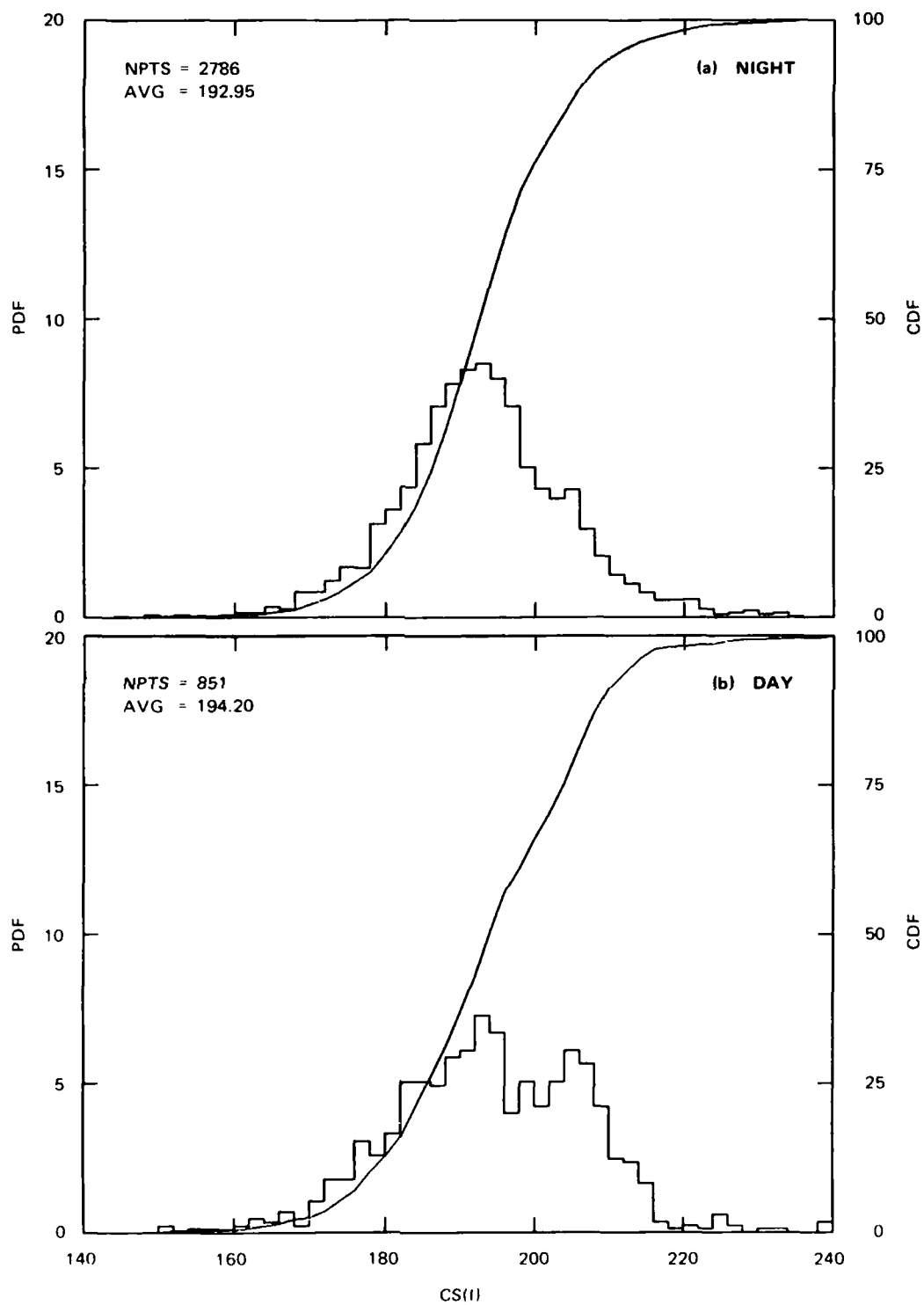
Figure II.C.17. Distribution of Sondrestrom equivalent three-dimensional turbulent strength for August 1984 to October 1984.
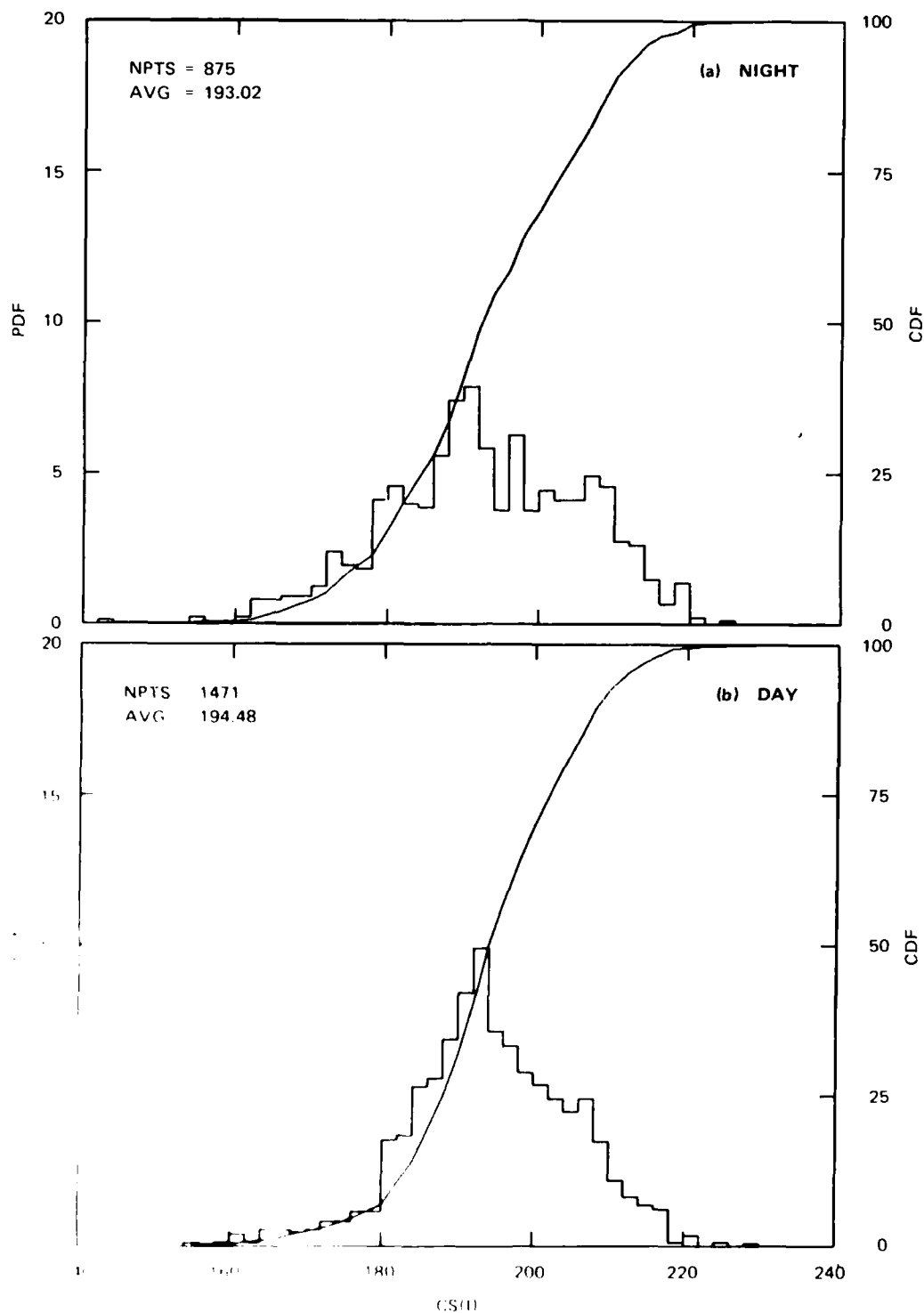
Figure II C 18   Distribution of Sondrestrom equivalent three-dimensional
turbulent strength for November 1984 to January 1985.
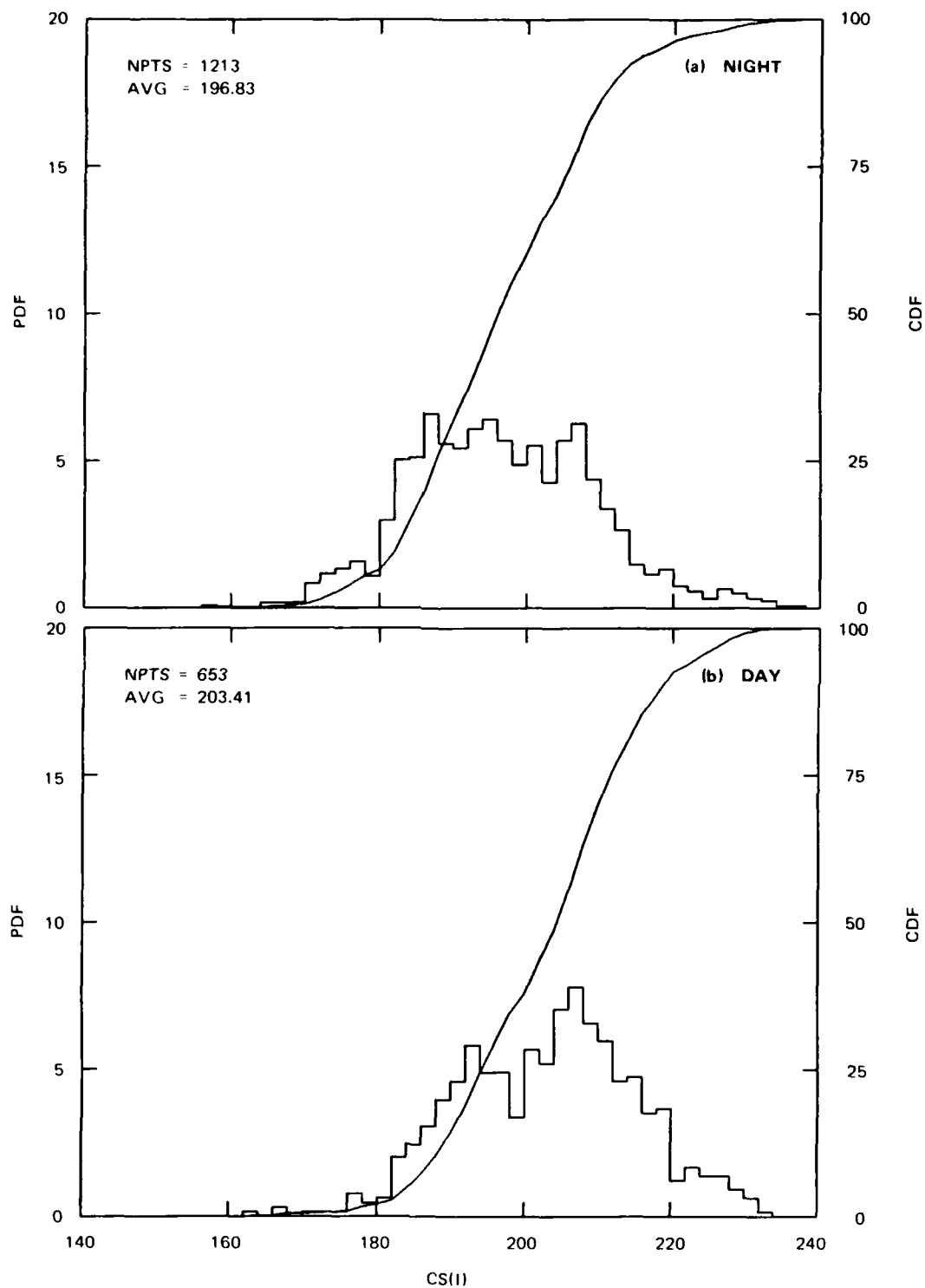
Figure II.C.19.   Distribution of Tromso equivalent three-dimensional turbulent strength for November 1983 to January 1984.
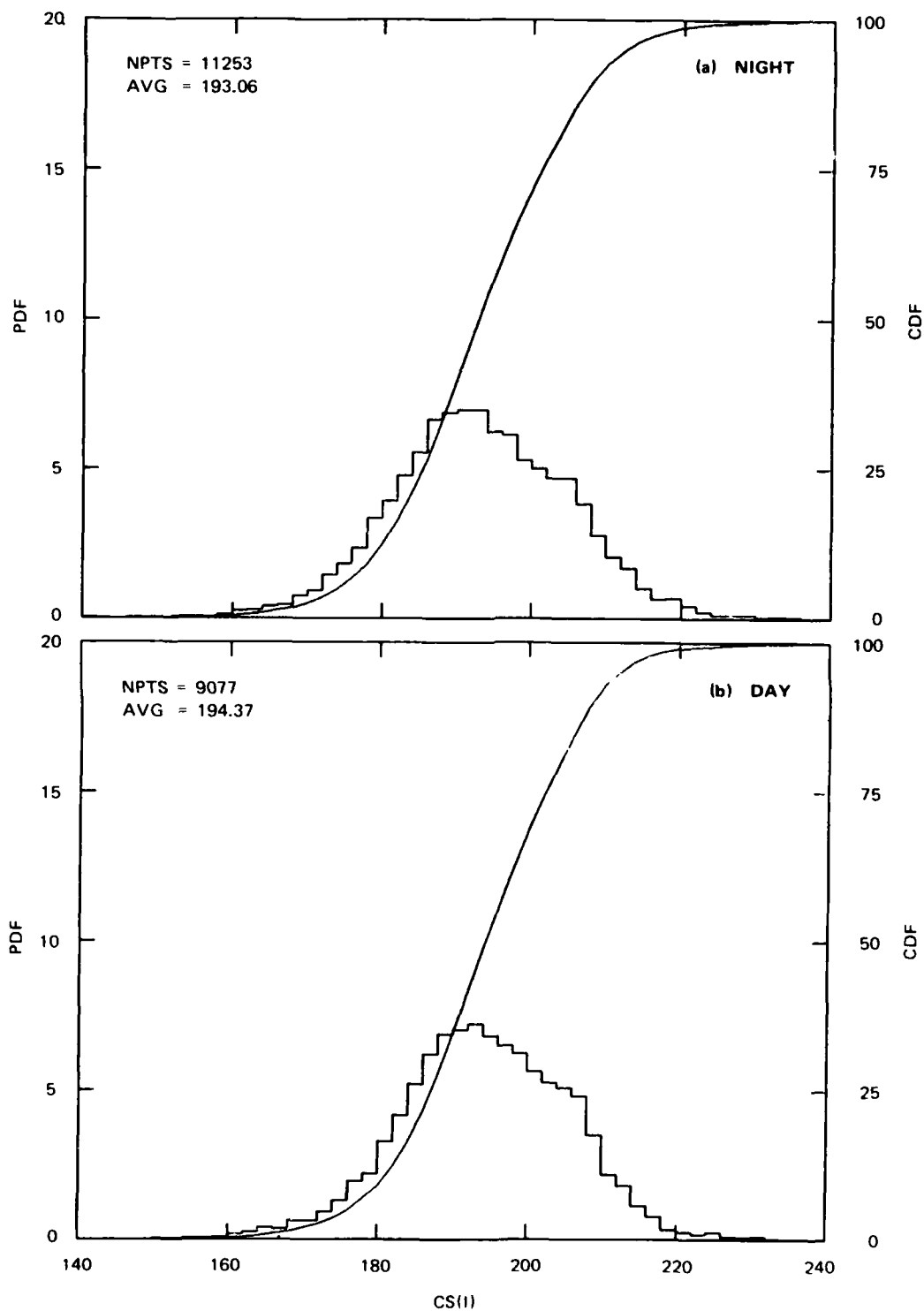
Figure II.C.20.   Distribution of Sondrestrom equivalent three-dimensional turbulent strength for all seasons.

58

from the first winter period show the largest average disturbance levels for both the day and the nighttime periods.

The lack of a distinct seasonal and solar-cycle dependence in C_s compared with that for TEC presented in Section II.B is curious. It may reflect an anticorrelation between TEC and F-layer peak density. This relationship is being investigated.

As a consistency check on these data, we have also computed the corresponding distributions of S_4 corrected for the path angle variation. Because S_4 is inherently high-pass filtered by diffraction effects, it is not sensitive to variations in v_{eff}. For the weak to moderate scintillation levels that dominate this data base, the corrected S_4 values track C_s very well. There are, as we should expect, differences in detail, but the general features are identical to those shown here in the C_s distributions.

These preliminary results suggest that some structuring mechanism sustains a background disturbance level that persists even when the F-region densities are comparatively low. Also, substorm activity, which we have not analyzed here, may be exerting a strong influence on the data, particularly as it affects the largest events. Thus, during this period of low solar activity, identifying the various structuring mechanisms will require an exacting comparative analysis of the entire complement of HILAT instruments.

D.   Refinement of the High-Latitude Structure Source Function for the Nighttime Auroral Zone

In the past, we have modelled the morphology of high-latitude irregularities by specifying (1) a source function of irregularities, (2) the lifetime of irregularities once produced, and (3) the redistribution of irregularities by magnetospheric convection [Vickrey and Kelley, 1982]. The previous modelling effort used, however, an overly simplified source function--namely an annular ring representing the auroral oval. In this

section, we combine more sophisticated source functions and convection patterns in an attempt to reproduce Chatanika radar observations.

Data obtained during elevation scans with the Chatanika incoherent-scatter radar have revealed the presence of ionization enhancements in the nightside auroral F-region with scale sizes ranging from tens of kilometers (medium scale) to hundreds of kilometers (large scale). We have attempted to identify the sources of these enhancements using the radar data and two models. One model combines a specified ionization-source region with a realistic high-latitude convection model so that the plasma distribution produced by various source regions can be compared with that mapped out by the radar measurements. The second model computes the distortions of drifting plasma blobs produced by convection in the absence of ionization sources and losses. The data and modelling indicate that the Harang discontinuity is an important source region for large- and medium-scale ionization enhancements and that distortion by convection of large-scale ionization enhancements can produce smaller-scale enhancements even in the absence of plasma instabilities or other structuring mechanisms.

F-region ionization in the high-latitude ionosphere has been studied extensively in recent years both by theoretical modelling and observations [e.g., Knudsen, 1974; Watkins, 1978; Vickrey and Kelley, 1982; Sojka et al., 1983; and Foster, 1984]. These efforts have been successful in accounting for large-scale features such as the midlatitude trough, the polar cavity, the plasma tongue extending into the polar cap from the cusp, and the aurorally enhanced F region. Smaller-scale structure in ionization has been investigated by Kelley et al. [1982]. The distribution of irregularities with kilometer-scale lengths was consistent with an assumed irregularity source located along the polar-cap boundary, a region commonly associated with soft-particle precipitation [Eather, 1969].

The sources of large- and medium-scale ionization enhancements need not be the same. The large-scale structures can be produced by sources that act over large portions of the polar regions, the small-scale structure requires either a structured source region, structured electric fields, or plasma instabilities that act on the large-scale enhancements.

60

Identification of the various sources requires direct measurements of F-region electron density, optimally as a function of latitude and local time. Such data can be obtained by incoherent-scatter radars. However, care must be taken in interpreting these observations because of temporal variations in the plasma distribution. When radar data are compared with the results of numerical modelling, the interpretation of the observations becomes less ambiguous.

In this section, we compare Chatanika radar measurements with results of two numerical models to identify possible source regions of F-region ionization enhancements in the nightside auroral zone. Our results pertain to enhancements with scale sizes ranging from tens of kilometers to hundreds of kilometers. We first show that the most prominent large-scale plasma features are produced by an ionization source in the region of the Harang discontinuity. We then discuss several mechanisms that can produce the smaller-scale features observed in the data.

In the following sections, we (1) describe the observational technique used to infer the latitude and local-time distribution of F-region ionization and plasma-drift velocity, (2) present the observational and modelling results separating those that pertain to large- and medium-scale enhancements and (3) discuss and summarize the results.

1.   Technique

The measurements described here were made using the Chatanika radar while the antenna was scanning in the magnetic meridian plane. In the following, we explain how electron density and vector electric fields are determined from these measurements, emphasizing the advantages and disadvantages of the elevation scan mode over other operating modes.

The time for one complete elevation scan is dictated by the angular extent of the scan and the desired spatial resolution. The spatial resolution is limited by the minimum feasible integration time, which is about 15 s for reliable ion-drift-velocity measurements using a 320-μs pulse length. To obtain measurements with a horizontal resolution of 30 km at 300-km altitude, the scan rate must be less than 6° in 15 s.

This holds only for measurements at the zenith. As the radar scans to lower elevation angles, the horizontal distance between measurements increases. Instead of operating the radar at a nonuniform scan rate to compensate for this effect, we chose to use a uniform rate of about 3° in 15 s. This gives 15-km resolution overhead and 40-km resolution at the extremities of the scan. The E-region spatial resolution is about half these values.

Although electron-density measurements can be made with an integration time as small as 5 s, they are usually obtained with the same 15-s integration time that is used for the velocity measurements. We display electron-density data from meridian scan measurements by constructing altitude profiles along lines of constant invariant latitude and then drawing contours through the values. Examples of contour plots of electron density are shown in Figure II.D.1. These data were obtained during scans on three different evenings. F-region structure observed on these three evenings is discussed below.

Our method for determining the vector electric field from meridian-scan measurements has been presented by de la Beaujardiere et al. [1977]. Briefly, the zonal electric field is determined directly from the line-of-sight F-region ion-drift velocity. The meridional electric field is inferred from the line-of-sight E-region ion-drift velocity measured below the F-region ion-drift velocity measurement along the same field line. To do this, we subtract that part of the E-region ion drift induced by the zonal electric field and neutral wind. The neutral wind effect is small for typical E-region wind velocities. The effects produced by the zonal electric field are eliminated by using the Hall mobility in the E region and the measured electron density. Fortunately, the zonal electric fields are usually small and, thus, the meridional electric field is approximately equal to the E-region ion drift times the effective Pedersen mobility. The technique suffers from smearing effects over 96 km (in range) when using a pulse length of 320 μs. This is effectively reduced to 48 km by the manner in which the data are sampled in the autocorrelator Although subject to these uncertainties, the electric fields measured in this manner have been found to be quantitatively accurate [e.g., Robinson et al., 1981].
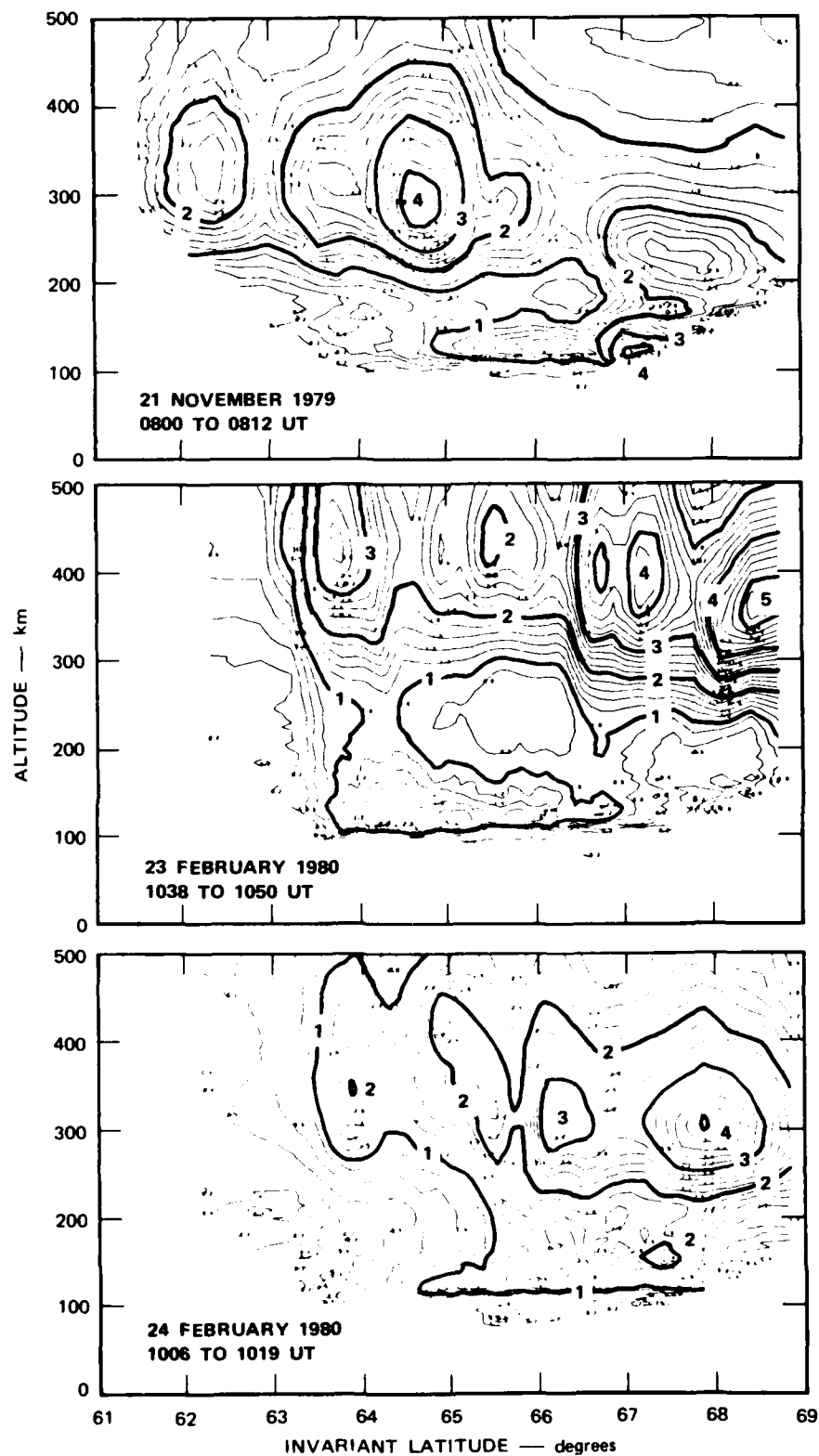
Figure II.D.1. Examples of elevation scan measurements of electron density obtained on three different evenings.

63

The advantages of the meridian scan over other operating modes is that a 6 to 10° (depending on altitude) latitudinal sector in the ionosphere can be viewed in as little as 12 min. Data from successive scans can be combined to provide information about temporal variations in electron density and drift. However, keep in mind the difficulty in distinguishing temporal variations from local-time variations.

One disadvantage of the elevation scan over other radar operating modes is that vector electric fields can only be measured where E-region measurements are possible. This limits the latitude over which electric fields are measured to about 5 or 6°. Techniques that use only F-region velocity measurements provide electric-field data over a much larger latitudinal range. Also, in the elevation scan the radar cannot measure the electric field when directed near the magnetic zenith. Despite these problems, the elevation scan is useful for measuring electron density and the electric field in ionospheric features with scale sizes as small as 10 km. We have taken advantage of this capability in the present study.

2.   F-Region Ionization and Plasma Drift

In this section, we present Chatanika radar data obtained on four evenings. The four days were chosen from a much larger set of days on which elevation scan measurements were made at Chatanika. The selection was made on the basis of the quality of the data and the continuity of the measurements through the local time of interest. In addition, however, the measurements are fairly representative of the data usually obtained during these experiments; in particular, they include examples of the most common F-region ionization enhancements.

Radar measurements obtained on the four days chosen are shown in Figure II.D.2. Only measurements made between 1800 and 0600 MLT are shown. At Chatanika, MLT = UT - 11.5 hrs. The upper panels in Figure II.D.2 show the electron density at the peak of the F layer as a function of invariant latitude and MLT. The data have been smoothed in the constructing of these plots, so that structures with scale sizes less than
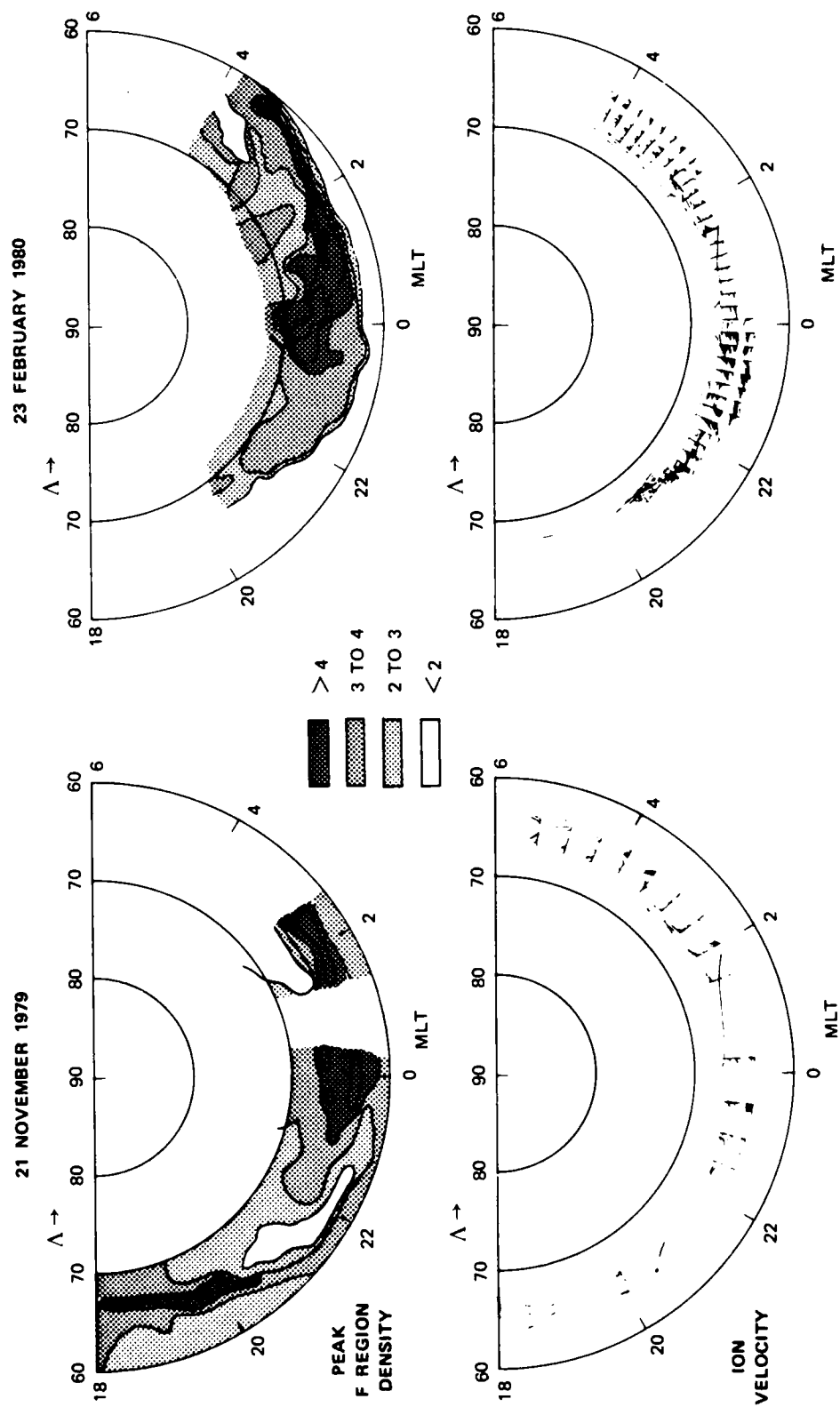
64

Figure II.D.2.   F-region peak density and F-region drift velocity as a function of invariant latitude and magnetic local time on four evenings.

65
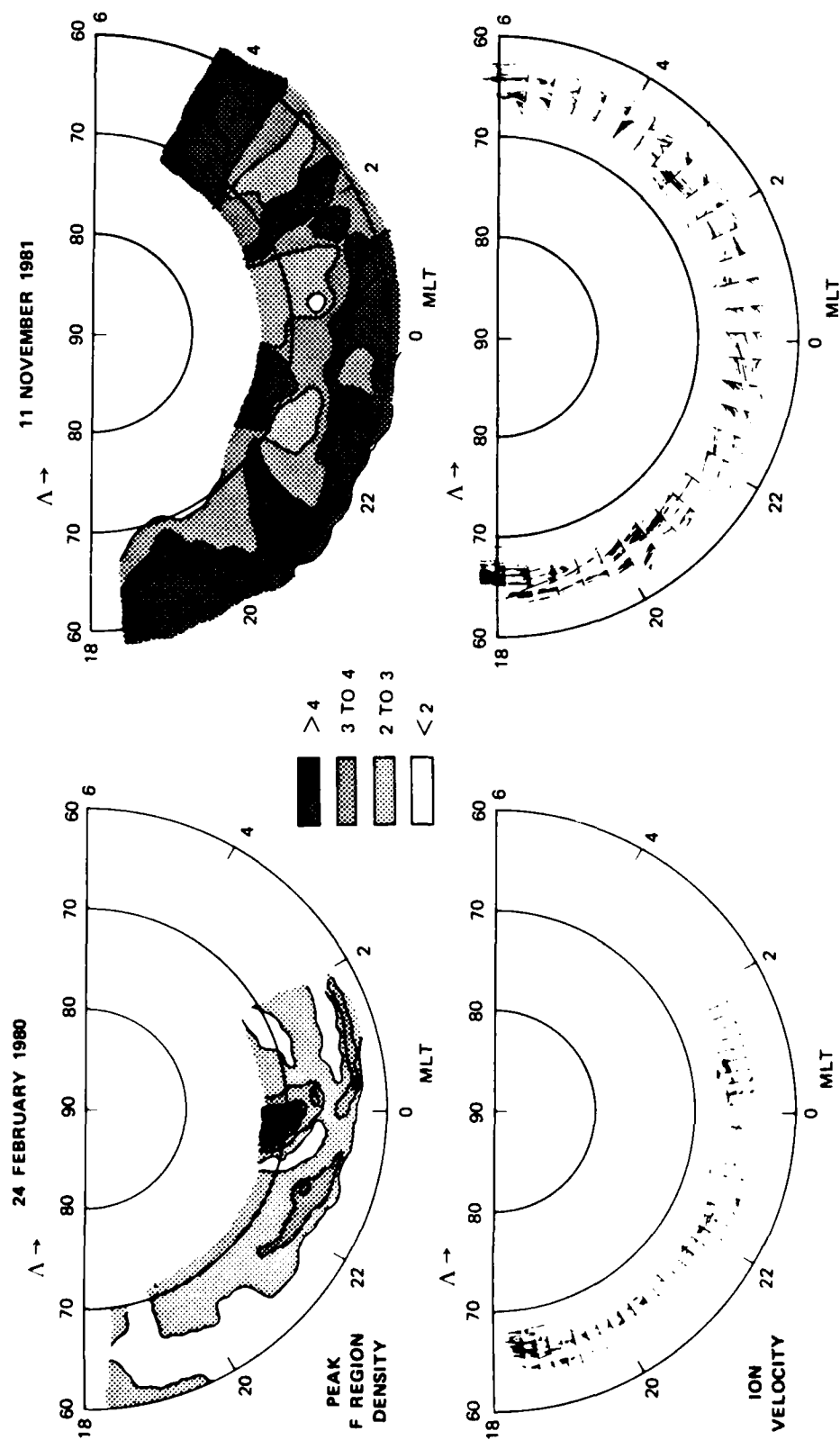
Figure II.D.2. F-region peak density and F-region drift velocity as a function of invariant latitude and magnetic local time on four evenings (Concluded).

about 50 km are not apparent. The large-scale ionization enhancements in

Figure II.D.2 are, in general, actually composed of numerous medium-scale

enhancements such as those shown in Figure II.D.1. Our identification of

an enhancement as either large or medium scale is based on the appearance

of the feature in the radar data. Some of the medium-scale enhancements

in Figure II.D.1 can actually be identified in many successive scans so

that their longitudinal extent may be hundreds of kilometers or more.

Thus, our identification of a feature as being either large or medium

scale is based on the latitudinal dimension of the enhancement. The dis-

cussion in this section is restricted to the source of the large-scale

ionization enhancements. Medium-scale structure will be addressed in the

following section.

The lower panels in Figure II.D.2 show the vector drift velo-

city as a function of invariant latitude and MLT. These were computed

from the electric field measurements described above assuming $\bar{E} \times \bar{B}$ drift.

Measurements of electric field with uncertainties greater than 10 mV/m

were excluded from the plots. Electric-field measurements with very large

uncertainties occur near the radar magnetic zenith and where the E-region

electron density is low. Thus, for example, in the data for 23 February

1980 the southern extent of the electric-field measurements in the evening

sector follows the equatorward edge of the diffuse aurora.

Before discussing the data in Figure II.D.2, some cautionary

remarks should be made. First, the plots of drift velocities cannot be

regarded as instantaneous pictures of F-region convection. Because the

plots were constructed from measurements made over 12 hours, any temporal

changes in the convection pattern will appear as spatial variations in the

data displayed in Figure II.D.2. Temporal variations in the convection

electric field usually occur in association with magnetic substorms.

Thus, ground-based magnetometer data can be studied to identify times when

these variations were likely. Perturbations in the H component of the

magnetic field measured at College, Alaska, are shown in Figure II.D.3.

All four evenings contained periods of magnetic activity to varying de-

grees. The perturbations in the H component recorded on 21 November 1979,

and 23 February 1980 can be interpreted in terms of rotation of the
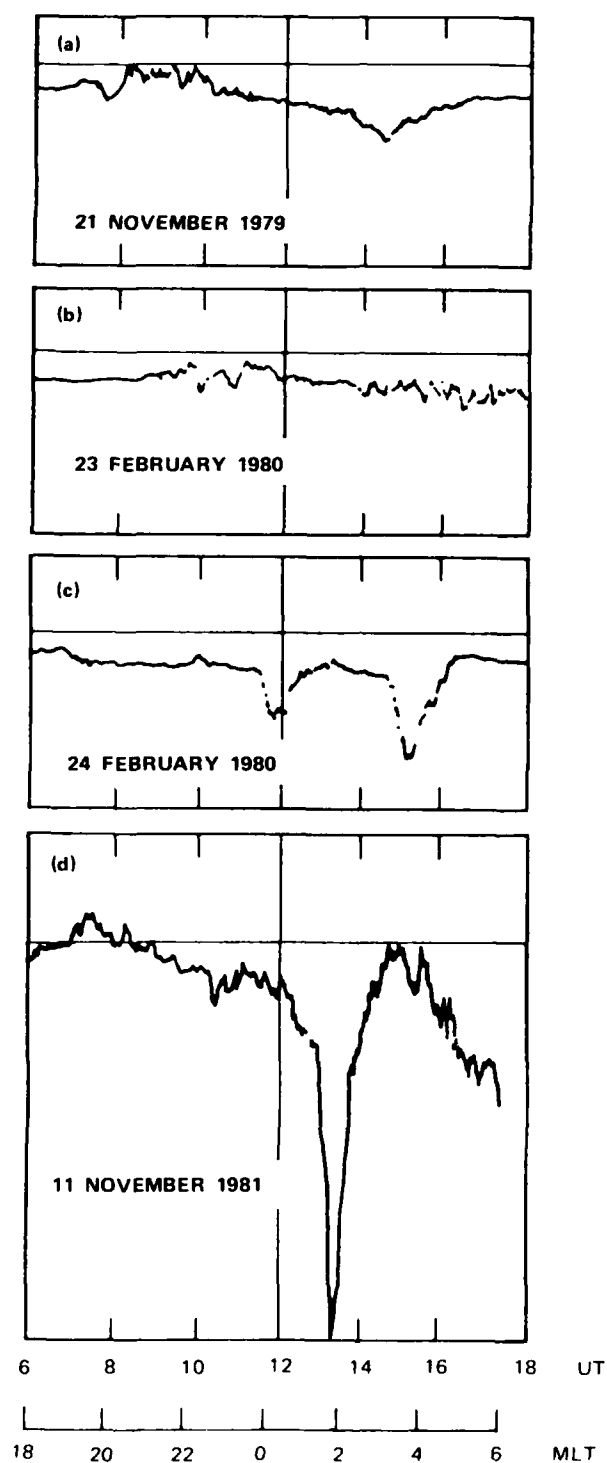
Figure II.D.3.   Perturbations in the H component of the geomagnetic field measured by the college magnetometer on the four days shown in Figure II.D.2.

68

earth beneath a stationary, two-cell convection pattern so that no indication of substorm activity on these two days is present. However, the data from 24 February 1980 and 11 November 1981 clearly contain large variations in the geomagnetic field associated with substorm activity. Thus, the radar data for these evenings must be interpreted more carefully.

Like the electric-field measurements, the F-region density measurements must be interpreted with care. The plasma distributions shown in Figure II.D.2 are not indicative of the instantaneous distribution of ionization even in the absence of substorm activity because the F-region plasma has a long lifetime and is convecting. For example, the data for 21 November 1979 indicate an ionization enhancement extending between 1800 and 2100 MLT. There is no way to tell from the radar measurements alone whether this was a localized enhancement corotating with the earth or was an elongated enhancement that convected through the radar field of view over the several hours required to make the measurements. In either case the radar measurements provide only a distorted view of the actual extent and distribution of F-region plasma.

To aid in interpreting the ionization data, we distinguish between two types of ionization enhancements. The distribution of F-region ionization that does not vary with time as viewed from an inertial reference frame we refer to as a standing feature. Any pattern of ionization whose appearance or location in the inertial frame changes with time we refer to as a transient feature. The distinction between standing and transient ionization features applies to both medium- and large-scale enhancements. The ionization distribution determined from the radar data over the twelve hours required for the measurements is a combination of standing features and transient features. It is clear that standing features can only be created by processes that do not vary with time; in particular they require the spatial relationship between the source and the convection pattern to remain unchanged. Although this requirement is seldom satisfied, it may be that some portions of the auroral convection pattern are more favorable for certain types of precipitation. Thus, the convection pattern may change but the precipitation may be tied to the convection in a deterministic way. This would favor the production of

69

large-scale ionization enhancements that are relatively permanent features of the auroral oval.

Possible examples of standing ionization features can be seen in the upper panels of Figure II.D.2. One is the longitudinally extended ionization enhancement that is apparent in the data of 21 November 1979, 23 February 1980, and 24 February 1980. These enhancements occur most often near the equatorward edge of the diffuse E-region aurora. In some cases their longitudinal extent exceeds ten hours of local time. Because of their location relative to the diffuse aurora we refer to them as boundary features. The "boundary blob" described by Tsunoda et al. [1985] and Weber et al. [1984] forms this longitudinally extended ionization enhancement. That is, the boundary feature is made up of one or more boundary blobs near the equatorward edge of the auroral oval.

A second feature that may be a standing feature is the enhancement extending through the midnight sector in the data from 21 November 1979 and 23 February 1980. When we compare the location of these enhancements to the drift velocity measurements, we find that these features occur near the Harang discontinuity. The Harang discontinuity marks the separation between westward drifting plasma and eastward drifting plasma. The discontinuity is extended in local time and slanted from northwest to southeast [Maynard, 1974]. The location of the Harang discontinuity is shown by the curved lines in the lower panels of Figure II.D.2. The ionization feature associated with this region we refer to as the midnight feature. The modelling described below suggests that the boundary feature and the midnight feature are both standing ionization features.

Unlike standing ionization features, the processes involved in producing transient ionization features are fairly common. Any change in the precipitation or convection pattern can produce a local enhancement or depletion in F-region electron density. After it is created, the plasma will drift at the $\bar{E} \times \bar{B}$ drift velocity. Substorms, in particular, may be responsible for many transient ionization features--depending on the lifetimes of F-region ionization, the enhancements produced during substorms may be observed far from the place that they are created. Transient ioni-

zation features may also be produced by time-varying processes acting along the dayside polar cusp, with the ionization features being subsequently transported across the polar cap. Weber et al. [1984] have recently reported such drifting patches in the polar cap.

Examples of transient ionization features are apparent in the data for 11 November 1981 and 24 February 1980. On 11 November, there are several intervals between 0100 and 0400 MLT during which the F-region ionization undergoes rapid changes. These correspond to simultaneous sudden changes in the geomagnetic field recorded by ground magnetometers (Figure II.D.3). They are most likely produced as a result of a sudden increase in auroral particle precipitation or the transit of a surge across the radar meridian. In the data in Figure II.D.2 for 24 February 1980, an ionization enhancement seems to extend down from the poleward edge of the radar field of view near midnight. This could be a portion of a larger patch that has convected across the polar cap. We emphasize that, in contrast to standing ionization features, transient features are highly distorted in the radar data because of the time required to make the measurements. Transient ionization features will, therefore, not be the primary topic of this section, although we will demonstrate that under certain circumstances transient ionization features may persist for several hours at the same magnetic latitude and local time.

Regardless of whether an observed ionization feature is standing or transient, its location cannot necessarily be regarded as the site of local auroral precipitation. This is because the F-region responds very slowly to in situ production. Kofman and Wickwar [1984] used measurements of electron density and temperatures made by the incoherent-scatter radar at Sondrestrom, Greenland, to calculate heat loss rates. In steady state and in the absence of heat conduction along field lines, the rates of heat loss indicate the rate of local heat production. Although Kofman and Wickwar [1984] obtained good results in the dayside auroral oval, similar calculations using the data shown here were largely inconclusive in revealing localized regions of enhanced production. This is either because the source regions on the nightside are not as pronounced as the dayside or because parallel heat conduction is more effective on the

71

nightside in carrying away locally deposited energy. Below, we infer the presence of local production by examination of E-region ionization in the vicinity of the F-region enhancements. Because of the rapid recombination times at low altitudes, E-region ionization reflects in situ production. Thus, when E-region ionization is present, it usually indicates the presence of local precipitation of electrons with energies greater than 1 keV. These energetic electrons are not as efficient in ionizing the F-region as electrons in the energy range of 0.1 to 1 keV. Moreover, we cannot assume that enhanced precipitation of keV electrons that would produce an auroral E region would necessarily be accompanied by enhanced precipitation at energies below a keV. Nevertheless, some indication about the nature of the precipitation can be extracted by comparing the E- and F-region ionization distributions. This comparison is described below.

3.   The Harang Discontinuity as a Source of Enhanced F-Region
      Ionization

        The data in Figure II.D.2 for 21 November 1979 and 23 February 1980 are similar in that both show a large region of enhanced ionization in the vicinity of the Harang discontinuity. This feature may be associated with enhanced particle precipitation or, alternatively, may be a region in which relatively dense plasma is preferentially convected. Electron-density contour plots and electric-field latitudinal profiles for scans within the midnight ionization feature on these two days are shown in Figure II.D.4. The data for the two days are remarkably similar. The ionization contours show a latitudinally extended narrow region of enhanced E-region density beneath a latitudinally extended region of structured F-region plasma. The electric-field data show that the E-region feature and the region south of it were on field lines that convected slowly westward (northward electric field). Immediately to the north was a region of strong eastward drift. The reversal in electric field and the E-region enhancement are the ionospheric signatures of the Harang discontinuity. The Harang discontinuity has been associated with enhanced particle precipitation and upward field-aligned current [Heppner et al.,

72
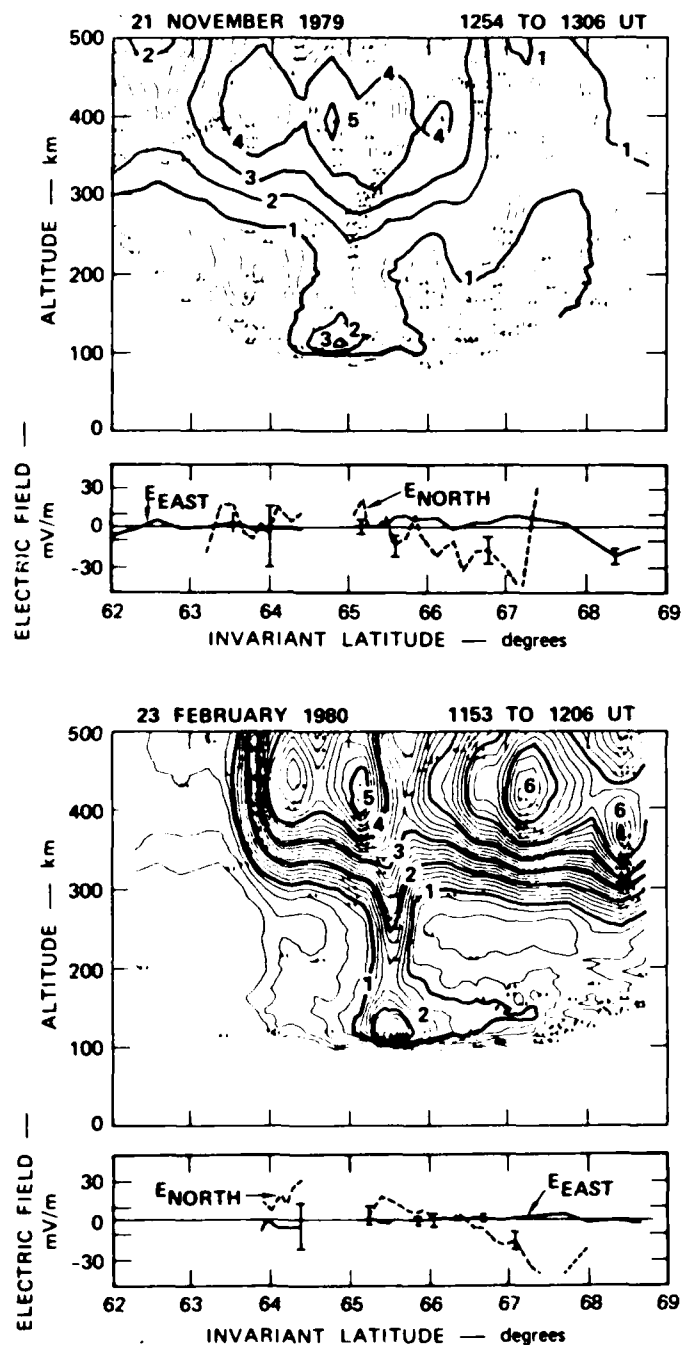
Figure II.D.4.   Electron density and electric-field
                 measurements made by the radar
                 during elevation scans in the
                 region of the Harang discontinuity
                 on 21 November 1979 and
                 23 February 1980.

73

1971]. The upward field-aligned current follows from current continuity; i.e., the ionospheric Pedersen currents along the discontinuity converge requiring current to flow out of the ionosphere.

Examination of data from scans before and after those shown in Figure II.D.4 revealed that the spatial relationship between E- and F-region ionization shown in the figure was maintained for several hours around midnight. Thus, the F-region-ionization enhancement referred to as the midnight feature appears to be spatially correlated with the E-region-ionization enhancement shown in Figure II.D.4. This suggests that the precipitation associated with the Harang discontinuity may be an important source of F region plasma. We provide further confirmation of this in the modelling described below. In addition, we show in the next section how the medium-scale-ionization enhancements apparent in Figure II.D.4 can also be produced by a source at midnight.

4.   F-Region Ionization Model

To identify those ionization features that may be considered standing features, we constructed a model of auroral production of F-region ionization in which the effects of various ionization sources could be investigated. Among the possible sources we examined were (1) a uniform distribution over the entire auroral zone (2) a band at the poleward edge of the auroral oval, (3) a band at the equatorward edge of the auroral oval, and (4) a broad region near midnight associated with upward currents at the Harang discontinuity. The model we constructed is similar to those of Knudsen [1974] and Watkins [1978] in that the electron continuity equation is reduced to the form

$$\frac{dN}{dt} = q - \beta N$$

where N is the electron density at the F layer peak, q is the ionization production rate, and β is the recombination rate. In this simple form, the equation neglects the rate of change of ionization by vertical diffusion. In the calculation, we assumed an F-region peak altitude of

74

300 to 400 km and accordingly used a value of β given by $2 \times 10^{-4} \text{s}^{-1}$.
This gives a characteristic time of 83 min for changing the F-region
ionization by a factor or e. For the ionization production rate, we used
$q = 40 \text{ cm}^{-3}\text{s}^{-1}$ for the auroral background source, $q = 60 \text{ cm}^{-3}\text{s}^{-1}$ for the
equatorward boundary source, and $q = 160 \text{ cm}^{-3}\text{s}^{-1}$ for the poleward boundary
and Harang discontinuity sources. The assumed values for q and β are
somewhat arbitrary. However, the objective of the modelling is to explain
the distribution of F-region ionization on the nightside qualitatively.
The maximum ionization that can be attained in the model is q/β; some
liberty was exercised in adjusting the two parameters to produce electron
densities similar to those observed.

The computational procedure used in the model is similar to
that of Watkins [1978]. That is, a given flux tube is followed along a
path from the polar cap through the nightside auroral zone. Our approach
differs from Watkins [1978] in that we made no attempt to follow a com-
plete path of the plasma back to its starting point making the initial and
final values agree. We assumed that the auroral zone was confined to
latitudes between 60° and 70° in the local-time interval between dusk and
dawn. All flux tubes enter the auroral zone at a latitude of 70° with an
F-region peak density of $1 \times 10^5 \text{cm}^{-3}$.

In choosing a convection model, we placed a good deal of em-
phasis on the representation of the Harang discontinuity. With this in
mind, we fashioned a convection model similar to that of Heppner [1977]
except that the Harang discontinuity was rotated so that it would be
situated nearer the postmidnight hours. This seemed to be more consistent
with the data in Figure II.D.2. An additional requirement of the convec-
tion model was that the electrodynamic properties of the region be
consistent with the presence of enhanced particle precipitation near the
Harang discontinuity. This involves showing that the convection model,
combined with a realistic conductivity model, yields a field-aligned-
current distribution with upward currents in the Harang discontinuity.

The upper panel of Figure II.D.5 shows the convection model
used. Plasma streamlines are shown at 5-kV intervals. A corotation field
has been added so that the pattern represents streamlines as seen from an

75
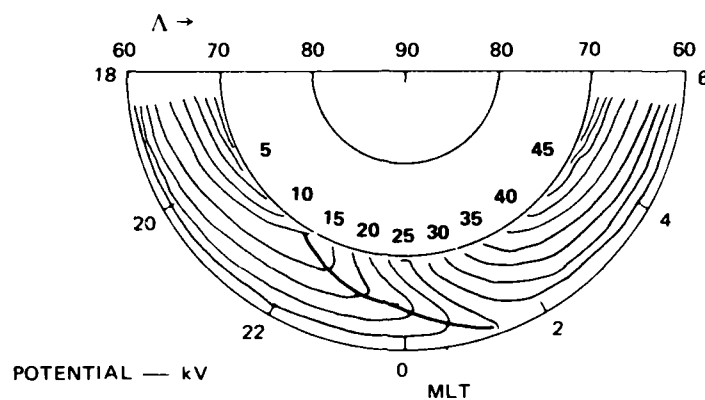
(a) CONVECTION MODEL
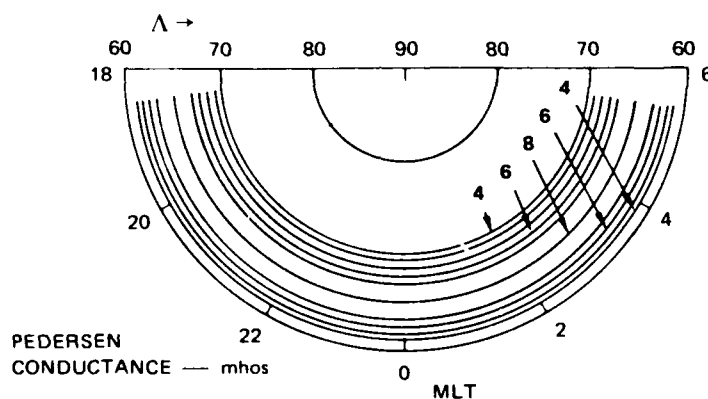
(b) ASSUMED CONDUCTANCE MODEL
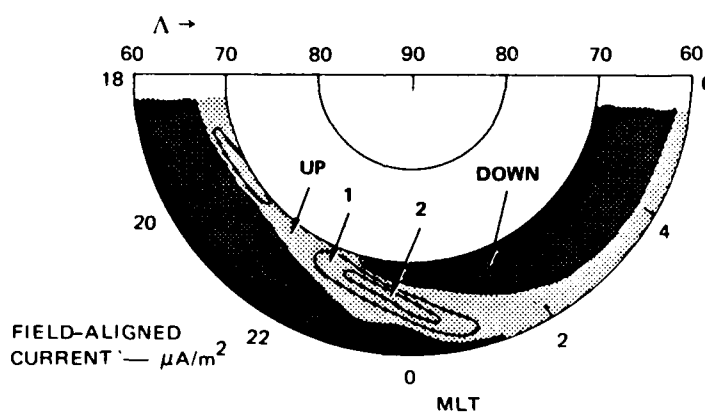
(c) FIELD-ALIGNED CURRENTS

Figure II.D.5. Auroral electrodynamic model. The field-aligned currents were computed by taking the divergence of the horizontal currents.

inertial frame of reference. The second panel in Figure II.D.5 shows a realistic conductivity model that might accompany this convection pattern. It is symmetric about the magnetic pole. Only the Pedersen conductance is shown in the figure. The Hall conductance was assumed to be 1.5 times larger. The latitudinal fall-off away from the peak is Gaussian. This conductivity distribution is based on the sounder data presented by Whalen [1983], which showed that diffuse auroral precipitation forms a circle with a Gaussian latitudinal profile centered on an offset pole. We have omitted the offset to make the conductivity distribution consistent with our convection pattern. Note that our conductivity model does not resemble the statistical conductance models of Wallis and Budzinski [1981] or Spiro et al. [1982], both of which tend to overestimate the quiet-time conductances in the midnight sector owing to the frequency of occurrence of auroral substorms. We feel this is justified because we are examining steady, not substorm, features.

The horizontal currents were computed by combining the height-integrated conductivities with the electric fields implied by the convection model in the corotating frame. The field-aligned currents were computed by taking the divergence of the horizontal currents. The results are shown in the bottom panel of Figure II.D.5. When compared with the upper panel, it is clear that the Harang discontinuity is the site of intense upward currents. Also note that the upward currents span a larger latitudinal range than the discontinuity itself. The latitudinal cross sections of electric fields and field-aligned currents resemble those implied by the data in Figure II.D.4.

One discrepancy with the above modelling is that the calculated upward currents are not necessarily consistent with the precipitation pattern as represented by the conductivity model. That is, the existence of upward field-aligned currents requires downward accelerated electrons that may alter the ionospheric conductance. Lyons [1980] examined this coupled problem and showed that inverted-V electron precipitation takes place where the divergence of electric field requires upward currents to flow. Without attempting to incorporate this effect here, we note that the field-aligned current and electric-field distribution in the Harang dis-

77

continuity in our model will probably require inverted-V-type potential structures. Electrons in the center portion of the event will have enough energy to ionize the E region. Away from the center, the fluxes of low-energy electrons will increase. These low-energy electrons will preferentially ionize the F region over a wider latitudinal range than the E-region enhancement. This agrees with the measurements shown in Figure II.D.4.

Figure II.D.6 shows the F-region peak density as a function of latitude and local time computed from the model using three different source distributions. In Figure II.D.6(a), a uniform distribution throughout the auroral zone was assumed. With $q = 40$ $cm^{-3}s^{-1}$, this yields a maximum density of 2×10^5 el/cm^3. This maximum is reached along the equatorward edge of the auroral zone in the premidnight hours. For a uniform distribution of precipitation the electron density on a given flux tube depends only on the amount of time the flux tube spends within the auroral zone. Flux tubes that cross the Harang discontinuity move relatively slowly, especially near the equatorward edge where the corotation electric field is comparable to the convection electric field. On the other hand, flux tubes that do not cross the discontinuity drift rapidly eastward causing the maximum F-region density to be reached near the dawn meridian.

Figure II.D.6(b) shows the results when we add a source at the poleward boundary of the auroral zone to the background source. The sum of the two sources yields a maximum possible steady state F-region density of 1×10^6 el/cm^3. In this case, the relative enhancement at the equatorward edge of the oval disappears, and the high plasma densities are found near the dawn and dusk meridians in the poleward portion of the auroral zone. The electron density never reaches its maximum value because flux tubes passing through the poleward boundary convect too quickly through the source. This is especially true just after midnight when corotation adds to the eastward drift velocities.

The effects of a source at the equatorward boundary of the oval are shown in Figure II.D.6(c). As expected, this source region produces a band of enhanced ionization along the equatorward boundary. In this case,

78

F REGION ELECTRON DENSTIY
(cm^{-3})
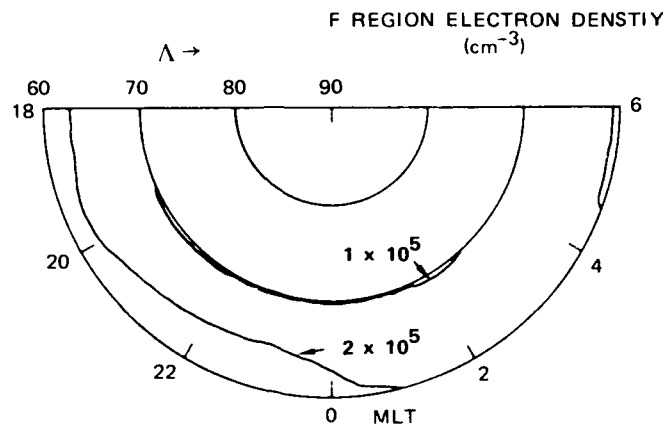
(a) **UNIFORM AURORAL BACKGROUND**
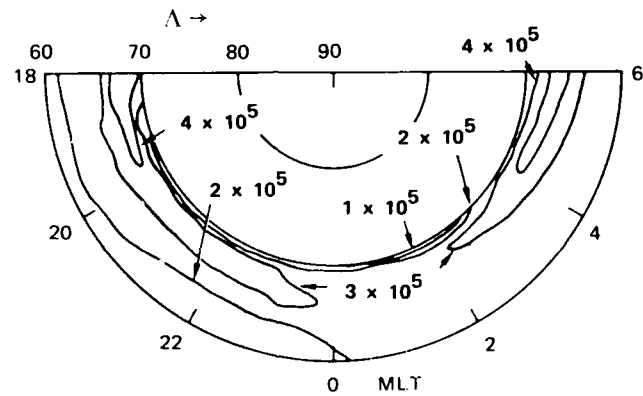
(b) **UNIFORM BACKGROUND AND POLEWARD BOUNDARY SOURCE**
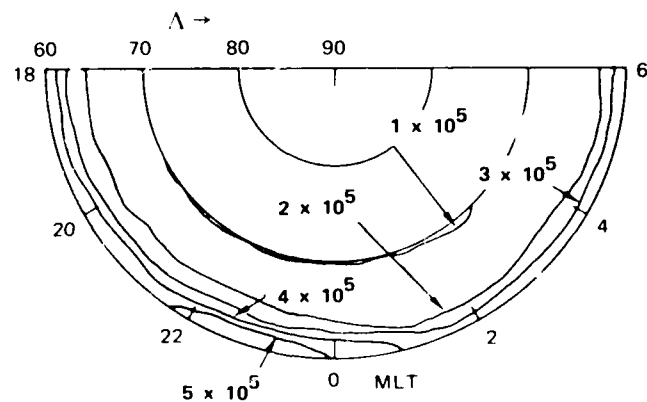
(c) **EQUATORWARD BOUNDARY SOURCE**

Figure II.D.6.   Results of model calculations for
three sources.

79

the enhanced ionization and the source region are coincident because the 60° latitude line in our convection model was an equipotential. Thus, plasma moves along this boundary, which happens to coincide with the source region. As suggested by Tsunoda et al. [1985] this produces a kind of resonance in which the plasma remains within the source region throughout its convection path. Ample time is available for the electron density to reach its maximum value which in this case is 5×10^5 el/cm^3. This value is reached at about 2300 MLT, which corresponds to a stagnation point in the convection model.

The results of placing a source region near the Harang discontinuity are shown in Figure II.D.7. Figure II.D.7(a) shows the source distribution that was added to the auroral background. The source was fashioned to resemble the upward current region shown in Figure II.D.5. Figure II.D.7(b) shows the resulting electron density. The electron density reaches its highest value near midnight within the Harang discontinuity region because the source is most intense there and because the plasma convects slowly through it. In addition to this maximum, a tail-like extension toward the morning hours represents ionization produced near midnight. This ionization can travel large distances toward the east before recombining because of the high convection speeds. In contrast, ionization produced at midnight that convects across the Harang discontinuity moves relatively slowly so that recombination depletes the F region before it can reach earlier local times. Note that the midnight source does not eliminate the relative peak in density at the equatorward boundary of the oval produced by the auroral background precipitation. The ionization feature in Figure II.D.7 is similar to those referred to as midnight ionization features in the data for 21 November 1979 and 23 February 1980 (Figure II.D.2).

5.   Production of Medium-Scale Features

As pointed out earlier, the large-scale ionization enhancements depicted in Figure II.D.2 are actually composed of many smaller-scale structures. In the modelling discussion above, we did not address the
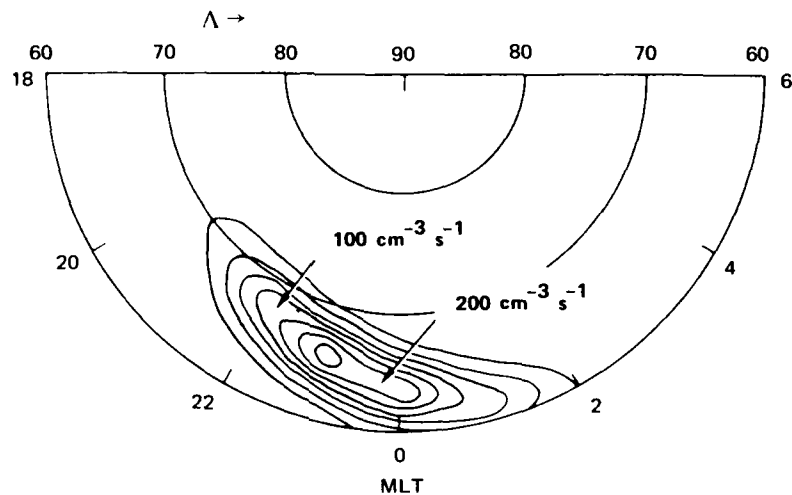
(a) THE DISTRIBUTION OF THE SOURCE—F-REGION IONIZATION-PRODUCTION RATE
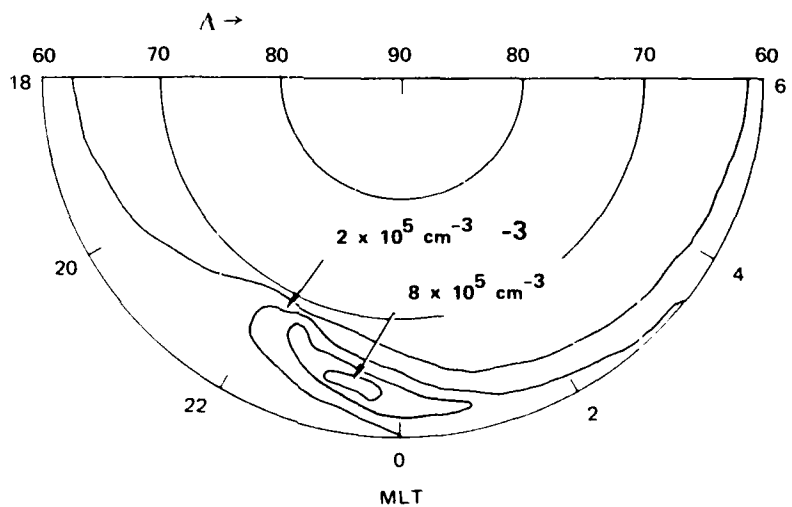
(b) RESULTING F-REGION ELECTRON DENSITY

Figure II.D.7.   Results of model calculations for the Harang
                  discontinuity source.

production of these structures. A structured source region does not produce a similarly structured F region unless the relative motion between the plasma and the source is optimal. This is because the sluggish response of F-region plasma to in situ production tends to smooth the resulting density structure. The time scale for significant changes in F-region density is tens of minutes during which time the plasma can move large distances. Thus, structure in F-region density depends on the direction of plasma drift relative to the direction in which the source is structured. We show here that a source region in the midnight sector has the properties required to produce small- and medium-scale plasma structure within the large-scale enhancements.

The typical flow geometry in the region of the Harang discontinuity is shown in the upper panel of Figure II.D.5. Plasma crosses the discontinuity convecting slowly equatorward as is apparent from the longitudinal spacing between adjacent equipotentials. Equatorward of the discontinuity the plasma turns and convects more rapidly westward. Because the flow is incompressible the difference in drift velocity between the plasma crossing the Harang discontinuity and the plasma at earlier local times will produce a change in the latitudinal scale size of structure. For example, assume that the precipitation varies sinusoidally with a wavelength L_0 along the Harang discontinuity where the magnitude of the electric field is E_0. If the electric field changes to a new value E_1 somewhere to the west of the Harang discontinuity, the structure will have a latitudinal scale size of L_1, where L_1 is given by

$$L_1 = E_0 \times L_0/E_1$$

Thus, variations with 100-km meridional scale length along the Harang discontinuity where $E = 5$ mV/m will appear as structure of 10-km scale length at dusk where $E = 50$ mV/m. We can see that if the convection pattern is such that most of the plasma crossing the Harang discontinuity convects into a latitudinally narrow channel near the dusk local-time sector, all variations in plasma density produced along the discontinuity will be mapped into this narrow region. The enhanced conductivity associated with

82

auroral precipitation tends to decrease the electric field in the oval.
If the total potential drop across the oval is to remain constant, the
electric field must be large in the regions of low conductivity, in this
case equatorward of the oval. This process can account for the enhanced
scintillation reported by Fremouw et al. [1977] at the equatorward edge of
the oval. It also explains the observations presented by Basu et al.
[1984] in which a shift in scintillation spectra in regions of high elec-
tric field indicated the presence of smaller-scale-size irregularities.
In addition, this mechanism increases the spatial gradients of the ioniza-
tion, so that plasma instabilities that depend on the magnitude of the
gradients would be favored at dusk rather than midnight.

The effects of plasma convection on the scale size of ioniza-
tion enhancements are important for transient ionization features as well.
As pointed out by Vickrey and Kelley [1983], a structured velocity pattern
can change the anisotropy of drifting irregularities. This concept was
used to explain the change in irregularity geometry observed by Livingston
et al. [1982]. Here, we have modelled the effects of a realistic convec-
tion pattern on the evolution of large-scale plasma enhancements in the
polar cap such as those observed by Weber et al. [1984]. The technique
involves solving the electron transport equation numerically. An example
of the results of these calculations is shown in Figure II.D.8. The
initial condition is shown by the isodensity contour in the first panel.
A circular large-scale enhancement of ionization is placed at 1800 LT and
a latitude of 75°. The convection pattern shown is that of Heelis et al.
[1982]. The motion and distortion of this blob at one-hour intervals are
shown by the subsequent panels. For these initial conditions, the large-
scale plasma feature drifts to the equatorward edge of the oval and elon-
gates along the boundary. The elongation is a result of the different
convection times associated with various streamlines on which the large-
scale enhancement is located. In fact, a portion of the large-scale
feature convects to a stagnation point, where it would remain until it
recombines after a suitable length of time. However, this enhancement may
remain for several hours, elongated along the equatorward edge of the oval
and becoming narrower as other portions of the enhancement convect slowly

83
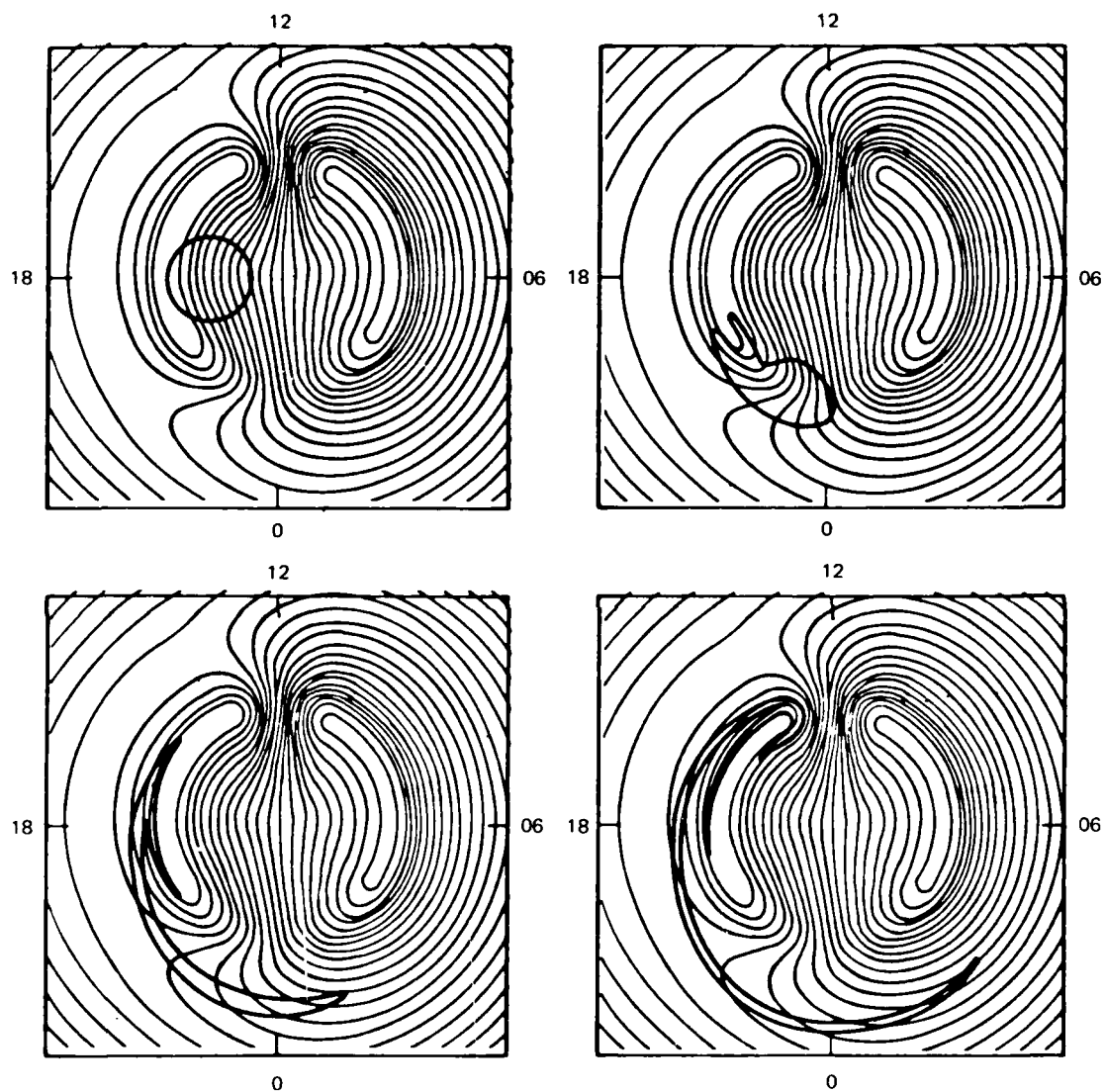
Figure II.D.8.   Distortion of a circular blob of ionization as it convects from
the polar cap through the auroral zone.

away. In this manner, a transient ionization feature may behave very much like a standing ionization feature. If, during the few hours that the enhancement is stretched out along the auroral-zone boundary, a second patch, also on streamlines connected to the stagnation point, crosses the polar cap, a second boundary feature will appear extremely close to the previous one but not overlapping. This process produces steep gradients in electron density and possibly enhanced scintillation effects. In addition, these gradients are ideal sites for structuring by flux tube interchange mechanisms. Note also the hook-shaped extensions of the enhancement in the dayside hours. These small-scale features are not artifacts of the calculations, but are actually produced by the incompressible flow in a well-behaved potential field. This structuring process can act on any scale-size enhancement, the important parameter is the size of the enhancement relative to the scale length for gradients in the electric field.

The behavior of the large-scale enhancement in Figure II.D.8 can be contrasted to that of one which is situated initially on the dawn side of the polar cap. This feature will convect rapidly equatorward, then eastward, missing the stagnation point and crossing the dawn meridian with much less distortion than that shown in Figure II.D.8. Because of the rapid convection relative to a large-scale enhancement that convects along the equatorward boundary of the oval, the dawn-sector enhancement should be much less common. Radar measurements have indicated that this is the case.

6.   Discussion and Summary

We have examined possible source mechanisms for medium-scale (tens of kilometers) and large-scale (hundreds of kilometers) ionization enhancements in the nightside auroral F region. The most prominent large-scale features in the Chatanika radar measurements are located in the midnight sector and along the equatorward boundary of the oval. Our modelling indicates that both of these features could be produced by combining a uniform auroral background source with a more intense and localized

85

source in the region of the Harang discontinuity. We noted that the presence of a strong source near the Harang discontinuity could account for some of the smaller-scale structure within large-scale ionization enhancements observed at earlier local times. We also showed that latitudinally narrow ionization enhancements are a natural consequence of the high-latitude convection pattern even without a localized source region.

A crucial question that must be addressed with regard to identification of an F-region source is which type of energetic electron energy distributions are most effective for producing ionization at high altitudes. Although electrons in the 0.1-to-1-keV range are more efficient in depositing energy in the F region, substantially more energy is often carried by the higher-energy electrons. These higher-energy particles deposit most of their energy at lower altitudes, but some fraction of the energy is deposited in the F region as well. Thus, auroral arcs may produce F-region enhancements as efficiently as polar-cusp precipitation that contains fewer high-energy particles. A careful modelling of the altitude distribution of ionization production rate for various input electron spectra is required to address this problem. Once such a study is done, statistical studies of the characteristics of electron precipitation in the auroral oval might reveal the most likely location of enhanced ionization.

In our modelling, we investigated the effects of source regions at the poleward and equatorward edges of the auroral oval and in the midnight sector near the Harang discontinuity. The results indicated that the source at the poleward edge of the auroral oval was the least effective in producing large-scale ionization enhancements. Evidence for the existence of this source region was presented by Eather [1969], who argued that the enhanced 630.0-nm emissions observed at the poleward edge of the oval were produced by low-energy-particle precipitation. Eather [1969] referred to this as the "soft zone." The poleward edge of the auroral oval is also the location at which most quiet auroral arcs are observed. As noted above, the inverted-V precipitation that produces auroral arcs, also contains significant fluxes of low-energy electrons, especially at

86

the edges. However, even though the premidnight, poleward boundary of the auroral oval may be an important source of low-energy particle precipitation, our modelling indicates that plasma crosses this region too quickly for any substantial increase in F-region ionization to occur. The westward electric field in auroral arcs is typically about 5 mV/m. The corresponding equatorward drift velocity is 100 m/s. Even if the arc is 100 km wide, a given flux tube is only within the source for about 16 m. This is not enough time for an appreciable increase in F-region ionization unless the source is very intense. In contrast, the equatorward drift through the Harang discontinuity is much slower. This is not a unique feature of our convection model, but it must be true in any reasonable convection model. The equatorward drift becomes smaller with decreasing latitude because in the Harang discontinuity the northward electric field decreases with local time. The condition $\nabla \times \bar{E} = 0$ ensures that the westward electric field must decrease with decreasing latitude.

An argument for a source region at the equatorward boundary of the oval can be made on the basis of recent observations by Tanskanen et al. [1981], who identified intense low-energy electron precipitation measured by the DMSP satellite. Similar observations were reported by Schield and Frank [1970], who examined OGO measurements at the equatorward edge of plasma sheet precipitation. However, these enhancements are not always present, and until information is available about the frequency of these events, their effects cannot be properly evaluated. As we have shown, the existence of an ionization enhancement at the equatorward edge of the auroral oval does not require a source. In fact, these enhancements can be produced by two other mechanisms. First, we showed that uniform precipitation over the auroral oval produces an enhancement along the equatorward boundary because flux tubes there have spent a longer time within the source region. Second, large-scale plasma enhancements in the polar cap can convect into the auroral oval and become tied to a stagnation point, creating a semi-permament ionization feature elongated along the boundary.

The greater efficiency of a source region at the Harang discontinuity relative to the sources mentioned above is a result of two factors First, convection is slow in the Harang discontinuity, thus allowing the precipitation to act longer on the F-region plasma. Second, the precipitation associated with the Harang discontinuity is tied to the convection pattern. Thus, although the overall convection pattern may change, the precipitation associated with the Harang discontinuity will change location accordingly. In an average sense, this favors the creation of ionization enhancements near midnight.

The ionization source in the Harang discontinuity acts on plasma convecting out of the polar cap from the dayside. Thus, the effects of this source are modulated by the level of ionization in the polar-cap F region. De la Beaujardiere et al. [1984] studied F-region plasma measured by three radars at different local times. They concluded that there was a strong dependence on UT in the level of F-region ionization owing to the displacement between the geographic and geomagntic poles. Depending on the geographic location of the observation, F-region plasma spends varying amounts of time exposed to ionizing solar radiation. The observation of this dependence on UT of F-region ionization does not preclude the existence of other sources acting in addition to photo-ionization. It is unlikely that photoionization acting alone can produce the medium- and large-scale ionization structures observed on the night-side. However, the path of the plasma before entering the midnight auroral zone must influence the overall level of ionization on which the sources act.

The small-scale structure that is observed within the large-scale ionization enhancements has several possible sources. The effects of various plasma instabilities have been reviewed by Fejer and Kelley [1980]. The possibility that structure in ionization is produced directly by structured particle precipitation is currently being examined using data from the HILAT satellite. The two mechanisms proposed here do not depend on plasma instabilities or highly structured particle precipitation. In one, case small-scale latitudinal structure arises out of

large-scale longitudinal variations in particle precipitation along the Harang discontinuity. In another case, small-scale structure is produced when a large-scale ionization feature drifts into regions of larger electric field. The distinction between these two effects is that one acts on standing ionization features while the other acts on transient ionization features. In both, the high-latitude convection pattern is crucial in determining the resulting structure.

SECTION III
MAGNETOSPHERIC TURBULENCE--
A SOURCE OF HIGH-LATITUDE PLASMA STRUCTURE

A.   The Voltage-Current Relationship of the Magnetospheric Generator

It has been proposed on theoretical grounds that structure in the magnetospheric convection velocity field could generate structure in F-region plasma density if allowed to act on an initial horizontal density gradient Fejer and Kelley [1980], Vickrey and Kelley [1983]. Such horizontal gradients abound in the high-latitude ionosphere. The idea is simply that electrostatic structure created by magnetosphere-solar wind interactions could be imposed on a "passive" F region, thereby stirring the plasma and interchanging flux tubes of varying plasma density. By "passive," we mean that the F region contributes little to flux tube integrated quantities such as conductivity and inertia. To examine this process quantitatively, we have conducted a series of experiments and theoretical studies of high-latitude electrodynamic structure and its effect on plasma density structure. We begin by examining of the current-voltage relationship for the magnetospheric generator that appears to depend on scale size.

1.   Large Scales

Ionospheric Pedersen currents are dissipative and therefore, must be driven by a source that is presumably located in the magnetosphere. Measurements of the Pedersen current can be used to study that portion of the ionospheric currents directly driven by the magnetospheric source. However, only measurements made by incoherent-scatter radar allow separation of the current into Hall and Pedersen components. Ground-based magnetometers respond to the total current.

We have combined radar measurements of electric field and conductivity with a simple model of field-aligned currents to deduce a relationship between the cross-polar-cap potential-drop and the resulting field-aligned current intensity. The model is shown in Figure III.A.1, which illustrates a pair of field-aligned current sheets in cross section, along with the ionospheric closure of the currents. The height-integrated Pedersen current in region B, J_p, is equal to the field-aligned current intensity J_0 (in A/km) in regions A and C. The radar measurements that we have used in this study were obtained while the radar scanned in elevation in the magnetic meridian. In regions A and C, the height-integrated Pedersen current is less than J_0, which implies that the maximum Pedersen current that can be measured by the radar with this particular current configuration is $J_p = J_0$.

We further assume in this model that the current J_0 depends on the cross-polar-cap potential drop alone. If we combine all measurements of the Pedersen current for any given value of the polar-cap potential drop, we should find a limiting value below which all the measurements are contained. This limiting value should be equal to J_0. In practice, separating radar data according to the polar cap potential drop is difficult, because this information is not always available. Instead, we sort the data according to K_p, which should be related in some way to the magnetospheric potential because it is a measure of magnetic activity. In Figure III.A.2 we show plots of electric field versus height integrated Pedersen conductivity for six different values of K_p. The plots include the total number of data points that are included in each K_p range. Over 200 hours of elevation scan experiments were used to obtain these distributions.

The most important feature to note in Figure III.A.2 is that the electric field is small when the conductivity is high, which confirms the idea that the Pedersen current is limited. The hyperbolas in Figure III.A.2 were drawn in each case to contain 95 percent of the data points. The equation of each hyperbola is given in the figure. As expected, for higher values of K_p the limiting Pedersen current is larger. We suggest that the limiting value is the quantity referred to as J_0 in the model above.

91
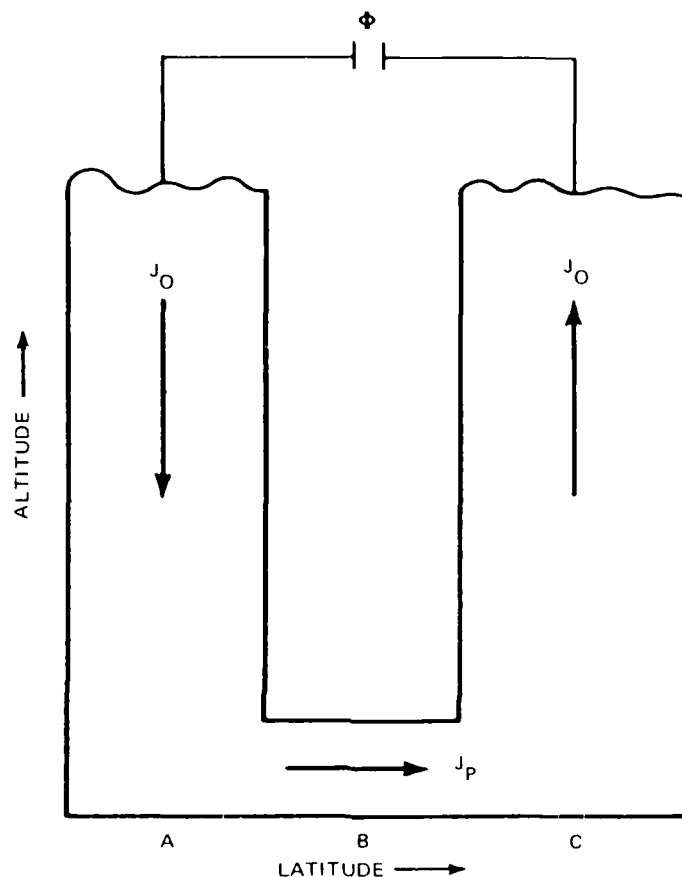
Figure III.A.1.   Schematic representation of the
                   coupling of field-aligned-current
                   regions by ionospheric Pedersen
                   currents.

Figure III.A.3 shows the limiting current versus K_p. The top of each bar plotted is the current intensity that contains 95 percent of the data for each value of K_p. The bottom of each bar is the current that contains 85 percent of the data. The length of each bar thus indicates the uncertainty in the value of the limiting current. The bars are longer for those K_p values that contained fewer measurements. A least-squares fit through the data, weighted according to the length of the bars, is shown by the straight line in Figure III.A.3.
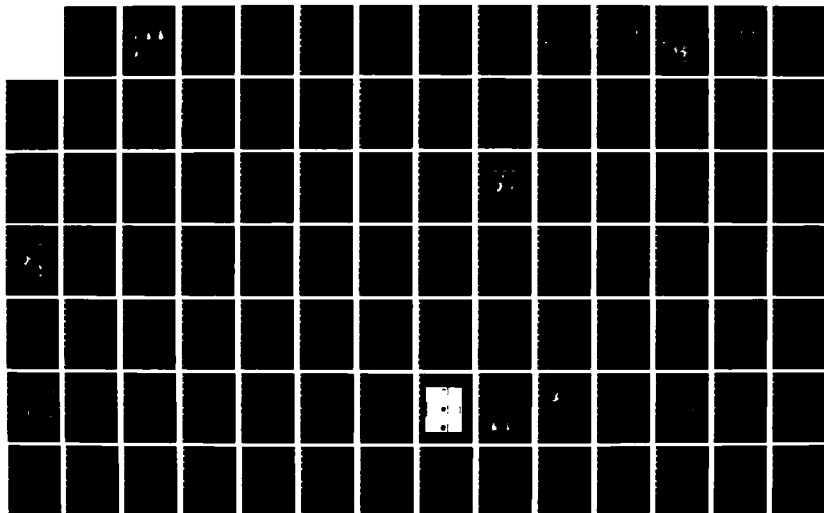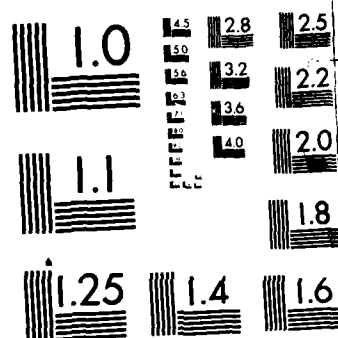
MICROCOPY RESOLUTION TEST CHART
NATIONAL BUREAU OF STANDARDS 1963 A
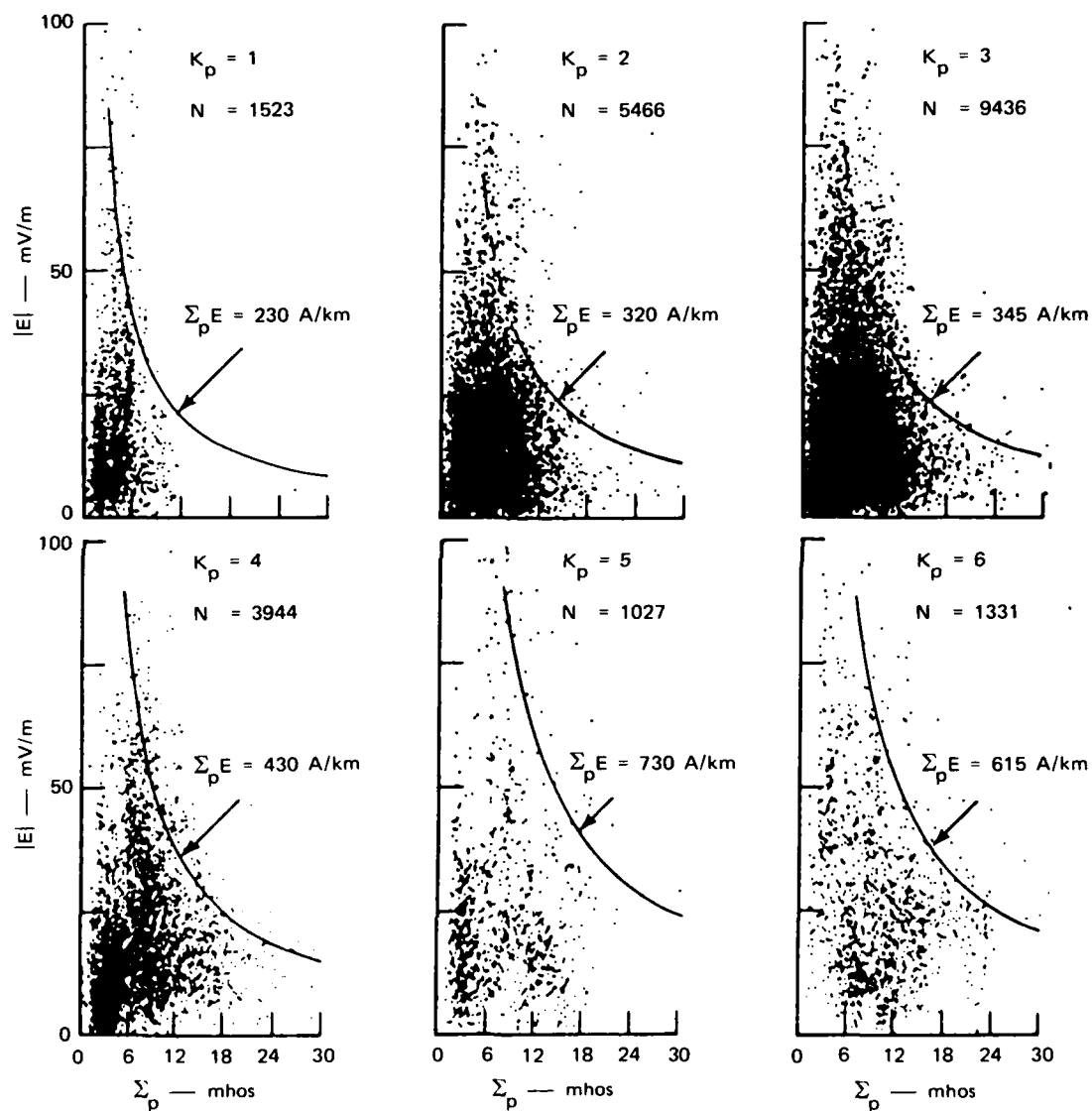
Figure III.A.2. The relationship between the ionospheric electric field and Pedersen conductivity for various values of K_p.
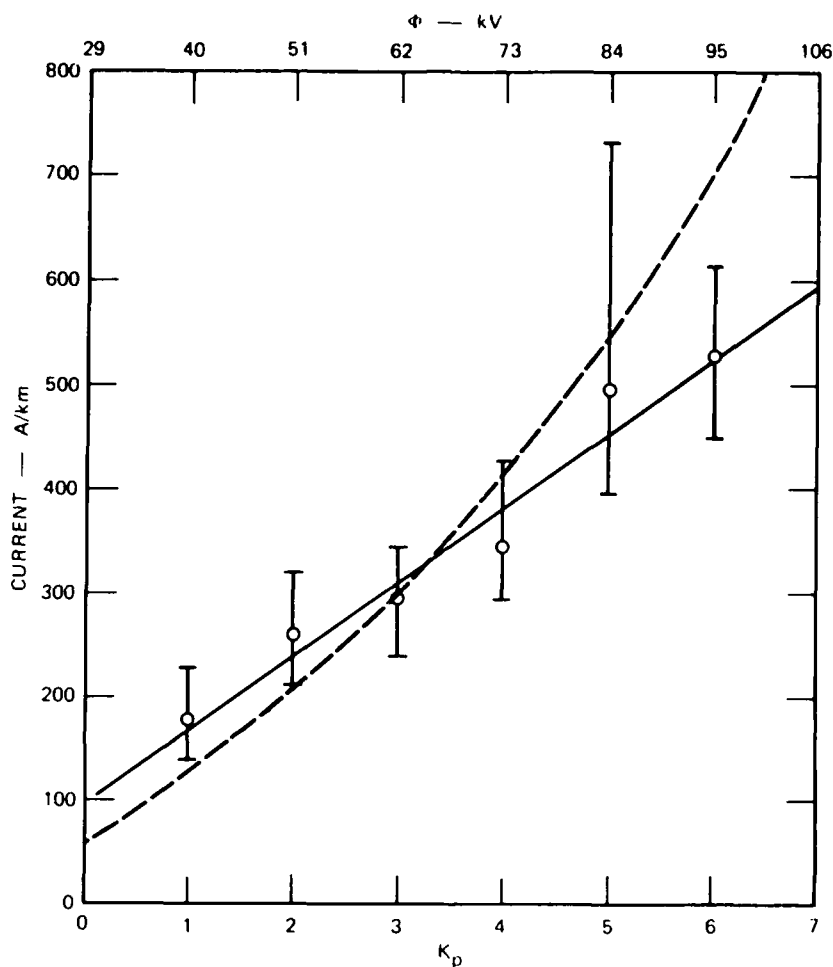
Figure III.A.3.   Statistical relationship between the limiting current J_0 and K_p.

Relating K_p to the polar-cap potential drop is difficult because K_p is a three-hour index. However, Reiff et al. [1981] used AE-C, AE-D, and S3-3 satellite electric-field measurements to obtain a relationship between K_p and polar-cap potential drop. The correlation coefficient for this fit was 0.55. We have used this relationship to include in Figure III.A.3 the value of the polar-cap potential drop.

As a check on these results we note that Iijima and Potemra [1978] used Triad satellite magnetometer data to deduce the average field-

aligned current intensity for K_p values between 2- and 4+. Their results
for the Region-1 current sheets (those directly linked to the magneto-
spheric generator) were 300 A/km and 250 A/km for the afternoon-to-
midnight and midnight-to-forenoon MLT sectors, respectively. These values
agree well with those shown in Figure III.A.3.

2. Small Scales

As mentioned earlier in this section, plasma density structure
may be produced by magnetospheric electrostatic structure imposed on a
plasma-density gradient. An important question is whether or not this
structure-production mechanism extends down to scintillation producing
scales. We begin this investigation by presenting evidence from a noon-
sector coordinated radar/HILAT pass that structure in magnetospheric
convection produced enhanced scintillation on the $\overline{E} \times \overline{B}$ stable side of an
F-region blob. After establishing such velocity structure as a source of
plasma-density structure (see also Section III.C for a separate case
study), we show that structure in the convection velocity field is en-
hanced in the winter hemisphere.

By combining HILAT and Sondrestrom measurements we are able to
examine in detail the stability of measured gradients and sort out pos-
sible candidates for structure production including current-driven and
electric field-driven convective instabilities. Figure III.A.4 shows the
geometry of the HILAT trajectory on day 344 of 1983 (10 December). Super-
imposed on the HILAT trajectory and the F-region beacon penetration point
in geodetic and magnetic coordinates is the position (at 350-km altitude)
scanned by the Sondrestrom radar. Figure III.A.5 shows the altitudinal
and latitudinal variations of electron density measured by the radar at
the time of the HILAT pass. The F-region ionization enhancement at 71°
appears to have been produced by an enhanced flux of soft particles, as
can be seen from the upper panels of the figure. The equatorward directed
density gradient was quite steep.
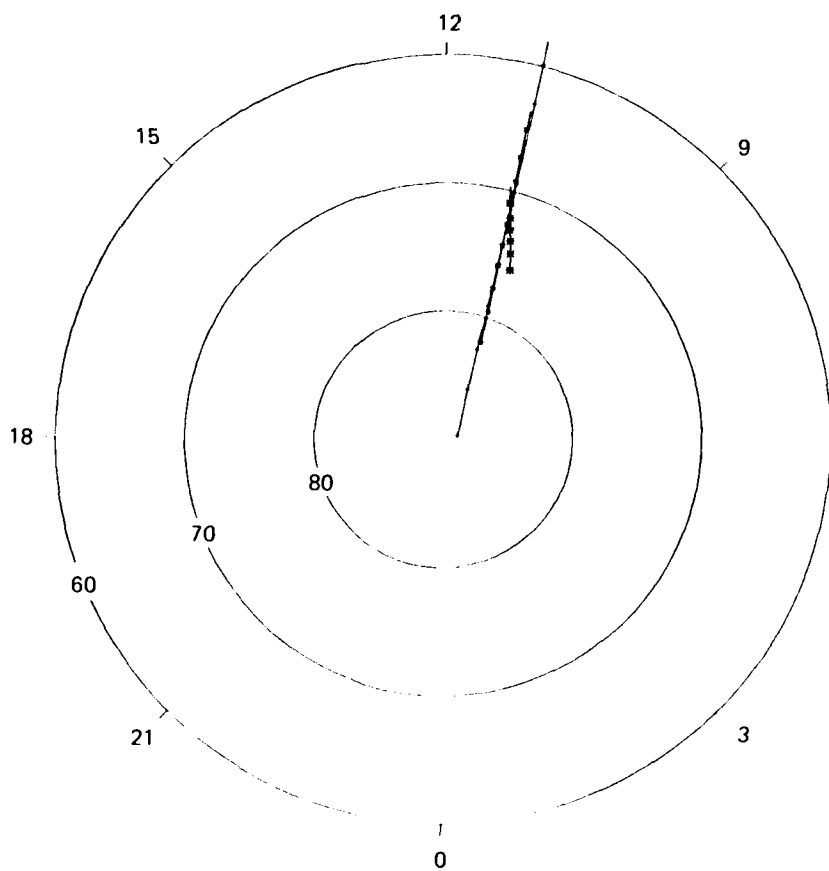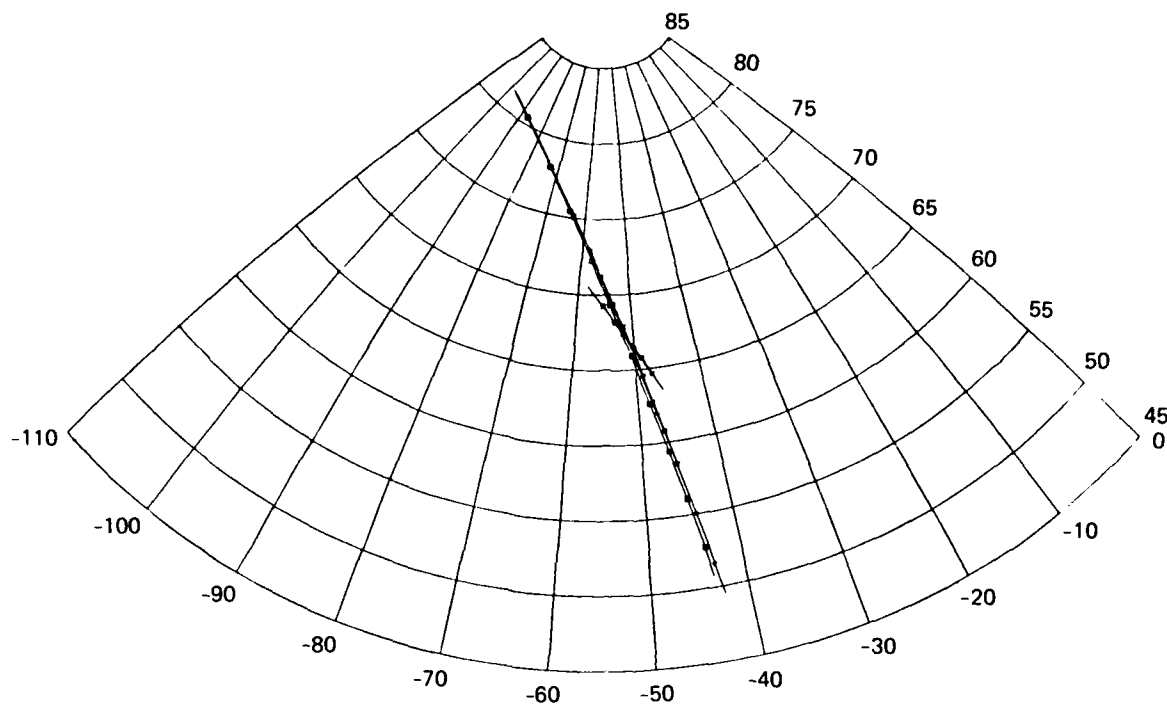
Figure III.A.4.   HILAT trajectory and radar scan in geodetic and magnetic coordinates.
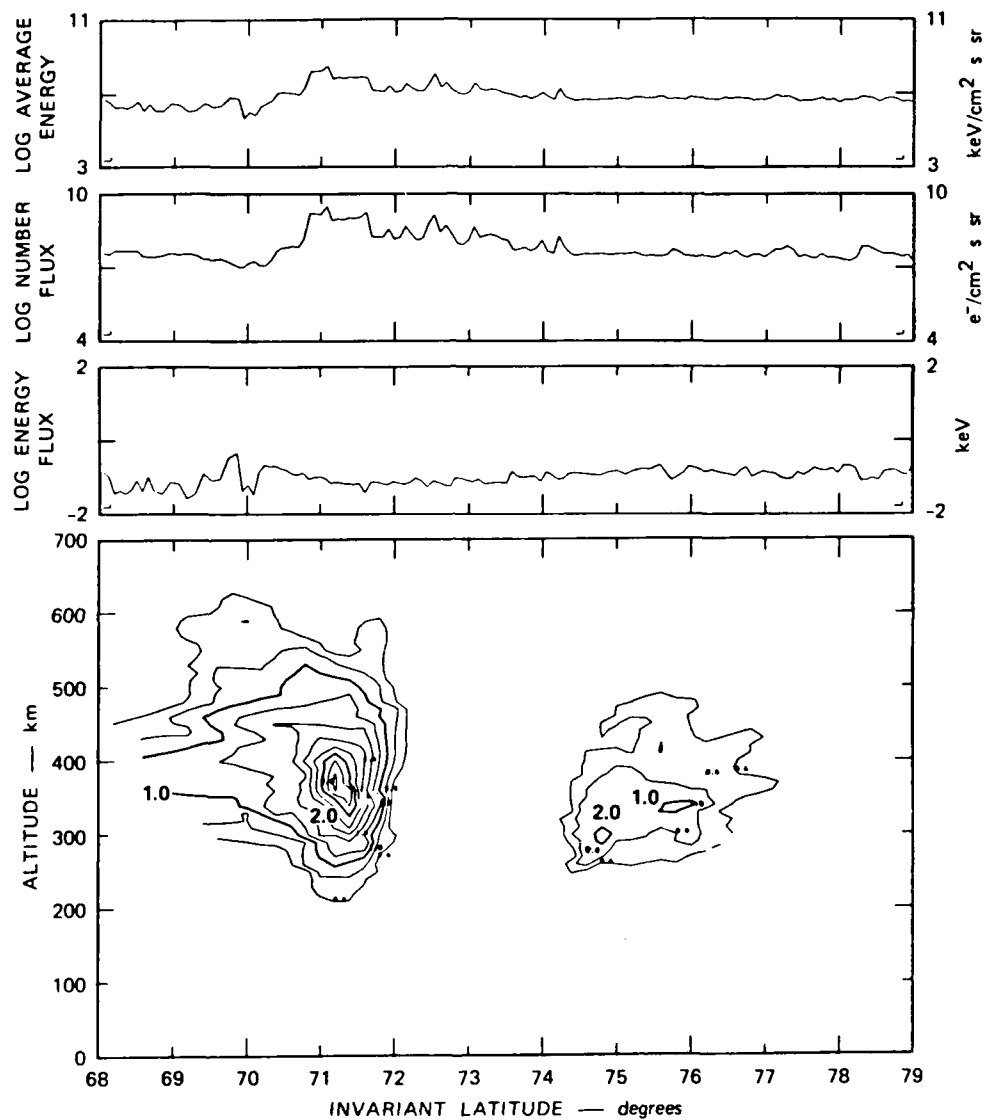
Figure III.A.5. Comparison of electron-spectrometer measurements and meridional electron-density contours measured by the Sondrestrom radar.

The magnetometer, beacon, and drift meter measurements are shown along with the radar measurements in Figure III.A.6. We see that there were rather intense upward and downward field-aligned currents equatorward of the steep density gradient. However, at the equatorward-directed gradient itself, the field-aligned current was quite small. The rms phase scintillation was larger on the equatorward gradient than on the poleward gradient. The radar measurements of ion velocity indicate that the meridional component of velocity was between 300 and 700 m/s, depending on latitude. If we assume a model neutral wind [Quegan et al., 1982] of approximately 50 m/s northward, we find that the $\bar{E} \times \bar{B}$ instability would not be operative on the equatorward gradient. This suggests that the linearly stable side of the density enhancement is associated with the small-scale structure in plasma density.

The ion drift meter measurements made during this pass are shown in the third panel of Figure III.A.6. The enhanced scintillation occurs where the zonal drift velocity component is large and highly structured, suggesting that in this particular case, the small-scale structure in the density may be related to small-scale structure in the magnetospheric convective flow.

To investigate structure in both convective flow and field-aligned currents in a quantitative way, we have examined the detrended standard deviation of the cross-track velocity, V_Y, and of the B_Y component of the magnetometer measurements. Figures III.A.7(a) through (c) show the structure of the B_Y component of the magnetometer for selected high elevation angle orbits. Figures III.A.8(a) through (c) show structure in the cross-track velocity. The quantities plotted are the square root of the integral of the spectra of $|\Delta B_Y|^2$ and $|\Delta V_Y|^2$ over the scale size regime between 80 and 30 km, i.e.,

$$\text{Velocity Structure} = \left\{ \int_{k_1}^{k_2} |\Delta V_Y|^2 (k) \, dk \right\}^{1/2} \text{ km/s}$$

98
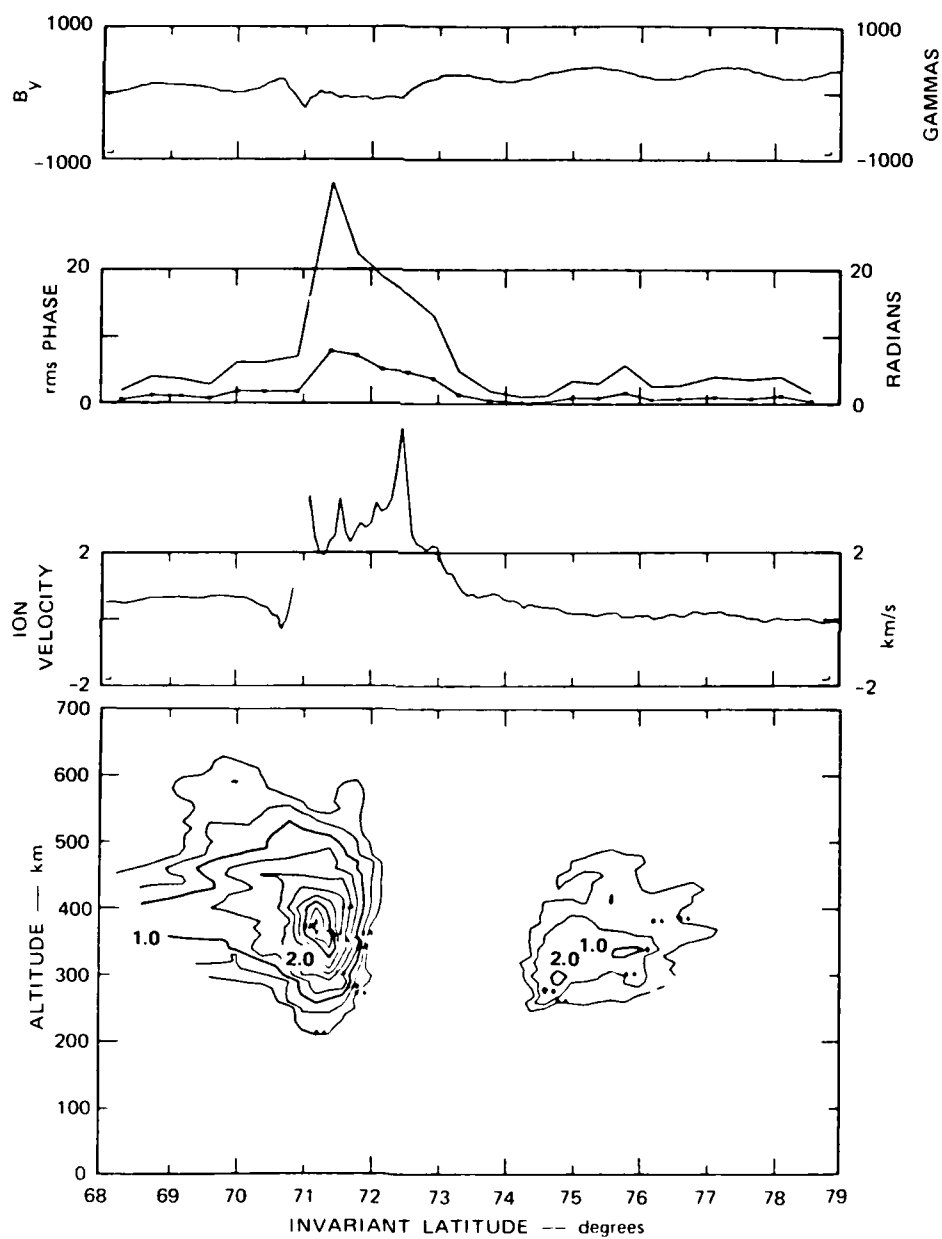
Figure III.A.6.   Comparison of HILAT magnetometer, beacon, drift-meter, and radar measurements.
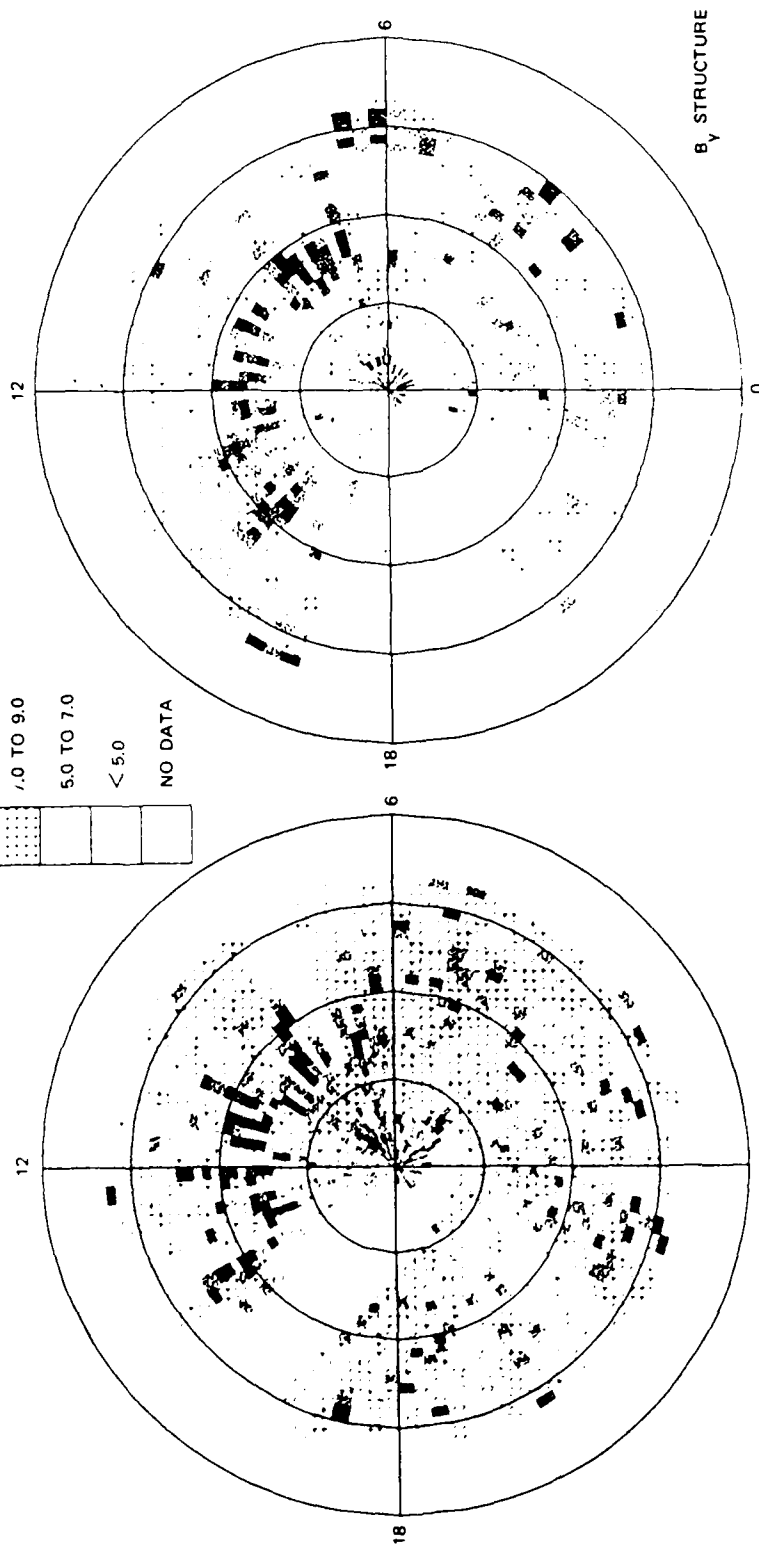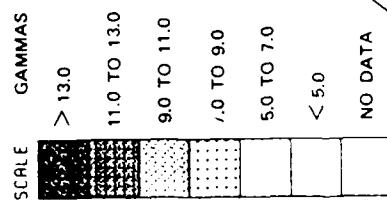
(a) WINTER 1983 (7 NOVEMBER 1983 TO 10 FEBRUARY 1984)

(b) SUMMER 1984 (5 MAY TO 8 AUGUST 1984)

SCALE GAMMAS

> 13.0

11.0 TO 13.0

9.0 TO 11.0

7.0 TO 9.0

5.0 TO 7.0

< 5.0

NO DATA

Figure III.A.7   Root-mean-square variation of detrended Y-component magnetometer data from HILAT in the scale-size regime 80 to 30 km for high-elevation angle passes over Sondrestrom.

B$_Y$ STRUCTURE

SCALE   GAMMAS

> 13.0

11.0 TO 13.0

9.0 TO 11.0

7.0 TO 9.0

5.0 TO 7.0

< 5.0

NO DATA

(c) WINTER 1984 (10 NOVEMBER 1984 TO 6 FEBRUARY 1985)
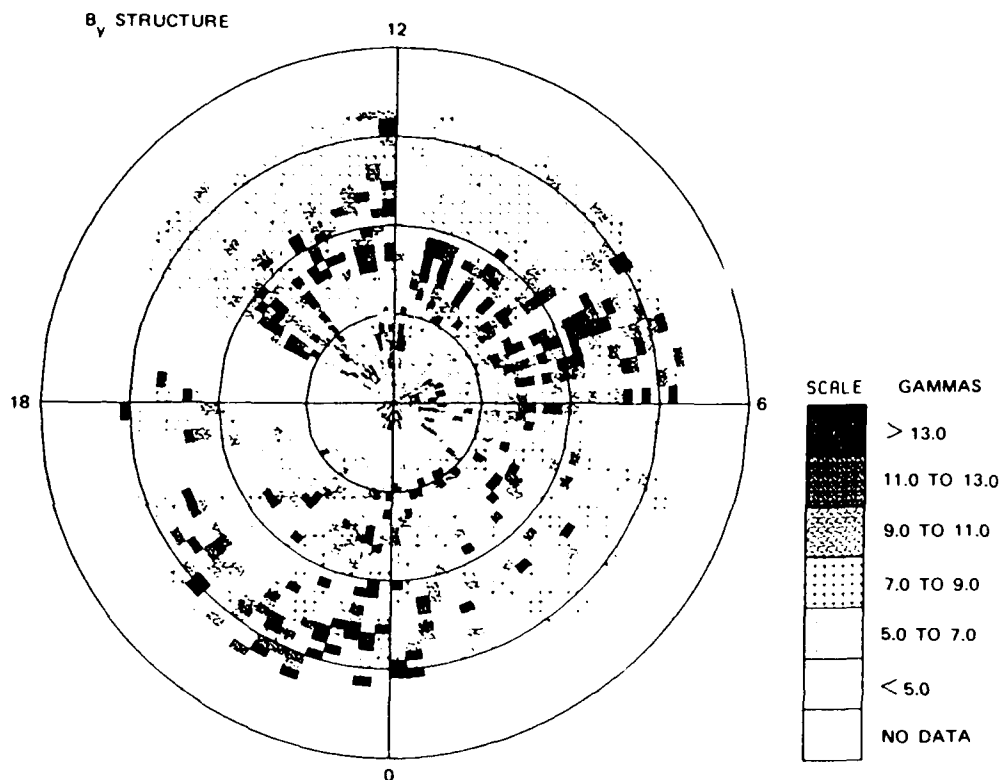
Figure III.A.7 (Concluded).

$$
B_Y \text{ Structure} = \left\{ \int_{k_1}^{k_2} |B_Y|^2 (k) \, dk \right\}^{1/2} \quad \text{Gammas} \quad ,
$$

Where $k_1 = 2\pi/80$ km, $k_2 = 2\pi/30$ km .

In both figures, the data are plotted in invariant latitude-corrected MLT coordinates. The rings represent 10° intervals of invariant latitude from 50° to the pole. The passes shown here are the same as those presented in Section II.B. in which the seasonal and solar cycle variations of in situ density and TEC were discussed. Data from both ascending and descending

101

SCALE km/s

> 0.07

0.06 TO 0.07

0.04 TO 0.06

0.03 TO 0.04

0.01 TO 0.03

< 0.01

NO DATA

(a) WINTER 1983 (7 NOVEMBER 1983 TO 10 FEBRUARY 1984)

(b) SUMMER 1984 (5 MAY to 8 AUGUST 1984)

VELOCITY STRUCTURE
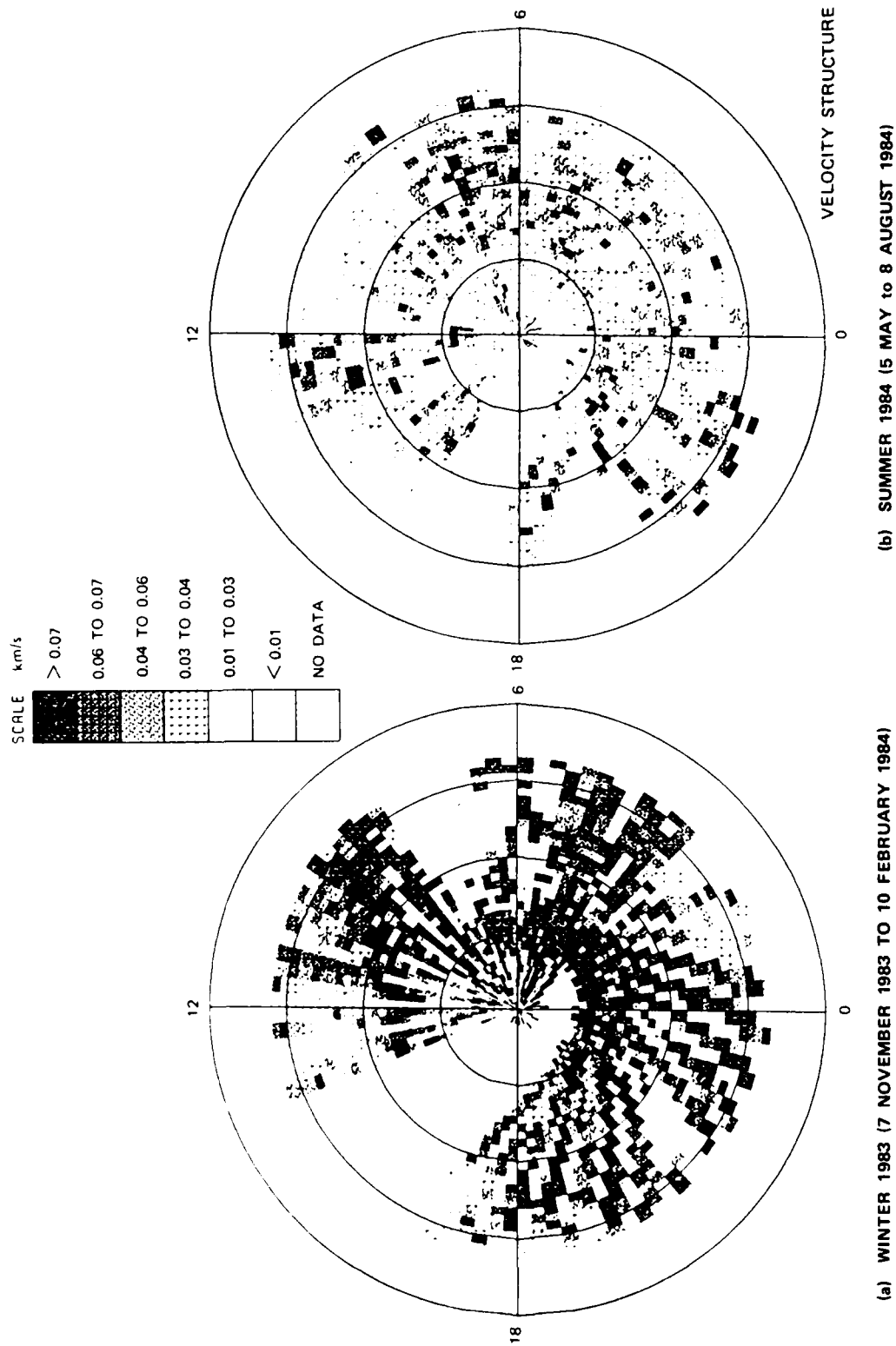
Figure III.A.8, Root-mean-square variation of detrended cross-track velocity measured by HILAT in the scale-size regime 80 to 30 km for high-elevation angle passes over Sondrestrom.

102

VELOCITY STRUCTURE

SCALE km/s

> 0.07

0.06 TO 0.07

0.04 TO 0.06

0.03 TO 0.04

0.01 TO 0.03

< 0.01

NO DATA
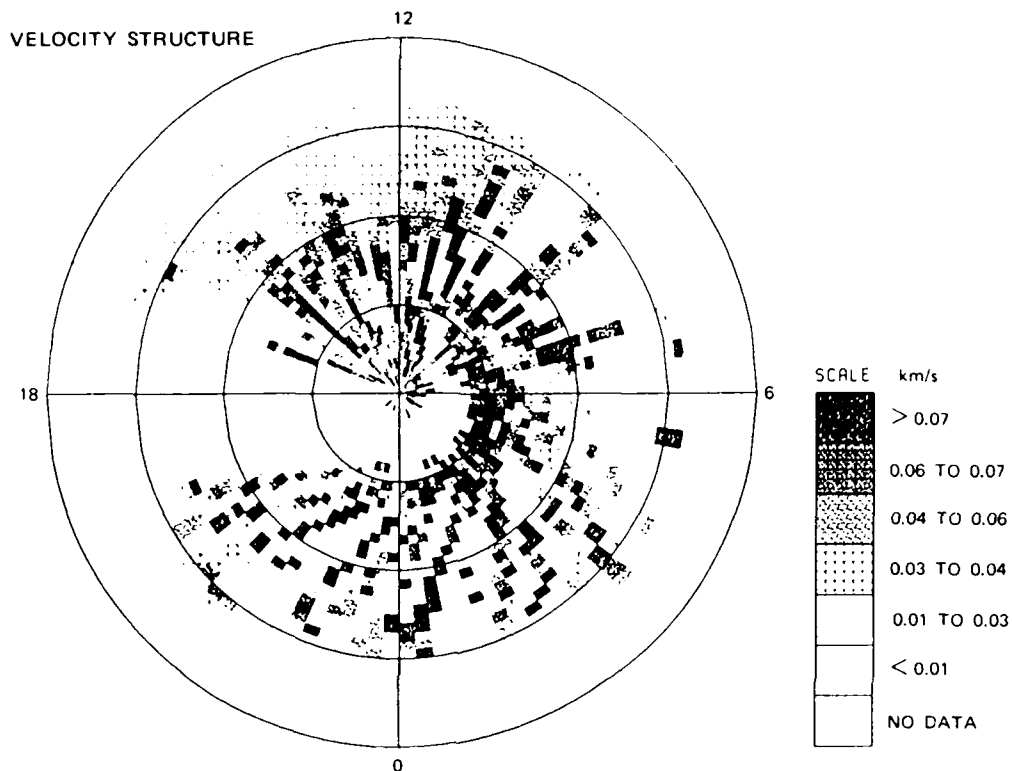
(c) WINTER 1984 (10 NOVEMBER 1984 TO 6 FEBRUARY 1985)

Figure III.A.8.(Concluded).

node passes have been averaged in bins of 15 min of corrected magnetic local time and 1° of invariant latitude. Only those passes whose maximum elevation angle exceeds 45° are shown. This reduces the ambiguity in any comparison with beacon data. Velocity data are also suppressed if the in situ density was less than 2×10^3 cm^{-3} because the data becomes noisy at lower densities.

The data in Figures III.A.7 show a persistent enhancement in B_Y structure on the dayside of the earth between approximately 70 and 75° invariant latitude. The amplitude of the structure in B_Y, which is a measure of the field-aligned current intensity in this scale-size regime,

103

does not seem to be a strong function of season. This implies that in the vicinity of the dayside cusp, the magnetosphere tends to behave as a constant current source--at least in this scale-size regime. As discussed below, this has dramatic implications for the seasonal variations of velocity structure and scintillation.

The amplitude of velocity structure shown in Figures III.A.8(a) through (c) shows very strong seasonal variations. In the summertime (Figure III.A.8(b), the velocity structure tends to maximize in the same regions where the structure in field-aligned current maximizes [see Figure III.A.7(b)]. This behavior is expected because the ionospheric conductivity in the summertime is very uniform.

In a quasi-neutral plasma, $\nabla \cdot (\sigma \bar{E}) \equiv 0$ at any point, where σ is the local conductivity and $\bar{E}$ is the electric field. Integrating in altitude over the ionosphere and assuming $\bar{E} \cdot \bar{B} \equiv 0$ yields

$$-j_\| = \Sigma \nabla \cdot \bar{E} + \bar{E} \cdot \nabla \Sigma$$

where $j_\|$ is the field-aligned current and Σ is the height-integrated conductivity.

In the summer, the E region is uniformly sunlit and relatively unstructured. Therefore, Σ is large, and $\nabla \Sigma$ is small. Velocity structure, represented by the term $(\nabla \cdot E)$ is collocated with $j_\|$ and hence, the B_Y structure. In the wintertime, the conductivity is in general lower and more structured because precipitation-produced ionization dominates over the background. Hence large velocity structure arises in the winter to maintain divergence-free current flow everywhere. As was pointed out in Section II.B these seasonal trends of magnetospheric electrostatic structure should tend to produce higher levels of scintillation in the winter as compared to summer.

104

B. Preliminary Assessment of the Effectiveness of F-Region Polarization Electric Fields at High Latitudes

In this section, we investigate the hypothesis that large-scale ($\approx$100-km) plasma-density enhancements (or "blobs") found in the auroral F layer become structured via a magnetic-flux-tube interchange (MFTI) process. In such a process, plasma structure is produced when spatially irregular electric fields transport higher-number-density plasma (from within the blob) into a region containing lower-number-density plasma (the background ionosphere), and vice versa. Direct experimental evidence of this process can be obtained by measuring concurrently the spatial distributions of F-region plasma density and electric field. Using the tristatic EISCAT radar facility, we measured these quantities in a two-dimensional plane transverse to the geomagnetic field, at 300-km altitude. We show, in a case study, that plasma-density structure found along the poleward wall of a blob was indeed accompanied by similar scale variations in the ionospheric electric field, and that the sense of relative motion between high- and low-number-density plasma is consistent with ongoing structuring of the plasma via an MFTI process. From the estimated growth rate of $3 \times 10^{-3} \text{s}^{-1}$, the observed plasma structure could have been produced in several minutes by the irregular pattern in the electric field. The source of the MFTI process, however, is not clear. The MFTI process did not appear to be driven by F-region polarization electric fields. This conclusion is based on (1) the apparent lack of inverse correlation between plasma density and "slip" velocity (i.e., velocity difference between plasma and neutrals) patterns and (2) the positive growth rate found along the poleward wall of the blob in the presence of a westward Pedersen current. This conclusion excludes (at least for this data set) the gradient-drift and current-convective instabilities as primary sources of the ongoing structuring process.

1. Background

The existence of large-scale plasma-density enhancements, or "blobs," in the auroral F layer has now been reported by a number of

researchers [e.g., Banks et al., 1974; Vickrey et al., 1980; Kelley et al., 1982a,b; Robinson et al., 1982, 1984; Tsunoda and Vickrey, 1985; Tsunoda et al., 1985; Weber et al., 1984]. Although the source mechanism for producing blobs is not yet known with any certainty, the researchers above have suggested soft-particle precipitation and solar-produced ionization as possible candidates. Blob dimensions are typically 100 km in latitude, a few hundred kilometers in altitude (along geomagnetic field lines), and several to many hundreds of kilometers in longitude (Section II.D). Peak plasma densities in these enhancements range from 10^5 el/cm^3 during solar-activity minimum to more than 10^6 el/cm^3 during solar activity maximum.

One of the more intriguing features of the auroral F layer is that kilometer-scale (i.e., scintillation producing) plasma-density irregularities are enhanced in the vicinity of blobs. This observation naturally points to the plasma-density gradient associated with a wall of a blob and the ionospheric electric field as sources of free energy for further irregularity production at scale sizes smaller than the blob itself. In other words, it is tempting to envision an irregularity cascade process [e.g., Kelley et al., 1982c] in which smaller-scale irregularities are produced by the fragmentation of larger-scale irregularities, of which the blob represents the largest scale size. For example, Vickrey et al. [1980] found that locally intense, radio-wave scintillations were associated with blobs. They suggested that localized kilometer-scale irregularities (in plasma density) responsible for scintillations were produced by current convective [Ossakow and Chaturvedi, 1979] and gradient-drift instabilities acting on the walls of blobs [Simon, 1963; Linson and Workman, 1970; Keskinen and Ossakow, 1982a,b].

If such an irregularity cascade process (e.g., driven by the gradient-drift instability) is operative along the wall of a blob, it would be desirable to characterize that structure in such a way that the source mechanism could be identified. The gradient-drift instability is an MFTI process that produces a structured pattern in plasma density that is most apparent when viewed in a two-dimensional plane transverse to the geomagnetic field (at F-region altitudes). In fact, computer simulations

of this instability process are most often illustrated in this plane [e.g., Keskinen and Ossakow, 1982a,b]. The only known technique for obtaining the plasma-density distribution in more than one dimension is incoherent-scatter radar. Even with this technique, it is extremely difficult to separate spatial variations from temporal variations, especially if we attempt to map a large volume of space with the radar.

Tsunoda and Vickrey [1985] used a different approach to this problem of minimizing ambiguity between spatial and temporal variations. By operating the Chatanika incoherent-scatter radar in a rapid meridian-scan mode, and by allowing a blob to convect zonally through the scanned sector, they were able to reconstruct two-dimensional cross-sections of a blob at several altitudes in planes transverse to the geomagnetic field. This "bread-slicing" technique of mapping the three-dimensional configuration of a blob is thought to be a valid approach because plasma in the F layer is virtually incompressible and its spatial distribution is dominated by the convection, not production and loss. This is certainly the case for the time scales (2 to 5 min) associated with the bread-slicing technique. Tsunoda and Vickrey [1985] showed in a case study that a blob was indeed structured as a function of longitude along one wall, and that the measured neutral wind directed out of that wall was consistent with the required driver for the gradient-drift instability.

Despite the circumstantial evidence presented thus far [Vickrey et al., 1980; Tsunoda and Vickrey, 1985] in support of the gradient-drift and current-convective instabilities operating in the auroral F-region ionosphere, serious questions remain about their effective growth rate for irregularity production because a highly conducting, auroral E layer is often present beneath blobs. It is well known that polarization electric fields set up by these instabilities can be short-circuited by closure currents through a conducting E layer [e.g., Haerendel et al., 1967, 1969; Volk and Haerendel, 1971; Shiau and Simon, 1974; Vickrey and Kelley, 1982]. For example, Vickrey et al. [1980] estimate that the ratio of height-integrated Pedersen conductivity (or Pedersen conductance) in the E layer to that in the F layer was (in their case) about 100. Because the auroral

107

E layer is almost always present beneath F-region blobs, the possibility of polarization shorting cannot be ignored.

The irregularity growth rates of these instabilities can be further reduced (even in the case of partial current closure) by velocity-shear effects produced by an electric field component parallel to the plasma density gradient [e.g., Perkins and Doles, 1975; Zalesak et al., 1982]. North-south electric fields that are parallel to plasma-density gradients of east-west-aligned blobs commonly occur in the auroral iono-sphere. In fact, north-south electric fields dominate over east-west electric fields in the evening and morning sectors where convective flow is almost purely zonal.

Given that the effect of F-region polarization electric fields is susceptible to significant reduction by E-region shorting (and velocity shear), we should (1) not accept proposed mechanisms for irregularity pro-duction in the auroral F region (such as the gradient-drift and current-convective instabilities) without definitive evidence, and (2) give consi-deration to other sources of plasma structure in blobs. Because MFTI act-ing on an existing plasma-density gradient is by far the most efficient process for producing strong irregularities, a first step is to consider other sources of irregular electric fields. Other sources include mag-netospheric turbulence, E-region polarization effects, and field-aligned currents.

It seems clear, therefore, that we need to establish (1) whether MFTI from irregular electric fields is indeed a viable means of producing plasma structure along a blob wall, and (2) if so, whether those irregular electric fields are generated by F-region polarization effects. A direct means of determining whether an MFTI process operates to produce blob structure is to measure the two-dimensional spatial pattern of plasma drift that accompanies a structured plasma-density distribution. If MFTI operates as a structuring mechanism, there should be (1) different plasma-drift velocities associated with lower and higher number-density regions, and (2) relative motion such that high-number-density regions move toward low number-density regions, and vice versa. Finally, if F-region polari-

zation effects are responsible for the MFTI, the slip velocity should be inversely correlated with plasma density.

An important distinction that makes the above requirements amenable to experimental verification is that those requirements are valid regardless of the time history of observed plasma structure. It does not matter what the original source of structure was before observation. The above requirements, therefore, can be used to verify MFTI as an ongoing structuring process and to determine the presence or absence (at the time of measurement) of F-region polarization electric fields.

Here, we present the first results from an experiment specifically designed to obtain the above information. Using data collected with the tristatic EISCAT radar facility, we show that MFTI was acting (during the observation period) on the poleward wall of a blob to produce structure. The estimated growth rate appeared to be rapid enough to have produced the observed structure in several minutes. We also show that the ongoing MFTI process could not have been controlled by F-region polarization electric fields, and conclude on that basis that neither the gradient-drift nor current-convective instability was active during the observation period. We suggest that the absence of the effects of F-region polarization can be attributed to the presence of a highly conducting E layer. More cases, however, need to be analyzed before we can discount, in general, the role of F-region polarization fields in blob-structuring.

2.   The experiment

During a recent Swedish EISCAT campaign (24 February to 15 March 1984), three two-hour experiments were conducted to determine (1) blob structure in a plane transverse to the geomagnetic field and (2) the associated plasma-neutral dynamics. Each of the three experiments were centered on times of closest approach of HILAT. Satellite pass times in the vicinity of the EISCAT radar facility varied between 2200 and 2230 UT. [Local solar time (LST) is ahead of UT by 1 hour, 28 min at the center of the scanned sector.] Data were collected on 24, 25, and 29 February 1984.

Geomagnetic activity was generally rather low, with the highest activity on 25 February.

The object of these experiments was measuring both the F-region plasma density and electric field locally, as a function of latitude and longitude. Because zonal convective flow usually dominates plasma motion in the auroral zone, we designed an antenna scan pattern so that longitudinal information could be inferred from the time-space conversion. In this sense, the approach is similar to that used by Tsunoda and Vickrey [1985]. The key difference from Tsunoda and Vickrey [1985] is that EISCAT is able to measure the local electric-field vector, not simply the line-of-sight velocity. This capability allows us to test whether an MFTI process is operating or not. In addition, we can estimate the relative drift (or slip) velocity between ions and neutrals. Originally, we wanted to use a Fabry-Perot interferometer to measure the F-region neutral wind. Unfortunately, the skies were cloudy. For this reason, we have estimated the neutral wind from incoherent-scatter measurements only. The analysis technique is described later in this section.

The EISCAT system is described by Folkestad et al., 1983. The "scan" geometry is shown in Figure III.B.1. The scan consisted of eight fixed positions spaced 0.25° in geographic latitude; the total coverage was approximately 65 to 67° in invariant latitude. The scan meridian in Figure III.B.1 is displaced to the east of Tromso; the displacement was chosen to improve the signal-to-noise (SNR) ratio of the incoherent-scatter returns received at Sodankyla. The geometry also allows for comparable accuracies in the estimate of all three velocity components.

The radar measurements were made as follows. As the antenna was step-scanned from north to south, data were recorded for 25 s at each of the eight antenna-dwell positions. The total scan cycle was 5 min 10 s, including the times to move between dwell positions. Two waveforms were used; a 200-μs pulsewidth (30-km range resolution) for monostatic reception at Tromso, and a 700-μs pulsewidth for bistatic reception at Kiruna and Sodankyla. [Note that in bistatic reception, the intersecting antenna beamwidths (0.6°) rather than pulsewidth determine range resolution.] Ten autocorrelation functions (ACF) were computed at Tromso,
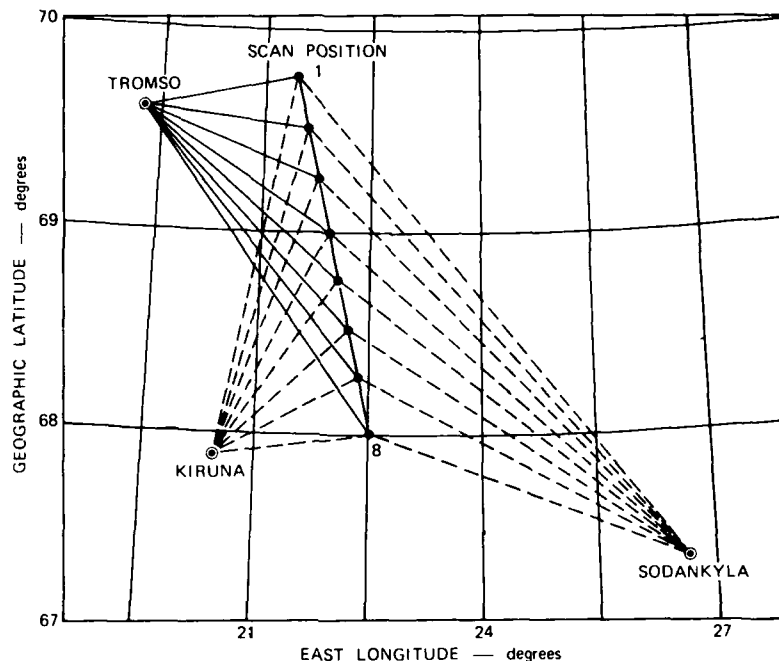
Figure III.B.1.   The EISCAT meridian-scan geometry
                   showing the eight dwell positions at
                   300-km altitude.

starting at 150-km range and at 30-km intervals. A single ACF was com-
puted at each of the remote sites, centered at an altitude of 300 km.

Because F-region neutral wind mesurements from the concur-
rently operated Fabry-Perot interferometer were not available, we extrac-
ted neutral-wind estimates from incoherent-scatter measurements. The
technique for deriving the meridional component of the neutral wind has
been described in detail by Evans [1971], Amayenc and Vasseur [1972], and
Wickwar et al. [1984]. The technique basically consists of using measure-
ments of plasma drift along geomagnetic field lines, correcting for
ambipolar diffusion, and solving for the meridional wind; a horizontal
wind is assumed responsible for plasma motion parallel to $\bar{B}$ through ion
drag. Although actual parallel measurements are best for this purpose,
the tristatic measurements used here provide reasonable estimates of

111

parallel drift. More importantly, three-component ion-velocity measurements allow us to compute the meridional neutral wind as a function of latitude. Comparisons of radar-derived meridional neutral wind with Fabry-Perot interferometer measurements have shown very good agreement [e.g., Nagy et al., 1974; Rees et al., 1984; Wickwar et al., 1984].

Determination of the zonal component of the F-region neutral wind is considerably more involved than that for the meridional component. Bates and Roberts [1977b] have demonstrated that it is possible to estimate the zonal component from the ion-energy equation. The energy equation requires knowledge of the ion and neutral temperatures as well as other components of the plasma drift velocity. If we assume that electron heating is small and use a model value for the neutral temperature, we can solve a quadratic equation for the zonal neutral wind. Bates [1978] has shown that the model neutral temperature is a reasonable approximation even during a heating event.

This technique has been refined and tested by Rees et al. [1984] and Haggstrom et al. [1984] on data taken simultaneously by EISCAT and a 630-nm Fabry-Perot interferometer. They have included electron heating of the ion gas and the effects of a bi-Maxwellian distribution that can occur under conditions of large electric fields [e.g., St.-Maurice and Hanson, 1982]. Rees et al. [1984] and Haggstrom et al. [1984] found good agreement in both components of the neutral wind measured by the two techniques. Significant error in the radar estimate of the zonal neutral wind occurred only at times when there were large increases in the neutral temperature (both used the MSIS model values [Hedin et al., 1977] for the neutral temperature). We show below that large increases in the neutral temperature do not seem to have occurred during the event under study. The analysis program used by Rees et al. [1984] and Haggstrom et al. [1984] has been used here to estimate the neutral wind-vector.

3.   Results

The results are presented in two parts. We first present an overview of magnetic and ionospheric conditions that occurred during the

experiment. We then describe the temporal behavior of mean electro-
dynamic parameters (plasma drift, neutral wind and slip velocity) assoc-
iated with an isolated negative bay event that was centered in our obser-
vation period. Because of similarities found between the negative bay
event and an auroral substorm [e.g., Gurnett and Akasofu, 1974; Lassen et
al., 1977], we have ordered our results according to substorm phase. We
find that the mean slip velocity (needed to drive the gradient-drift
instability) was small during the growth phase but increased to large
values with a generally poleward direction during the peak and recovery
phases. These are unfavorable conditions for ongoing structuring via F-
region polarization effects along the poleward wall of a blob.

In Section 3.b we consider detailed spatial relationships be-
tween plasma and electrodynamic parameters in evaluating the roles of MFTI
and the effects of F-region polarization during the measurement period.
We present two-dimensional patterns of plasma density, velocities, and
temperatures in a plane transverse to the geomagnetic field and point out
observed correlations. We show that MFTI was causing the plasma to struc-
ture along the poleward wall of a blob, but that F-region polarization
electric fields were not driving the MFTI. The absence of F-region polar-
ization effects is attributed to the presence of a conducting E layer.
The unambiguous existence of spatially (rather than temporally) irregular
electric fields that may have driven the MFTI process is demonstrated by
examining the eastward component of plasma drift measured simultaneously
at several closely spaced longitudes. The fact that irregular electric
fields existed in the absence of F-region polarization effects implies
that the irregular electric fields must be driven by some source other
than gradient-drift instability, such as magnetospheric turbulence, or E-
region polarization effects.

a. Overview of Mean Electrodynamic Parameters

1) Geomagnetic Conditions

For an overview, we use magnetograms obtained at
Kiruna to characterize magnetic conditions during the experiment. (Cloudy
skies prevented ground-based optical coverage for this period.) The period

113

of interest is between 2100 and 2300 UT on 25 February 1984. The Kiruna magnetogram showed magnetically quiet conditions six hours before the experiment and 10 hours after completion of the experiment. This period of prolonged magnetic quiescence was interrupted by a single isolated negative bay, centered within the two-hour period of the experiment.

An eight-hour segment of the magnetogram centered on the experiment is presented in Figure III.B.2. The X, Y, and Z components of the magnetic perturbations correspond to geographic north, east, and vertically down directions, respectively. (Geomagnetic north is 12° west of geographic north.) The negative bay, seen in the X component, can be characterized by three phases: (1) a growth phase that started around 2100 UT, (2) a peak phase when the magnetic perturbation reached a maximum value of -130 γ around 2140 UT, and (3) a recovery phase that lasted from 2200 UT to around 2300 UT. The negative bay was produced by a westward electrojet flowing in the auroral E layer. The positive Y component reflects the extent to which the westward electrojet direction was rotated south of geographic west. The negative Z component indicates that the centroid of auroral current was situated poleward of Kiruna. Combining the X and Y components, we find that the maximum horizontal perturbation vector during the peak phase (at 2150 UT) was -170 γ, directed 28° east of geomagnetic south. We compare this magnetic perturbation vector to the mean plasma drift velocity described below.

Mean electrodynamic parameters were extracted from EISCAT data taken during 17 meridian scans, starting at 2115:42 UT (Scan 1) and ending at 2242:12 UT (Scan 17). We see from Figure III.B.2 that this period essentially brackets the three phases of the negative bay event. The mean plasma drift velocity was computed by averaging drift velocities from the eight antenna positions in a given scan. Similar computations were made for the mean neutral wind and mean slip velocity. The three mean velocity vectors are presented as a function of scan number in Figure III.B.3, with their azimuthal directions shown in the top panel and their magnitudes shown in the bottom panel. Magnetic east is shown in the top panel by a horizontal line.

114
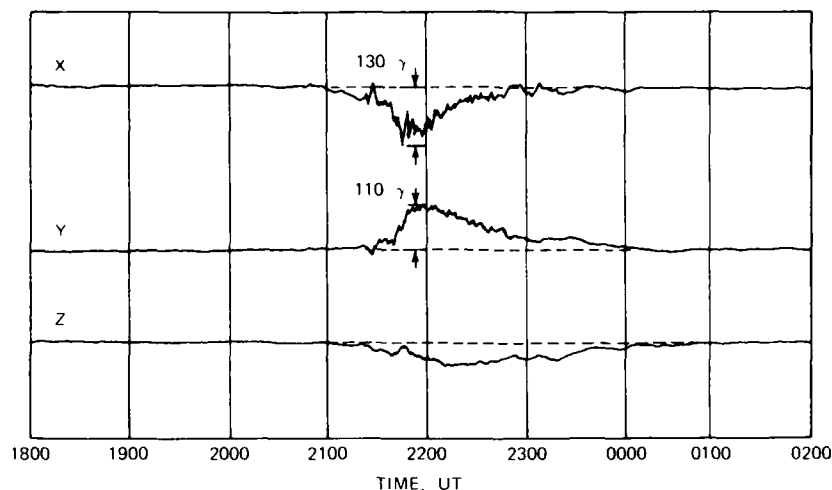
Figure III.B.2.   Kiruna magnetogram showing the isolated
                   negative bay that occurred during the
                   EISCAT experiment.

             The mean plasma drift velocity varied in concert
with the phases of the negative bay event. The drift speed decreased from
436 m/s in Scan 1 down to 183 m/s in scan 2, before recovery to 394 m/s in
Scan 5. This temporary decline in drift speed is closely followed by a
southward turning of the plasma drift vector (between Scans 2 and 3). The
southward turning of the drift velocity during the growth phase of the
negative bay is similar to the development of a westward electric field
during the growth phase of an auroral substorm [e.g., Gurnett and Akasofu,
1974; Rino et al., 1974; Lassen et al., 1977].

             During the peak and recovery phases (Scans 5
through 17), only the direction of mean plasma drift appeared to display
substorm-related behavior. As its speed decreased more or less monotoni-
cally through this period, the plasma drift vector rotated from a south-
eastward direction back toward magnetic east (Scans 9 to 11) and remained
there throughout the recovery phase. The southeastward direction of the
plasma drift vector therefore is identified with the growth and peak

115

25 FEBRUARY 1984
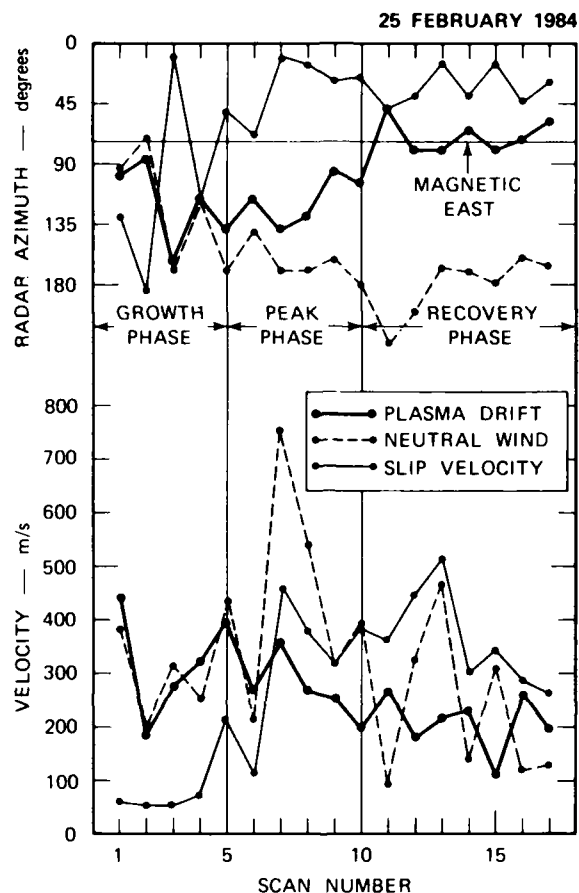
Figure III.B.3.   Mean plasma drift, neutral
wind, and slip velocity
plotted as a function of
substorm phase.

phases of the negative bay event, and a purely eastward drift is as-
sociated with the recovery phase.

Given the mean plasma drift in the F region and the
magnitude of magnetic disturbance, we can estimate the conductance of the
E region. At 2150 UT (during the peak phase), the drift velocity was 270
m/s directed at $-50°$ south of geomagnetic west. For a magnetic perturba-
tion vector that was -170 γ directed $28°$ east of geomagnetic south, the

116

average current vector must have been directed 12° clockwise of the electric field vector. This implies that the Pedersen conductance was about 4.7 times greater than that of the Hall conductance. This ratio is extremely high and implies an average energy of precipitating electrons that is less than 1 keV [e.g., Spiro et al., 1982]. If we use an infinite current-sheet approximation, we obtain a Pedersen conductance of 20 mhos.

2) Mean Neutral Wind

The mean neutral wind in Figure III.B.3 displays time-varying characteristics that are not simply related to the plasma drift velocity variations described in the previous section. During the growth phase, the neutral wind tracked the plasma drift velocity very closely. Both the substorm-related, southward turning of the plasma drift vector and the temporary decline in speed are reflected in the neutral wind. This behavior implies strong coupling of the neutrals to the plasma and dominance of nearby convection electric fields over pressure gradients as the source of the neutral wind. The response time of neutrals to changes in plasma motion is about an hour for typical plasma densities at 300-km altitude [Fedder and Banks, 1972]. Close tracking of the plasma by neutrals, therefore, suggests the absence (or relative ineffectiveness) of other transient or spatially varying forces on the neutral gas during the prolonged period of magnetic quiescence that preceded substorm activity.

The peak-phase negative bay onset was followed (within 10 min) by a substantial increase in the mean neutral wind speed, reaching 750 m/s during Scan 7. The direction of the neutral wind remained unchanged during this surge. This "gust" of neutral wind lasted about 20 min and was not preceded nor accompanied by a locally large plasma drift velocity. The wind source, therefore, was (1) situated around magnetic midnight, (2) located poleward of the EISCAT field of view, and (3) configured in the form of a narrow channel of large antisunward convection velocity or heat source.

The behavior of the mean neutral wind toward the end of the peak phase and the start of the recovery phase did not reflect

117

the strong coupling to plasma drift seen during the growth phase. As the
plasma drift vector changed from a southerly direction back toward mag-
netic east, the neutral wind did not track the rotating plasma drift
vector. Instead, it remained in a southerly direction. This behavior can
be understood if we recognize that the ion-neutral interaction is not a
reciprocal process. While the neutrals are freely moved (with a time con-
stant of several tens of min) by plasma convection, the plasma cannot be
moved across magnetic field lines by the frictional ion drag applied by a
neutral wind.

A southward surge of the neutral wind in the mid-
night sector of the auroral zone appears to be a common feature [Nagy
et al., 1974; Bates and Roberts, 1977a; Hays et al., 1979; Roble et al.,
1982; Wickwar et al., 1984]. Because of its consistent occurrence around
magnetic midnight, the southward surge does not necessarily seem to be re-
lated to substorms. From observed characteristics, the source of the
midnight surge is likely to be ion drag by antisolar convection in the
polar cap. The high wind speed seen in our data without locally large
plasma drift is consistent with that hypothesis.

The wind speed in the midnight surge has also been
shown to be related indirectly to the strength of the polar cap electric
field. Bates and Roberts [1977a] have shown that the logarithm of wind
speed is directly proportional to the magnetic K_p index. For $K_p = 3$
(i.e., conditions during the experiment), a wind speed of 770 m/s would be
predicted by their empirical relationship. Our measured wind was 750 m/s,
in excellent agreement with that prediction.

An alternate explanation, however, for the short-
lived gust in neutral wind seen during Scan 7 is the transient occurrence
of a vertical wind. Bates and Roberts [1977a] and Wickwar et al. [1984]
have suggested that at least some of the apparently large surges in the
meridional neutral wind (estimated from incoherent-scatter observations)
may be produced by atmospheric gravity waves. The notion of gravity-wave
influence on computed winds is supported by the recurrence of another peak
in wind speed during Scan 13 (see Figure III.B.3).

The possibility of gravity-wave contamination of our neutral wind estimates seems to be discounted, however, by the temporal behavior of the F-layer peak. We show below that the F-layer peak altitude moved upward with development of the southward surge. More importantly, upward movement of the peak altitude occurred simultaneously over several degrees of latitude. This widespread lifting of the F layer is more consistent with a southward neutral wind than the passage of an atmospheric gravity.

3) Slip Velocity

The dynamic interaction of plasma with neutral gas is best described by the slip velocity vector that is plotted in Figure III.B.3. As might be expected from the above description, the slip speed was small during the growth phase. The slip speed increased rather abruptly during Scan 7 because of the large southward surge in neutral wind. The slip speed remained above 250 m/s during the remainder of the scans, with relative maxima occurring in Scans 7 and 13. Throughout this period, the slip velocity vector was magnetically directed northeast.

From the behavior of the mean slip velocity, we can draw some conclusions regarding the expected plasma structuring process. If we assume the blob is elongated in longitude, the gradient-drift instability can only weakly be operative during the growth phase of the negative bay. The large poleward-directed slip velocities that existed during the peak and recovery phases suggests structuring (damping) along the equatorward (poleward) wall of the longitudinally elongated blob.

4) Plasma Density Profiles

The analysis up to this point has focused on characteristics of mean electrodynamic parameters. We also require some knowledge of the plasma parameters, i.e., plasma density, electron and ion temperatures. It is desirable to estimate E-region Pedersen conductance, as a function of substorm phase. Also because of the importance of neutral wind characteristics to the conclusions drawn regarding F-region

119

polarization effects, it is desirable to cross-check those measurements wherever possible.

The plasma-density profiles measured at Tromso during Scans 1, 7, and 17, are presented in Figure III.B.4. The abscissa scale for each set of profiles is referenced to a nearby vertical line that corresponds to 10^5 el/cm^3 for that data set. Although these profiles were obtained along nonvertical lines of sight from Tromso, they are useful as general descriptors of plasma density distribution in altitude. We use profiles from Scan 1 as representative of the growth phase, those from Scan 7 as representative of the peak phase, and those from Scan 17 as representative of the recovery phase.

We first use the plasma-density profiles to determine the morphology of keV electron precipitation. The description, in this case, is limited to a narrow range of latitudes covered by the E-region penetration points of the Tromso beam during meridian scans. Latitudinal coverage of the eight E-region range gates corresponds to Positions 1 to 4 in Figure III.B.1 referenced to 300-km altitude. During the growth phase (Scan 1), E-layer plasma densities ranged from 1.5×10^5 el/cm^3, to as little as 9×10^4 el/cm^3. Examining individual profiles, we find an increase in plasma density with decreasing latitude; we cannot determine if the gradient is spatial or temporal. During the peak phase (Scan 7), E-region plasma densities reached 3.5×10^5 el/cm^3, indicating increased particle precipitation. Again, there is variability in the latitudinal pattern. During the recovery phase (Scan 17), the E-region profiles were relatively uniform with a peak value of 4×10^5 el/cm^3, indicating little if any reduction in precipitation from that seen during the peak phase.

From the above, we can reconstruct the auroral process associated with the substorm. The relatively high plasma drift during growth and early peak phases suggests that negative bay onset was produced by an abrupt increase in particle precipitation, not an enhancement in convection velocity. The recovery phase appears to have been associated with a gradual decrease in mean convection speed, and not by a reduction in the number flux of keV electron precipitation.

120
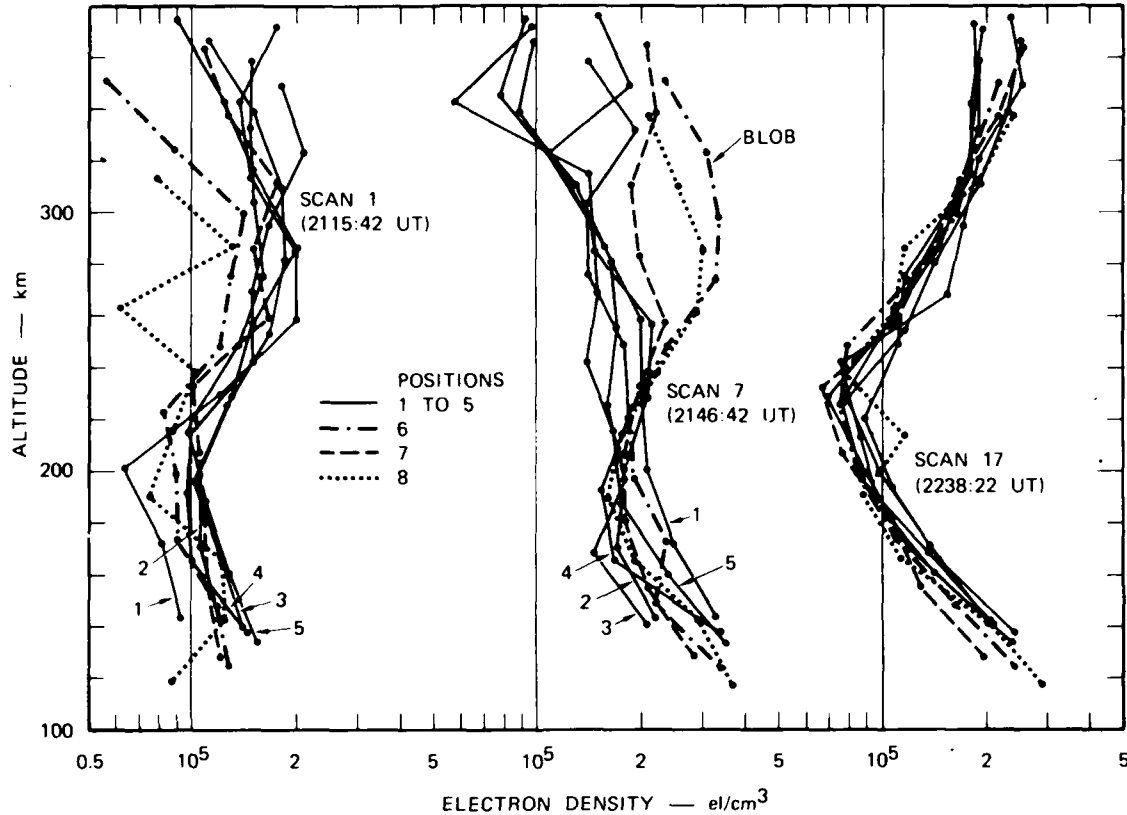
Figure III.B.4.   Plasma density profiles obtained during the growth phase
(Scan 1), the peak phase (Scan 7), and the recovery phase
(Scan 17).

To augment our single, crude estimate of E-region
Pedersen conductance, we present other estimates based on the plasma-
density profiles in Figure III.B.4. Because the peaks of E-layer profiles
were not measured, we simply matched our peak plasma density to one in
Figure 10 of Vickrey et al. [1981] to estimate the Pedersen conductance.
This approach is valid because we have measurements of plasma density as
low as 118-km altitude; the largest contribution to Pedersen conductance
comes from 125- to 130-km altitude. We obtain a peak value of about 8
mhos for Scan 7. The Pedersen conductance was one-half that of the Hall
conductance (much smaller than that estimated from magnetic records). If

121

we further assume that the profile shape does not significantly alter the Pedersen conductance, the conductance should scale as the plasma density. On this basis, we find the Pedersen conductance varied from 2 mhos during the growth phase to 8 mhos during the peak and recovery phases. Although smaller than our previous estimate, these values are still large compared to a typical F-layer Pedersen conductance of 0.1 mho [Vickrey et al., 1980].

The blob of interest is seen in plasma density profiles from Scan 7 in Figure III.B.4. The blob corresponds to the two profiles containing enhanced F-layer plasma densities, reaching a value of 3.3×10^5 el/cm^3. The other F-layer profiles in Scan 7 represent the background ionosphere poleward of the blob, measured during the peak phase of the substorm. The altitude of the F-layer peak in the blob is around 300 km. In comparison, F-layer profiles from Scan 1 represent the background ionosphere, also poleward of the blob but measured during the growth phase. The peak plasma densities from Scan 1 are slightly higher than those background measurements in Scan 7. The F-layer peak in Scan 1 is below 300-km altitude. The third set of profiles in Figure III.B.4 correspond to the background ionosphere equatorward of the blob, measured during the recovery phase. Peak plasma densities are seen to approach those in the blob. The most striking feature, however, is the altitude of F-layer maximum, reaching at least 350 km. The profiles are also characterized by their similarity in shape and number density. The lower background plasma densities found in Scan 7 compared to Scan 1 may have resulted from enhanced electron loss rates initiated by the large slip velocities [Schunk et al., 1976].

The increase in altitude of the F-layer peak is consistent with the presence of a southward neutral wind. Watkins and Richards [1979] have shown that a 400-m/s neutral wind, when directed equatorward, lifts the peak of the layer from 300- to 380-km altitude. The actual displacement depends on the length of time that the neutral wind has been applied (90 min in their example). Their modelling results are in good agreement with our neutral-wind estimates and plasma-density

profiles. We, therefore, conclude that a substantial equatorward-directed neutral wind was present during the peak and recovery phases of the substorm.

We now address the question of soft particle precipitation as an F-layer ionization source. We use plasma densities measured between 150- and 200-km altitude as a measure of softer-electron precipitation. Loss rates in this altitude range are still rapid enough that the plasma density distribution reflects production rates and not transport effects. Examining profiles in Figure III.B.4, we find a precipitation morphology that differs from the harder keV electron precipitation responsible for the E layer. The plasma density (at, say, 200-km altitude) has increased from Scan 1 to Scan 7, as expected. The plasma density decreased substantially however, from Scan 7 to Scan 17. This difference in precipitation morphology at the two altitudes is also manifested in Figure III.B.4 as a change in the slope of the topside E-layer profile.

The effect of soft electron precipitation in producing plasma density at altitudes above 200 km is small. At 300 km altitude, the e-folding ionization rate is greater than an hour [e.g., Roble and Rees, 1977; Watkins and Richards, 1979; Weber et al., 1984]. In this convection dominated region, a variety of plasma-density profiles are found. Although the highest plasma densities are found in Scan 7, some of the lowest values are also found during that scan. The profiles in Scan 17 are characterized by their similarity in shape and value to one an-other, indicating a uniform plasma-density distribution at all altitudes. One possible interpretation of this is that the region poleward of the blob is more irregular in plasma density than that equatorward of the blob.

5) Plasma Temperature Profiles

Because it is virtually impossible to detect the occurrence of soft-particle precipitation at F-layer altitudes on the basis of plasma-density profiles we turn to an analysis of plasma tem-

123

peratures. Roble and Rees [1977] have shown that electron temperature peaks with the ionization rate, with a time constant of 10 s or less, and begins to decay only after the plasma density has become significant. This time constant is on the order of 10^3 s. The situation is not so simple if precipitation occurs in the presence of existing high plasma density. We can however, argue that, for a given plasma density, elevated electron temperatures imply ongoing or very recent precipitation, whereas low or normal temperature may or may not be associated with precipitation. Typical electron temperatures produced by soft-particle precipitation range from 2000 K to 3250 K [Roble and Rees, 1977].

The degree to which electron temperature is elevated by particle heating can be estimated by comparing the electron temperature at a given altitude to the corresponding ion temperature. The ion-temperature profiles are presented in Figure III.B.5. Except for some scatter in the prof les from Scans 1 and 17, the ion temperatures are similar, all approaching an asymptotic value of about 1000 K at the highest altitudes. (The large increases in ion temperatures around 340-km altitude in Scan 7 are not thought to be real.)

The electron temperature profiles are presented in Figure III.B.6. Keeping in mind that the asymptotic value for the ion temperature was 1000 K, we notice that the electron temperature is considerably enhanced. The enhancements occurred above 220-km altitude and are evident in all profiles, including those obtained during the growth phase. The most dramatic variation occurred in Scan 7 where there appears a distinct gradient in electron temperature. The highest temperatures occurred at the north end of the scan; the temperatures decreased rapidly with latitude, reaching a minimum within the blob. The behavior of electron temperature in Scan 17 is most like that of the ion temperature. The electron temperatures in Scan 7 are about 500 K greater than those seen during Scan 17. These temperature results clearly indicate soft-particle precipitation in the region poleward of the blob, particularly during the peak phase of the substorm.

124
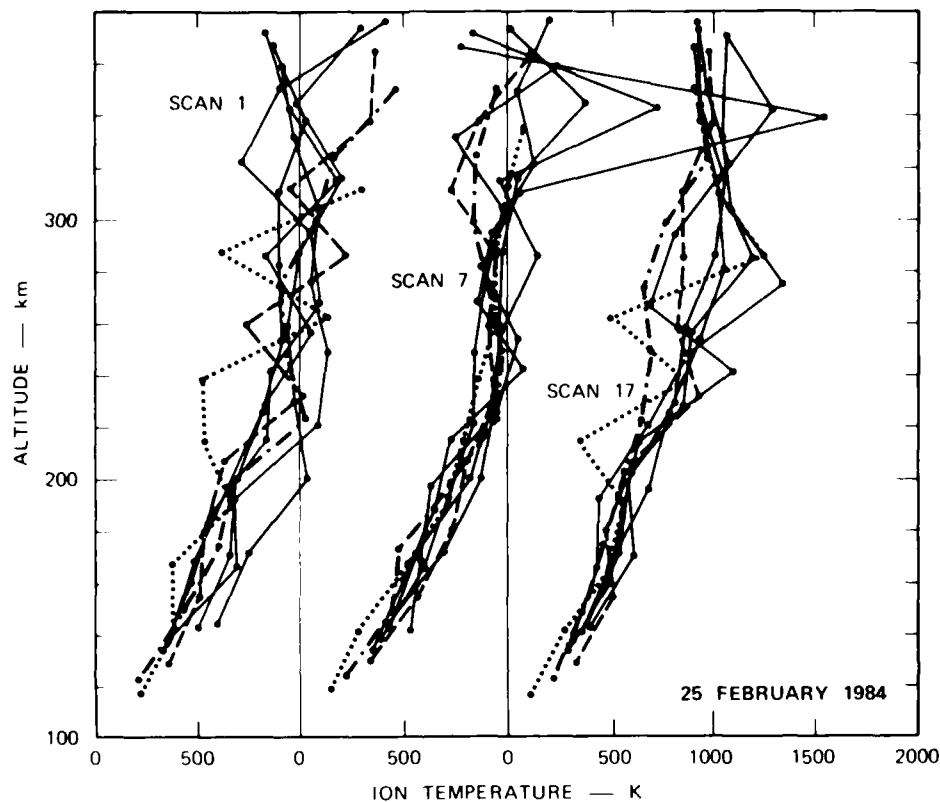
Figure III.B.5.   Ion-temperature profiles obtained during the
three phases of the auroral substorm.

b.   Interelationships Among Plasma Density, Plasma Motion,
and Electron and Ion Temperatures

In this section, we present an analysis of more detailed
spatial relationships between two-dimensional patterns of plasma para-
meters and electrodynamic parameters, at 300-km altitude. We demonstrate
that plasma along the poleward wall of the blob was being structured by
MFTI, but that F-region polarization effects were not operative. The rate
of MFTI could have produced the observed structure along the poleward wall
of the observed blob, if that rate were sustained for several minutes.

125
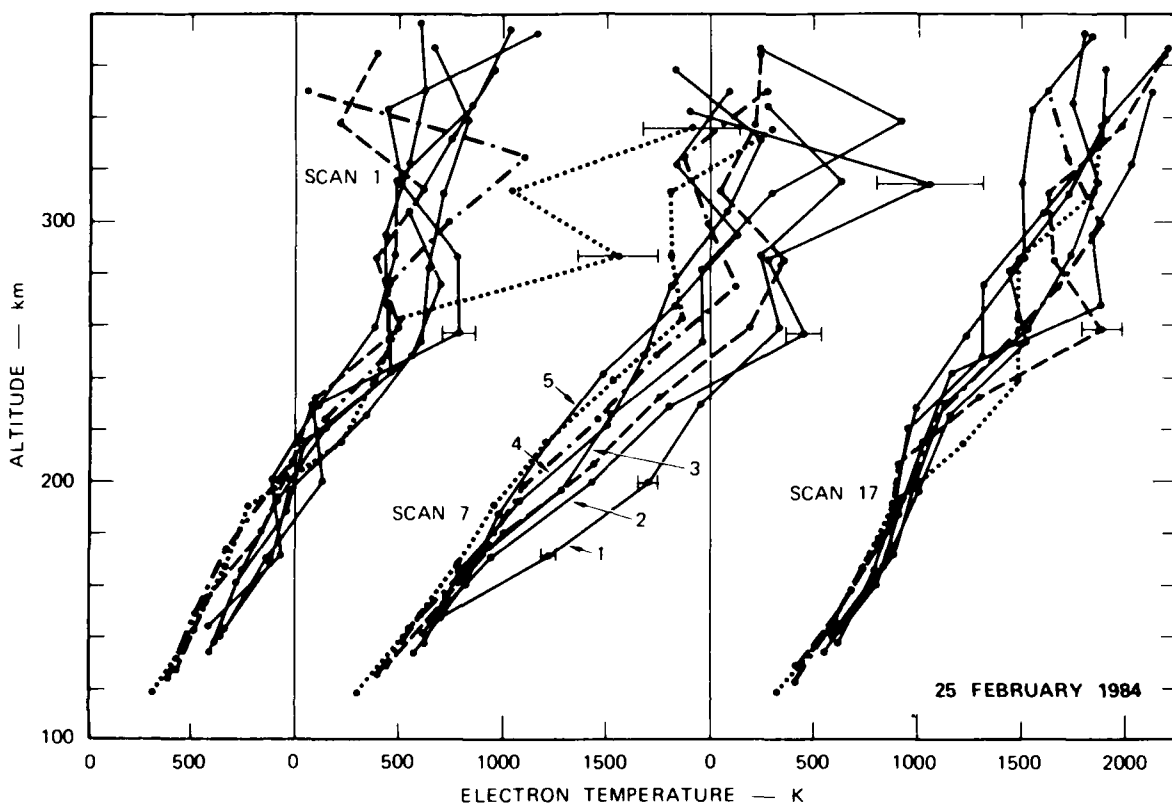
Figure III.B.6.   Electron-temperature profiles obtained during the three phases of the auroral storm.

1)   Plasma Density

A two-dimensional map of the plasma density measured at a nominal altitude of 300 km is presented in Figure III.B.7(a). The distribution of plasma density is illustrated by isodensity contours and plotted in geomagnetic coordinates. Adjacent contours represent a change in plasma density of 2×10^4 el/cm^3. Geomagnetic north is directed along the ordinate and geomagnetic east is directed along the abscissa. The ordinate scale of approximately 28 km between tick marks corresponds to the spacing between scan dwell positions. The abscissa scale of about 67 km between scans (i.e., tick marks) is based on an average eastward drift of 220 m/s measured during the 17 meridian scans. For purposes of discussion,
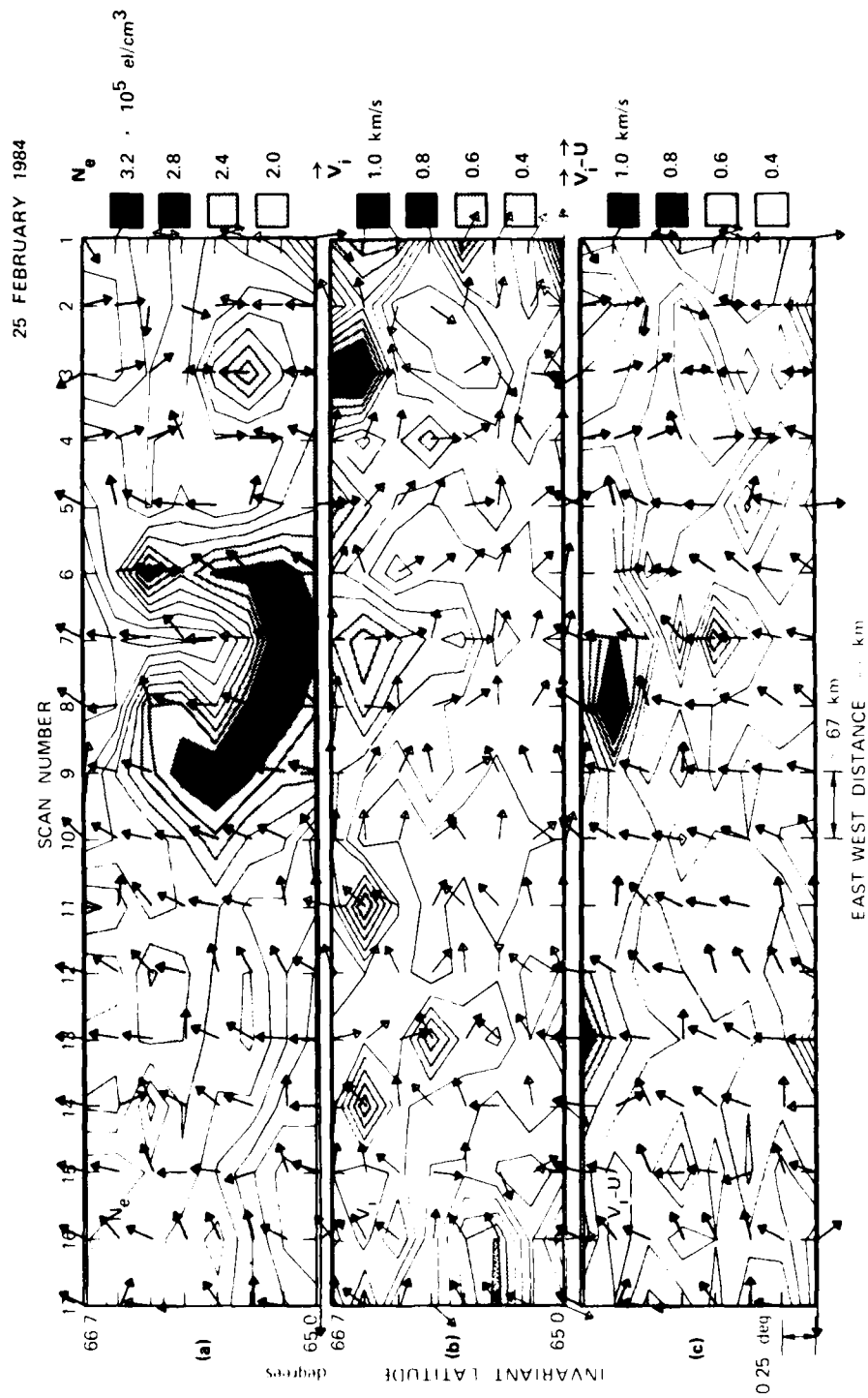
Figure III.B.7 Two-dimensional patterns of plasma density, ion velocity, and slip velocity in a plane transverse to the geomagnetic field at 300-km altitude.

we have superimposed unit vectors that represent the direction of the slip velocity on the contours of plasma density.

The plasma-density contours shown in Figure III.B.7(a) were constructed from Tromso incoherent-scatter measurements at Range Gate 7. The altitude of that range gate varied from 316 km at the north end of the scan to 263 km at the south end of the scan and was about 300 km at the center. The upward movement of the F layer, produced by a large southward neutral wind, and shown in Figure II.B.4, gradually decreased the plasma densities at 300-km altitude in the later scans. Fortunately, the basic structural pattern shown in Figure III.B.7(a) was not significantly distorted by the gradual altitude change of Range Gate 7 nor by the lifting of the F layer.

The feature of most interest in Figure III.B.7(a) is the region of enhanced plasma density outlined by the 2×10^5 el/cm^3 contour (i.e., the most lightly shaded region). The blob pattern was tilted with respect to the geomagnetic east-west direction, and visible in 12 successive scans. Because the average eastward drift was 220 m/s, the blob pattern was apparently elongated in longitude over 750 km. The most interesting blob features are the pronounced spatial undulations of the 2×10^5 el/cm^3 (heavy line) contour along the poleward wall of the blob, and the relatively smooth equatorward wall. The modulation depth along the poleward wall is about 80 km. Except for its location along the poleward (rather than equatorward) wall of the blob, the east-west structure is similar to that reported by Tsunoda and Vickrev [1985]. For the estimated 67-km interval between scans, we obtain an average spacing between the enhanced plasma protrusions, or "fingers," of about 200 km. Tsunoda and Vickrey [1985] found the fingers along the equatorward wall of their blob were spaced about 150 km apart.

Beside spatial undulations in the 2×10^5 el/cm^3 contour, we find that the peak plasma density within the blob varied as a function of longitude, or time. The variation occurred primarily during Scans 6 through 9 with peak plasma density reaching 3.3×10^5 el/cm^3.

These scans were made between 2141:32 and 2200:52 UT, during the peak phase of negative bay activity. These enhanced plasma densities were also seen in Figure III.B.4 and pointed out as time coincident with substorm-related precipitation. Recall however, that F-region ionization production by soft-particle precipitation is a slow process.

We estimate that the ratio of plasma density within the blob to that between the fingers and also to that in the background ionosphere is $\leqslant 2.0$. In comparison, Tsunoda and Vickrey [1985] found ratios greater than a factor of 4.

The plasma density distribution in Figure III.B.7(a) seems to be inconsistent with the hypothesis that the gradient-drift instability was responsible for the observed structure. The mean slip velocity was directed poleward and therefore would be expected to reduce any existing structure by the gradient-drift instability. For the same reason, structure growth would be expected along the equatorward wall of the blob. We also found that the ratio of blob plasma density to that of the background F layer was small, and that the E-layer Pedersen conductance was high during the period of negative bay activity.

2) Ion Velocity

The conclusions drawn in the previous section can be taken a step further by analyzing the two-dimensional pattern of the plasma drift. We cannot unambiguously identify all contributing sources to the observed plasma structure along the poleward wall of the blob without knowing its time history. We can, however, determine (1) whether MFTI was occurring between high- and low-number-density plasma during the observation period, and (2) if so, whether the gradient-drift process was reducing plasma structure along the poleward wall.

The transverse component of the ion velocity vector is displayed in Figure III.B.7(b). The velocity pattern is seen to be structured; the scale of velocity variations appears comparable to those in the plasma-density contours, suggesting a degree of coherence between the patterns. At scales on the order of the blob fingers, we find two

regions of large ion velocity that appear to be well correlated with the "depleted" plasma regions between fingers. Large velocities were observed primarily during Scans 4 and 7. These velocities are seen to be directed southward, whereas velocities within the blob are smaller and directed slightly more eastward. For example, the blob velocity in Scan 7 is 215 m/s while the depleted region is convecting into the blob at a velocity of 534 m/s.

These observations of relative plasma motion between high- and low-number-density regions represent direct evidence of ongoing plasma structuring via an MFTI process. For example, the southward-directed depleted region in Scan 7 must force the blob to distort its configuration in a manner to preserve incompressibility of the plasma. The depleted plasma will, therefore, push its way into the more dense plasma region resulting in longer fingers. This is, by definition, the MFTI process by which plasma is structured. The e-folding growth time for the finger in Scan 6 is roughly estimated to be about 6 min (or equivalently, a growth rate of 3×10^3 s^{-1}).

There remains the question of space-time ambiguity. That is, the electric field could be time varying in a manner that results in the pattern observed. Doubt regarding our interpretation that might be cast by this ambiguity question is reduced by considering two points. First, the apparent spatial anticorrelation found in Figure III.B.7 consisted of two high-velocity, low-plasma-density regions, and three low-velocity, high-plasma-density regions. We feel that the repetition of the anticorrelated patterns is more likely to be spatial than temporal. For example, if the poleward wall of the blob were actually smooth and time-varying east-west electric fields were responsible for the apparent modulations seen from scan to scan, we would expect (1) the equatorward wall to be similarly modulated as the poleward wall, and (2) the Y-component of the Kiruna magnetogram to contain temporal oscillations. Neither is seen in the data. And second, we present additional velocity measurements that demonstrate unambiguously the existence of longitudinal variations in plasma drift velocity, consistent with the MFTI process.

130

The spatial anticorrelation found between plasma density and ion velocity, and the sense of relative motion between high- and low-density plasma is not only direct evidence for the MFTI process but also demonstrates the relative ineffectiveness of F-region polarization effects during this period. As pointed out earlier, the mean westward Pedersen current that is driven by the northward directed slip velocity should act through F-region polarization electric fields to dampen structure development along the poleward wall of a blob. In other words, if the gradient-drift instability process were operative during the measurement period, the relative motion of high- and low-number-density plasma should be opposite in sense to that shown in Figure III.B.7(b). This contradiction in the sense of relative plasma drift is strong evidence that F-region polarization electric fields did not develop (e.g., because of short-circuiting by a conducting E layer) or that MFTI was driven by other stronger electric fields that dominated over F-region polarization effects.

The presence of F-region polarization electric fields becomes even more doubtful when we compare the velocity pattern with plasma-density distribution in Scans 10 to 15. Rather than finding anticorrelation between the two quantities, we find a certain degree of correlation. For example, the ion velocity associated with the finger in Scan 11 is 835 m/s and directed poleward at an angle nearly perpendicular to the blob's major axis. At the same time, we find velocities between 78 and 196 m/s in the depleted regions adjacent to the finger.

Another piece of evidence against the importance of F-region polarization electric fields is the occurrence of very large ion velocities in the upper right-hand corner of Figure III.B.7(b). Polarization electric fields are set up by charge accumulation along gradients in plasma density, in the presence of current flow. It is clear from Figure III.B.7(a) that there were no significant plasma-density gradients in the vicinity of those large observed velocities. From the above discussion, we conclude that F-region polarization electric fields could not have been responsible for the ongoing structuring by MFTI. Additional proof is presented in the next subsection.

131

3) Slip Velocity

Although observed relative streaming between en-
hanced and depleted plasma regions represents ongoing structuring via the
MFTI process, the slip velocity pattern in relation to the plasma-density
pattern provides a true measure for the effectiveness of F-region
polarization electric fields. In other words, if F-region polarization
effects were operating during this period, we should find spatial anti-
correlation between plasma density and slip velocity (similar to that
found between plasma density and ion velocity).

The slip velocity pattern is presented in Figure
III.B.7(c). We note that the striking anticorrelation found between
plasma density and ion velocity, particularly between Scans 3 and 9, is no
longer as evident when the plasma density pattern is compared to that for
the slip velocity. For example, the enhanced ion velocities measured be-
tween fingers during Scans 4 and 5 are replaced by much smaller slip
velocities (also see Figure III.B.3). In the region between Scans 6 and
8, the slip velocities remain enhanced but were directed poleward, rather
than equatorward as in the case for ion velocities. [This spatial compar-
ison of slip velocity direction with blob plasma density is facilitated by
superimposing the directions of the slip velocity onto Figure III.B.7(a)].
This absence of inverse correlation between the two patterns is further
evidence that F-region polarization effects were absent.

Finally, a poleward directed slip velocity should
(in the absence of a conducting E layer) render the equatorward wall of a
blob unstable to the gradient-drift process. From the shallow undulations
in plasma density along the equatorward wall and the small ion (and slip)
velocities found there, we would have to conclude that the gradient-drift
growth rate must have been quite small.

4) Electron and Ion Temperatures

The electron temperatures computed from Tromso ACF
data at Range Gate 7 are plotted in Figure III.B.8(b). The temperatures
ranged from 1380 K to 3007 K. On the largest scale, we see that elevated

132
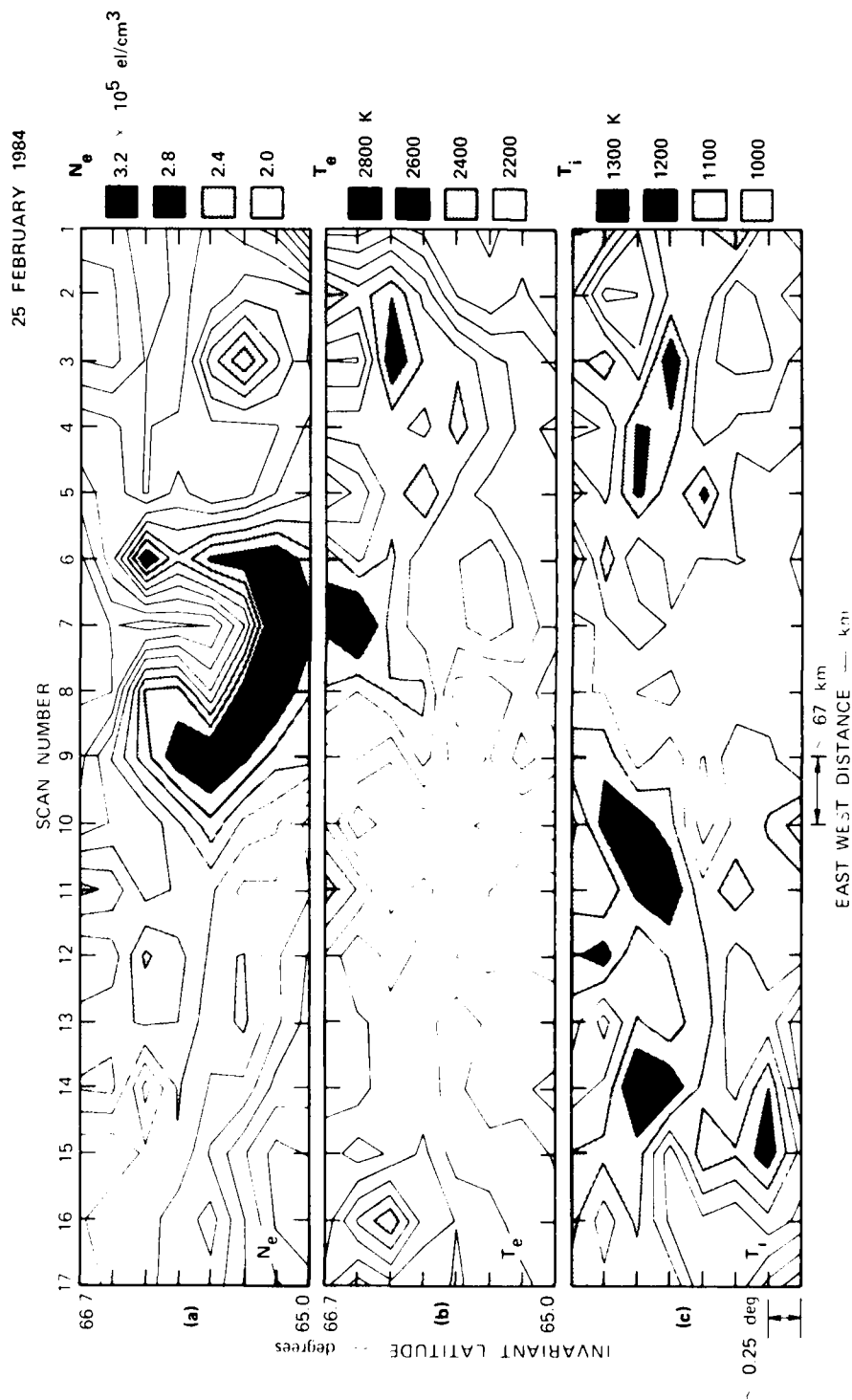
Figure III.B.8. Two-dimensional patterns of plasma density, electron temperature, and ion temperature in a plane transverse to the geomagnetic field at 300-km altitude.

electron temperatures (> 2200 K; i.e., shaded regions) were confined to regions poleward of the blob [Figure III.B.8(a)]. Typical temperatures in that region ranged from 2600 K to 2800 K. In comparison, the mean temperature within the blob in regions where the plasma density exceeded 2.8 × 10^5 el/cm^3 was 2000 K. Electron temperatures in less-dense regions of the blob were between 1600 K and 1800 K. In comparison, the electron temperature in the background ionosphere ranged from 1400 K to 2000 K. The regions in which most energy was deposited (at 300-km altitude) by particle precipitation, therefore, appears to have occurred poleward of the blob and in the highest plasma-density region of the blob (between Scans 5 and 10).

On scale sizes comparable to those of the fingers in Figure III.B.8(a), we find that elevated electron temperatures occurred in the vicinity of the finger tips. The electron temperatures in fingers observed during Scans 3, 6, 8, and 11, were 2100 to 2350 K, 2450 K, 2300 to 2400 K, and 2200 to 2500 K respectively. These electron temperatures are higher by 100 to 500 K than that in the highest plasma-density region of the blob, and higher by 200 to 400 K than those in less dense portions of the blob. On this basis, enhanced soft-particle precipitation seems to have occurred at the tips of the fingers.

Some caution, however, must be exercised when we attempt to infer any increase in plasma density produced by soft-particle precipitation. The regions of highest electron temperature are not usually spatially coincident with regions of largest plasma density. For example, we find the highest electron temperature at the top of Scan 7 to be in a region of very low plasma density. It, therefore, is conceivable that all the plasma was at the same temperature at some time, but that cooling was slower where the electron density was low.

The ion temperature is of some interest in this kind of investigation because it is proportional to the square of the slip velocity. The slip velocity, together with the horizontal gradient in plasma density, control the development of F-region polarization electric fields. The use of ion temperature for this purpose, however, is not straightforward because the ion temperature is also proportional to the

134

plasma density. Despite the complexity in interpretation, we include ion
temperature for completeness.

The ion temperature was computed together with
electron temperature from the Tromso ACF data in Range Gate 7. The ion
temperature presented in Figure III.B.8(c) ranged in value from 710 K to
1325 K. On the largest scale, elevated ion temperatures appear to occur
outside the blob region of highest plasma density. Because plasma density
is highest there, the ion temperature should be most sensitive to the slip
velocity in that region. The finding of lowest ion temperatures in the
densest portion of the blob indicates the presence of smallest slip
velocities.

5)   Additional Evidence of Spatially Irregular
       Electric Fields

In Section III.B.3.b.2, we raised the question of
whether the irregular electric fields (or ion velocity) presented in
Figure III.B.7(b) were produced by spatial or temporal variations.
Although the velocity variations from one scan position to the next is
less likely to be temporal than those observed from one scan to the next,
some doubt can reasonably exist. For this reason, we present additional
evidence that unambiguously demonstrates the presence of spatially ir-
regular electric fields.

For this purpose, we examined the line-of-sight
velocities measured from Tromso whenever the antenna was fixed at Scan
Position 1. The line of sight from Tromso was directed toward magnetic
east, thus allowing measurements of the eastward component of plasma
drift. Spatial information was obtained by plotting the eastward drift
measured in the last nine range gates. Of these, all but the first were
at altitudes above 165 km and, therefore, provide a measure of the $\bar{E} \times \bar{B}$
plasma drift velocity. For an elevation angle of 72.9°, the range gates
were spaced at 8-km intervals in ground distance, starting 52 km east of
Tromso. Any variation found in velocity as a function of range gate,
therefore, represents a true spatial variation, averaged over 25 s.

135

The eastward plasma drift speed obtained as a func-
tion of range gate is presented in Figure III.B.9. Velocity estimates
from the nine range gates are connected by line segments. Total ground
coverage by these nine gates is 64.7 km. Successive scans are plotted
next to each other, with each scan separated from one another by a long
tick mark. We note that these velocities are measured at the top edge of
the two-dimensional maps in Figures III.B.7 and III.B.8.
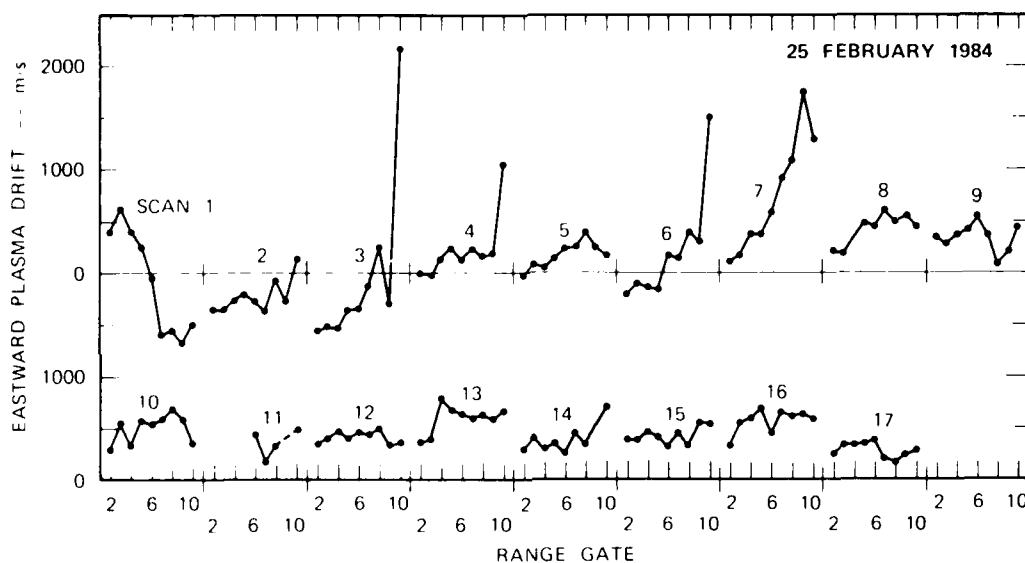
Figure III.B.9.   Longitudinal variations in eastward plasma drift computed
                   from line-of-sight velocity measurements at dwell position 1
                   from Tromso during the 17 meridian scans.

We find that the velocity varied substantially
during Scans 1 through 7 and much less so thereafter. During Scan 1, we
see a velocity reversal in which an eastward drift of 500 m/s became a
westward drift of comparable speed, over a ground distance of about 30 km.
The westward drift slowly decreased during Scans 2 and 3, reversing to an
eastward drift in Scan 4. Large eastward velocity spikes are seen during
Scans 3, 4, 6, and 7. The fractional velocity errors associated with
these measurements all suggest that these large velocities are probably

136

real, although those seen in Scans 6 and 7 are the most convincing.
Amidst these large velocity variations, we also find periods of relative
calm, e.g., Scans 2 and 5. From Scan 8 on, we find a relatively well-
behaved eastward drift of about 500 m/s.

The amplitude of velocity fluctuations appears to
be (1) larger poleward of the blob than equatorward of it and (2) larger
during the peak phase of the substorm than during the recovery phase. The
first conclusion is based on comparisons of velocity fluctuations found in
Scans 1 through 7 to those in Scans 11 through 17. In particular, the
velocity fluctuations in Scan 1 that occurred at the start of the growth
phase were much larger than those in the later scans. A preliminary ex-
amination of electric-field measurements made by HILAT also appear to
support this observation. The second conclusion is apparent from Figure
III.B.9. The large variations in velocity in Scans 3 through 7 appear to
be consistent with the vector velocities shown in Figure III.B.7(b). The
large spikes in Figure III.B.9 occurred only during a period when there
existed large vector velocities. The appearance of the spikes is consis-
tent with simple rotation of the velocity vector as a function of longi-
tude.

Because the plasma is incompressible at F-region
altitudes, any longitudinal gradient in eastward plasma drift must be ac-
companied by a corresponding latitudinal change in northward plasma drift.
But, because the longitudinal gradient in eastward drift varied with lon-
gitude, we conclude that there was also a longitudinal gradient in the
northward drift. On this basis, we conclude that there existed eddy-like
turbulent flows with a scale size on the order of tens of kilometers. The
presence of a horizontal plasma density gradient in this irregular
electric field pattern will result in plasma structuring by the MFTI
process.

We note in passing that irregular electric fields
have been observed in the past [e.g., Haerendel et al., 1969; Cauffman and
Gurnett, 1972; Gurnett, 1972; Heppner, 1972, 1977; Aggson and Heppner,

1977; de la Beaujardiere and Heelis, 1984; Saflekos et al., 1985]; how-
ever, in most of those observations, the irregular electric fields were
observed as a function of latitude.

4.   Summary of Results

We have obtained the following results:

(1)   An F-region plasma-density enhancement, or blob, was found
       around magnetic midnight in a zone of eastward convection.

(2)   The two-dimensional spatial pattern of the blob (in a plane
       transverse to the geomagnetic field at 300-km altitude) was
       found to be elongated in longitude with substantial structure
       along its poleward wall.

(3)   Structure along the poleward wall appeared in the form of four
       fingerlike protrusions with an average length (or north-south
       modulation depth) of 80 km and an average east-west spacing
       between fingers of about 200 km.

(4)   Relative plasma motion was measured between enhancements and
       depletions in plasma density, providing direct evidence of
       ongoing plasma structuring by the MFTI process.

(5)   Spatially irregular north-south electric fields were measured
       as a function of longitude, indicating on the basis of plasma
       incompressibility that there also existed a corresponding
       variation in the east-west electric field (i.e., that respon-
       sible for the MFTI).

(6)   Mean plasma-electrodynamic conditions indicated that any plasma
       structure that existed along the poleward wall of the blob
       should have been in the process of being damped by the
       gradient-drift instability, a result that implies [when com-
       bined with item (4)] the absence of F-region polarization elec-
       tric fields during the observation period.

(7)   The slip velocity was not anticorrelated with plasma density,
        a result that also argues against the presence of F-region
        polarization electric fields.

(8)   Estimates of Pedersen conductance in the E and F layers
        indicated that E-region current closure and the low ratio of
        Pedersen conductance between blob and background ionosphere
        could easily account for the absence of F-region polarization
        electric fields.

(9)   Evidence against the presence of F-region polarization electric
        fields implies the ineffectiveness of both the gradient-drift
        and current-convective instabilities in this data set.

(10)   Soft-particle precipitation, as inferred qualitatively from
        electron temperature measurements, appeared to be most intense
        poleward of the blob with perhaps some precipitation occurring
        in the blob.

5.   Discussion

        The major finding of this section is that the fingers (particu-
larly that seen in Scan 6) along the poleward wall of a blob were shown to
be participating in an ongoing plasma structuring process involving MFTI,
but that the MFTI was not driven by F-region polarization electric fields.
We presented direct evidence that there was relative motion (produced by
irregular electric fields) between adjacent regions of high and low plasma
density (along the poleward wall of the blob); furthermore, the sense of
that motion was consistent with ongoing plasma structuring via MFTI.
Although the estimated growth rate was high enough to have produced the
observed fingers within several minutes, whether it did or not is not the
issue. We have simply demonstrated that there can exist MFTI that can
rapidly structure a blob. The temporal persistence of a spatially irre-
gular electric field pattern has not been addressed.

        The conclusion that F-region polarization effects were absent during
the observation period is based on the following findings. First and

139

foremost is the fact that if F-region polarization effects were present, the relative motion of the plasma in the fingers and depleted regions should have had an opposite sense from that observed. That is, relative plasma motion should have been in a direction that would reduce the size of the fingers. Second, the spatial patterns of the slip velocity vector and plasma density were not anticorrelated with each other, as expected from polarization effects. Third, E-region Pedersen conductance was high, and the ratio of Pedersen conductance associated with the blob to that with the background ionosphere was small. And fourth, we found no obvious evidence of velocity shear. Velocity shear is expected when the background Pedersen conductance is finite but small when compared to the blob Pedersen conductance [e.g., Zalesak et al., 1982].

Several researchers [Haerendel et al., 1967, 1969; Volk and Haerendel, 1971; Shiau and Simon, 1974; and Vickrey and Kelley, 1982] have shown that the gradient-drift instability (F-region polarization electric fields) can be stabilized (short circuited) by the presence of a conducting background. In this case, the F-region polarization electric field is shorted out by field-aligned currents that close through the conducting background. Rishbeth [1971] has shown the effectiveness of a sunlit E layer in keeping the F-region dynamo from operating during the day. Tsunoda [1985] has shown experimentally that equatorial F-region irregularities, produced by a process (collisional Rayleigh-Taylor instability) identical to the gradient-drift instability are strongly controlled by E-region conductivity effects.

Perkins and Doles [1975], Zalesak et al. [1982], and Huba et al. [1983] have shown that velocity shear effects set up by the electric field component along the plasma-density gradient result in damping of the gradient-drift instability. Both the blob analyzed in this paper and that reported by Tsunoda and Vickrey [1985] occurred in the presence of an electric-field component in the direction of the mean plasma-density gradient. Interestingly, we find little or no evidence in Figure III.B.7(b) of velocity shear. If velocity shear was present, theory would predict the occurrence of tilted fingers away from perpendicularity with the blob

140

major axis. The absence of tilt also supports the conclusion that F-region polarization electric fields were not present.

A remaining question is, what is the source of the irregular electric fields? A possible interpretation is that the blob analyzed in this paper was situated (or produced) at a magnetospheric boundary of some kind. This possibility arose while analyzing Figures III.B.4, III.B.7, and III.B.8, i.e., plasma-density profiles, electron temperatures, and ion velocities. As described earlier, electron temperature and ion velocity were substantially higher on the poleward side than on the equatorward side of the blob. A possibility is that the blob structure is simply an ionospheric signature of a magnetospheric process. For example, it is conceivable that wave structure and instability occurs at the magneto-spheric boundary, producing irregular electric fields that map into the auroral ionosphere. Such a possibility has been suggested by several re-searchers [e.g., Fejer and Kelley, 1980; Vickrey and Kelley, 1982, Saflekos et al., 1985].

Lui et al. [1982] reported large-scale (200- to 900-km) undulations along the equatorward boundary of the diffuse aurora. They interpreted these optical observations in terms of surface waves propagating along the inner edge of the plasma sheet. While their results support the notion that magnetospheric wave structure could be observed in the ionosphere, their observations were made under conditions that were completely dif-ferent from ours. Their structure is seen only in the afternoon-evening sector during magnetic storm activity.

We hope to shed more light on this matter after we analyze the HILAT satellite data obtained over the EISCAT scan sector during this experi-ment. Instruments on HILAT should provide further information regarding (1) the E layer Pedersen conductance, (2) the presence of field-aligned currents, (3) the latitudinal variations of electric field and particle characteristics, and (4) the characteristics of km-scale irregularities responsible for radio-wave scintillation.

141

C. Plasma Structure and Statistical Turbulence Theory

1. Introduction

Ionospheric irregularities occur over an enormous range of scale sizes, from planetary waves with horizontal wavelengths exceeding one hundred kilometers to centimeter plasma waves approaching the Debye length limit. Kelley et al. [1982b] have identified five scale-size subregimes for vertical and horizontal irregularities. Their Figure 1 is reproduced here for reference as Figure III.C.1. The scale height for the neutral atmosphere is a natural upper bound for statistically homogeneous irregularities. Thus, below ~10 km ($k > 2\pi/10$ km), we have some hope that statistical models can be used to characterize and ultimately predict the observed irregularity characteristics. This is the upper limit for the intermediate scale, which is common to both horizontal and vertical irregularity structures.

The quantity of primary interest is the SDF, which is formally defined as

$$\Phi(k) = \langle |\hat{N}(k)|^2 \rangle \qquad (III.C.1.1)$$

where $N(k)$ is the spatial Fourier transform of the electron density $N(r)$ and the angle brackets denote ensemble averaging. As a practical matter, only a one-dimensional SDF obtained from a scan of $N(r)$ along some direction $\hat{n}$ has been measured. The relation between the one-dimensional SDF and $\Phi(k)$ is

$$\Phi_1(k;\hat{n}) = \int\int \Phi(k)\hat{n} \cdot dk/(2\pi)^2 \qquad . \qquad (III.C.1.2)$$

In general, $\Phi_1(k;\hat{n})$ depends on the direction of the scan.

In Figure III.C.2, we show a schematic diagram of the one-dimensional SDF deduced from disturbed Wideband satellite equatorial scintillation data, AE-E satellite data, and in situ rocket probes [Rino et

HORIZONTAL SCALE
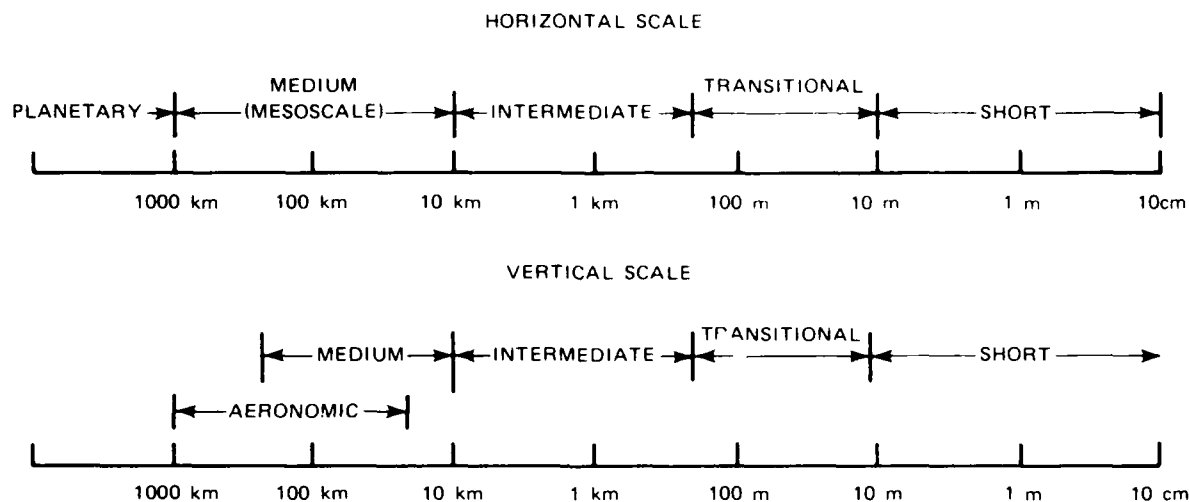
VERTICAL SCALE

[Source: Kelley, et al., (1982b)]

Figure III.C.1.   Definitions of characteristic scales in the horizontal and vertical direction.

al., 1981: Livingston et al., 1981; Kelley et al., 1982a; 1982b]. The outer-scale wave number k_o marks the point at which well-defined power-law behavior begins. Although it has not yet been measured adequately, $k_o \sim 2\pi/10$ km seems to be a conservative lower bound. Between k_o and k_b, the one-dimensional SDF has the power-law form k^{-p_1}, with $1 < p_1 < 2$. We have observed consistently a systematic change in p_1, with the more highly disturbed data favoring p_1 closer to unity [Livingston et al., 1981]. The change in slope of the spectrum at k_b is a well-defined and repeatable feature. Basu et al. [1983] report a median wavelength $(2\pi/k_b)$ of ~750 m. Thus, k_o and k_b essentially delineate the intermediate-scale regime.

Between k_b and k_g, the one-dimensional in situ SDF admits a similar power-law form with p_1 greater than 2. In fact, p_1 can be significantly larger than 2 in the transitional regime. Equatorial data from Ascencion Island are consistent with spectral index values at least as high as 4 [Franke and Liu, 1983]. The abrupt steepening expected at the

143
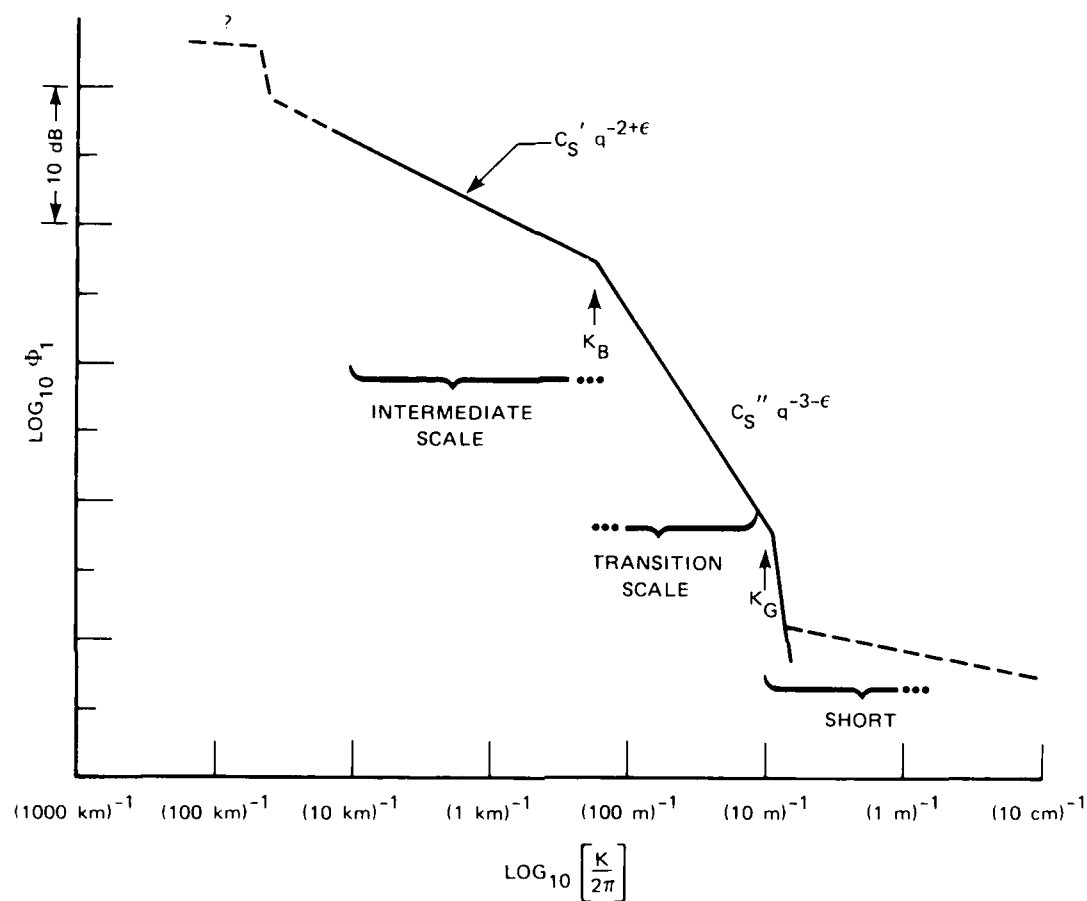
Figure III.C.2.   Schematic representation of one-dimensional in situ spectral density function.

ion gyro radius has been elusive but evidently has been observed in rocket data [Singh and Szuszczewicz, 1984]. The shape of the measured one-dimensional spectrum at the equator does not seem to depend on whether the scans are primarily vertical (rocket data) or horizontal (satellite and scintillation data).

In most of our predictive modeling to date, the mathematical model

$$\Phi(k) = \frac{abC_S}{\left[q_o + q^2\right]^{\nu+1/2}}$$ (III.C.1.3)

has been used. To accommodate anisotropy, q^2 is a quadratic form in k_x, k_y, and k_z with coefficients that depend on the axial ratios along and transverse to the magnetic field, a and b, respectively. The ν index is related to p_1 as

$$p_1 = 2\nu - 1$$ (III.C.1.4)

The applications to propagation theory are summarized in Rino [1982]. Phenomenology codes such as SCENARIO predict the electron density variance, $\langle |N_e|^2 \rangle$. With an assumed value of q_o, the structure or turbulence level C_S is determined from a relation such as

$$\langle \Delta N_e^2 \rangle = C_S q_o^{-(2\nu-2)} \Gamma(\nu - 1) / \left[8\pi^{3/2} \Gamma(\nu + 1/2)\right]$$, (III.C.1.5)

which is obtained by integrating Eq. (III.C.1.3) over all k. Although this relatively simple formulation provides reasonable estimates for systems studies, we would ultimately like a physics-based model that is consistent with the one-dimensional SDF in Figure III.C.2.

This is a formidable task that has eluded researchers for nearly twenty years. Although no complete solution to the problem is yet in sight, the mechanisms that potentially can affect the spectral regimes in Figures III.C.1 and III.C.2 are being modelled. The fact that in the intermediate-scale regime the spectral index is less than 2 implies that a range of irregularity scale sizes are contributing. For k values larger than k_b, however, the shape of the individual irregularities is primarily responsible for the spectral characteristics. The shallow intermediate-scale spectral index suggests a cascade of structure in that scale-size

regime that may be amenable to analysis using statistical turbulence theory. At these large scales, we may justifiably ignore diffusion as well, as discussed in Section III.C.3. Beyond k_b, however, complex diffusive processes clearly play an important role in determining the shape of the SDF.

To date, the diffusion-free and diffusion-dominated regimes have been studied independently, the hope being that these two pieces ultimately can be incorporated into a unified model. In Section III.C.2, we review the general theory and suggest how that link might be made. The results will also set the background for the turbulence theory.

2. The Coupled Potential and Continuity Equations

A thorough review of fluid theory as it is formulated for numerical simulations can be found in Zalesak et al., [1985]. For our purposes here, we shall summarize only the principal functional elements of the theory. From the momentum balance equations for ions and electrons, we can derive a formal expression for the transverse currents of the form

$$J_\perp = k_P \Delta F + k_H \Delta F \times \hat{a}_z \quad , \qquad (III.C.2.1)$$

where ΔF is the difference between the instantaneous forces that act on the ions and the electrons. Four forces are involved: (1) external forces from applied electric fields, neutral winds, and gravity; (2) inertial forces including advection; (3) pressure gradients; and (4) polarization fields, which maintain overall charge neutrality ($N_i = N_e = N$). Following Zalesak [1985], we separate the polarization potential into two components

$$\phi(\rho,z) = \phi_C(\rho) + \phi_D(\rho,z) \quad , \qquad (III.C.2.2)$$

146

where $\phi_C(\rho)$ is the convection potential, which does not vary with height, and $\phi_D(\rho,z)$ supports the diffusive process. We shall give a precise definition of $\phi_C(\rho)$ shortly.

To derive an equation for ϕ, we use the charge-neutrality condition $\nabla \cdot J = 0$. Integrating $\nabla \cdot J$ along the magnetic field gives the formal expression

$$\int_0^\infty \nabla_\perp \cdot J = \int_0^\infty \frac{\partial}{\partial z}(J_{11})(z)dz \qquad . \qquad (III.C.2.3)$$

Perkins et al. [1973] showed that in a uniform isolated plasma, the integral on the right-hand side is zero; however, we can introduce fixed parallel currents, as with the current convective instability [Ossakow and Chaturvedi, 1979]. If the right-hand side of Eq. (III.C.2.3) is zero, the z-dependent part of ϕ is effectively removed from the problem. In all cases, however, Zalesak et al. [1985] showed that when the inertial forces are neglected, Eq. (III.C.2.3) gives rise to an equation for ϕ_C of the form

$$\nabla \cdot \left[\Sigma_P \nabla \phi_C \right] + H\left(\Sigma_P, \Sigma_H, \phi_C \right) = D \cdot \nabla \Sigma_P \qquad (III.C.2.4)$$

where Σ_P is the height-integrated Pedersen conductivity and Σ_H is the height-integrated Hall conductivity, D is the equivalent fixed electrostatic force or driver that moves the plasma across magnetic field lines. The exact form of the Hall term is given in Zalesak et al. [1985].

To complete the specification of the problem, we introduce the continuity equation

$$\frac{\partial N}{\partial t} + \nabla \cdot \left[\bar{v}_i N \right] = 0 \qquad . \qquad (III.C.2.5)$$

The component of v_i driven by ϕ_C can be isolated, giving an equivalent expression of the form

$$\frac{\partial N}{\partial t} + \frac{\hat{a}_z \times \nabla \phi_C}{B} \cdot \nabla N = F(N; \phi_D) \qquad . \qquad (III.C.2.6)$$

147

The equation for ϕ_D can be written in the form

$$\nabla\left[\sigma_P \nabla\phi_D\right] = G\left(N;\phi_D\right) \qquad\text{(III.C.2.7)}$$

where $\sigma_P = kN$ is the local Pedersen conductivity. The functions F and G depend only on the instantaneous plasma configuration and Φ_D. Their exact form is unimportant for the development here.

The formal solution to the problem is conceptually straight-forward. From the configuration of the plasma at any instant in time, one first computes σ_P and then solves Eq. (III.C.2.4) for ϕ_C. One then solves Eq. (III.C.2.7) for ϕ_D. Finally, one integrates Eq. (III.C.2.6) forward a small step in time to determine a new plasma configuration. For a single uniform layer, or a simple system of coupled layers, the problem reduces to the solution of the equations

$$\frac{\partial N_T}{\partial t} + \frac{\hat{b}\times\nabla\phi_C}{B}\cdot\nabla N_T = K\nabla^2 N_T \qquad\text{(III.C.2.8)}$$

and

$$\nabla\cdot\left[N_T \nabla\phi_C\right] = D\cdot\nabla N_T \quad , \qquad\text{(III.C.2.9)}$$

where K is an effective diffusion coefficient and N_T is the integrated electron density.

In the remainder of this section, we shall consider the evolution of plasma structure governed by Eqs. (III.C.2.8) and (III.C.2.9), which is the simplest system that preserves both a nonlinear coupling mechanism and diffusion. The solution to the more general system Eq. (III.C.2.6) should admit similar spectral characteristics at small wave numbers where direct diffusive effects are negligible. The basic assumption here, which remains to be tested, is that as long as the rate at which diffusive processes remove structure at small scale sizes is the same, the large-scale spectral characteristics will be essentially the

148

same. Turbulence theory attempts to deduce these spectral characteristics.

3. Turbulence Theory

Stated formally, the problem is to characterize the structure evolution of the two-dimensional scalar field, $N(\rho,t)$, as governed by the coupled nonlinear differential Eqs. (III.C.2.8) and (III.C.2.9). The vector ρ is two dimensional and lies in the plane normal to the unit vector $\hat{b}$. The diffusion coefficient K has units of l^2/t. The "driver" D when normalized to the magnetic field intensity B has units of $1/t$. The initial configuration, $N(\rho,t_o)$, completes the specification of the problem.

Virtually any initial configuration of N with $D \cdot \nabla N \neq 0$ will evolve with time, ultimately developing highly irregular spatial variations. Small changes in the initial configuration cause large differences in the "late-time" structure, but evidently the average characteristics remain essentially the same. Also, the large-scale structure of the initial configuration seems to have more effect on the time it takes to reach a quasi-steady late-time configuration than on its average characteristics. These are conditions under which we expect statistical turbulence theory to be applicable.

Following Kraichnan [1975], we consider only initial configurations that admit spectral decompositions of the form

$$\begin{Bmatrix} N(\rho;t) \\ \phi(\rho;t) \end{Bmatrix} = \frac{1}{A} \sum \begin{Bmatrix} \hat{N}(k;t) \\ \hat{\phi}(k;t) \end{Bmatrix} \exp\{ik\cdot\rho\} \qquad (\text{III.C.3.1})$$

where

$$k = \left(n\Delta k_x,\ m\Delta k_y\right) \quad , \qquad (\text{III.C.3.2})$$

$$\Delta k_x = 2\pi/L_x \quad , \qquad \Delta k_y = 2\pi/L_y \qquad (\text{III.C.3.3a,b})$$

149

and

$$A = L_x L_y \quad . \tag{III.C.3.4}$$

Both N and ϕ are periodic in L_x and L_y. Effectively, the realizations are confined to a finite area. This is not restrictive for applications, because below some small spatial wave number, k_o, Fourier modes cannot maintain the uncorrelated phase structures (a necessary condition for statistical homogeneity) that are assumed in developing the theory. Our goal is to determine the form of the SDF from k_o to k_b where diffusion effects become important.

By substituting Eq. (III.C.3.1) into (III.C.2.9), it can be shown that

$$\frac{\partial \hat{N}(k)}{\partial t} + Kk^2 \hat{N}(k) = \frac{1}{A} \sum^{\Delta} \left(\frac{\hat{b} \cdot k' \times k''}{B} \right) \hat{\phi}(k') \, \hat{N}(k'') \tag{III.C.3.5}$$

The symbol Δ indicates that the summation includes only those wave vectors k' and k'' that satisfy the triangle equality

$$k = k' + k'' \quad . \tag{III.C.3.6}$$

Multiplying Eq. (III.C.3.5) by $\hat{N}(k)^*$, we obtain the equation for the instantaneous spectral intensity

$$\frac{1}{2} \frac{\partial |\hat{N}(k)|^2}{\partial t} + Kk^2 |\hat{N}(k)|^2 = \frac{1}{A} \sum^{\Delta} \left(\frac{\hat{b} \cdot k' \times k''}{B} \right) \hat{\phi}(k') \, \hat{N}(k'') \, \hat{N}^*(k) \tag{III.C.3.7}$$

It can be shown that the summation of the nonlinear convection term over all k is zero. Thus, the nonlinear mode coupling can change the shape of the spectral intensity but not the scalar variance, which changes only through diffusion. In the absence of diffusion ($K=0$), Eq. (III.C.3.7) conserves the scalar variance, which we define as

$$\Omega = \frac{1}{A} \sum |\hat{N}(k)|^2 \quad . \tag{III.C.3.8}$$

We can write the general relation

$$\frac{\partial \Omega}{\partial t} = \chi \quad , \tag{III.C.3.9}$$

where

$$\chi = -(2K/A)\sum k^2 |\hat{N}(k)|^2 \tag{III.C.3.10}$$

where χ is the rate at which scalar variance is lost through diffusion. To achieve a truly stationary configuration, we must somehow supply scalar variance at the rate χ. If a more complex diffusion process is operative, the form of Eq. (III.C.3.10) would change, but not Eq. (III.C.3.9). This is the formal basis for assuming that the detailed diffusive mechanism that removes structure at small scale sizes will not affect the spectral characteristics at long wavelength.

Ott and Farley [1974] first pointed out the similarity between the continuity equation for convectively unstable plasmas, Eqs. (III.C.2.8) and (III.C.2.9), and the two-dimensional Navier-stokes (NS) equation. When written in terms of the vorticity, ω, defined by

$$\omega \hat{a}_z = \nabla \times \mathbf{v} \quad , \tag{III.C.3.11}$$

where $\mathbf{v}$ is the two-dimensional fluid velocity vector, the NS equation is

$$\frac{\partial \omega}{\partial t} + \mathbf{v} \cdot \nabla \omega = \nu \nabla^2 \omega \quad , \tag{III.C.3.12}$$

where ν is the kinematic viscosity.

The similarity is purely formal, however, because Eqs. (III.C.3.11) and (III.C.3.12) characterize inertially driven turbulence. In the absence of viscosity, both mechanical energy, which is proportional to the variance of v^2, and the variance of vorticity, which is called enstrophy, are conserved by Eqs. (III.C.3.11) and (III.C.3.12), whereas Eqs. (III.C.2.8) and (III.C.2.9) admit only one conserved quantity, Ω.

151

Systems with two or more "rugged invariants" [Kraichnan, 1967, 1975; Fyfe et al., 1977; Seyler, 1975] have been studied extensively, but the results do not seem to be readily applicable to turbulence in convective plasmas.

The formal difference between the two systems can be best illustrated by letting v in the NS system be represented in terms of a potential function, ϕ_v, as

$$v = \hat{a}_z \times \nabla \phi_v \quad . \qquad \text{(III.C.3.13)}$$

Then, Eq. (III.C.3.11) can be rewritten as

$$\nabla^2 \phi_v = \omega \quad , \qquad \text{(III.C.3.14)}$$

which is Poisson's equation, whereas Eq. (III.C.2.9) is equivalent to

$$\nabla^2 \phi + \nabla \phi \cdot \nabla N = D \cdot \nabla N / N \quad . \qquad \text{(III.C.3.15)}$$

Thus, even if the nonlinear term in Eq. (III.C.3.15) is neglected, the relationship between ϕ_v and ω is fundamentally different from the relationship between ϕ and N.

There are, however, plasma systems in which the density is related to a potential function via Poisson's equation, and Seyler [1975] has treated these collisionless guiding-center plasmas in detail. If we are to look for more direct parallels, ion-inertial effects must be considered in conjunction with ion-neutral collisions. Kelley and Ott [1978] have argued that when inertial effects dominate, the velocity field can be characterized by the known results from classical turbulence theory. Although this is possibly correct in the collisionless regime, the problem of characterizing the structure of the electron density remains.

Another parallel can be drawn. Equation (III.C.2.6) is also identical in form to the equation of a passive scalar. Passive scalars are important in turbulence theory, and they have been studied extensively. The SDF of the passive scalar can be determined in three regimes:

the inertial convective, convective dissipative, and viscous convective
[Batchelor, 1959]. A passive scalar, such as temperature or a dye, how-
ever, should not affect the velocity field in which it is immersed.
Clearly, this is not the case in a convective plasma system nor for scalar
vorticity in the NS system because the velocity structure is determined by
the current plasma configuration. Nonetheless, there are situations in
which turbulent velocity fields are mapped along field lines into the
ionosphere (Sections III.A and III.B). In that case, at least one com-
ponent of the density structure may behave like a passive scalar. At the
same time, however, charge neutrality Eq. (III.C.2.3) must hold.

Thus, we believe that Eqs. (III.C.2.6) and (III.C.2.7) must be
attacked directly rather than through parallels to classical turbulence
theory. By using dimensional arguments, Ott and Farley [1974] showed that

$$\Phi_1(k;\hat{n}) = (\chi/V)f\big(\theta,K/(Vk)\big)k^{-1} \quad , \qquad \text{(III.C.3.16)}$$

where

$$V = D/B \qquad \text{(III.C.3.17)}$$

is the simplest form Φ_1 can take that is dimensionally correct and con-
sistent with a diffusion-free structure cascade regime. The angle θ is
the angle between D and $\hat{n}$. The form of Eq. (III.C.3.16) is also consis-
tent with the result derived by Batchelor [1959] for the viscous convec-
tion subrange of a passive scalar, but from Batchelor's analysis it is
clear that Eq. (III.C.3.16) is a general property that applies whenever
the velocity field has a high degree of spatial coherence compared to the
spatial coherence of $N(\rho,t)$. The scalar structure becomes highly elon-
gated and Eq. (III.C.3.16) applies across the direction of elongation.
Thus, Eq. (III.C.3.16) is a general limiting form that sets a lower bound
of unity on the spectral index.

4.   Spectral Characteristics Deduced from Numerical Simulations

Numerical simulations have been used extensively to study the non-linear evolution of isolated plasma enhancements since the early formulation of the theory by Simon, [1970]; Linson and Workman [1970]; Volk and Harendel, [1971]; and Perkins et al., [1973]. Pioneering work was done by Zabusky et al., [1973]; McDonald et al., [1974]; and Scannapieco et al., [1976], and has been reviewed by Ossakow [1979]. Numerical simulations were singularly successful in explaining the non-linear evolution of large-scale plasma depletions at the equator.

The numerical techniques have undergone many refinements, but two basic limitations remain. The first is purely practical because finite computation speed and memory size limitations to date have precluded simultaneously treating structures over more than approximately three decades in scale size. Thus, we cannot follow the dynamic evolution of background structures while resolving the small-scale structure that is generated as the instability progresses.

The second limitation is more subtle. The process of steepening and bifurcation ultimately will generate structure at the resolution limit of the computation grid. This structure is removed by a diffusion process that may or may not be an artifact of the computational limitation. At large scale sizes, real diffusion is relatively ineffective compared to the short scale-size regime where diffusion actively removes structure. However, the numerical method that is used to control the removal of small-scale structure can affect the structure levels and spectral shape at all scale sizes. We believe, nonetheless, that, in a diffusion-free regime that encompasses at least a decade range of structure sizes, numerical simulations should reproduce a one-dimensional SDF that agrees with measured one-dimensional spectra if the theory is correct.

To date, all the reported spectral measurements from numerical simulations have produced spectral indices steeper than 2. These values may be appropriate for the subkilometer scale transition regime in which

154

diffusion is important in controlling the shape of the spectrum as well as its intensity. However, it certainly does not explain the observations in their entirety.

It is useful, therefore, to review the simulation results to determine why the discrepancy between theory and experiment exists. We suspect that the simulations that have been performed to date have not been configured to emphasize the intermediate scale regime. The studies have emphasized either the evolution of comparatively large-scale structure [Zalesak et al., 1982; Keskinan and Ossakow, 1982, or the transition to small-scale structure [Keskinan et al., 1980, 1982].

Keskinan and Ossakow [1981] investigated the effects of different initial conditions on the evolution of structure in a convecting slab. The slab was seeded with both periodic and random initial perturbations. We have reproduced two of their runs here in Figures III.C.3 through III.C.6. Figure III.C.3 shows the temporal evolution of a slab seeded with a 15 percent amplitude periodic perturbation, $K = 1 \ m^2/s$, and an initial gradient scale of 6 km. Figure III.C.5 shows the corresponding evolution for a 15 percent rms random perturbation.

The configurations after 2400 s shown in Figures III.C.3(d) and 5(d) are very similar in spite of the very different intermediate states the structures passed through. This late-time similarity is reflected in the corresponding one-dimensional spectra shown in Figures III.C.4 and III.C.6.

In the spectra measured along (k_y) and across (k_x) the drivers are distinctly different in their low-frequency behavior, but have similar power-law indices of 2.2 to 2.4 in their respective high-frequency regimes The k_y spectra measured across the striations sustain a low-frequency plateau to much shorter wavelengths than the corresponding k_x spectra, particularly for the randomly seeded slab. Thus, the spectrum is anisotropic with more low-frequency content along the direction of the driver.

0 s

200 s

(a)

(b)

Y — km

1000 s

2400 s

(c)

(d)

Y — km

X — km

X — km
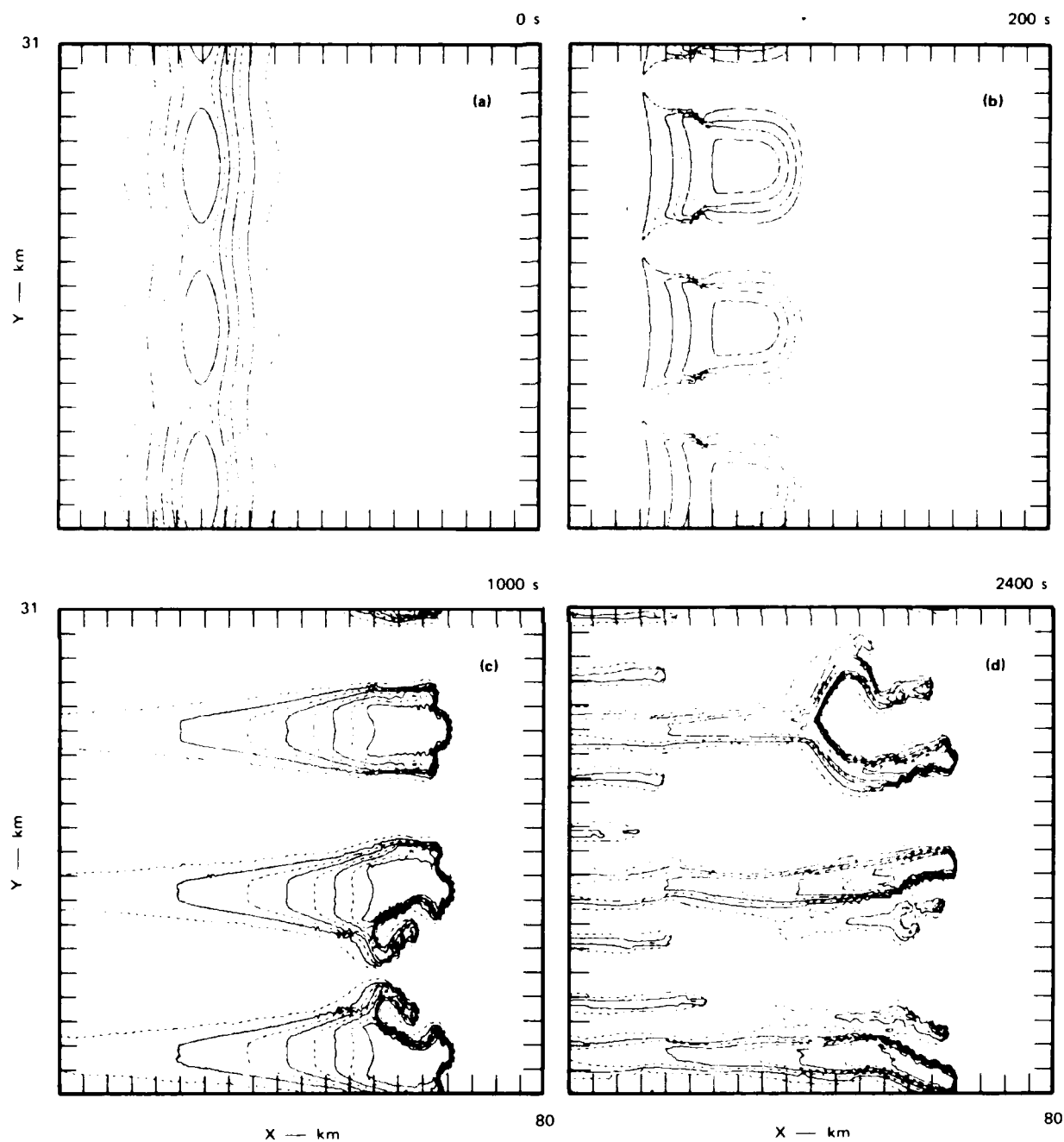
[Source: Keskinen and Ossakow, 1981]

Figure III.C.3.   Real-space isodensity contour plots of $\Sigma(x,y)/\Sigma_0$ for $L = 6$ km using the 15 percent monochromatic initial conditions at (a) $t = 0$ s, (b) $t = 200$ s, (c) $t = 1000$ s, and (d) $t = 2400$ s.
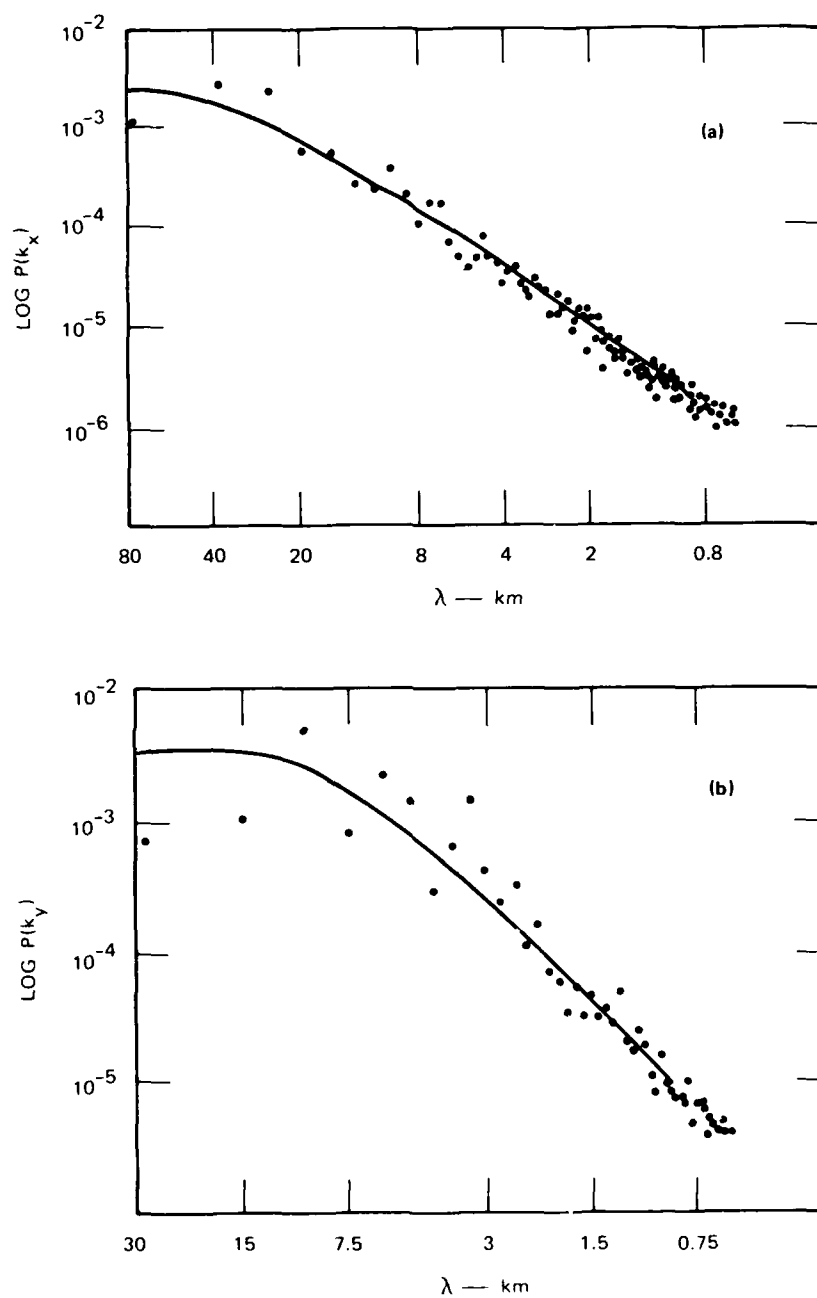
[Source: Keskinen and Ossakow, 1981]

Figure III.C.4.   One-dimensional (a) x power spectra $P(k_x)$ and (b) y power spectra $P(k_y)$ at t = 2400 s for L = 6 km using the 15 percent monochromatic initial conditions with n_x = 2.2 and n_y = 2.1.

0 s

200 s

(a)

(b)

1000 s

2400 s

(c)

(d)

X — km   80

X — km   80

Y — km

3↑

31
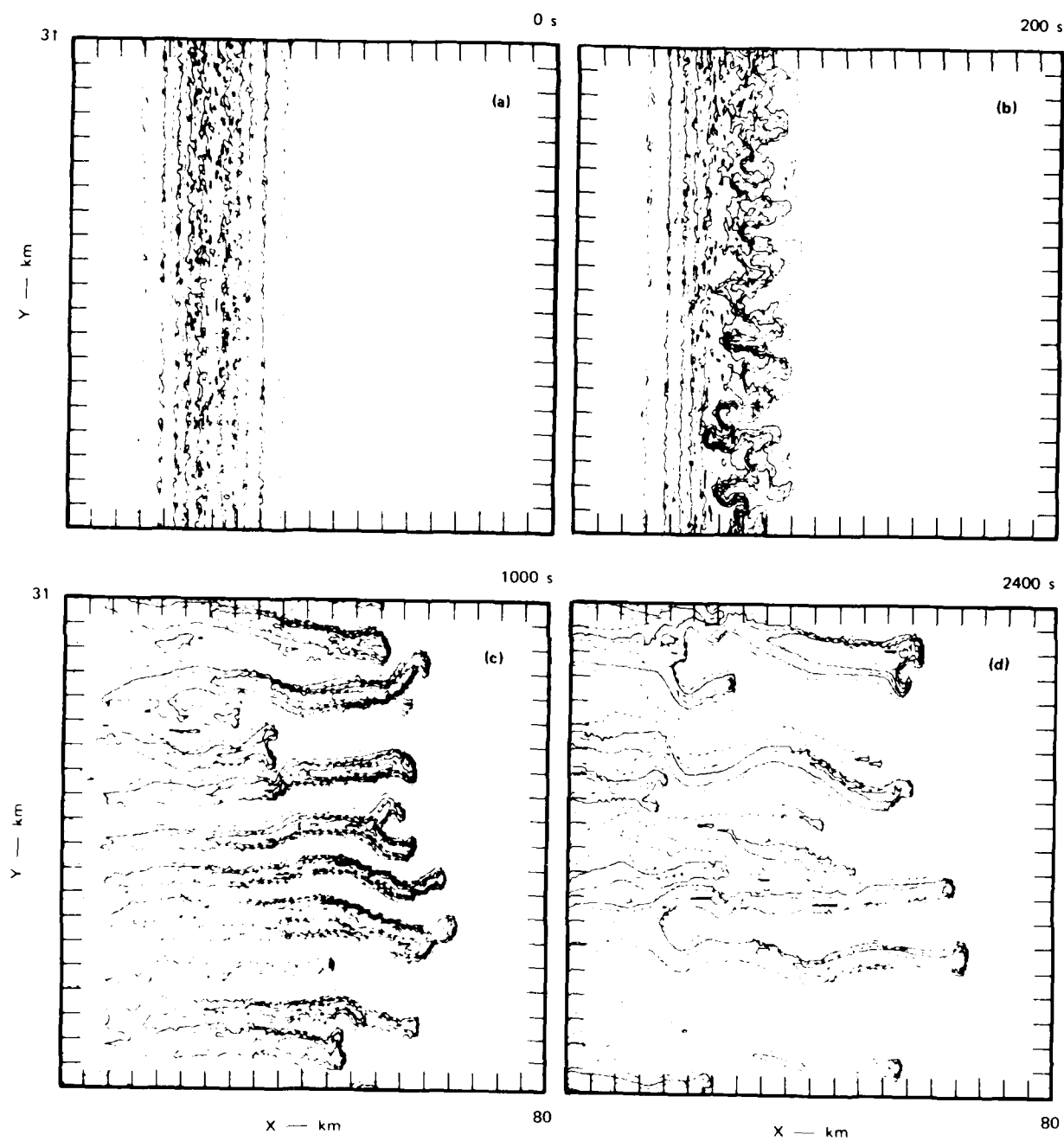
[Source   Keskinen and Ossakow, 1981]

Figure III.C.5.   Real-space isodensity contour plots of $\Sigma(x,y)/\Sigma_0$ for L = 6 km using the 15 percent random initial conditions at (a) t = 0 s, (b) t = 200 s, (c) t = 1000 s, and (d) t = 2400 s.

158
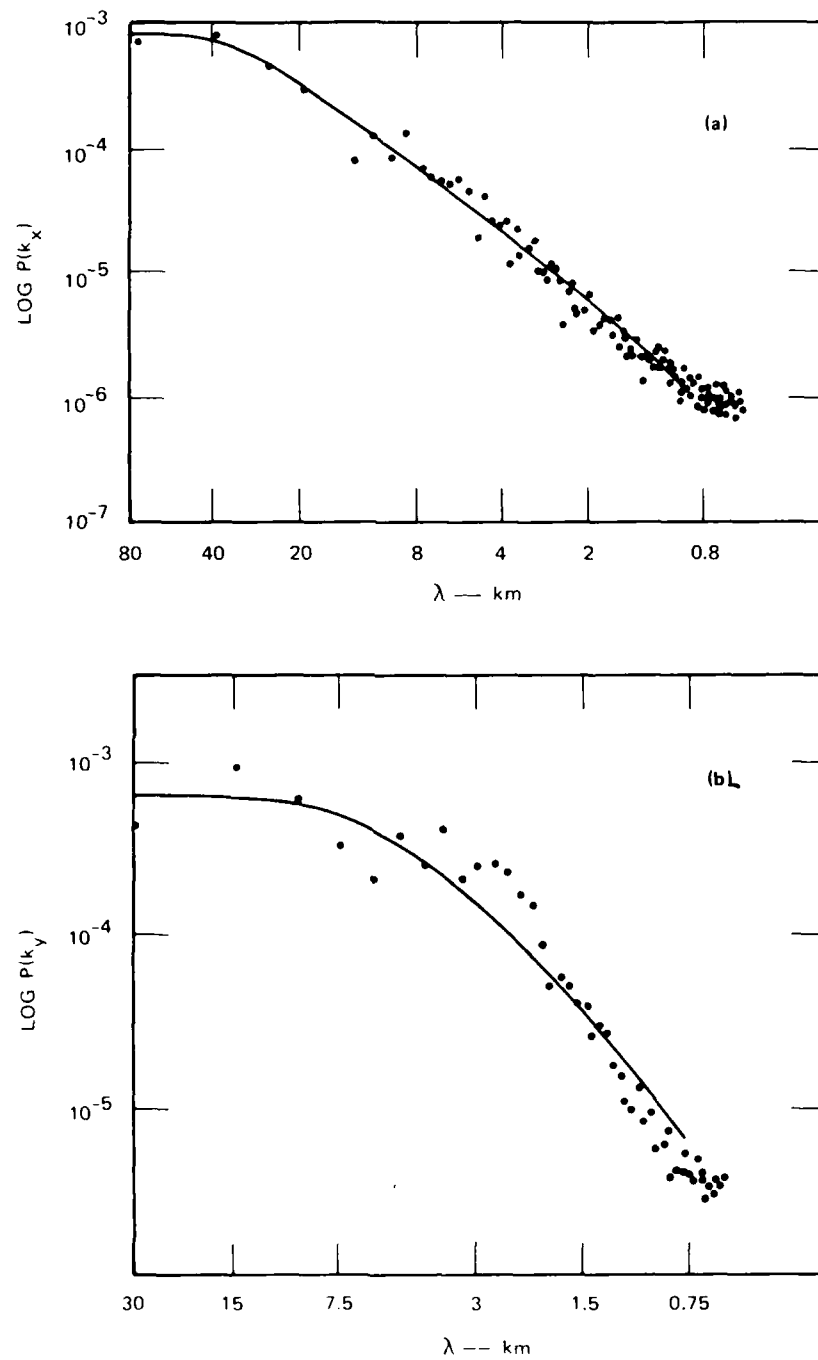
[Source: Keskinen and Ossakow, 1981]

Figure III.C.6. One-dimensional (a) x power spectra $P(k_x)$
and (b) y power spectra $P(k_y)$ at $t = 2400$ s
for $L = 6$ km using the 15 percent random
initial conditions with $n_x = 2.0$, $2\pi/k_{ox} = 30$ km
and $n_y = 2.3$, $2\pi/k_{oy} = 3.9$ km.

Keskinan and Ossakow [1981] used the simple power law form

$$\Phi_1(k) = \frac{C}{[k_o^2 + k^2]^{n/2}} \qquad\qquad (III.C.4.1)$$

to fit the k_x and k_y spectra; however, the data suggest that the low fre-
quency regimes of the k_y spectra could just as well be fit to a second
more shallowly sloped power-law segment. The corresponding power-law
index is less than unity and reflects the distribution of striation sizes
present in the late-time configuration. Because this spectral regime
contains most of the structure intensity, it dominates spectra that are
measured at angles to $\bar{D}$ that are not close to 90°.

Similar behavior is observed in the evolution of a simple
linear gradient seeded by purely random structure. Figures III.C.7 and
III.C.8 are reproduced from Keskinan and Ossakow [1980]. Figure III.C.7
shows the structure after 4500 s, and Figures III.C.8(a) and 8(b) show the
corresponding spectra along and across the driver, respectively. For this
simulation gravity supplied the force to move structure across field lines
rather than an electric field, but this change has no effect on the form
of the basic equations. In should also be noted that Keskinan and Ossakow
[1980] used a time-varying recombination rate in place of electron diffu-
sion to simulate the removal of structure on the bottom side of a rising F
layer.

Turning to the intermediate or size-dominated regime, in Figure
III.C.8(a) we have drawn in a k^{-1} power law at the low-frequency end of
the SDF to emphasize the presence of a size distribution. An important
question for bringing theory and experiment into better agreement is how
to determine the conditions under which a larger intermediate regime would
manifest itself.
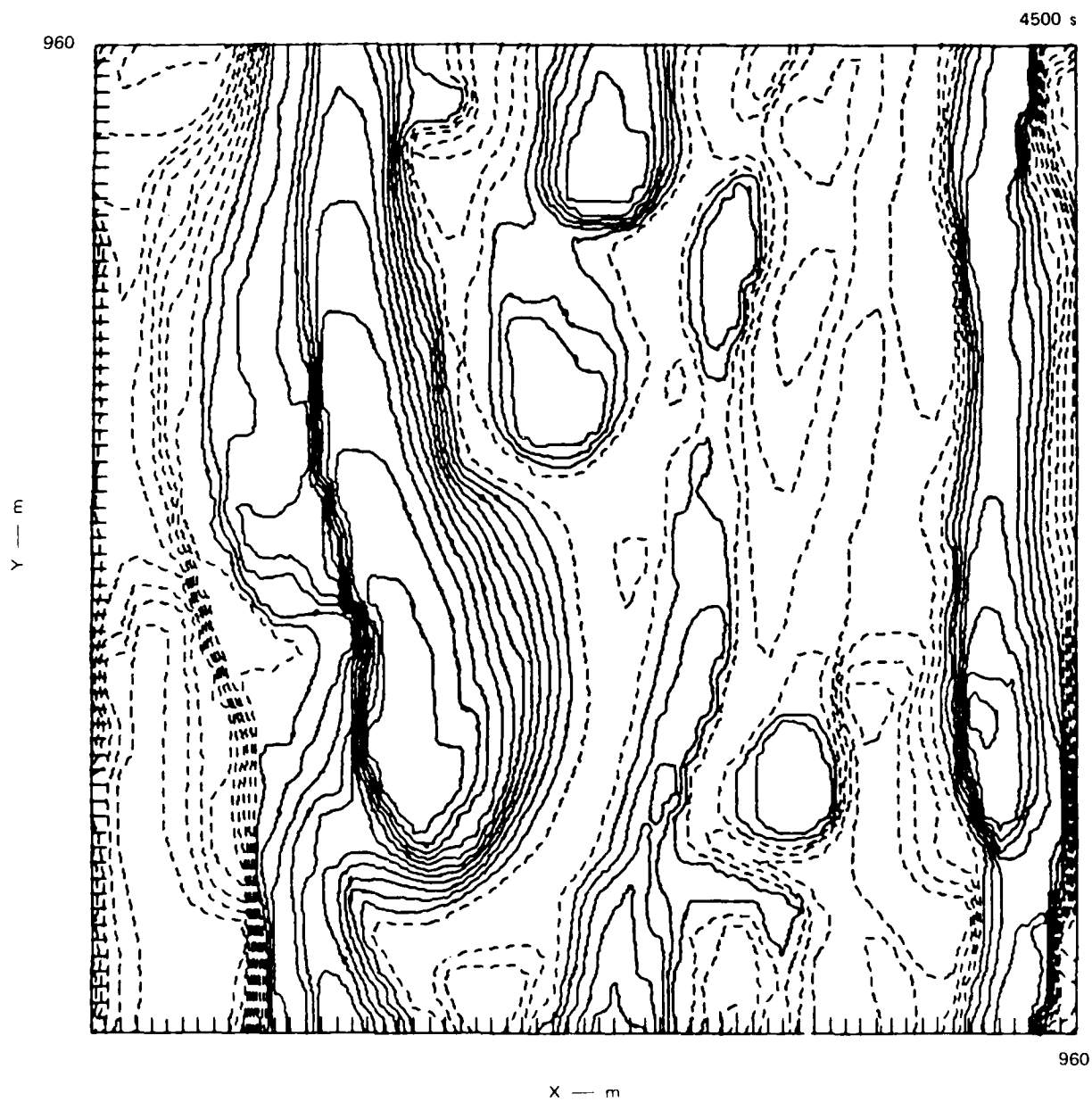
Figure III.C.7.   Same as Figure III.C.5 but at t = 4500 s.   Maximum enhancement and depletion are + 66 percent and - 56 percent.

161
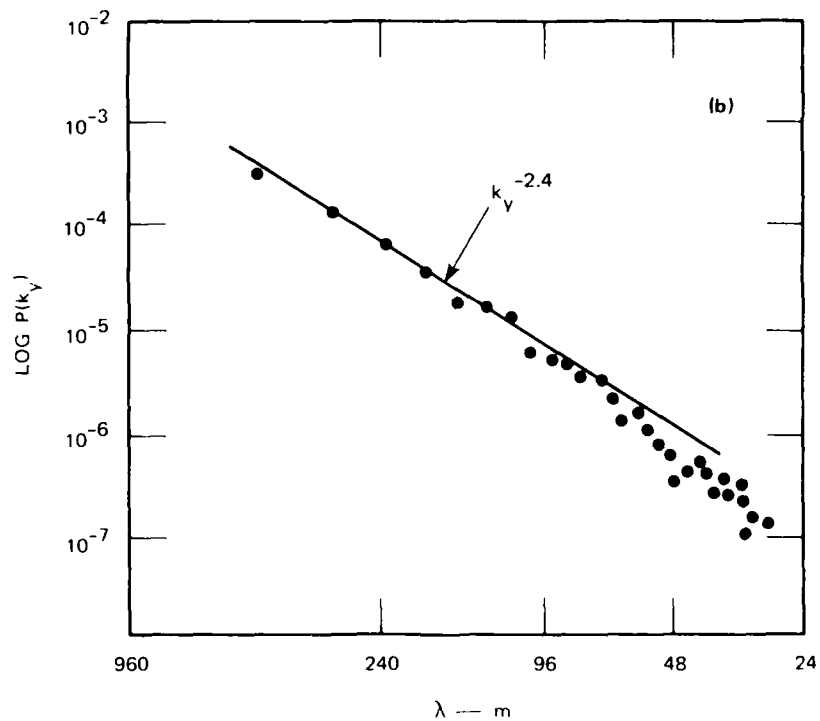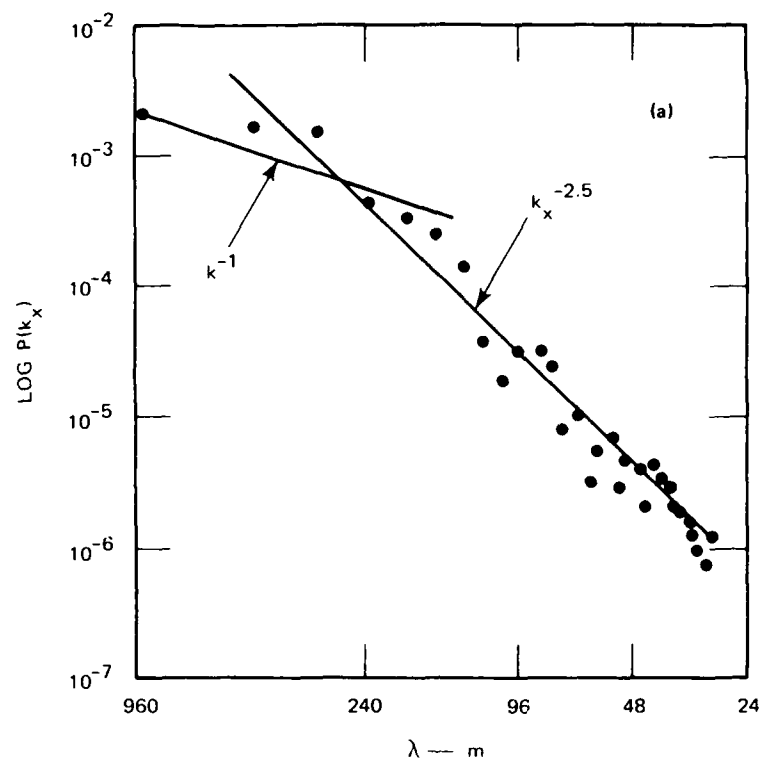
Figure III.C.8.   One-dimensional (a) horizontal $P(k_x)$ and (b) vertical $P(k_y)$ spatial power spectra versus k_x and k_y, respectively, for $L = 8$ km at $t = 4000$ s.   The solid lines are least squares fits to the numerical simulations (dots) and $k_0 = 2\pi/960$ m.

162

Two possibilities emerge: If turbulence theory is strictly applicable, the tendency to generate a range of scale sizes depends only on the rate at which large-scale structure is supplied, not on the details of how it is supplied. Thus, increasing the range of the intermediate scale should require only a proportionate increase in the size of the computational grid. Alternatively, the large range of scale-size-dominated structure observed in naturally occurring irregularities may yet be a consequence of the initial configuration of the plasma or of the nonlinear steepening, which is an intrinsic part of the process. We suspect that both conditions occur. At the present time, we are pursuing a collaborative study with the Naval Research Laboratory to investigate this aspect of the convective instabilities using numerical simulations.

SECTION IV

DIFFUSION PROCESSES IN A MAGNETIZED PLASMA

Previous sections of this report have emphasized various sources of plasma structure. However, to understand both the amplitude of irregularities and the detailed shape of irregularity spectra completely, the complicated balance of sources and sinks of structure must be addressed. We cannot rule out the possibility that both sources and sinks of structure may have unique scale-size dependencies. In this section, we examine experimentally and theoretically the scale-size dependence of plasma diffusion and the effect of diffusion on radio-wave scintillation observations.

A.   Irregularity Decay in an Isolated Plasma Bubble

We describe complex signal scintillation of an isolated and decaying equatorial plasma bubble. Multiple scans through the bubble made from the Air Force Geophysics Laboratory (AFGL) Airborne Ionospheric Observatory, show evolution of irregularity energy over a broad range of scale sizes. At wavelengths larger than about 4 km, the energy remains nearly constant with time. At shorter scale sizes, the spectrum maintains an approximate power law form (f^{-n}) and n increases with time. This behavior suggests that the effective cross-field diffusion rate in the F region depends on scale size.

1.   Introduction

Irregularity generation in the nighttime equatorial F region is dominated by the large-scale electron density structures that have come to be known as plasma bubbles. These depleted regions and the irregularities that they produce as they develop are clearly associated with radar back-

scatter, ionogram spread F, airglow depletions, and radio-wave scintillation [Ossakow, 1979, and references cited therein]. Typically, the experimental effort has been directed toward understanding the growth and full-development phases of plasma bubbles in the early-evening local-time sector. In this report, we describe measurements of a much weaker, decay phase bubble. By making repeated scans through that bubble, detailed changes in its irregularity content have been measured.

The observations were made using the AFGL's Airborne Ionospheric Observatory. Previous measurements using the aircraft have established the bottomside airglow and spread-F and intensity scintillation signatures of equatorial plasma bubbles [e.g., Weber et al., 1980]. In early 1979, the scintillation measurement capability of the aircraft was expanded to record complex signal measurements from CW satellite sources using a technique outlined in Livingston [1983]. The phase of a trans-ionospherically propagated signal is not strongly affected by diffraction at the frequencies and perturbation levels of interest here [Rino, 1979], and its power spectrum provides an almost direct mapping of the in situ irregularity continuum. The inherent sensitivity of the phase measurements also makes it possible to observe subtle changes in that continuum over a large range of spatial scales. This time/wavelength dependence of spectral energy is an essential element in the definition of irregularity decay.

2. Experiment Background

The observations included in this section were made during a flight from Ascension Island on 27 and 28 March 1979; the objective of that flight was to locate an isolated, eastward-drifting plasma depletion and to make repeated scintillation measurements through the disturbance as it decayed. A route was selected far enough south of the magnetic equator to ensure high background airglow intensities of 6300 Å to contrast with the plasma bubbles and associated airglow depletions. Early in the flight, one moderate airglow depletion was observed, but the structure had decayed before any propagation raypaths intersected the disturbance. A second

depletion was encountered shortly afterwards, and at local times between 2300 to 0130, a series of east-west legs were flown to make repeated scintillation and optical measurements of the bubble as it decayed.

Figure IV.A.1 is a map of the F-region (350-km) penetration point scanned by the aircraft during the multiple east-west flight legs. The successive tracks are nearly parallel, and each is at a constant dip latitude near 13°. The radio-scintillation source used throughout the scintillation measurements was a 249-MHz signal from a geostationary satellite located due west of the aircraft at an elevation of 73°. The aircraft speed was nearly constant in both eastward and westward directions producing a cross-field penetration velocity component of slightly greater than 200 m/s at F-region altitudes.
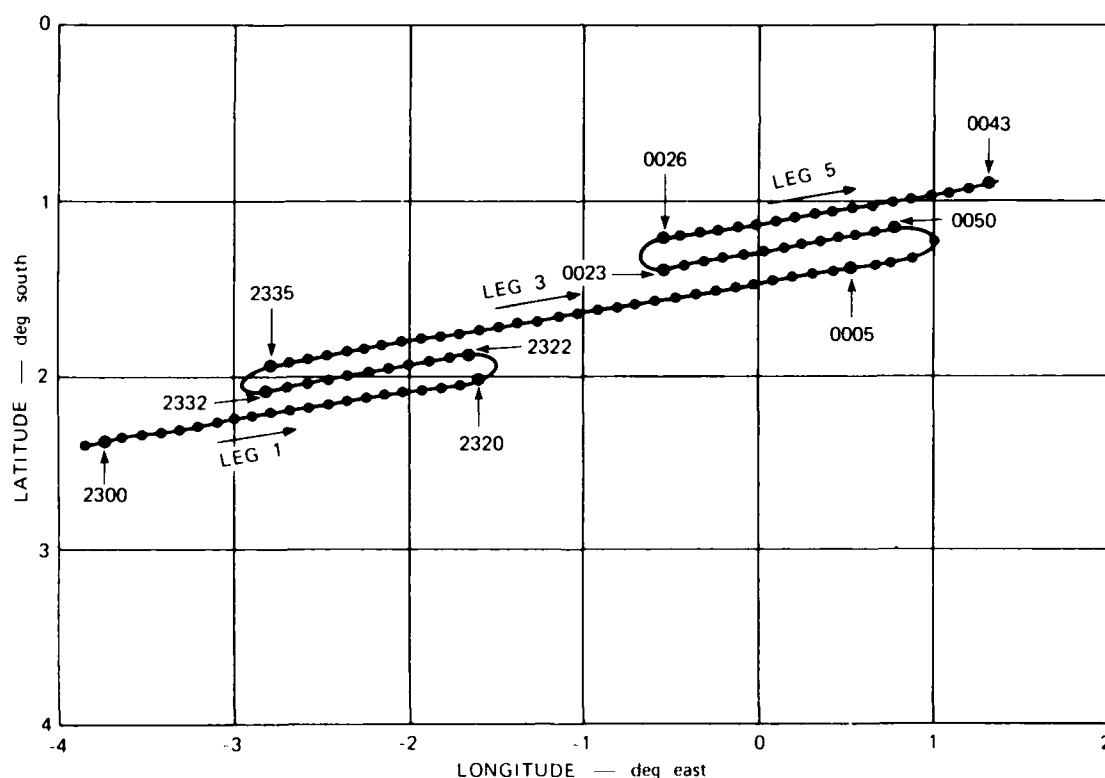
Figure IV.A.1.   Map of the 350-km altitude ionosphere penetration point for consecutive east-west flight legs.

166

Figure IV.A.2 shows the all-sky 6300-Å airglow images for three times during the flight. The dots indicate the propagation-path intersection at the assumed airglow emission height of 250 km, where the all-sky lens images a circle of 600-km radius in the ionosphere. The airglow depletions visible in Figure IV.A.2, although structured, are relatively weak compared to others measured near Ascension Island in 1978 [Weber et al., 1980]. They do, however, verify that it is the same structure that is being intercepted on consecutive aircraft passes.

3.   Structure of Total Electron Content and Intensity Scintillation

Figure IV.A.3(a) shows the signal intensity and large-scale dispersive phase variation, flying eastward for Leg 1, the first scan through the bubble. The onset of intensity scintillation, which is caused by irregularities of $\sim$ 200-m cross-field dimension, is very rapid on the western edge of the disturbance and is associated with a gradient in TEC, which entails a decrease in column density of about 1×10^{17} electrons/m^2.

The generation of plasma bubbles in the nighttime equatorial ionosphere is by now a much-studied and reasonably well-understood process. In some cases, the bubble growth is moderate or stalls at an early stage, leaving a large, westward tilted density depletion in the bottomside F-region [Tsunoda, 1981]. Although the large-scale growth stage of the bubble itself has ended, its edges can structure as a result of the gradient drift instability. At these local times, the zonal neutral wind is large ($\geqslant$ 150 m/s) and, eastward so that westward-directed plasma gradients are unstable. Therefore, the westward edge of an upwelling is most likely to develop intermediate-scale structure. This behavior is consistent with Figure IV.A.4, which is a simple model based upon our ΔTEC and scintillation data for Leg 1. The vertical extent of the bubble can only be guessed. There is no question, however, that the west wall is structured in regions where the plasma drift vector and the density gradients are parallel.
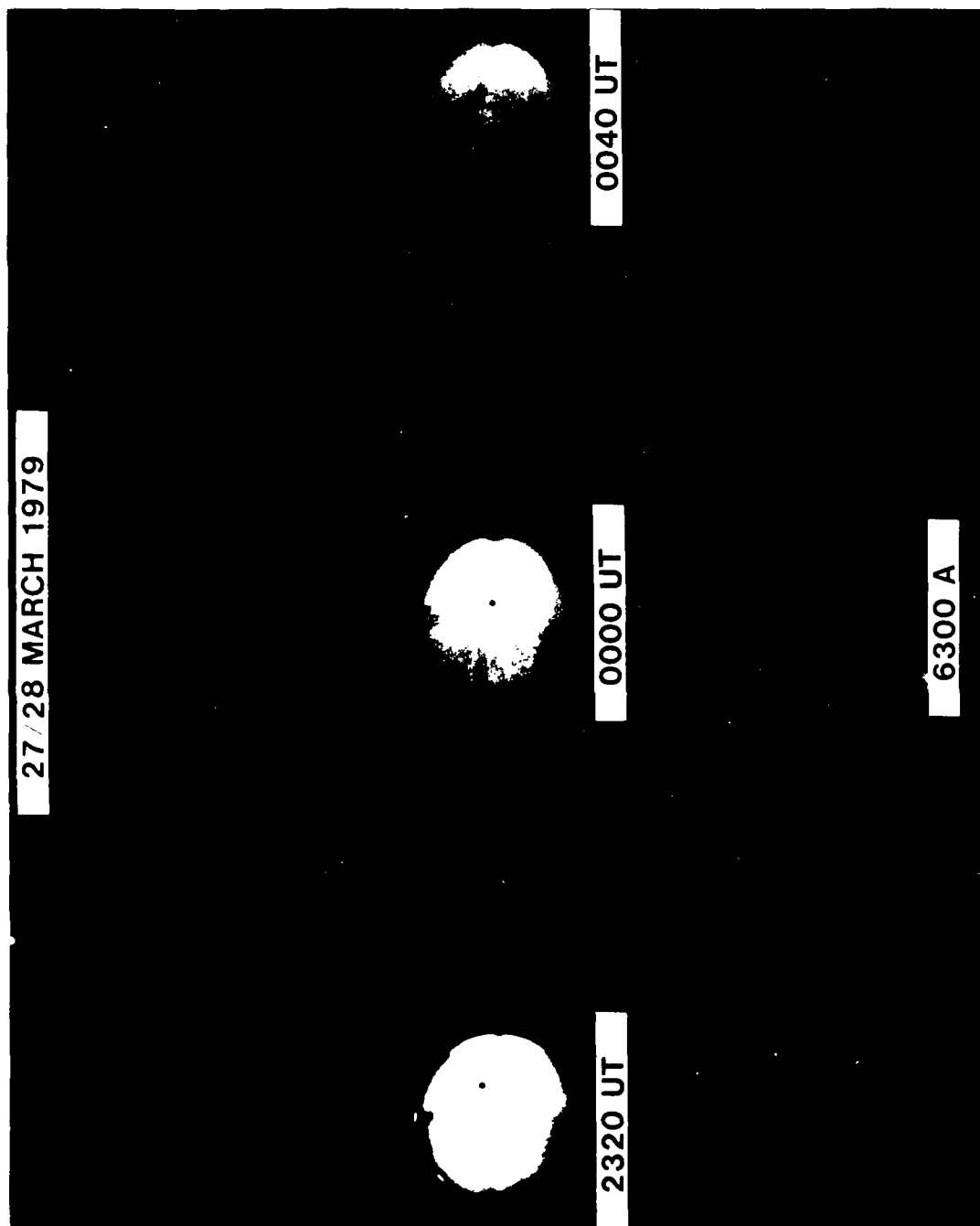
Figure IV.A.2. 6300-Å airglow images of the bubble, with the ionosphere penetration point indicated.

168
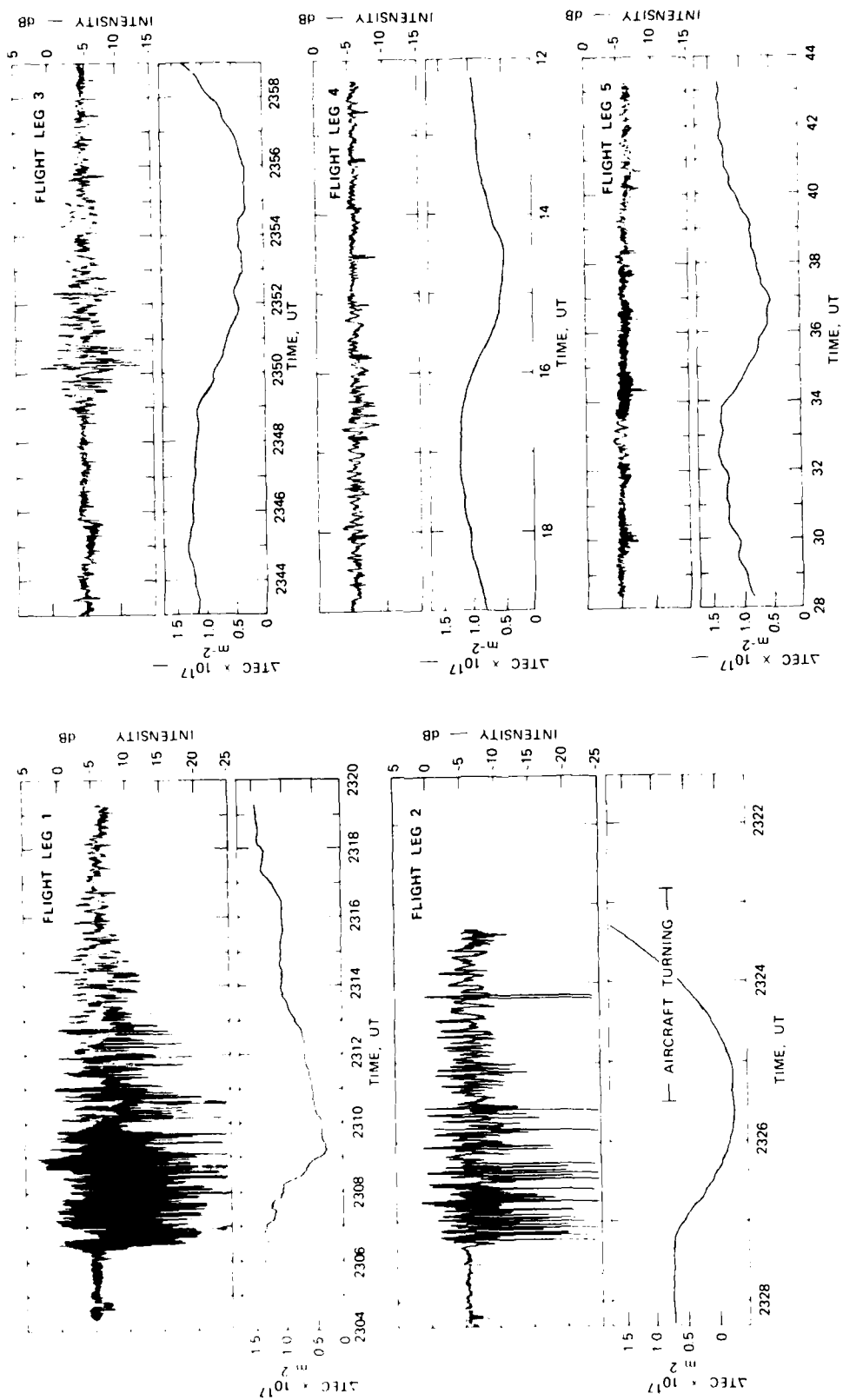
Figure IV.A.3. Intensity and phase records for scans through the bubble.

169
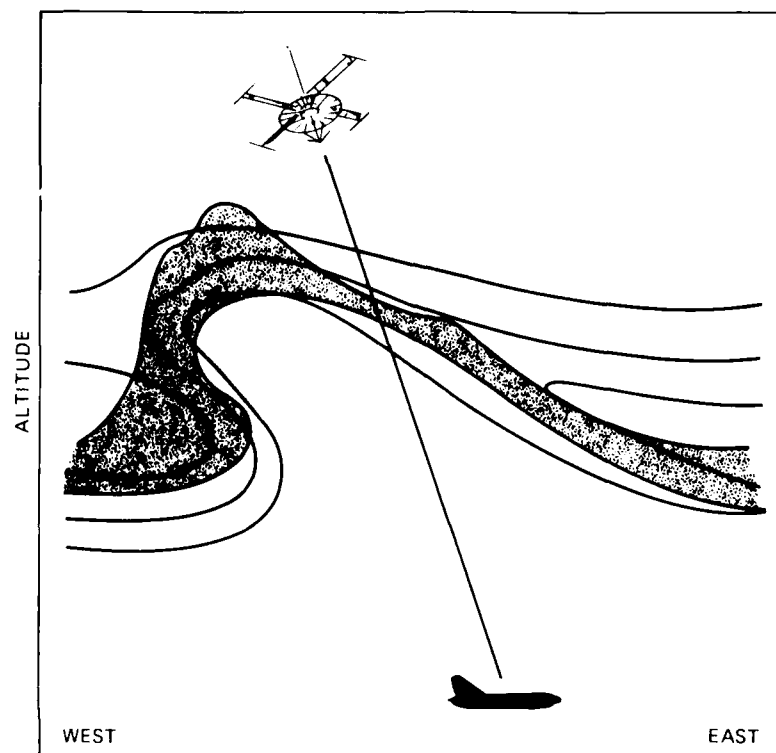
Figure IV.A.4.   One possible configuration of electron
                  density (contours) and irregularity
                  distribution (shaded) that duplicates
                  the observed signal structure.

In Figures IV.A.3(b) through IV.A.3(e), the intensity scintil-
lation and ΔTEC for subsequent cuts through the drifting bubble are shown.
For westward legs, the time scales have been reversed and expanded to
match those eastward, in both direction and distance.   The relative
eastward/westward time scales were ascertained by first locating, in space
(Figure IV.A.1), the westward intensity scintillation or depletion bound-
aries for consecutive legs.   This yields a cross-field, macroscale drift
of ~ 90 m/s throughout the observation period at a penetration altitude of
350 km.

By comparing flight legs in Figure IV.A.3, we see that the
intensity scintillation declines rapidly to a level indistinguishable from

the noise level by the fourth leg, but the ΔTEC pattern remains nearly constant in form. (On the second leg, the phase data is distorted before 2325 UT by rapid aircraft deviation from straight and level flight.)

4.   Phase Spectra and Irregularity Decay

The intensity records in Figure IV.A.3 effectively illustrate the east-west asymmetry in, and temporal decay of > 400-m spatial scale irregularities. The phase data and, in particular, the temporal changes in energy and the shape of the phase spectra from leg to leg, can be used to determine the decay rate quantitatively and provide information about possible decay mechanisms.

In Figure IV.A.5, the phase spectra of the overall bubble are shown for the three eastbound legs (Legs 1, 3, and 5). These have been offset from one another by 10 dB for clarity. By including the entire bubble in each spectrum, we can observe structure in spatial wav⸱⸱⸱⸱ ⸱s from the ~ 80-km outer scale down through about 400 m. For the east-bound flight, the bubble drifts with the aircraft, producing an effective scan rate of ~ 110 m/s. This establishes the correspondence between the temporal and irregularity cross-field spatial scales shown.

The spectrum for Leg 1 is in a familiar experimental form (although no theory has yet successfully predicted this power-law index). It is nearly power law with an average spectral index near -2.5; this slope and the spectral density levels agree well with those observed in morphological studies of irregularity spectra at the equator [e.g., Livingston et al., 1981]. Such a phase spectral index corresponds to a one-dimensional rocket or satellite spectrum with index of -1.5. We consider it, then, to be the signature of a region sampled during or shortly after Rayleigh-Taylor or gradient drift structuring or both, as already suggested. For Legs 3 and 5, however, sampled some 40 and 70 min after Leg 1, the spectra have considerably steepened through energy decay at short spatial scales. For purposes of discussion, we will use the break in the spectra, which this decay creates near 4 km, as the dividing line between two different regimes.
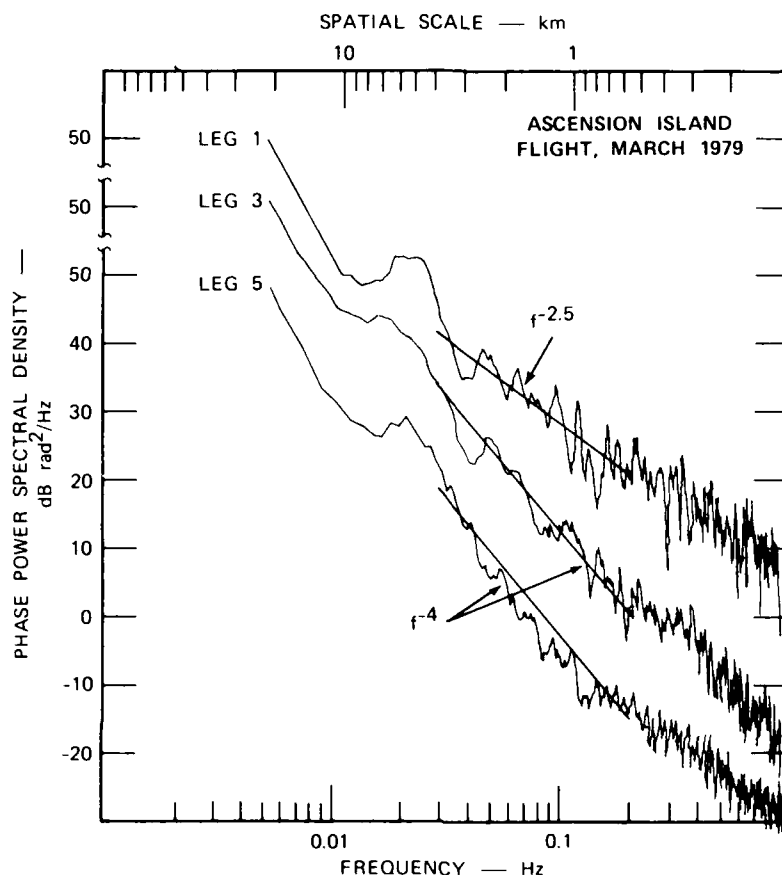
Figure IV.A.5.   Phase power spectra for the bubble.

At spatial scales larger than about 4 km, the spectra are nearly equal in shape and in energy content for all flight legs. The decay at the peak is only about 5 dB in 70 min. Because the scintillation technique is sensitive to $(\Delta N)^2$ rather than $(\Delta N/N)^2$, however, some of the decrease may be caused by lower absolute plasma density. A detailed interpretation of the spectral features in this large-scale regime, which is dominated by aeronomic processes [Booker, 1979], is beyond the scope of this paper. The broad enhancement in energy centered near 7 km, which is made conspicuous by the energy depletion near 15 km, may be a remnant of the larger-scale perturbation (e.g., a gravity wave), which initiated the bubble. We note that this feature is very similar to that seen in the in situ electron-density spectra presented by Kelley et al. [1982a].

172

Of more interest to the present study and in contrast to the stability of large-scale structure, energy at short scales decays rapidly during the observation period. For example, at an irregularity scale size near 1 km, the energy decays at an even rate of $\sim$ 9 dB per hour from Leg 1 to Leg 3 to Leg 5. Using the relationship

$$|\Delta N|^2 \ (k, \ t_o + \tau) = |\Delta N|^2 \ (k, \ t_o) \ \exp - \{2k^2 D\tau\} \quad , \quad (IV.A.1)$$

we find a diffusion coefficient for $k = (2\pi/1000 \text{ m})$ of 7 m^2/s. On the other hand, the classical ambipolar cross-field diffusion coefficient (which is equal to twice the electron perpendicular diffusion coefficient) is given by

$$D_{\perp c} = 2\rho_e^2 \upsilon_e \simeq 0.96 \ m^2/s \quad . \quad (IV.A.2)$$

The diffusion coefficient at the 1-km scale is thus considerably greater than the classical ambipolar rate.

As we discuss more fully below, an enhanced diffusion rate is not difficult to explain. What is more interesting is that a single diffusion coefficient (independent of k) cannot be used to describe the process. For example, by choosing $D = 7 \ m^2/s$, we can match the decay rate at 1 km, but that is the only scale at which the decay rate is matched by the classical formula given in Eq. (IV.A.1). This result is illustrated in Figure IV.A.6 where Eq. (IV.A.1) has been solved at a time, τ_o, corresponding to Leg 5 with an input spectrum $|\Delta N|^2 \ (k, \ t_o)$ matched to the Leg 1 data (the straight line in Figure IV.A.6 is the least squares fit to the data in Leg 1). The solution matches the observed spectrum at 1 km. However, the experimental decay rate is considerably higher at longer wavelengths and considerably slower at shorter scales.

The data in Figure IV.A.5 provide an opportunity to determine empirically the scale-size dependance of the diffusion rate, $D_{\perp}(k)$. Over the scale-size regime 400 m $< \lambda <$ 4 km, the spectra in Figure IV.A.5 are nearly power law with slopes of -2.5, -4, and -5, respectively. By equat-
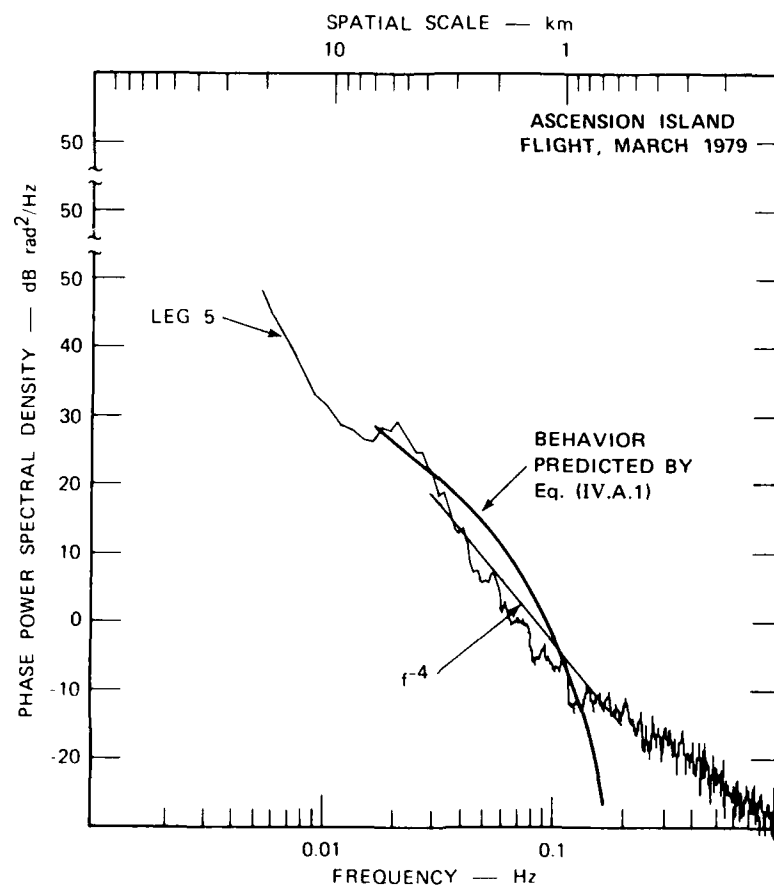
Figure IV.A.6.   Comparison of observations of
theoretical predictions based on
Eq. (IV.A.1).

ing the value of $|\Delta N|^2$ at 4 km for three such power-law spectra and dif-
ferencing the curves at all other scale sizes, we can solve Eq. (IV.A.1)
for $D_\perp(k)$. The result is plotted in Figure IV.A.7. The curve represents
the average between differencing Leg 5 and Leg 1 and Leg 3 and Leg 1. The
error bars indicate the differences in the two estimates. This empirical
$D_\perp(k)$, of course, depends on the model in the sense that Eq. (IV.A.3)
assumes that each Fourier mode decays independently of the adjacent modes.
As discussed below, it is unlikely that the classical mechanism or mechan-
isms that lead to anomalous decay characteristics share the property of

174
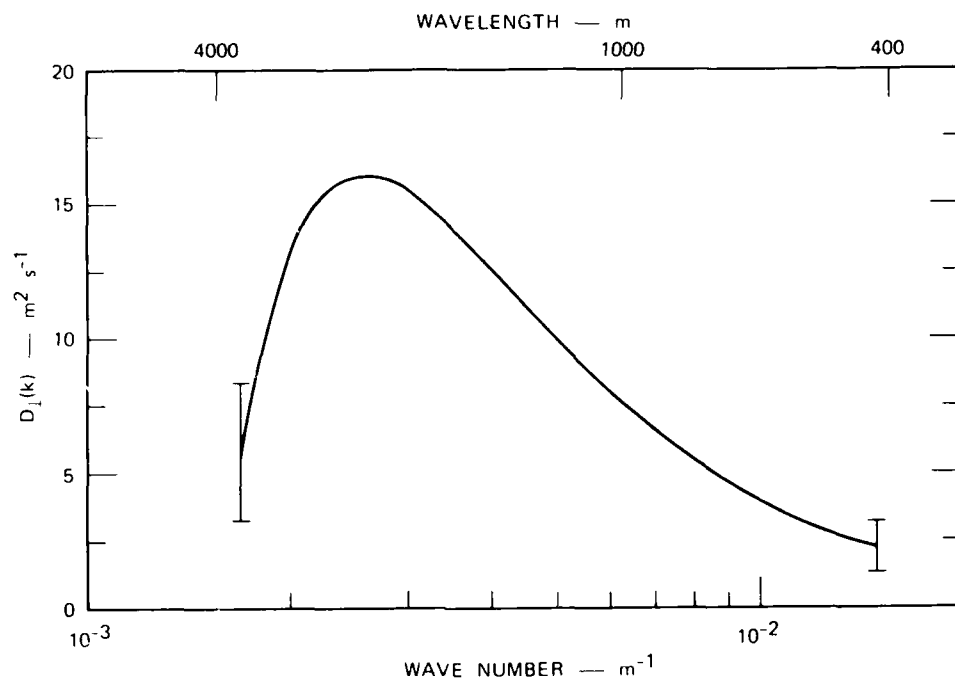
Figure IV.A.7.   Empirically derived diffusion coefficient.

mode independence. The $D_\perp(k)$ that we have found should thus be regarded as both empirical and model dependent.

5.   Discussion

a.   Enhanced Classical Diffusion.

A diffusion coefficient enhanced with respect to the ambi-bipolar rate can be understood as follows. The ambipolar rate occurs when the more rapid perpendicular ion diffusion leads to a space-charge electric field that severely limits the ion flow and slightly enhances the electron cross-field velocity component. An equilibrium results in which the two fluids diffuse at the same rate. Now if field-aligned currents can flow, for example, to a "conducting end plate" such as the E region in the auroral zone [Vickrey and Kelley, 1982], the ambipolar electric field can be "shorted out" and diffusion proceeds at the faster rate determined by

175

$$D_{\perp c} = \frac{\Sigma_i^F}{\Sigma_i^F + \Sigma_e^F + \Sigma_P^E}(D_{\perp e} - D_{\perp i}) + D_{\perp i} \quad , \qquad (IV.A.3)$$

where the Σ_P are the height-integrated Pedersen conductivities. The E region is of little importance in the nighttime equatorial zone. However, the conjugate F region has a comparable conductivity that, when substituted for Σ_P^E above, implies that $D_{\perp c} \simeq 0.5\ D_{\perp i}$. Taking $\nu_{in} = 0.6\ s^{-1}$ and $\rho_i = 5$ m corresponding to a height of 350 km yields $D_{\perp c} = 7\ m^2/s$. Thus, the enhanced diffusion rate is not as surprising as the observed wave-length dependence; i.e., the rate of diffusion could be explained classically, but the spectrum of decaying turbulence is another matter. In the next two sections, we investigate two mechanisms that produce diffusion whose rate depends on scale size.

b.   The Drift-Wave Hypothesis.

Costa and Kelley [1978a,b], Burke et al. [1979], Huba and Ossakow [1981], Kelley [1982], and perhaps others have suggested that drift waves play an important role in F-region diffusion. In linear theories these waves are destabilized by gradients in the plasma and, in their nonlinear state, act to smooth out the gradients that produce them. The result is anomalous diffusion of the driving structure.

Gary [1980] has analyzed anomalous diffusion caused by drift waves. The waves grow at wavelengths such that $k_\perp \rho_i \gtrsim 1$, which corresponds to wavelengths below about 40 m. Kelley et al. [1982b] and Kelley [1982] have compared the amplitude and spectral forms of both density and electric-field fluctuations in this wavelength regime predicted by Gary [1980] and by Bernhardt et al. [1982], and found excellent agreement with data obtained in the topside equatorial spread-F environment (i.e., altitudes > 280 km).

176

Gary's analytical form for the anomalous diffusion coefficient is

$$D_a = \frac{\pi}{9} \left(\frac{KT}{M}\right)^{3/2} \left(\frac{1}{\Omega i}\right)^2 \left(\frac{1}{n} \frac{dn}{dx}\right) \quad , \qquad \text{(IV.A.4)}$$

which can also be written

$$D_a = 1.29 \, D_{\perp i} \, (K\ell) \qquad \text{(IV.A.5)}$$

where ℓ is the ion mean free path parallel to the magnetic field, (V_{ith}/ν_{in}), and K corresponds to the gradient scale-length, $(1/n \, dn/dx)^{-1}$, wave number. For a sinusoidal driver with wavelength of 3 km, corresponding to the break in the spectrum and a mean free path of 450 m, $D_a = 1.2 \, D_{\perp\perp} \approx 17 \, m^2/s$.

This result is in reasonable agreement with the present data set in the sense that the enhanced decay at long wavelengths may be explained. Because the drift waves themselves occur only at very short wavelengths, however, we must hypothesize a link in k space for this mechanism to be valid. In fluid turbulence theory, such a linkage occurs in the inertial subrange where energy is passed between adjacent wave numbers leading to a cascade from large to small scales (Section III.C). The net effect is to maintain the energy level in the intermediate range, with dissipation occurring at short wavelengths.

These arguments must remain somewhat speculative because turbulence theory is not as well developed in plasma applications. The data are not inconsistent with these concepts, however, provided an analog of the inertial subrange exists in plasmas.

c.   The Image Formation Process.

An alternative mechanism that produces a scale size dependent loss of F-layer structure has been proposed by Vickrey et al. [1984], who have investigated the formation of image striations in the E

177

layer theoretically. Images result from the finite compressibility of the E-region ion gas. Because the electron gas is incompressible in both the E and F regions, however, the image formation process redistributes electrons along the magnetic field line such that $\nabla \cdot J \equiv 0$.

The model calculations of Vickrey et al. [1984], show that the saturated E-region image spectrum has a peak near 1 km scale size in agreement with near-equatorial rocket observations. Because the image irregularities grow at the expense of F-layer plasma, Vickrey et al. [1984], argued that the "effective" diffusion rate in the F layer would reflect, at least qualitatively, the scale-size dependence of the image formation process. The present observations support that argument. It should be kept in mind, however, that the observed spectrum is a balance between possibly scale-size dependent drivers and loss mechanisms. Nevertheless, the present observations support a "nondriven" situation in which the spectral evolution is determined purely by diffusion processes. A quantitative time-dependent cross-field diffusion model including magnetic field-line coupling effects is described in Section IV.C.

B.   The Effects of Diffusive Decay on Spectral Measurements

Diffusion is an important consideration in all phases of the development of irregularity structure. For most applications, the structure evolution is characterized by the convection equation

$$\frac{\partial N}{\partial t} + \frac{\hat{b} \times \nabla \phi}{B} \cdot \nabla N = K \nabla^2 N \qquad , \qquad \text{(IV.B.1)}$$

where N is the electron density, ϕ is the electrostatic potential, and K is a diffusion coefficient. Equation (IV.B.1) characterizes the structure evolution in the plane transverse to the magnetic field $B\hat{b}$.

If we define the mean square density fluctuation as

$$N^2 = \frac{1}{A} \sum_{\vec{\rho}} N^2 = \frac{1}{A} \sum_{\vec{k}} |\hat{N}(\vec{k})|^2 \quad , \qquad \text{(IV.B.2)}$$

178

where A is a normalization factor, it can be shown that

$$\frac{\overline{\partial N^2}}{\partial t} = 2K \overline{N \nabla^2 N} \quad . \qquad (IV.B.3)$$

Thus, in the absence of diffusion, $(K = 0)$ $\overline{N^2}$ is conserved. The nonlinear term in Eq. (IV.B.1) can only redistribute structure among the Fourier modes. It follows that diffusion and the instability drivers are the parameters that determine the perturbation strength and its spectral characteristics.

One means of measuring diffusion is to observe the decay of structure at a time when the driver is known or believed to be very small, e.g., in a decaying equatorial plume. In that case, Eq. (IV.B.1) becomes a simple diffusion equation

$$\frac{\partial N}{\partial t} = K \nabla^2 N \quad . \qquad (IV.B.4)$$

The conditions under which Eq. (IV.B.4) can be applied, however, necessarily involve long observation intervals. Thus, diffusion may well change the spectrum over the period that it is being measured. We have developed a model to evaluate this effect.

1.   Diffusion Model

A general solution to Eq. (IV.B.4) is

$$N(\vec{\rho}; t) = \sum \hat{N}(\vec{k}) \exp\{-Kk^2 t\} \exp\{-i\vec{k} \cdot \vec{\rho}\} \quad , \qquad (IV.B.5)$$

which can be easily verified by direct substitution. The one-dimensional temporal SDF derived from a moving probe, or a scintillation measurement if appropriate conversions are made, is

$$\varphi(w) = \left\langle \left| \frac{1}{T} \int_{t_o}^{t_o+T} N(\vec{v}t, t) \exp\{-iwt\} \, dt \right|^2 \right\rangle \quad , \qquad (IV.B.6)$$

where T is the length of the measurement interval and $\vec{v}$ is the scan velocity.

By substituting Eq. (IV.B.5) into Eq. (IV.B.6) it can be shown by direct computation that

$$\mathcal{D}(w) = \sum_{k} \Phi(\vec{k}) \, g_T(w - \vec{k} \cdot \vec{v}; \, K)\big|^2 \quad , \qquad \text{(IV.B.7)}$$

where

$$g_T(\alpha; K) = \frac{\exp\left\{-2Kk^2 t_o\right\}}{T^2} \; \frac{1 - \exp\left\{-2Kk^2 T\right\} - 2\cos(\alpha T)\exp\left\{-Kk^2 T\right\}}{\alpha^2 + K^2 k^4} . \text{(IV.B.8)}$$

If $K = 0$,

$$g_T(\alpha; \, o) = \frac{\sin^2 \alpha T}{(\alpha T)^2} \quad , \qquad \text{(IV.B.9)}$$

which is the usual form of the window function for an unweighted spectral estimate. As the diffusion effects become dominant (as they must for sufficiently large k), the weighting function rolls the spectrum exponentially.

2.   Numerical Computations

To illustrate the effects of diffusion on spectral estimates, we have evaluated Eq. (IV.B.7) for parameters that are typical of equatorial scintillation measurements--using a geosynchronous satellite as a signal source. Figure IV.B.1 shows the decay of $k^{-2.5}$ one-dimensional ($q^{-3.5}$ two-dimensional) SDF measured over a 10-min interval at $t_o = 0$, 2700, and 5400 s. The dominant effect is clearly the overall wavelength-dependent decay of the spectrum controlled by the leading term in Eq. (IV.B.8).

Figure IV.B.2 shows the same computation for $K = 5$ m^2/s. Here, the effects of diffusion are more pronounced and persist to scale sizes
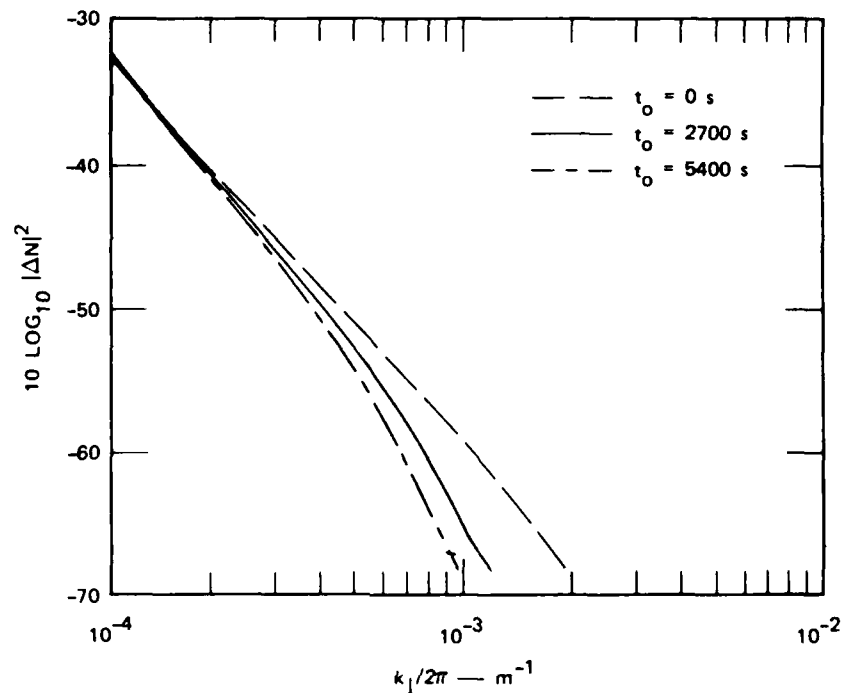
Figure IV.B.1.   Temporal decay of a one-dimensional irregularity spectrum for $K = 1$ m^2/s.

well above 1 km. The effects of diffusion within the measurement interval as manifested, for example, by the departure from simple power-law form for $t_o = 0$, are significant below ~ 1-km scale sizes.

As a general rule, therefore, diffusion effects within typical intervals used for spectral estimation ($T \leqslant 600$ s) can be ignored for scale sizes greater than 1 km.

C.   Electrical Coupling Effects on the Temporal Evolution of F-Layer Plasma Structure

In this section, we examine a time-dependent model of F-region structure decay by "classical" cross-field diffusion and electrical coupling along magnetic field lines to the E region. The temporal behavior of the

181
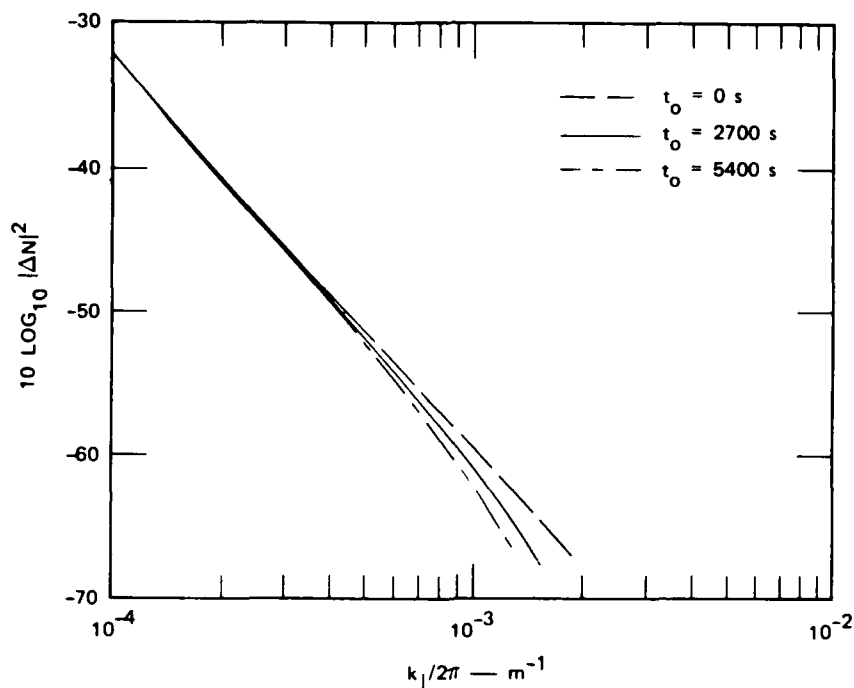
Figure IV.B.2. Temporal decay of a one-dimensional irregularity spectrum for $K = 5$ m^2/s.

ion concentration fluctuations is determined by the electric field in the coupled system as well as by the initial perturbation spectra and the E-region recombination rate. The formation of image structure in the E-region ion concentration affects the lifetime of F-layer structure in a scale-size dependent way. Once an image is formed, the image amplitude and the driving F-region structure amplitude decay at the same rate. At large scale sizes, $\lambda(\lambda = 2\ \pi/k)$, this rate is proportional to k^2 and the ratio of the temperatures in each region. At small-scale sizes, it depends on the E-region recombination rate and the temperatures of the two regions but only very weakly depends on k. The background E-region concentration determines the wave number beyond which the structure amplitude decay rate is almost independent of its scale size.

182

1. Introduction

Structure in the ion concentration and ambient electric field in the ionospheric F region exists at scale sizes ranging from global scales to centimeters. The sources of this structure vary with location. At the equator, for example, nighttime F-region structure results from instabilities that can dominate the plasma motion. At high latitudes, plasma instabilities are accompanied by structured particle precipitation, strong and highly structured magnetospheric convection electric fields and field-aligned currents, all of which can produce variations in ion concentration [Fejer and Kelley, 1980]. The ultimate spectrum of fluctuations in ion concentration that is observed experimentally is a balance between the strength and scale-size dependencies of the sources and sinks of structure. In this section, we concentrate on the scale-size dependence of one structure removal process—classical diffusion. Other processes (i.e., anomalous diffusion, nonlinear mode coupling, and the like) may produce additional scale size dependencies in the loss process that are not considered here. In our treatment, all scale sizes evolve independently.

We show that electrical coupling along magnetic field lines to the E layer can strongly affect the temporal evolution of a decaying F-region irregularity. The effects of E-region conductivity on the cross-field diffusion of plasma gradients in the F region has been studied by Vickrey and Kelley [1982]. They show that, for an insulating E region, F-region diffusion may only proceed at the electron rate, but that the diffusion rate increases with increases in E-region conductivity. In the presence of a perfectly conducting E region, F-region diffusion proceeds at the ion rate. Further work in this area has shown, however, that the presence of F-region irregularities can produce image irregularities in the E region by virtue of the polarization fields generated by the F-region structure. Vickrey et al. [1984] have shown evidence for the existence of such images in the equatorial ionosphere and have shown theoretically that their power spectrum has a peak near 1 km. The situation they modeled was driven, not purely decaying as will be treated here.

Nonetheless, because the E-region structure is driven at the expense of F region structure, they argued that the effective F-region diffusion rate (or loss rate) must also depend on scale size.

Here, we examine quantitatively the effects of E region image formation on the decay of F-region structure. We show that the loss rate for F-region structure depends on scale size and investigate the factors that determine the scale size at which maximum loss occurs. The effects of E- and F-region conductivities and E-region recombination are included.

In what follows, it is important to draw a distinction between an effective diffusion rate appropriate to a plasma structure and the plasma loss rate from that structure. An effective diffusion rate may be defined by assuming that the temporal evolution of a perturbation density, ΔN, at some scale size, k, can be expressed in the form

$$\Delta N(k, t + \Delta t) = \Delta N(k,t) \exp[-\Delta t\, D(k,t)] \quad . \quad \text{(IV.C.1)}$$

Here, $D(k,t)$ is the diffusion rate that in the classical case, [e.g., Vickrey and Kelley [1982] is proportional to k^2 and independent of t. Vickrey and Kelley [1982] have shown that if the effects of a conducting E region are considered, and if any structure is assumed to have a negligible effect on the local conductivity and its gradient, then the effective ion diffusion rate is given by

$$D(k,t) = \frac{\Sigma_o^E}{\Sigma_o^E + \Sigma_o^F}\, d_{i\perp}^F\, k^2 \quad \text{(IV.C.2)}$$

where $d_{i\perp}^F$ is the F-region ion-diffusion coefficient and Σ_o denotes the height-integrated background Pedersen conductivity in either the E or the F regions.

An alternative approach to the problem is to examine the plasma loss rate, or the time rate of change of the perturbation density $\partial/\partial t$ $[\Delta N(k,t)]$. Such an approach is more appropriate here because the effective diffusion rate is a function of k and t and thus loses its usefulness.

184

2.   Theoretical Background

The variation of plasma concentration, N, and velocity, V, as a function of time, t, in the ionosphere is determined by the continuity and momentum equations

$$\partial N/\partial t = P - L - \underline{\nabla} \cdot (N\underline{V}) \quad . \tag{IV.C.3}$$

$$d\underline{V}_i/dt = 1/N \; \underline{\nabla}(NbT_i) + e(\underline{E} + \underline{V}_i \times \underline{B}) - m_i \, \nu_{in} \, (\underline{V}_i - \underline{U}) \quad . \tag{IV.C.4}$$

$$\underline{\partial V}_e/\partial t = -1/N \; \underline{\nabla}(NbT_e) - e(\underline{E}+\underline{V}_e \times \underline{B}) - m_e\nu_{en}(\underline{V}_e-\underline{U}) - m_e\nu_{ei}(\underline{V}_e-\underline{V}_i) \tag{IV.C.5}$$

Here P and L denote the production and loss rates for the ion species, T is the temperature, and E is the electric field. The quantities b, e, ν, and B are Boltzman's constant, the electronic charge, the collision frequency for momentum transfer, and the earth's magnetic-field vector, respectively. Subscripts i, e, and n denote the particles, ion electron or neutral, to which the parameter refers. In Eq. (IV.C.4), we have neglected the effects of electron-ion collision on the ions, and if we further assume that the neutral gas velocity U is identically zero, then manipulation of Eq. (IV.C.4) yields an expression for the ion Pedersen drift velocity.

$$V_{ip} = \frac{e \, \nu_i}{m_i(\Omega_i^2 + \nu_i^2)} \, E - \frac{bT\nu_i}{Nm_i(\Omega_i^2 + \nu_i^2)} \, \nabla_p N \quad . \tag{IV.C.6}$$

Here ν_i refers only to ion-neutral collisions, the subscript P denotes the component in the direction of the electric field (i.e., the Pedersen direction), and Ω_i is the ion gyro-frequency.

Similar manipulation of Eq. (IV.C.5) yields an expression for the electron Pedersen drift:

$$V_{ep} = \frac{-e\nu_e}{m_e(\Omega_e^2 + \nu_e^2)} \, E - \frac{bT\nu_e}{Nm_e(\Omega_e^2 + \nu_e^2)} \, \nabla_p N + R \, V_{ip} \quad . \tag{IV.C.7}$$

185

Here, ν_e denotes the sum of the electron-neutral and electron-ion momentum transfer collision frequencies. The ion Pedersen drift is included because we cannot ignore electron-ion collisions on the electrons and the multiplicative factor, R, is given by

$$R = \frac{\Omega_e^2 \nu_{ie}/\nu_{in} + \nu_{ei}\nu_e}{\Omega_e^2 + \nu_e^2} \qquad . \qquad (IV.C.8)$$

Equations (IV.C.6) and (IV.C.7) are used to derive the Pedersen current [cf. Francis and Perkins, 1975].

$$J_P = [(1-R)\sigma_{ip} + \sigma_{ep}]E - e[(1-R)d_{i\perp} - d_{e\perp}]\nabla_p N \qquad (IV.C.9)$$

where

$$\sigma_{\ell p} = \frac{e^2 \nu_\ell N}{m_\ell (\Omega_\ell^2 + \nu_\ell^2)}$$

$$d_{\ell\perp} = \frac{bT_\ell \nu_\ell}{m_\ell (\Omega_\ell^2 + \nu_\ell^2)}$$

and the subscript ℓ denotes either ions or electrons. Keeping in mind the validity of our assumptions and using appropriate values for the parameters, Eq. (IV.C.9) can be used at all altitudes.

In our study of the effects of E-region conductivity and images on F-region structure, we adopt a simple plane geometry shown schematically in Figure IV.C.1. The E and F regions are considered as slabs connected by vertical, infinitely conducting magnetic field lines. In both the E and the F regions, the Hall current is assumed to be divergence free.

If additionally we assume that no current flows out of the top of the F region or out of the bottom of the E region, then current continuity at the E-F region boundary demands that

186
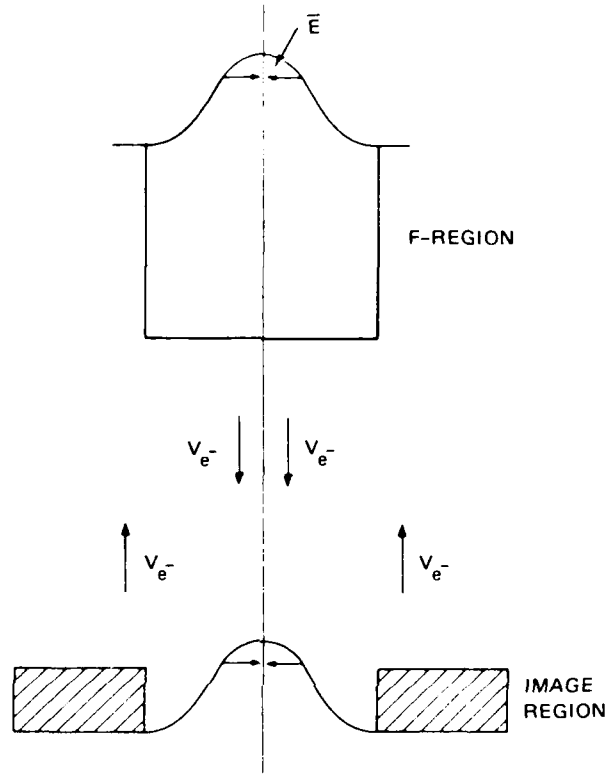
Figure IV.C.1.   Schematic illustration of
the plane geometry assumed
in the model.

$$\nabla_P J_P^E = - \nabla_P J_P^F \qquad (IV.C.10)$$

where J is the height-integrated current in the region, the subscript P
again refers to the Pedersen direction, and the superscripts E and F refer
to the E and F regions, respectively.

Equation (IV.C.10) represents the fundamental electrical coupling
relation by which E- and F-region structures and their associated electric
fields affect each other. In order to examine the effects of such struc-
ture, we follow the bulk flow of the plasma in response to an imposed
electric field. Because we treat only the linear problem, there is no

187

interaction between different scale sizes. Thus we may consider the total ion-concentration structure and the electric-field structure it creates (designated by asterisks) at each k as a simple wave form, such that

$$N^*(k) = N_o(1 + \Delta N^*(k)/N_o) \qquad (IV.C.11)$$

where

$$\Delta N^*(k) = \Delta N(k) \sin(kx + \theta_1) \qquad (IV.C.12)$$

and

$$E^*(k) = E(k) \sin(kx + \theta_2) \quad . \qquad (IV.C.13)$$

Here N_o is the background undisturbed ion concentration, the Pedersen direction is denoted by the coordinate x, and the scale size λ of the perturbation is given by $\lambda = 2\pi/k$. Then, using Eq. (IV.C.9) and assuming $\Delta N^*(k)/N_o$ is independent of altitude in both the E and F regions, we can show for each region that

$$J_p(k) = \Sigma_o[1 + \frac{\Delta N^*}{N_o}(k)] E^*(k) - eD_o \nabla_p \frac{\Delta N^*}{N_o}(k)] \qquad (IV.C.14)$$

where

$$\Sigma_o = \int_{bottom}^{top} [(1-R)\sigma_{ip} + \sigma_{ep}]dz$$

$$D_o = \int_{bottom}^{top} [(1-R)d_{i\perp} - d_{e\perp}]dz$$

The integrals extend over the altitude extent of each slab. In this work we have used the term "E region" rather loosely to denote the ionospheric layer between 100-km and 200-km altitude. We treat this region and the F

188
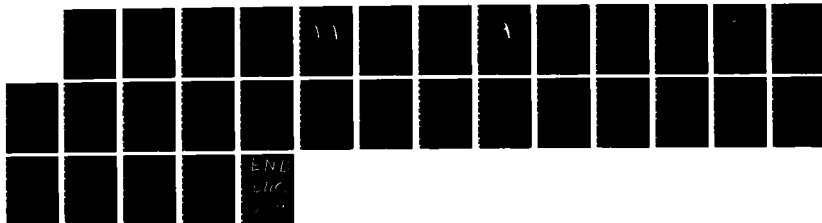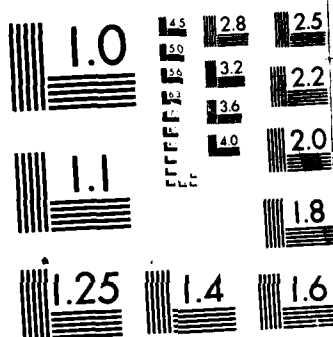
MICROCOPY RESOLUTION TEST CHART

NATIONAL BUREAU OF STANDARDS 1963-A

region above 200 km in a height-integrated fashion such that the quantity $\Delta N/N$ and the electric field are assumed to be uniform throughout them. This assumption may be reasonable in the F region, but in the E region the distribution of irregularities will depend upon the details of the electric field mapping. The limitations of our work in this regard will be dealt with in some detail later.

Equations (IV.C.10) and (IV.C.14) yield an expression for the electric field throughout the system that can be linearized to the form

$$[\Sigma_o^F + \Sigma_o^E] \; E(k) = -ek[D_o^F \; \frac{\Delta N^F}{N_o^F}(k) + D_o^E \; \frac{\Delta N^E}{N_o^E}(k)] \qquad \text{(IV.C.15)}$$

Here and henceforth, the subscript "o" refers to a property of the background ion and electron plasma. Having established the electrical coupling properties of the region, we now return to the local continuity Eq. (IV.C.3). In the F region, we neglect the chemical loss process because it affects N_o and ΔN equally and, therefore, will not affect $\Delta N/N_o$. Then, assuming all gradients are in the Pedersen direction, Eqs. (IV.C.3), (IV.C.6), and (IV.C.14) give

$$\frac{\partial}{\partial t} \left| \overline{\Delta N^F(k)} \right| = -k \; \frac{\Sigma_i^F}{e} \; E(k) - k^2 \; D_i^F \; \frac{\Delta N^F}{N_o^F}(k) \qquad . \qquad \text{(IV.C.16)}$$

In the E region, we assume that the background ion concentration N_o is maintained in equilibrium against chemical recombination with rate α. Then retaining first order terms in $\Delta N^E(k)$ we have

$$\frac{\partial}{\partial t} \left| \overline{\Delta N^E(k)} \right| = -\overline{2\alpha(N_o^E)^2} \; \frac{\Delta N^E}{N_o^E}(k) - k \; \frac{\Sigma_i^E}{e} \; E(k) - k^2 D_i^E \; \frac{\Delta N^E}{N_o^E}(k) \qquad . \qquad \text{(IV.C.17)}$$

In both equations, bar quantities represent height integrals over the appropriate region, and the subscript i denotes the height-integrated parameter applicable only to the ions. Substituting for the electric

189

field E(k) in Eqs. (IV.C.16) and (IV.C.17) from (IV.C.15) yields equations that can be solved for $\Delta N^F(k)$ and $\Delta N^E(k)$ as a function of time. Such a procedure allows us to investigate the evolution of E- and F-region irregularities from a given initial state assuming that there is no interaction between different scale sizes.

3. Results and Discussion

We have investigated the effects of E-region image formation on the decay of F-region structure by solving the height-integrated continuity equations in the E and F layer. In these equations, the loss processes for the irregularities are local cross-field ion diffusion and, in the E layer, chemical recombination. The ambipolar diffusion electric field that opposes ion diffusion, however, has now changed from the local value, $bT(\nabla N/N)/q$, to include the electrical coupling between the E and F regions. It should be pointed out that in these calculations we assume that the electric field maps unattenuated throughout the E region for all the scale sizes we consider. The early work of Farley [1959] and subsequent work by Goldman et al. [1976] have shown, however, that this is not the case, which affects the conclusions that may be drawn from this height-integrated slab model. If we examine the applicability of the various height-integrated parameters in different regions of the slab, we can see that, in addition to not properly accounting for the electric-field mapping process, we cannot properly consider the effects of chemical recombination for different scale sizes generated at different altitudes. In the upper E region, where the small-scale size image structure will form by electric-field mapping, the height-integrated recombination rate we have used is too large. But we have also considered the presence of this image structure at lower altitudes where it may not form. Thus to some extent the the inadequacies in our model may compensate. In order to examine the validity of our findings, we will also discuss the results obtained, assuming the E region lies only in the height range between 180 km and 200 km, where we can safely assume the electric field mapping is ideal.

Throughout this work, we must be careful not to attribute too much significance to the precise spectral forms of the irregularities in the E region but turn our attention to their effects on the temporal decay of F-region structure. Further discussion of this point will appear following the results. At this stage, we proceed in the belief that some insight into the effects of electrical coupling can be obtained from this simple approach even though it does not properly describe the evolution of the irregularity spectra. Ultimately, the height-integrated approximation will need to be removed to attach physical significance confidently to the calculated spectral shapes. Before illustrating the effects of this coupling in detail, it is worth pointing out some of its basic properties.

If the E-region conductivity is infinite, then the ambipolar electric field produced by an F-region structure is shorted out com-pletely, and the decay of F-layer structure depends only on the local ion diffusion constant $d_{i\perp}F$. The existence of E-region structure does not affect this situation. At the other extreme, if we assume that the E-region conductivity is zero, then E region structure cannot exist, and we can show that the coefficient of ΔN^F in Eq. (IV.C.16) depends only on the local electron diffusion coefficient $d_{e\perp}F$.

Figure IV.C.2 illustrates the temporal evolution of F-region structure in the presence of a conducting E region in which no images are formed. Here we have arbitrarily selected an initial F-region spectrum that has the form [Vickrey et al., 1984]

$$\left| \frac{\Delta N^F}{N_o^F} \right|^2 (k) = \frac{1}{1 + (k/k_c)^2} \ (m) \quad . \quad\quad (IV.C.18)$$

We have not investigated the F-region spectrum that would result from the evolution of structure in the presence of the coupling mechanism described here but have chosen a value for k_c of $3 \times 10^{-3} \ m^{-1}$ to best fit observa-tions. Panels A and B show the decay of this initial spectrum when the peak E-region ion concentration is $10^5 \ cm^{-3}$ and $10^4 \ cm^{-3}$, respectively.

191

WAVELENGTH — m

POWER SPECTRAL DENSITY $\left|\frac{\Delta N}{N}\right|^2$ — dB

$N_0^E = 1 \times 10^4 \text{ cm}^{-3}$; $\Sigma_0^E / \left(\Sigma_0^F + \Sigma_0^E\right) = 0.55$

$N_0^E = 1 \times 10^5 \text{ cm}^{-3}$; $\Sigma_0^E / \left(\Sigma_0^F + \Sigma_0^E\right) = 0.92$

WAVE NUMBER — m^{-1}
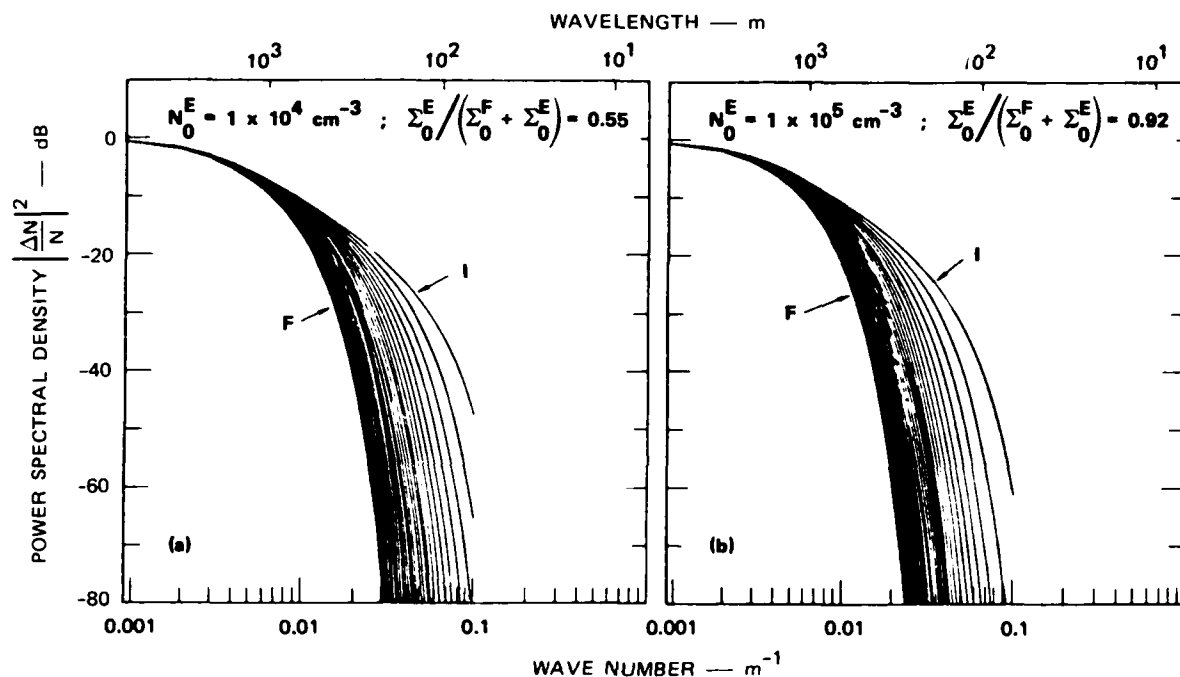
Figure IV.C.2. Temporal evolution of F-region structure from an initial arbitrary spectrum of irregularity amplitudes. The curve labeled I evolves after 5 min; that labeled F occurs after 3 hours. Intermediate states are shown every 5 min. Different evolutions depend only on the different effective E-region conductivity, shown in (a) and (b).

The curve labelled F shows the spectrum after a three-hour decay period; the intermediate spectra are shown every 5 min. The curve labelled I shows the state of the structure after 5 min. It should be pointed out that the evolution of the spectral shape is a function of the initial shape chosen; however, by dealing with a spectrum, we can contrast the behavior at different scale sizes. The initial spectral shape chosen is based on observed irregularity spectra, but in the physical situation that we are modelling all scale sizes evolve independently.

In both cases illustrated in Figure IV.C.2, the irregularities decay in the manner expected from our previous discussion. That is, $\Delta N^F / N_o^F$ decreases exponentially, but the diffusion coefficient in the

192

exponent is reduced from its local value by the ratio $\Sigma_o^E/(\Sigma_o^F + \Sigma_o^E)$. In Case A this ratio is very close to unity because the E region is an extremely good conductor. The F-region decay, therefore, occurs at close to its maximum rate. In Case B, however, the diffusion coefficient is reduced by approximately 50 percent and the associated reduction in the decay rate can be seen by comparing the initial temporal evolution and the final spectrum in the two cases. Figure IV.C.3 shows the rate of change of height-integrated density perturbation (i.e., $\partial/\partial t[\Delta N^F]$) for Case B as a function of time and wave number k. Several features of structure loss with a diffusion coefficient that is independent of time are evident. Most easily seen is the existence of a peak in the loss rate as a function of k and the movement of this peak to smaller values of k as time increases. It can be shown in fact that the maximum loss rate occurs at

$$k = (\tau D)^{1/2}$$

where D is the diffusion constant and τ is the time over which the structure has decayed.

Vickrey et al., [1984] have already pointed out that in order to affect the behavior shown in Figures IV.C.2 and IV.C.3 significantly, an E-region image structure must develop substantially against chemical recombination. In a highly conducting E-region, with its associated high ion concentration, the image amplitude is expected to be small. Figure IV.C.4 shows this to be the case. It illustrates the temporal evolution of F-region structure and its associated E-region image (in the same format and) under the same initial conditions as Figure IV.C.2 Here, we have used a recombination rate of α of $\sim 4 \times 10^{-7}$ cm^{-3} s^{-1}. Comparison of the F-region spectra in Figures IV.C.4 and IV.C.2 show that the E-region image, despite its small amplitude, significantly affects the F-region decay. This example also illustrates some fundamental features of the image structure and its temporal evolution.

The image formation process has been described in some detail by Vickrey et al. [1984]. The pressure gradient associated with F-region plasma structure causes plasma diffusion in a direction opposite to the

193

WAVELENGTH — m
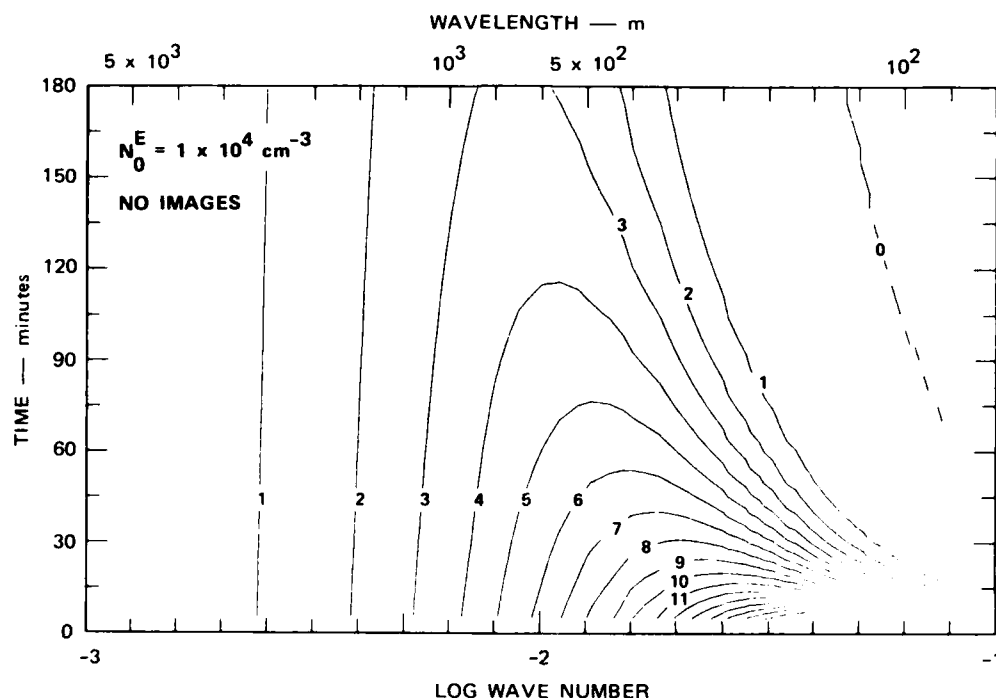
Figure IV.C.3. Loss rate of the F-region column content associated with the structure in Figure IV.C.2(a). Contours of constant loss rate in m^{-2} s^{-1} $\times$ 10^{10} are shown as a function of time and scale size.

gradient in electron number density. The resulting polarization electric field maps along the magnetic field to the E layer where the ion gas is relatively compressible. If at some altitude in the E layer, the ions are compressed together by this electric field at a rate γ_{comp} that is more rapid than they either diffuse away or recombine (at the rates γ_{diff} and γ_{chem}, respectively) then an "image" structure will form. These rates can be identified with the second, third, and first terms, respectively, in Eq. (IV.C.17).

The evolution of the E-region image structure shown in Figure IV.C.4 can be understood by considering the modelled situation. We begin with some perturbation density in the F region. This perturbation pro-

194

WAVELENGTH — m

POWER SPECTRAL DENSITY $\left|\frac{\Delta N}{N}\right|^2$ — dB

$N_0^E = 1 \times 10^5 \text{ cm}^{-3}$; $\Sigma_0^E / \left(\Sigma_0^F + \Sigma_0^E\right) = 0.92$

F-REGION

E-REGION

WAVE NUMBER — m^{-1}
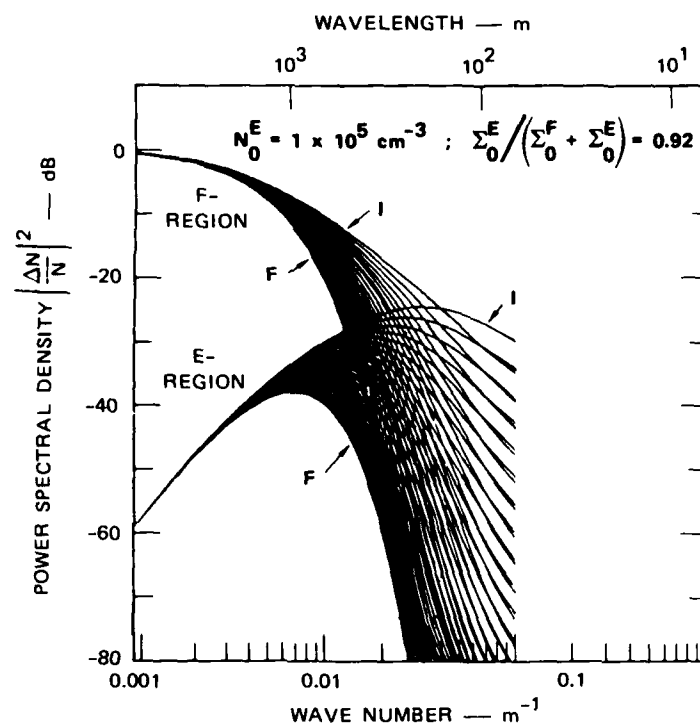
Figure IV.C.4.   Temporal evolution of F-region and E-region structures from an initial arbitrary spectrum of irregularities in the F region.   E-region structure is produced by the image formation process in a background concentration 10^5 cm^{-3}, and conditions are identical to those for Figure IV.C.2(b).

duces an image structure in the E region, and they both evolve: the E region growing, and the F region decaying until

$$\frac{\partial}{\partial t} \left(\overline{\Delta N^E} \right) = 0 \quad .$$

This condition is satisfied when

$$\frac{\Delta N^E(k)/N_o^E}{\Delta N^F(k)/N_o^F} = \frac{k^2 \Sigma_i^E D_o^F}{2\alpha(N_o^E)^2 \left(\Sigma_o^F + \Sigma_o^E\right) + k^2 \Sigma_o^F D_i^E} \quad . \qquad (IV.C.19)$$

195

From that point on, both spectra decay. Note that at large scale sizes (small k), the image amplitude is prevented from becoming very large by E-region recombination. This phenomenon was also seen in the evolution of barium clouds by Doles et al. [1976] and will tend to produce a peak naturally in any E-region image spectrum [Vickrey et al., 1984].

After 5 min, both E and F region spectra are seen to decay in Figure IV.C.4, implying that the E-region growth is very rapid and the structure reaches its maximum amplitude in less than 5 min. Because the E-region spectrum is produced entirely by the F region, both spectra can decay only if they do so in the quasi-equilibrium state given by Eq. (IV.C.19). Then Eqs. (IV.C.16) and (IV.C.19) show that

$$\frac{\partial}{\partial t}\left[\log\frac{\Delta N^F}{N_o^F}\,(k)\right] = \frac{\partial}{\partial t}\left[\log\frac{\Delta N^E}{N_o^E}\,(k)\right] = \frac{-2k^2 D_i^F \Sigma^E \,\overline{\alpha(N_o^E)^2}}{N_o^F[2\alpha(N_o^E)^2(\Sigma_o^F+\Sigma_o^E)+k^2\Sigma_o^F D_i^E]} \qquad . \quad (IV.C.20)$$

Examination of Eq. (IV.C.20) shows that the relative importance of the two terms in the denominator of the right-hand side will determine how the irregularity amplitude will decay. For the conditions applicable in Figure IV.C.4, these two terms are equal when k = 0.05 so that for large-scale sizes (λ > 125 m) the irregularity amplitude will decay so that

$$\frac{\partial}{\partial t}\left[\log\frac{\Delta N}{N_o^F}\,^F(k)\right] \approx -\frac{k^2 D_i^F \Sigma_o^E}{N_o^F(\Sigma_o^E + \Sigma_o^F)} \qquad . \qquad (IV.C.21)$$

At small scale sizes (λ < 125 m), the irregularity spectral shapes will be preserved as they decay since

$$\frac{\partial}{\partial t}\left[\log\frac{\Delta N^F}{N_o^F}\,(k)\right] \approx -\frac{\overline{2\alpha(N_o^E)^2}}{N_o^F}\,\frac{D_i^F \Sigma_o^E}{\Sigma_o^F D_i^E} \qquad . \qquad (IV.C.22)$$

As has been pointed out by Vickrey and Kelley [1982], the amplitude of an image structure depends strongly on the E-region recombination rate or,

196

identically, the E-region background ion concentration. This can be seen from Eq. (IV.C.19) and by contrasting Figures IV.C.5 and IV.C.4. In these figures, which correspond to maximum E-region concentrations of 10^4 cm^{-3} and 10^5 cm^{-3}, respectively, the peak amplitudes of the image irregularities differ by about 20 dB. The temporal behavior of the image spectrum in Figure IV.C.5 appears markedly different from that of Figure IV.C.4 but the differences simply reflect the characteristics of Eqs. (IV.C.21) and (IV.C.22). As the effective recombination rate $\alpha(N_o^E)^2$ decreases, the k value beyond which the spectral shape is preserved moves to smaller k (longer wavelengths) leading to a preserved spectral shape over much of the scale-size range contained in the figure. In this case the transition between the behavior described by Eqs. (IV.C.21) and (IV.C.22) takes place about $\lambda \approx 1.25$ km.

These effects can be emphasized by allowing the E-region recombination rate to become zero. In this case, the E-region irregularity will continue to grow until

$$\frac{\Delta N^E(k)/N_o^E}{\Delta N^F(k)/N_o^F} = \frac{T^F}{T^E} \qquad \qquad \text{IV.C(23)}$$

where we have assumed that the ion and electron temperatures are equal at all heights within a region. This condition was also derived by Vickrey and Kelley [1982] by determining the E-region gradient necessary to produce an electric field equal to the ambipolar diffusion electric field that F-region ions would experience if the E layer were nonconducting. Once the condition in Eq. (IV.C.23) is reached, the E- and F-region spectra will not decay. This behavior is seen in Figure IV.C.6. It should be noted that at large scale sizes (small k) the time required to reach the equilibrium condition in Eq. (IV.C.23) is much longer than the 3-hour period we have studied, and so the E-region spectrum is continually growing in this figure. The image formation process that we have described assumes that the electric field and Pedersen current are distributed throughout the E-region slab. If we were to assume that in fact the image forms in only a very limited altitude range near the top of the E

197

WAVELENGTH — m

POWER SPECTRAL DENSITY $\left|\frac{\Delta N}{N}\right|^2$ — dB

$N_0^E = 1 \times 10^4$ cm^{-3} ; $\Sigma_0^E / \left(\Sigma_0^F + \Sigma_0^E\right) = 0.55$

WAVE NUMBER — m^{-1}
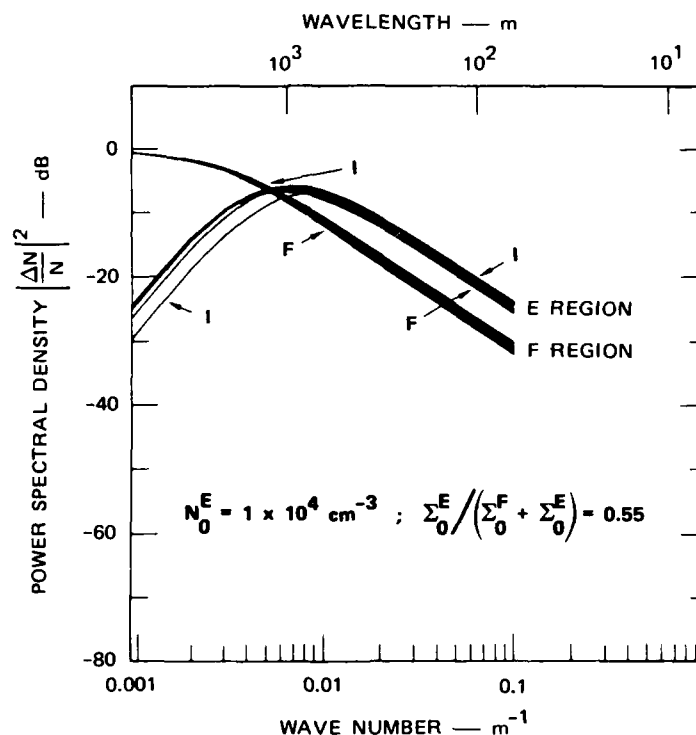
Figure IV.C.5.   Temporal evolution of F-region and E-region structures from an arbitrary spectrum of F-region irregularities. E-region structure is produced by the image formation process in a background concentration of 10^4 cm^{-3}. Conditions are identical to those in Figure IV.C.4(a).

region, then Eqs. (IV.C.19) and (IV.C.20) indicate that no qualitative change in our findings would result. We in fact performed calculations assuming that the E region (image region) lies only between 180 and 200 km with the same qualitative behavior as that described but with an image amplitude some 20 dB larger than previously calculated. This behavior can be expected by considering the effect in Eq. (IV.C.19) of considerably reducing the magnitude of the E-region terms. Finally, we note that the E-region image spectrum that we are examining depends strongly on the F-region driving spectrum and its evolution. Nevertheless it can be shown

WAVELENGTH — m
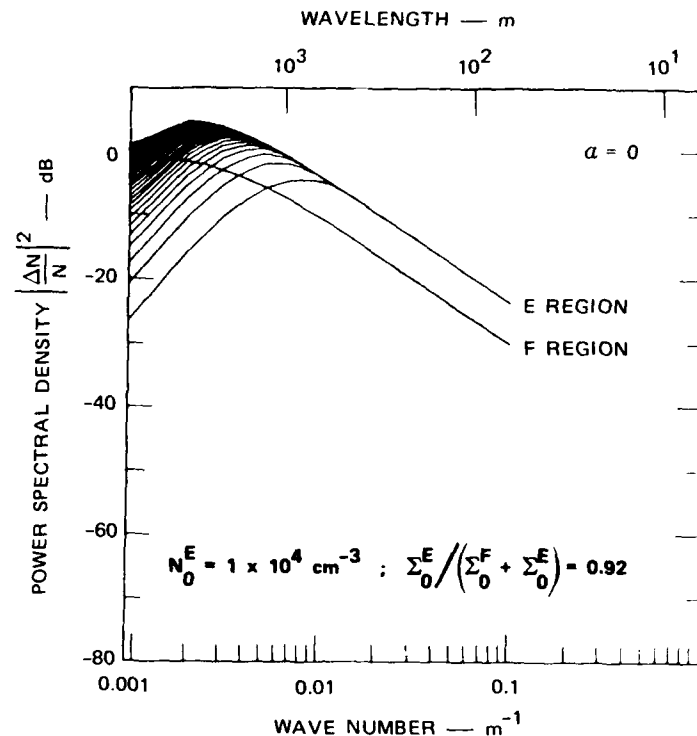
Figure IV.C.6.   Same as Figure IV.C.5 except that
the E-region recombination rate is
reduced to zero.

that a maximum in the E-region spectrum must occur for all reasonable
(i.e., monotonically decreasing) F-region spectral shapes, and that it can
only occur at a place where the F-region spectral slope is less than k^{-2}.
This would typically occur at scale sizes between 1 and 5 km.

The effects of image formation on the rate at which an F-region
perturbation density is lost can be seen in Figure IV.C.7. Contours of
constant perturbation loss rate are shown as a function of k and t for the
same ionospheric conditions that apply to Figure IV.C.5. This figure
should be compared with Figure IV.C.3, which is appropriate for the same
conditions but assumes that the image structure does not form. As is

199

WAVELENGTH — m
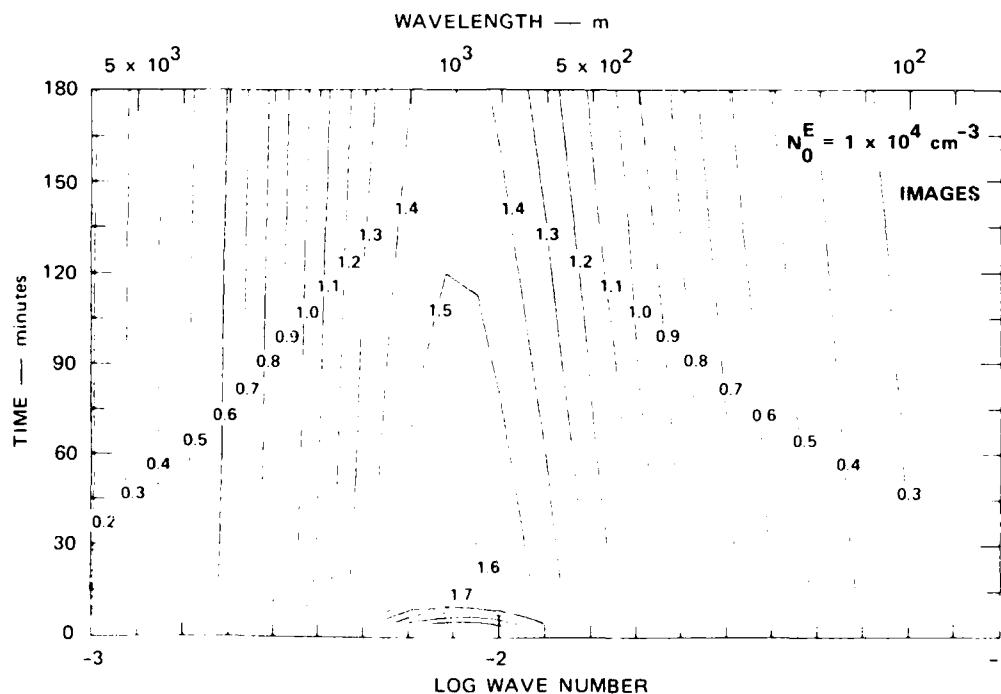
Figure IV.C.7.   Loss rate of the F-region column content associated with the structure in Figure IV.C.5.   Contours of constant loss rate in m^{-2} s^{-1} $\times$ 10^{10} are shown as a function of time and scale size.   Note a peak in the loss rate at a scale size that remains relatively constant in time.

evident from the image spectrum, the maximum F-region perturbation loss occurs where the maximum E-region growth appears, and for the conditions chosen here, that scale size remains relatively constant with time.   A comparison of the absolute loss rates in Figures IV.C.3 and IV.C.7 can be deceiving because in addition to the coupling effects themselves the loss rate also depends on the magnitude of the perturbation density.   In fact, an examiniation of Figures IV.C.2 and IV.C.4 shows that the image forma- tion process tends to preserve structure in the F region at all scale sizes, although the scale size at which preservation becomes significant depends upon the background E-region number density.

200

WAVELENGTH — m
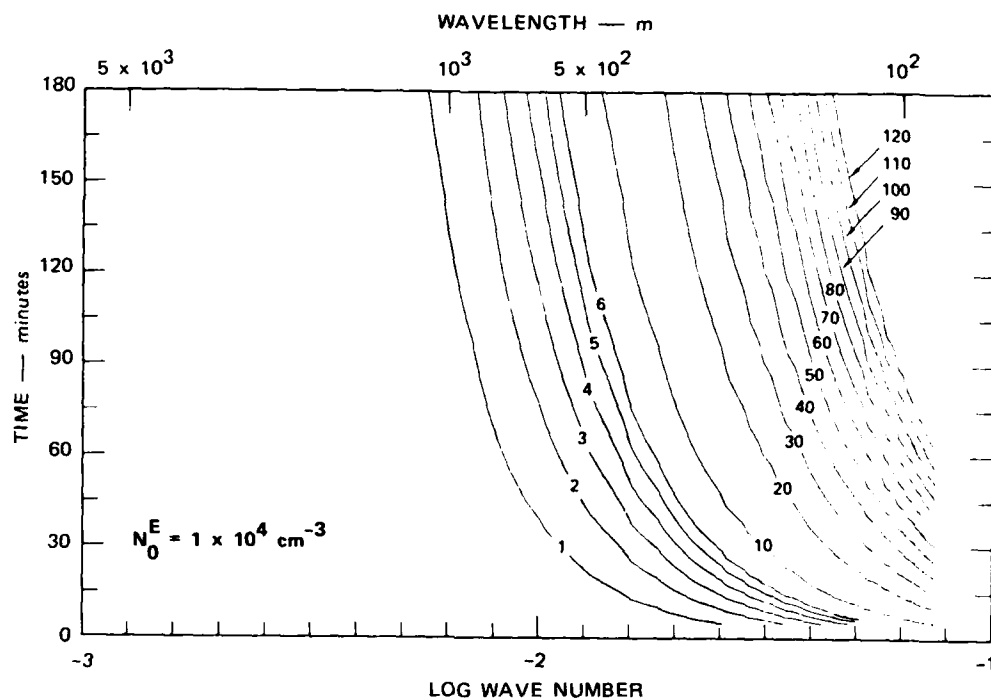
Figure IV.C.8. Temporal evolution of the ratio of F-region structure amplitude when the image-formation process is neglected to that when it is included. Contours of constant amplitude ratio are shown as a function of time and scale size. Structure is preserved at all scale sizes, although little effect is seen at very large scale sizes. Conditions are appropriate to Figure IV.C.2(a) and Figure IV.C.5.

Figure IV.C.8 shows contours of the ratio of F-region spectral amplitudes that result from our calculations when decay is allowed to proceed with and without the formation of E-region images. Little change in the temporal evolution is seen for large scale sizes, and indeed the loss rate in Eq. (IV.C.21) is identical to that obtained for the case of no image formation. At smaller scale sizes, the decaying spectral amplitude may be many tens of decibels higher than we would expect if the image formation process is neglected.

201

4. Conclusions

We have presented a model of the temporal evolution of a decaying spectrum of F-region irregularities that includes electrical coupling along magnetic field lines to a compressible E-region plasma and considers only a "classical" cross field diffusion process. The existence of F-region structure induces irregularities in an initially uniform E layer in a scale-size selective way. Because E-region images form at the expense of F layer plasma, the k dependence of the F-region structure loss rate is strongly influenced by coupling to the E layer. The density gradients associated with image structure affect the driving electrostatic field and parallel current that couple the two layers. The net result is that images prolong the lifetime of F-layer structure in a scale size dependent manner.

We have also shown that the amplitude of the E-region image irregularities are related to the driving F-region irregularity in a manner that allows the image-spectral amplitude to be a constant multiple of the F-region spectral amplitude for all wave numbers beyond a particular value. This condition may be routinely achieved where the E-region density is low (i.e., in the winter polar cap, in equatorial spread F or in barium clouds). In this condition, the E- and F-layer spectra decay with a common spectral shape at a rate determined by E-region chemistry.

SECTION V

LIST OF REFERENCES

Aggson, T., and J. P. Heppner, "Observations of Large Transient Magneto-spheric Electric Fields," J. Geophys. Res., 82, 5155 (1977).

Amayenc, P., and G. Vasseur, "Neutral Winds Deduced from Incoherent Scatter Observations and their Theoretical Interpretation," J. Atmos. Terr. Phys., 34, 351 (1972).

Banks, P. M., and G. Kockarts, Aeronomy., Part A, Academic Press, New York, NY (1973).

Banks, P. M., C. L. Rino, and V. B. Wickwar, "Incoherent Scatter Radar Observations of Westward Electric Fields and Plasma densities in the Auroral Ionosphere, 1." J. Geophys. Res., 79, 25 (1974).

Banks, P. M., R. W. Schunk, and W. J. Raitt, "NO^+ and O^+ in the High Latitude F Region," Geophys. Res. Letts., 1, 239 (1974).

Baron, M. J., C. J. Heinselman, and J. Petriceks, "Solar Cycle and Seasonal Variations of the Ionosphere Observed with the Chatanika Incoherent-Scatter Radar," Radio Sci., 18, 895-900 (1983).

Basu, S., S. Basu, J. P. McClure, W. B. Hanson, and H. E. Whitney, "High Resolution Topside in-situ Data of Electron Densities and VHF/GHz Scintillations in the Equatorial Region," J. Geophys. Res., 88, 403 (1983).

Basu, S., S. Basu, E. MacKenzie, W. R. Coley, W. B. Hanson, and C. S. Lin, "F-Region Electron Spectra near Auroral Acceleration and Shear Regions," J. Geophys. Res., 89, 5554 (1984).

Batchelor, G. K., "Small-Scale Variation of Convected Quantities Like Temperature in Turbulent Fluid," J. Fluid Mech., 113, 8 (1959).

Bates, H.F., "Computed Bounds on the F-Region Zonal Wind During Joule Heating," J. Atmos. Terr. Phys., 40, 1123 (1978).

Bates, H. F., and T. D. Roberts, "The Southward Midnight Surge in F-Layer Wind Observed with the Chatanika Incohererc Scatter Radar," J. Atmos. Terr. Phys., 39, 87 (1977a).

Bates, H. F., and T. D. Roberts, "A Technique for Using Incoherent Scatter to Estimate F-Region Zonal Winds During Joule Heating," J. Atmos. Terr. Phys., 39, 1293 (1977b).

Bernhardt, P. A., M. B. Pongratz, S. Peter Gary, and M. F. Thomsen,
"Dissipation of Ionospheric Irregularities by Wave-Particle
and Collisional Interactions," J. Geophys. Res., 87, 2356 (1982).

Booker, H. G., "The Role of Acoustic Gravity Waves in the Generation of
Spread-F and Ionospheric Scintillations," J. Atmos. Terr. Phys.,
41, 501, (1979).

Burke, W. J., D. E. Donatelli, R. C. Sagalyn, and M. C. Kelley, "Low
Density Regions Observed at High Altitudes and their Connection with
Equatorial Spread F," Planet. Space Sci., 27, 593 (1979).

Cauffman, D. P., and D. A. Gurnett, "Satellite Measurements of High
Latitude Convection Electric Fields," Space Sci. Rev., 13, 369
(1972).

Costa, E., and M. C. Kelley, "On the Role of Steepened Structures and
Drift Waves in Equatorial Spread F," J. Geophys. Res., 83, 4359
(1978a).

Costa, E., and M. C. Kelley, "Linear Theory for the Collisionless Drift
Wave Instability with Wavelengths near the ion Gyroradius,"
J. Geophys. Res., 83, 4365 (1978b).

de la Beaujardiere, O., and R. A. Heelis, "Velocity Spike at the Poleward
Edge of the Auroral Zone," J. Geophys. Res., 89, 1627 (1984).

de la Beaujardiere, O., R. R. Vondrak and M. J. Baron, "Radar Observations
of Electric Fields and Currents Associated with Auroral Arcs,"
J. Geophys. Res., 82, 5051 (1977).

de la Beaujardiere, O., J. D. Craven, G. Caudel, J. Holt, L. A. Frank,
V. B. Wickwar, L. Brace, D. Evans, J. D. Winningham, "Universal
Time Dependence of Nighttime F-Region Densities at High Latitudes,"
J. Geophys. Res., 90, 4319 (1985).

Doles, J. H., N. J. Zubusky, and F. W. Perkins, "Deformation and
Striation of Plasma Clouds in the Ionosphere, 3, Numerical Solutions
of a Multilevel Model with Recombination Chemistry," J. Geophys.
Res., 81, 5987 (1976).

Eather, R. H., "Latitudinal Distribution of Auroral and Airglow Emissions:
The ʹSoftʹ Auroral Zone," J. Geophys. Res., 74, 153 (1969).

Evans, J. V., "Observations of F Region Vertical Velocities at Millstone
Hill, 1, Evidence for Drifts Due to Expansion, Contraction and
Winds," Radio Sci., 6, 609 (1971).

Farley, D. T., "A Theory of Electrostatic Fields in a Horizontally Stratified Ionosphere Subject to a Vertical Magnetic Field," J. Geophys. Res., 64, 1225 (1959).

Fedder, J. A., and P. M. Banks, "Convection Electric Fields and Polar Thermospheric Winds," J. Geophys. Res., 77, 2328 (1972).

Fejer, B. G., and M. C. Kelley, "Ionospheric Irregularities," Revs. Geophys. Space Phys., 18, 401 (1980).

Folkestad. K., T. Hagfors, and S. Westerlund, "EISCAT: An Updated Description of Technical Characteristics and Operational Capabilities," Radio Sci., 18, 867 (1983).

Foster, J. C., "Ionospheric Signatures of Magnetospheric Convection," J. Geophys. Res., 89, 855 (1984).

Francis, S. H., and F. W. Perkins, "Determination of Striation Scale Sizes for Plasma Clouds in the Ionosphere," J. Geophys. Res., 80., 3111 (1975).

Franke, S. J., and C. H. Liu, "Observations and Modeling of Multi-Frequency VHF and GHz Scintillations in the Equatorial Region," J. Geophys. Res., 88, 7075 (1983).

Fremouw, E. J., C. L. Rino, R. C. Livingston, and M. D. Cousins, "A Persistent Subauroral Scintillation Enhancement Observed in Alaska," Geophys. Res. Letts., 4, 539 (1977).

Fremouw, E. J., C. L. Rino, J. F. Vickrey, D. A. Hardy, R. E. Huffman, F. J. Rich, C.-I. Meng, K. A. Potocki, T. A. Potemra, W. B. Hanson, R. A. Heelis, and L. A. Wittwer, "The HILAT Program," EOS, 64, 163 (1983).

Fyfe, D., D. Montgomery, and G. Joyce, "Dissipative, Forced Turbulence in Two-Dimensional Magnetohydrodynamics," J. Plasma Phys., 17, Pt. 3, 369 (1977).

Gary, S. P., "Waveparticle Transport from Electrostatic Instabilities," Phys. Fluids., 23, 1193 (1980).

Goldman, S. R., L. Baker, S. L. Ossakow, and A. J. Scannapieco, "Striation Formation Associated with Barium Clouds in an Inhomogeneous Ionosphere," J. Geophys. Res., 81, 5097 (1976).

Gurnett, D. A., "Injun 5 Observations of Magnetospheric Electric Fields, and Plasma Convection," in Earth's Magnetospheric Processes, B. M. McCormac, ed., D. Reidel Pub. Co., Dordrecht-Holland, p. 233 (1972).

Gurnett, D. A., and S.-I. Akasofu, "Electric and Magnetic Field Observations During a Substorm on February 24, 1970," J. Geophys. Res., 79, 3197 (1974).

Haerendel, G., R. Lust, and E. Rieger, "Motion of Artificial Ion Clouds in the Upper Atmosphere," Planet. Space Sci., 15, 1 (1967).

Haerendel,G., R. Lust, E. Reiger, and H. Volk, "Highly Irregular Artificial Plasma Clouds in the Auroral Zone," in Atmosheric Emissions, B. M. McCormac and A. Omholt, eds., p. 293, Van Nostrand Reinhold, NY (1969).

Haggstrom, I., J. Murdin, and D. Rees, "Determination of the Thermospheric Neutral Wind from Incoherent Scatter Radar Measurements," Preprint 1984.

Hayes, P. B., J. W. Meriwether, and R. G. Roble, "Nighttime Thermospheric Winds at High Latitudes," J. Geophys. Res., 84, 1905 (1979).

Hedin, A. E., J. E. Salah, J. V. Evans, C. A. Reber, G. P. Newton, N. W. Spencer, D. C. Kayser, D. Alcayde, P. Bauer, L. Cogger, and J. P. McClure, "A Global Thermospheric Model Based on Mass Spectrometer and Incoherent Scatter Data. MSIS 1. N2 Density and Temperature," J. Geophys. Res., 82, 2139 (1977).

Heelis, R. A., J. K. Lowell, and R. W. Spiro, "A Model of the High-Latitude Ionospheric Convection Pattern," J. Geophys. Res., 87, 6339 (1982).

Heppner, J. P., "Empirical Models of High Latitude Electric Fields," J. Geophys. Res., 82, 1115 (1977).

Heppner, J. P., "The Harang Discontinuity in the Auroral Belt and Ionospheric Currents," Geofys. Publ., 29, 105 (1972).

Heppner, J. P., J. D. Stolarik, and E. M .Wescott, "Electric Field Measurements and the Identification of Currents Causing Magnetic Disturbances in the Polar Cap," J. Geophys. Res., 76, 6028 (1971).

Huba, J. D. and S. L. Ossakow, "Diffusion of Small-Scale Density Irregularities During Equatorial Spread F," J. Geophys. Res., 86, 9107 (1981).

Huba, J. D., S.L. Ossakow, P. Satyanarayana, and P. N. Guzdar, "Linear Theory of the E x B Instability with an Inhomogeneous Electric Field," J. Geophys. Res., 88, 425 (1983).

Iijama, T., and T. A. Potemra, "Large-Scale Characteristics of Field-Aligned Currents Associated with Substorms," J. Geophys. Res., 83, 599 (1978).

Kelley, M. C., "Nonlinear Saturation Spectra of Electric Fields and Density Fluctuations in Drift Wave Turbulence," Phys. Fluids., 25, 1002 (1982).

Kelley, M. C., and E. Ott, "Two-Dimensional Turbulence in Equatorial Spread F," J. Geophys. Res., 83, 4369 (1978).

Kelley, M. C., R. Pfaff, K. D. Baker, J. C. Ulwick, R. Livingston, C. Rino, and R. Tsunoda, "Simultaneous Rocket Probe and Radar Measurements of Equatorial Spread F--Transitional and Short Wavelength Results," J. Geophys. Res., 87, 1575 (1982a).

Kelley, M. C., R. C. Livingston, C. L. Rino, and R. T. Tsunoda, "The Vertical Wave Number Spectrum of Topside Equatorial Spread F: Estimates of Backscatter Levels and Implications for a Unified Theory," J. Geophys. Res., 87, 5217 (1982b).

Kelley, M. C., J. F. Vickrey, C. W. Carlson, and R. Torbert, "On The Origin and Spatial Extent of High-Latitude F-Region Irregularities," J. Geophys. Res., 87, 4469 (1982).

Kelly, J. D., "Sondrestrom Radar--Initial Results," Geophys. Res. Letts., 10, 1112 (1983).

Kelly, J. D., and V. B. Wickwar, "Radar Measurements of High Latitude Ion Composition Between 140 and 300 km Altitude," J. Geophys. Res., 86, 7617 (1981).

Keskinen, M. J., and S. L. Ossakow, "Non Linear Evolution of Plasma Enhancements in the Auroral Ionosphere: 1. Long Wavelength Irregularities," J. Geophys. Res., 87, 144 (1982).

Keskinen, M. J., and S. L. Ossakow, "Non-Linear Evolution of Convecting Plasma Enhancements in the Auroral Ionosphere, 2. Small Scale Irregularities," J. Geophys. Res., 88, 474 (1982).

Keskinen, M. J., and S. L. Ossakow, "Effect of Different Initial Conditions on the Evolution of the E x B Gradient Drift Instability in Ionospheric Plasma Clouds," NRL Memorandum Report 4490, Naval Research Laboratory, Washington, DC (1981).

Keskinen, M. J., and S. L. Ossakow, "Preliminary Report of Numerical Simulations of Intermediate Wavelength Collisional Rayleigh-Taylor Instability in Equatorial Spread F," J. Geophys. Res., 85, 1775 (1980).

Kofman, W. and V. B. Wickwar, "Very High Electron Temperatures in the Daytime F-Region at Sondrestrom," Geophys. Res. Letts., 1, 919 (1984).

Knudsen, W. C., "Magnetospheric Convection and the High Latitude F_2 Ionosphere," J. Geophys. Res., 79, 1046 (1974).

Kraichnan, R. H., "Statistical Dynamics of Two-Dimensional Flow," J. Fluid Mech., 67, 155 (1975).

Kraichnan, R. H., "Inertial Ranges in Two-Dimensional Turbulence," Phys. of Fluids, 10, 1417 (1967).

Lassen, K., J. R. Sharber, and J. D. Winningham, "The Development of Auroral and Geomagnetic Substorm Activity after a Southward Turning of the Interplanetary Magnetic Field Following Several Hours of Magnetic Calm," J. Geophys. Res., 82, 5031 (1977).

Linson, L. M., and J. B. Workman, "Formation of Striations in Ionospheric Plasma Clouds," J. Geophys. Res., 75, 3211, (1970).

Livingston, R. C., "Heater-Generated Intermediate-Scale Irregularities: Spatial Distribution and Spectral Characteristics," Radio Sci., 18, 253 (1983).

Livingston, R. C., C. L. Rino, J. Owen, and R. Tsunoda, "The Anisotropy of High-Latitude Nighttime F Region Irregularities," J. Geophys. Res., 87, 10,519 (1982).

Livingston, R. C., C. L. Rino, J. P. McClure, and W. B. Hanson, "Spectral Characteristics of Medium-Scale Equatorial F-Region Irregularities," J. Geophys. Res., 86, 2421 (1981).

Lui, A. T. Y., C.-I. Meng, and S. Ismail, "Large Amplitude Undulations on the Equatorward Boundary of the Diffuse Aurora," J. Geophys. Res., 87, 2385 (1982).

Lyons, L. R., "Generation of Large-scale Regions of Auroral Currents Electric Potentials and Precipitation by the Divergence of the Convection Electric Field," J. Geophys. Res., 85, 17 (1980).

Maynard, N. C., "Electric Field Measurements Across the Harang Discontinuity," J. Geophys. Res., 79, 4620 (1974).

McDonald, B. E., T. P. Coffey, S. Ossakow, and R. N. Sudan, "Preliminary Report of Numerical Simulation of Type 2 Irregularities in the Equatorial Electrojet," J. Geophys. Res., 79, 2551 (1974).

Nagy, A. F., R. J. Cicerone, P. B. Hays, K. D. McWatters, J. W.
    Meriwether, A. E. Belon, and C. L. Rino, "Simultaneous Measure-
    ment of Ion and Neutral Motions by Radar and Optical Techniques,"
    Radio Sci., 9, 315 (1974).

Ossakow, S. L., "Ionospheric Irregularities," Rev. Geophys. Space Phys.,
    17, 521 (1979).

Ossakow, S. L., and P. K. Chaturvedi, "Current Convective Instability in
    the Diffuse Aurora," Geophys. Res. Letts., 6, 322 (1979).

Ott, E., and D. T. Farley, "The K Spectrum of Ionospheric Irregularities,"
    J. Geophys. Res., 79, 2469 (1974).

Perkins, F. W., and J. H. Doles III, "Velocity Shear and the E x B
    Instability," J. Geophys. Res., 80, 211 (1975).

Perkins, F. W., N. J. Zabusky, and J. H. Doles, III, "Deformation and
    Striation of Plasma Clouds in the Ionosphere, 1." J. Geophys. Res.,
    78 (1973).

Quegan, S., G. J. Bailey, R. J. Moffett, R. A. Heelis, T. J. Fuller-
    Rowell, D. Rees, and R. W. Spiro, "A Theoretical Study of the Distri-
    bution of Ionization in the High-Latitude Ionosphere and the Plasma-
    sphere: First Results on the Mid-Latitude Trough and the Light-Ion
    Trough," J. Atmos. Terr. Phys., 44, 619 (1982).

Rees, D., N. Lloyd, P. J. Charleton, M. Carlson, J. Murdin, and I.
    Haggstrom, "Comparison of Plasma Flow and Thermospheric Circulation
    over Northern Scandinavia using EISCAT and a Fabry-Perot Interfero-
    meter," Preprint (1984).

Reiff, P. H., R. W. Spiro, and T. W. Hill, "Dependence of Polar Cap
    Potential Drop on Interplanetary Parameters," J. Geophys. Res., 86,
    7639 (1981).

Rino, C. L., "On the Application of Phase Screen Models to the Interpre-
    tation of Ionospheric Scintillation Data," Radio Sci., 17, 855
    (1982).

Rino, C. L., "A Power Law Phase Screen Model for Ionospheric Scintillation
    Studies, 1. Weak Scatter," Radio Sci., 14, 1135 (1979).

Rino, C. L., R. C. Livingston, R. T. Tsunoda, R. M. Robinson, J. F.
    Vickrey, C. Senior, M. D. Cousins, J. Owen, and J. A. Klobuchar,
    "Recent Studies of the Structure and Morphology of Auroral Zone
    F-Region Irregularities," Radio Sci., 18, 1167 (1983).

Rino, C. L., R. T. Tsunoda, J. Petriceks, and R. C. Livingston, "Simultaneous Rocket-Borne Beacon and in-situ Measurements of Equatorial Spread F--Intermediate Wavelength Results," J. Geophys. Res., 86, 2411 (1981).

Rino, C. L., V. B. Wickwar, P. M. Banks, S.-I. Akasofu, and E. Rigger, "Incoherent Scatter Radar Observations of Westward Electric Fields, 2." J. Geophys. Res., 79, 4669 (1974).

Rishbeth, H., "Polarization Fields Produced by Winds in the Equatorial F Region," Planet. Space Sci., 19, 357 (1971).

Robinson, R. M., R. R. Vondrak, and T. A. Potemra, "Electrodynamic Properties of the Evening Sector Ionosphere within the Region 2 Field-Aligned Current Sheet," J. Geophys. Res., 87, 731 (1982).

Robinson, R. M., E. A. Bering, R. R. Vondrak, H. R. Anderson and P. A. Cloutier, "Simultaneous Rocket and Radar Measurements of Currents in an Auroral Arc," J. Geophys. Res., 86, 7703 (1981).

Roble, R. G., and M. H. Rees, "Time-Dependent Studies of the Aurora: Effects of Particle Precipitation on the Dynamic Morphology of Ionospheric and Atmospheric Properties," Planet. Space Sci., 25, 991 (1977).

Roble, R. G., "The Thermosphere", in Studies in Geophysics: The Upper Atmosphere and Magnetosphere, chap. 3, pp. 57-71, The National Research Council, Washington, DC (1977).

Roble, R. G., R. E. Dickinson, and E. C. Ridley, "Global Circulation and Temperature Structure of Thermosphere with High-Latitude Convection," J. Geophys. Res., 87, 1599 (1982).

Saflekos, N. A., W. J. Burke, and P. F. Fougere, "Large Amplitude Electric Field Fluctuations Near the Harang Discontinuity," Accepted by Radio Sci., 1985.

Scannapieco, A. J., S. L. Ossakow, S. R. Goldman, and J. M. Pierre, "Plasma Cloud Late Time Striation Spectra," J. Geophys. Res., 81, 6037 (1976).

Schiel, M. A., and L. A. Frank, "Electron Observations Between the Inner Edge of the Plasma Sheet and the Plasmasphere," J. Geophys. Res., 75, 5401 (1970).

Schunk, R. W., and P. M. Banks, "Auroral N2 Vibrational Excitation and the Electron Density Trough," Geophys. Res. Letts., 2, 239 (1975).

Schunk, R. W., P. M. Banks, and W. J. Raitt, "Effects of Electric Fields And Other Processes Upon the Nighttime High-Latitude F Layer," J. Geophys. Res., 81, 3271 (1976).

Senior, C., R. M. Robinson, and T. A. Potemra, "Relationship Between Field-Aligned Currents, Diffuse Auroral Precipitation and the Westward Electrojets in the Early Morning Sector," J. Geophys. Res., 87, 10469 (1982).

Seyler, C. E., Y. Salu, D. Montgomery, and G. Knorr, "Two-Dimensional Turbulence in Inviscid Fluids or Guiding Center Plasmas," Phys. of Fluids, 18, 7 (1975).

Shiau, J., and A. Simon, "Barium Cloud Growth and Striation in a Conducducting Background," J. Geophys. Res., 79, 1895 (1974).

Simon, A., "Growth and Stability of Artificial Ion Clouds in the Ionosphere," J. Geophys. Res., 75, 6287 (1970).

Simon, A., "Instability of a Partially Ionized Plasma in Crossed Electric and Magnetic Fields," Phys. Fluids, 6, 382 (1963).

Singh, M., and E. P. Szuszczewicz, "Composite Equatorial Spread F Wave Number Spectra from Medium to Short Wavelengths," J. Geophys. Res., 89, 2313 (1984).

Sojka, J. J., R. W. Schunk, J. V. Evans, J. M. Holt, and R. H. Wand, "Comparison of Model High-Latitude Electron Densities with Millstone Hill Observations," J. Geophys. Res., 88, 7783 (1983).

Spiro, R. W., P. H. Reiff, and L. J. Maher, Jr., "Precipitating Electron Energy Flux and Auroral Zone Conductances--An Empirical Model," J. Geophys. Res., 87, 8215 (1982).

St.-Maurice, J. P., and W. B. Hanson, "Ion Frictional Heating at High Latitudes and Its Possible Use for an in-situ Determination of Neutral Thermospheric Winds and Temperatures," J. Geophys. Res., 87, 7580 (1982).

Tanskanen, P. J., D. A. Hardy, and W. J. Burke, "Spectral Characteristics at Precipitating Electrons Associated with Visible Auroral in the Premidnight Oval During Periods of Substorm Activity," J. Geophys. Res., 86, 1379 (1981).

Tsunoda, R. T. "Control of the Seasonal and Longitudinal Occurrence of Equatorial Scintillations by the Longitudinal Gradient in Integrated E-Region Pedersen Conductivity," J. Geophys. Res., 90, 447 (1985).

211

Tsunoda, R. T., "Time Evolution and Dynamics of Equatorial Backscatter Plumes, 1. Growth Phase," J. Geophys. Res., 86, 139 (1981).

Tsunoda, R. T., and J. F. Vickrey, "Evidence of East-West Structure in Large-Scale F-Region Plasma Enhancements in the Auroral Zone," Submitted to J. Geophys. Res., 1985.

Tsunoda, R. T., R. M. Robinson, and C. Senior, "Two Possible Types of Plasma-Density Enhancements in the Auroral F Layer," Submitted to Radio Sci., 1985.

Vickrey, J. F., and M. C. Kelley, "Irregularities and Instabilities in the Auroral F Region," in High Latitude Space Plasma Physics, B. Hultqvist and T. Hagfors, eds., Plenum Publishing Corp., pp. 95-113 (1983).

Vickrey, J. F., and M. C. Kelley, "The Effects of a Conducting E Layer on Classical F-Region Cross-Field Plasma Diffusion," J. Geophys. Res., 87, 4461 (1982).

Vickrey, J. F., R. R. Vondrak, and S. M. Matthews, "The Diurnal and Latitudinal Variations of Auroral Zone Ionospheric Conductivity," J. Geophys. Res., 86, 65 (1981).

Vickrey, J. F., C. L. Rino, and T. A. Potemra, "Chatanika/TRIAD Observations of Unstable Ionospheric Enhancements in the Auroral F-Region," Geophys. Res. Letts., 7, 789 (1980).

Vickrey, J. F., M. C. Kelley, R. Pfaff and S. R. Goldman, "Low-Altitude Image Striations Associated with Bottomside Equatorial Spread F--Observations and Theory," J. Geophys. Res., 89, 2955 (1984).

Volk, H. J., and G. Haerendel, "Striations in Ionospheric Ion Clouds, 1," J. Geophys. Res., 76, 4541 (1971).

Wallis, D. D., and E. E. Budzinski, "Empirical Models of Height Integrated Conductivities," J. Geophys. Res., 86, 125 (1981).

Watkins, B. J., "A Numerical Computer Investigation of the Polar F-Region Ionosphere," Planet. Space Sci., 26, 559 (1978).

Watkins, B. J., and P. G. Richards, "A Theoretical Investigation of the Role of Neutral Winds and Particle Precipitation in the Formation of the Auroral F Region Ionosphere," J. Atmos. Ter. Phys., 41, 179 (1979).

Weber, E. J., J. Buchau, and J. G. Moore, "Airborne Studies of Equatorial F-Layer Ionospheric Irregularities," J. Geophys. Res., 85, 4631 (1980).

Weber, E. J., R. T. Tsunoda, J. Buchau, R. E. Sheehan, D. J. Strickland, W. Whiting, and J. G. Moore, "Coordinated Measurements of Auroral Zone Plasma Enhancements," J. Geophys. Res., 90, 6497 (1985).

Whalen, J. A., "A Quantitative Description of the Spatial Distribution and Dynamics of the Energy Flux in the Continuous Aurora," J. Geophys. Res., 88, 7155 (1983).

Wickwar, V. B., J. W. Meriwether, P. B. Hays, and A. F. Nagy, "The Meridional Thermospheric Neutral Wind Measured by Radar and Optical Techniques in the Auroral Region," J. Geophys. Res., 89, 10987 (1984).

Zabusky, N. J., J. H. Doles, III, and F. W. Perkins, "Deformation and Striation of Plasma Clouds in the Ionosphere, 2. Numerical Simulation of a Nonlinear Two-Dimensional Model," J. Geophys. Res., 78, 711 (1973).

Zalesak, S. T., S. L. Ossakow, and P. K. Chaturvedi, "Nonlinear Equatorial Spread F: The Effect of Neutral Winds and Background Pedersen Conductivity," J. Geophys. Res., 87, 151 (1982).

Zalesak, S. T., P. K. Chaturvedi, S. L. Ossakow, and J. A. Feder, "Finite Temperature Effects on the Evolution of Ionospheric Barium Clouds in the Presence of a Conducting Background Ionosphere, I. The Simplest Case: Incompressible Background Ionosphere, Equipotential Magnetic Field Lines, and an Altitude-Invariant Neutral Wind," J. Geophys. Res., 90, 4299 (1985).

214

DISTRIBUTION LIST

DEPARTMENT OF DEFENSE

DEFENSE ADVANCED RSCH PROJ AGENCY
 ATTN: GSD R ALEWINE
 ATTN: T TETHER

DEFENSE INTELLIGENCE AGENCY
 ATTN: RTS-2B

DEFENSE NUCLEAR AGENCY
 ATTN: NATF
 ATTN: NAWE
3 CYS ATTN: RAAE
 ATTN: RAAE P LUNN
 ATTN: RAEE
 ATTN: RAEE K SCHWARTZ
 ATTN: STNA
4 CYS ATTN: STTI-CA

DEFENSE TECHNICAL INFORMATION CENTER
12 CYS ATTN: DD

FIELD COMMAND DEFENSE NUCLEAR AGENCY
 ATTN: FCPR
 ATTN: FCTT W SUMMA
 ATTN: FCTXE

DEPARTMENT OF THE ARMY

BMD ADVANCED TECHNOLOGY CENTER
 ATTN: ATC-O W DAVIES
 ATTN: ATC-R D RUSS
 ATTN: ATC-R W DICKSON

HARRY DIAMOND LABORATORIES
 ATTN: DELHD-NW-R R WILLIAMS 22000
2 CYS ATTN: SCHLD-NW-P

U S ARMY ATMOSPHERIC SCIENCES LAB
 ATTN: SLCAS-AE-E

U S ARMY COMM-ELEC ENGRG INSTAL AGENCY
 ATTN: CC-CE-TP W NAIR

U S ARMY COMMUNICATIONS R&D COMMAND
 ATTN: DRDCO-COM-RY W KESSELMAN

U S ARMY FOREIGN SCIENCE & TECH CTR
 ATTN: DRXST-SD

U S ARMY NUCLEAR & CHEMICAL AGENCY
 ATTN: LIBRARY

U S ARMY SATELLITE COMM AGENCY
 ATTN: DOCUMENT CONTROL

U S ARMY STRATEGIC DEFENSE CMD
 ATTN: BMDSC-LEH R C WEBB
 ATTN: DASD-H-SAV

U S ARMY STRATEGIC DEFENSE COMMAND
 ATTN: DASD-H-L M CAPPS
 ATTN: DASD-H-S W DAVIES
 ATTN: DASD-H-SA R C WEBB
 ATTN: DASD-H-Y D RUSS

DEPARTMENT OF THE NAVY

LEAHY CG 16
 ATTN: WEAPONS OFFICER

NAVAL OCEAN SYSTEMS CENTER
 ATTN: CODE 532
 ATTN: CODE 5322 M PAULSON
 ATTN: CODE 5323 J FERGUSON

NAVAL RESEARCH LABORATORY
 ATTN: CODE 4108 P RODRIGUEZ
 ATTN: CODE 4187
 ATTN: CODE 4700
 ATTN: CODE 4700 S OSSAKOW
 ATTN: CODE 4720 J DAVIS
 ATTN: CODE 4780
 ATTN: CODE 6700
 ATTN: CODE 7500 B WALD
 ATTN: CODE 7950 J GOODMAN

NAVAL SPACE SURVEILLANCE SYSTEM
 ATTN: J BURTON

OFFICE OF NAVAL RESEARCH
 ATTN: CODE 412, W CONDELL

SPACE & NAVAL WARFARE SYSTEMS CMD
 ATTN: CODE 3101 T HUGHES
 ATTN: CODE 501A
 ATTN: PDE-110-X1 B KRUGER
 ATTN: PDE-110-11021 G BRUNHART
 ATTN: PME 106-4 S KEARNEY
 ATTN: PME 117-20
 ATTN: PME-106 F W DIEDERICH

STRATEGIC SYSTEMS PROGRAMS (PM-1)
 ATTN: NSP-2141
 ATTN: NSP-2722
 ATTN: NSP-43 TECH LIB

THEATER NUCLEAR WARFARE PROGRAM OFC
 ATTN: PMS-423 D SMITH

DEPARTMENT OF THE AIR FORCE

AIR FORCE GEOPHYSICS LABORATORY
 ATTN: CA A STAIR
 ATTN: LID J RAMUSSEN
 ATTN: LIS J BUCHAU
 ATTN: LS
 ATTN: LS H GARDINER
 ATTN: LS R O'NIEL
 ATTN: LYD K CHAMPION

DEPT OF THE AIR FORCE (CONTINUED)

AIR FORCE WEAPONS LABORATORY, AFSC
ATTN: NTN
ATTN: SUL

AIR FORCE WRIGHT AERONAUTICAL LAB/AAAD
ATTN: A JOHNSON
ATTN: W HUNT

ROME AIR DEVELOPMENT CENTER, AFSC
ATTN: OCDS R SCHNEIBLE
ATTN: TSLD

SPACE COMMAND
ATTN: DC T LONG

DEPARTMENT OF ENERGY

LOS ALAMOS NATIONAL LABORATORY
ATTN: D SAPPENFIELD
ATTN: D SIMONS
ATTN: J WOLCOTT
ATTN: MS 664 J ZINN
ATTN: R JEFFRIES
ATTN: T KUNKLE, ESS-5

SANDIA NATIONAL LABORATORIES
ATTN: D DAHLGREN
ATTN: D THORNBROUGH
ATTN: ORG 1231 R C BACKSTROM
ATTN: ORG 1250 W BROWN
ATTN: ORG 4231 T WRIGHT
ATTN: SPACE PROJECT DIV
ATTN: TECH LIB 3141

OTHER GOVERNMENT

CENTRAL INTELLIGENCE AGENCY
ATTN: OSWR/NED
ATTN: OSWR/SSD FOR K FEUERPFETL

DEPARTMENT OF DEFENSE CONTRACTORS

AEROSPACE CORP
ATTN: D OLSEN
ATTN: E RODRIGUEZ
ATTN: I GARFUNKEL
ATTN: J KLUCK
ATTN: J STRAUS
ATTN: K S CHO
ATTN: R SLAUGHTER
ATTN: T SALMI
ATTN: V JOSEPHSON

AUSTIN RESEARCH ASSOCIATES
ATTN: J THOMPSON

AUTOMETRIC, INC
ATTN: C LUCAS

BDM CORP
ATTN: A VITELLO
ATTN: L JACOBS

BERKELEY RSCH ASSOCIATES, INC
ATTN: C PRETTIE
ATTN: J WORKMAN
ATTN: S BRECHT

CORNELL UNIVERSITY
ATTN: D FARLEY JR
ATTN: M KELLY

EOS TECHNOLOGIES, INC
ATTN: B GABBARD
ATTN: W LELEVIER

GENERAL RESEARCH CORP
ATTN: B BENNETT

INSTITUTE FOR DEFENSE ANALYSES
ATTN: E BAUER
ATTN: H WOLFHARD

JAYCOR
ATTN: J SPERLING

JOHNS HOPKINS UNIVERSITY
ATTN: C MENG
ATTN: J D PHILLIPS
ATTN: J NEWLAND
ATTN: K POTOCKI
ATTN: R STOKES 1-W250
ATTN: T EVANS

KAMAN TEMPO
ATTN: B GAMBILL
ATTN: DASIAC
ATTN: W MCNAMARA

KAMAN TEMPO
ATTN: DASIAC

M I T LINCOLN LAB
ATTN: D TOWLE L-230
ATTN: I KUPIEC L-100

M/A COM LINKABIT INC
ATTN: H VAN TREES

MAXIM TECHNOLOGIES, INC
ATTN: J LEHMAN
ATTN: J MARSHALL
ATTN: R MORGANSTERN

MISSION RESEARCH CORP
ATTN: C LAUER
ATTN: D KNEPP
ATTN: F FAJEN
ATTN: F GUIGLIANO
ATTN: G MCCARTOR
ATTN: R BIGONI
ATTN: R BOGUSCH
ATTN: R DANA
ATTN: R HENDRICK
ATTN: R KILB
ATTN: S GUTSCHE
ATTN: TECH LIBRARY

216

DEPT OF DEFENSE CONTRACTORS (CONTINUED)

PHOTOMETRICS, INC
    ATTN: I KOFSKY

PHYSICAL DYNAMICS, INC
    ATTN: E FREMOUW

PHYSICAL RESEARCH, INC
    ATTN: R DELIBERIS
    ATTN: T STEPHENS

PHYSICAL RESEARCH, INC
    ATTN: J DEVORE
    ATTN: J THOMPSON
    ATTN: W SCHLUETER

R & D ASSOCIATES
    ATTN: B MØLLER
    ATTN: C GREIFINGER
    ATTN: F GILMORE
    ATTN: G STCYR
    ATTN: H ORY
    ATTN: M GANTSWEG
    ATTN: M GROVER
    ATTN: P HAAS
    ATTN: R TURCO
    ATTN: W KARZAS
    ATTN: W WRIGHT

R & D ASSOCIATES
    ATTN: B YOON

R & D ASSOCIATES
    ATTN: G GANONG

SCIENCE APPLICATIONS INTL CORP
    ATTN: C SMITH
    ATTN: D HAMLIN
    ATTN: E STRAKER
    ATTN: L LINSON

SRI INTERNATIONAL
    ATTN: C RINO
    ATTN: D MCDANIEL
    ATTN: D NIELSON
    ATTN: G PRICE
    ATTN: G SMITH
    ATTN: J VICKREY
    ATTN: N WALKER
    ATTN: R HEELIS
    ATTN: R LEADABRAND
    ATTN: R LIVINGSTON
    ATTN: R ROBINSON
    ATTN: R TSUNODA
    ATTN: T DABBS
    ATTN: W CHESNUT
    ATTN: W JAYE

TOYON RESEARCH CORP
    ATTN: J GARBARINO
    ATTN: J ISE

UTAH STATE UNIVERSITY
    ATTN: A STEED
    ATTN: D BURT
    ATTN: K BAKER, DIR ATMOS & SPACE SCI
    ATTN: L JENSEN, ELEC ENG DEPT

VISIDYNE, INC
    ATTN: J CARPENTER

END

DTIC

7-86